UC Irvine

UC Irvine Electronic Theses and Dissertations

Title

Exploring the Mysterious Physical Properties in Silver-Indium Binary System and its Applications in High-Temperature Power Electronics

Permalink

https://escholarship.org/uc/item/7qf7w9km

Author

Huo, Yongjun

Publication Date

2017

Peer reviewed|Thesis/dissertation

eScholarship.org Powered by the California Digital Library
University of California

UNIVERSITY OF CALIFORNIA,
IRVINE

Exploring the Mysterious Physical Properties in Silver-Indium Binary System and its Applications in High-Temperature Power Electronics

DISSERTATION

submitted in partial satisfaction of the requirements
for the degree of

DOCTOR OF PHILOSOPHY

in Engineering

by

Yongjun Huo

Dissertation Committee:
Professor Chin C. Lee, Chair
Professor Frank G. Shi
Professor Daniel Mumm

2017

© 2017 Yongjun Huo

DEDICATION

To

my dear family

Whose affections, unconditional love and encouragement
make it possible for me to complete this work,

I love you!

TABLE OF CONTENTS

		Page
LIST OF FIGURE		vi
LIST OF TABLES		xiii
ACKNOWLEDGMENTS		xvi
CURRICULUM VITAE		xvii
ABSTRACT OF THE DISSERTATION		xix
CHAPTER 1	INTRODUCTION	1
1.1	The Dawn of Energy Revolution	1
1.2	Silicon Carbide Material Properties	3
1.3	High-Temperature Power Devices and Electronics	5
1.4	Die-attachments in Electronic Packaging	6
1.5	Dissertation Outline	10
CHAPTER 2	Instrumentations and Experimental Techniques	15
2.1	Introduction	15
2.2	Material Synthesis and Processing	16
2.3	Material Characterizations	25
2.4	Summary	40
CHAPTER 3	Mechanical Properties of Silver-Indium Solid Solution	42
3.1	Introduction	42
3.2	Material Preparation and Characterization	43
3.3	Tensile Test	50
3.4	Stress vs. Strain Characterization	52

3.5 Fractography 55

3.6 Conclusion 60

CHAPTER 4 Anti-tarnishing Property of Silver-Indium Solid Solution 64

4.1 Introduction 64

4.2 Design of Sulfurization Experiment 66

4.3 Experimental Results and Discussions 69

4.4 Summary 78

CHAPTER 5 Anti-tarnishing Mechanism in Silver-Indium Binary System 82

5.1 Introduction 82

5.2 Material Preparation and Characterization 84

5.3 Experimental Results 87

5.4 HSAB Principle and Discussions 97

5.5 Anti-Tarnishing Mechanism 104

5.6 Concluding Remarks 110

CHAPTER 6 Solid Solution Softening Phenomenon in Ag-based Solid Solutions 119

6.1 Introduction 119

6.2 Material Preparation and Characterization 121

6.3 Tensile Test 128

6.4 Experimental Results and Discussions 129

6.5 Fractography 135

6.6 Concluding Remarks 140

CHAPTER 7 Thermal, Electrical and Optical Properties of Ag-In Solid Solution 144

7.1 Introduction 144

7.2 Thermal Property of Ag-In Solid Solution 144

7.3 Electrical Property of Ag-In Solid Solution 147

7.4 Optical Property of Ag-In Solid Solution 149

7.5 Summary 152

CHAPTER 8 Bondable Copper Substrates with Silver Solid Solution Coating for High-Temperature Power Electronic Application 154

8.1 Introduction 154

8.2 Experimental Process 157

8.3 Solid-State Bonding Experimental Results and Discussions 162

8.4 Bondable Copper Substrates Quality Evaluations 167

8.5 TEM Evaluation of 4H-SiC Chip with Cr/Au Metallization Layers 171

8.6 Summary 175

CHAPTER 9 Conclusions and Future Perspectives 178

LIST OF FIGURES

		Page
Figure 2.1	The triangle of material science and engineering	15
Figure 2.2	The schematic set-up of hydrogen-oxygen torch operation system	17
Figure 2.3	Normal pressures of gauges for hydrogen cylinder (left) and for oxygen cylinder (right) at working status	17
Figure 2.4	The picture of quartz tube (top) and filled with metallic shots (bottom)	18
Figure 2.5	Demonstration of vacuum sealing procedures	18
Figure 2.6	The engineering sketches (left) and 3D model (right) of capsules holder	19
Figure 2.7	Metal shots before casting (left) and grown ingot (right) after casting	20
Figure 2.8	The schematic set-up of E-beam evaporation system in general	21
Figure 2.9	Angstrom Engineering EvoVac Glovebox Evaporator	22
Figure 2.10	An illustration of the vacuum furnace: (a) quartz cylinder, (b) upper stainless plate, (c) base plate, (d) graphite platform, (e) heating wire, (f) electrical feed-throughs, (g) platform thermocouples and (h) sample thermocouple	23
Figure 2.11	Different level of material structures characterizations of XRD	25
Figure 2.12	Essential hardware components of Rigaku SmartLab X-ray diffractometer	26
Figure 2.13	Bragg–Brentano optics setting vs. Parallel Beam optics setting	27
Figure 2.14	The interactions between X-ray beams and materials in Bragg–Brentano optics setting	28
Figure 2.15	Three different scanning modes in Parallel Beam optics setting	28
Figure 2.16	The principle of grazing incidence X-ray diffraction (GIXRD) schematic demonstration, tilting X-ray scattering vector (left) and ratios of signal contribution of GIXRD (upper right) and out-plane setting (lower right)	29
Figure 2.17	In-plane XRD schematic demonstration and real machine setting	29

Figure 2.18 The physical scale of dimension for bulk, thin film materials and material surface analysis 30

Figure 2.19 The principle of photoelectric process in X-ray photoelectron spectroscopy (left) and AXIS Supra by Kratos Analytical instrument (right) 31

Figure 2.20 The interaction volume and all of the signals produced by the interaction between the electron beam and sample material 33

Figure 2.21 Philips XL-30 FEG SEM 34

Figure 2.22 FEI Quanta 3D FEG Dual Beam SEM/FIB Instrument 35

Figure 2.23 SEM imaging at 52 °(left) and FIB imaging at 0 °(right) of FIB deposited Pt strip layer 36

Figure 2.24 SEM imaging at 0 °(left) and FIB imaging at 52 °(right) of TEM sample attaching TEM grid by using Omniprobe 36

Figure 2.25 FEI/Philips CM-20 conventional TEM 38

Figure 2.26 Keysight 7500 AFM 39

Figure 3.1 Silver-indium binary phase diagram 44

Figure 3.2 (a) (Ag)-9.5In disk SEM/EDX tested region (left), and (b) (Ag)-19In disk SEM/EDX tested region (right). 46

Figure 3.3a XRD pattern of pure silver disk sample 47

Figure 3.3b XRD pattern of (Ag)-9.5In disk sample 48

Figure 3.3c XRD pattern of (Ag)-19In disk sample 48

Figure 3.4 The geometry of tensile test sample, in accordance with ASTM standard E8/ E8M- 08 51

Figure 3.5 The engineering stress-strain curve of pure silver, (Ag)-9.5In, and (Ag)-19In 52

Figure 3.6 The true stress-strain curve of pure silver, (Ag)-9.5In, and (Ag)-19In 53

Figure 3.7 Fractography of Ag tensile test sample, SEM image at 5000× magnification 56

Figure 3.8 Fractography of (Ag)-9.5In tensile test sample, SEM image at 5000× magnification 56

Figure 3.9a	Fractography of (Ag)-19In tensile test sample, SEM image at 100× magnification	57
Figure 3.9b	SEM image at 1000× magnification	58
Figure 3.9c	SEM image at 2500× magnification	58
Figure 3.9d	SEM image at 10000× magnification	59
Figure 3.10	Representative morphology of dimpled rupture on the fracture surface of (Ag)-19In tensile test sample	59
Figure 4.1	The configuration of the designed closed system for sulfurization experiment	67
Figure 4.2	Equilibrium pressure of sulfur, Σ_i is the total pressure, 2≤ n ≤8, are partial pressures of S_n	68
Figure 4.3	Dektak XT Profilometer measurement profile of silver sulfide layer on pure silver sample	69
Figure 4.4a	The top-view optical microscope image of pure silver disk sample	71
Figure 4.4b	The top-view optical microscope image of Argentium silver disk sample	71
Figure 4.4c	The top-view optical microscope image of (Ag)-9.5In disk sample	72
Figure 4.4d	The top-view optical microscope image of (Ag)-19In disk sample after 15 mins sulfurization experiment	72
Figure 4.5a	The top-view optical microscope image of pure silver disk sample	72
Figure 4.5b	The top-view optical microscope image of Argentium silver disk sample	73
Figure 4.5c	The top-view optical microscope image of (Ag)-9.5In disk sample	73
Figure 4.5d	The top-view optical microscope image of (Ag)-19In disk sample after 30 mins sulfurization experiment	73
Figure 4.6a	The top-view optical microscope image of pure silver disk sample	74
Figure 4.6b	The top-view optical microscope image of Argentium silver disk sample	74
Figure 4.6c	The top-view optical microscope image of (Ag)-9.5In disk sample	74
Figure 4.6d	The top-view optical microscope image of (Ag)-19In disk sample	

after 60 mins sulfurization experiment 75

Figure 4.7 The plot of silver sulfide layer thickness vs. time after sulfurization experiments for pure silver, Argentium silver, (Ag)-9.5In, and (Ag)-19In disk samples. 77

Figure 4.8 The plot of silver sulfide growth rate vs. indium concentration of (Ag)-xxIn solid solution experiment 77

Figure 5.1 GIXRD patterns of the Ag-In thin film samples 86

Figure 5.2 The plot of calculated average lattice constants of Ag-In bulk samples, thin film samples and ICDD standard powder samples with linear fitting curves 86

Figure 5.3a X-ray photoelectron spectra of Ag 3d region 89

Figure 5.3b Chemical shift of Ag 3d 5/2 peaks of Ag-In thin film samples 89

Figure 5.4a X-ray photoelectron spectra of O 1s region 92

Figure 5.4b The trend of O 1s region major peaks shift of Ag-In thin film samples 92

Figure 5.5a Ultraviolet photoelectron spectra of valence bands 96

Figure 5.5b Normalized spectra of Ag valence 4d-bands of Ag-In thin film samples 96

Figure 5.6 The plot of total ground state energy vs. total number of electrons curves in 4d-bands of Ag-In thin film samples 103

Figure 5.7a The plot of logistic fitting curves for calculated total charge transfer and energy lowering of reactions with S_2 molecule and experimental reactions rates with S_8 molecule 108

Figure 5.7b Schematic diagram of Ag tarnishing mechanism 109

Figure 5.7c Ag-In solid solution anti-tarnishing mechanism 109

Figure 5.7d Ag_9In_4 IMC anti-tarnishing mechanism 110

Figure 5.8 Anti-tarnishing mechanism in Ag-In binary system from HSAB principle point of view 111

Figure 6.1a Silver-Aluminum binary phase diagram 122

Figure 6.1b Silver-Gallium binary phase diagram 123

Figure 6.1c Silver-Tin binary phase diagram 123

Figure 6.2a XRD pattern of (Ag)-10Al solid solution disk sample 125

Figure 6.2b XRD pattern of (Ag)-10Ga solid solution disk sample 125

Figure 6.2c XRD pattern of (Ag)-8Sn solid solution disk sample 126

Figure 6.3 The geometry of tensile test sample, in accordance with ASTM standard E8/ E8M- 08 128

Figure 6.4 The representative engineering stress-strain curves of (Ag)-10Al, (Ag)-10Ga, (Ag)-9.5In and (Ag)-8Sn with that of pure Ag in comparison 130

Figure 6.5 The representative true stress-strain curves of (Ag)-10Al, (Ag)-10Ga, (Ag)-9.5In, and (Ag)-8Sn with that of pure Ag in comparison 131

Figure 6.6 The graphs of strain hardening rates of pure Ag, (Ag)-10Al, (Ag)-10Ga, (Ag)-9.5In, and (Ag)-8Sn 132

Figure 6.7a Fractography of (Ag)-10Al representative tensile test sample, SEM image at 2000× magnification 136

Figure 6.7b SEM image at 5000× magnification 137

Figure 6.8a Fractography of (Ag)-8Sn representative tensile test sample, SEM image at 2000× magnification 137

Figure 6.8b SEM image at 5000× magnification 138

Figure 6.9a Fractography of (Ag)-10Ga representative tensile test sample, SEM image at 1000× magnification 138

Figure 6.9b SEM image at 5000× magnification 139

Figure 6.9c SEM image at 10000× magnification 139

Figure 7.1 Flash method for thermal diffusivity measurement, laser pulse shape (left), schematic of the flash method (middle), characteristic thermal curve for the flash method (right) 146

Figure 7.2 The requirement of the sample for the four-point probe electrical sheet resistance measurement (left) and a picture of real thin film sample during the measurement (right) 148

Figure 7.3	Optical reflectivity spectrum of Ag-In alloy thin film under the visible and infrared range	150
Figure 7.4	AFM measurement results of Ag-In thin film sample on quartz substrate with 5μm × 5μm measured area size, topography AFM image (left) and friction AFM image (right)	150
Figure 7.5	AFM measurement results of Ag-In thin film sample on quartz substrate with 1μm × 1μm measured area size, topography AFM image (left) and friction AFM image (right)	151
Figure 7.6	3D Topography AFM Image Ag-In thin film sample on quartz substrate with 5μm × 5μm measured area size (left) and 1μm × 1μm measured area size (right)	151
Figure 8.1a	GIXRD patterns of (Ag)-9.5In on Cu substrate	158
Figure 8.1b	GIXRD patterns of (Ag)-19In on Cu substrate	159
Figure 8.2a	XPS survey quantification results of (Ag)-9.5In film coating	161
Figure 8.2b	XPS survey quantification results of (Ag)-19In film coating	161
Figure 8.3a	Optical microscope images of solid-state bonding results between (Ag)-9.5In coated bondable substrate and silicon chip at 100× magnification	163
Figure 8.3b	Optical microscope images of solid-state bonding results between (Ag)-9.5In coated bondable substrate and silicon chip at 1000× magnification	164
Figure 8.4a	Scanning electron microscope image of solid-state bonding results between (Ag)-9.5In coated bondable substrate and silicon chip at 2000 × magnification	165
Figure 8.4b	Scanning electron microscope image of solid-state bonding results between (Ag)-9.5In coated bondable substrate and silicon chip at 5000 × magnification	166
Figure 8.4c	Scanning electron microscope image of solid-state bonding results between (Ag)-9.5In coated bondable substrate and silicon chip at 20000 × magnification	166
Figure 8.4d	Scanning electron microscope image of solid-state bonding results between (Ag)-9.5In coated bondable substrate and silicon chip at 50000 × magnification	167

Figure 8.5 The SEM image of the surface of bondable Cu substrate 168

Figure 8.6a The SEM cross-sectional image of bondable Cu substrate after Pt deposition and FIB cutting 169

Figure 8.6b Zoomed-in SEM cross-sectional image of bondable Cu substrate after Pt deposition and FIB cutting with direct measurement of the (Ag)-9.5In coating layer 169

Figure 8.7 AFM measurement results of (Ag)-9.5In coating layer of bondable copper substrate sample with 5μm × 5μm measured area size, topography AFM image (left) and friction AFM image (right) 170

Figure 8.8 AFM measurement results of (Ag)-9.5In coating layer of bondable copper substrate sample with 1μm × 1μm measured area size, topography AFM image (left) and friction AFM image (right) 170

Figure 8.9 3D Topography AFM Image (Ag)-9.5In coating layer of bondable copper substrate sample with 5μm × 5μm measured area size (left) and 1μm × 1μm measured area size (right) 171

Figure 8.10 FIB cut/lift-off TEM sample as attached to the TEM grid and detached from Omniprobe (left) and the TEM sample electron electron-beam transparent thickness as finished the final steps of FIB thinning with low voltage (5 kV) and small current 173

Figure 8.11 The bright field TEM imaging of Cr/Au E-beam layers on the 4H-SiC chip 173

Figure 8.12 HRTEM imaging of Cr/Au layers on the 4H-SiC single crystal (left) and FTT electron diffraction patterns under the view of HRTEM (right) 174

LIST OF TABLES

Page

Table 1.1 A summary of popular die attachment materials with melting and operating temperatures 7

Table 3.1 SEM/EDX results of chemical compositions for (Ag)-9.5In and (Ag)-19In disks in the tested region 46

Table 3.2 A summary of Rigaku SmartLab X-ray diffractometer measurement conditions and parameters 47

Table 3.3a A summary of XRD measurement data of pure silver disk sample 49

Table 3.3b A summary of XRD measurement data of (Ag)-9.5In disk sample 49

Table 3.3c A summary of XRD measurement data of (Ag)-19In disk sample after PDXL analysis 49

Table 3.4 The dimensions of tensile test sample, in accordance with ASTM standard E8/ E8M- 08 51

Table 3.5 A summary of mechanical properties of (Ag)-9.5In and (Ag)-19In with pure Ag in comparison 54

Table 4.1 A summary of sulfurization experimental results of Argentium silver, (Ag)-9.5In and (Ag)-19In with pure silver in comparison 75

Table 5.1 A summary of Ag 3d regions spectral peaks position, FWHM and chemical shift of Ag-In thin film samples 88

Table 5.2 A summary of O 1s regions spectral peaks position of Ag-In thin film 93

Table 5.3 A summary of normalized UPS spectra characteristic information of Ag-In thin film samples 95

Table 5.4 A summary of absolute electronegativity, chemical hardness, and chemical softness of Ag-In thin film samples and molecular gases 104

Table 5.5 A summary of calculated total charge transfer and energy lowering of reactions with S_2 molecule and experimental reactions rates with S_8 molecule 106

Table 6.1a	A summary of XRD measurement data of (Ag)-10Al solid solution disk sample	126
Table 6.1b	A summary of XRD measurement data of (Ag)-10Ga solid solution disk sample	126
Table 6.1c	A summary of XRD measurement data of (Ag)-8Sn solid solution disk sample	127
Table 6.2	SEM/EDX spectrum mapping quantification results of chemical compositions for (Ag)-10Al, (Ag)-10Ga and (Ag)-8Sn disk samples	127
Table 6.3	The dimensions of tensile test sample, in accordance with ASTM standard E8/ E8M- 08	129
Table 7.1	The summary of thermal diffusivity measurement results and calculated thermal conductivity results for pure Ag, Ag-In, Ag-Al, Ag-Ga, and Ag-Sn solid solutions	146
Table 7.2	Electrical resistivity, relative electrical conductivity and relative thermal conductivity of the Ag-In alloy thin film samples	148
Table 8.1a	Crystallographic information of silver-indium solid solutions of (Ag)-9.5In film	159
Table 8.1b	Crystallographic information of silver-indium solid solutions of (Ag)-19In film	159

ACKNOWLEDGMENTS

I consider myself to be a truly lucky person to have so many great people who helped me tremendously during these years of my PhD. study. Without the help and contribution from them, I could barely imagine and would never complete the research works written in this dissertation.

First of all, I would express my gratitude towards my PhD. advisor, Professor Chin C. Lee, who has been always providing the great academic guidance and supported me both financially and spiritually all along the way through my PhD. study. I will always remember all of his words with wisdoms in teaching me how to conduct scientific research with great originality. I will always be indebted to my PhD. advisor for the rest of my life.

I would also express my gratitude towards my PhD. committee members, Professor Frank G. Shi, Professor Daniel R. Mumm and Professor James Earthman, in providing their great insights and constructive comments to my research works. I deeply appreciated it for their help and guidance in various milestones my PhD. study.

Secondly, I would thanks to my colleagues, Dr. Shou-Jen Hsu, Dr. Yuan-yun Wu, Dr. Yi-ling Chen, Jiaqi Wu, Shao-wei Fu, and Yipin Wu for contributing their expertise, discussions and collaborations, and in creating a family-like working environment during my PhD. study. In addition, I am also indebted to IMRI staff members, Dr. Jian-Guo Zheng and Dr. Qiyin Lin for providing laboratory assistantship to me and teaching me various very useful experimental techniques. Financially, I would express my gratitude towards II-VI Foundation and Henry Samueli Fellowship.

Lastly, I would like to say something to my dear family. I would like to express my love towards great my parents, Ping Huo and Xiyun Liu, for their unconditional love to me: I am so lucky to be your son and I am truly happy if I could let you feel proud about your son.
To my soul-mate, Xiao-Ting Yang: Sorry for letting you wait me all these years and I will be loving you, as always.

CURRICULUM VITAE

Yongjun Huo

2012 — Bachelor of Engineering,
School of Materials Science and Engineering,
Beijing Institute of Technology

2014 — Master of Science in Engineering,
Concentration in Materials and Manufacturing Technology,
The Henry Samueli School of Engineering,
University of California, Irvine

2013 — 2017 — Graduate Research Assistant,
Materials and Manufacturing Technology
University of California, Irvine

2014 — 2016 — Teaching Assistant,
Department of Electrical and Computer Engineering,
University of California, Irvine

2014 — 2017 — Laboratory Assistant,
Irvine Materials Research Institute,
University of California, Irvine

2017 — Doctor of Philosophy in Engineering,
Concentration in Materials and Manufacturing Technology,
The Henry Samueli School of Engineering,
University of California, Irvine

PUBLICATIONS

Journal Publications

1. **Y. Huo** and C. C. Lee. “The Growth and Stress vs. Strain Characterization of the Silver Solid Solution Phase with Indium”, *Journal of Alloys and Compounds*, vol. 661, pp. 372-379, March 2016.

2. **Y. Huo**, S. Fu, Y. Chen and C. C. Lee. “A Reaction Study of Sulfur Vapor with Silver and Silver-Indium Solid Solution as a Tarnishing Test Method”, *Journal of Materials Science: Materials in Electronic*s, vol. 27, No. 10, pp. 10382–10392, October 2016.

3. **Y. Huo**, J. Wu, and C. C. Lee. “Study of Anti-tarnishing Mechanism in Ag-In Binary System by Using Semi-Quantum-Mechanical Approach”, *Journal of Electrochemical Society*, accepted, 2017.

4. **Y. Huo**, J. Wu, and C. C. Lee. “The Mechanical Properties of the Silver Solid Solution Phase with Solute Elements of Aluminum, Tin and Gallium”, under preparation.

Proceedings of Conference Presentations

1. **Y. Huo** and C. C. Lee. “Bondable Copper Substrates with Silver Solid Solution Coatings for High-Power Electronic Applications”, *Electronic Components and Technology Conference (ECTC)*, 2017 IEEE 67th. IEEE, in press, 2017.

2. Y. Chen, **Y. Huo** and C. C. Lee. "Design and Fabrication of Silver Solid Solution Layer on Silicon and its Solid-State Bonding Applications", *Electronic Components and Technology Conference (ECTC)*, 2016 IEEE 66th. IEEE, pp. 420-425, 2016.

3. **Y. Huo** and C. C. Lee. "Anti-Tarnishing Evaluations of Silver Solid Solution Phase with Indium", *Electronic Components and Technology Conference (ECTC)*, 2015 IEEE 65th. IEEE, pp. 2180-7, 2015.

ABSTRACT OF THE DISSERTATION

Exploring the Mysterious Physical Properties in Silver-Indium Binary System and its Applications in High-Temperature Power Electronics

By

Yongjun Huo

Doctor of Philosophy in Engineering

With Concentration in Materials and Manufacturing Technology

University of California, Irvine, 2017

Professor Chin C. Lee, Chair

Upon the dawn of the new millennium, a new generation of energy revolution is incoming. With the advent and development of wide bandgap (WBG) semiconductor materials, i.e., silicon carbide (SiC) and gallium nitride (GaN), the figure of merits of high-temperature power electronics have been largely improved by breaking the fundamental physical boundaries set by traditional silicon-based semiconductor devices. In order to fulfill the full potential of WBG-based technology, it is indeed essential and necessary to develop compatible electronic packaging materials that can sustain high operating temperature. Silver-indium (Ag-In) solid solution is such one of the promising candidates of metallic material for high-temperature and power electronics.

In the content of this dissertation, the author had systematically investigated multi-physical material properties of the Ag-In and other Ag-based solid solution. First of all, the author had discovered that Ag-In solid solution possessed the superior mechanical

properties, i.e., low yield strength, high mechanical strength, and high ductility, which had proved to be an ideal combination for solid-state bonding applications. Secondly, the author had also discovered that Ag-In solid solution exhibited a great anti-tarnishing property, which could potentially solve the problematic tarnishing issues involved in Ag and its alloy applications. Moreover, a quantitative and theoretical model had been established by the author to explain the underlying anti-tarnishing mechanism within the context of HSAB principle, conceptual DFT formalization and Hammer-Nørskov (HN) d-band model, using an original semi-quantum-mechanical approach. Furthermore, the abnormal phenomenon that had been found in Ag-In system, namely, solid solution softening, was further studied and discussed in Ag-Al, Ag-Ga, and Ag-Sn binary systems. In addition, various physical properties of Ag-In alloys, i.e., thermal, electrical and optical properties, were studied to enable to the multi-physical co-designs, leading to Ag-In alloys potential various applications. Based on the findings above, an advanced solid-state bonding technology had been proposed using Ag-In solid solution for high-temperature power electronics applications. Finally, the concluding remarks and future research perspectives were discussed, where a unified multi-physical theorem and material co-design principles for electronic packaging could be developed in the future study.

Chapter 1

INTRODUCTION

1.1 The Dawn of Energy Revolution

Technology advancement is one of basis and momentum of human civilization and modernization. The development of semiconductor materials and devices has been changing and reshaping the world over and over again during past half century. With the advent of first germanium (Ge)-based semiconductor bipolar transistors [1], it gave the birth to solid state electronics, subsequently silicon (Si)-based semiconductors materials, devices and integrated circuits (ICs) [2], and eventually personal computers (PCs), thereby changing the lifestyles of almost everyone in the modern society. Due to the invention of metal-oxide-semiconductor field effect transistors (MOSFETs) [3], silicon-based technology has great technological advantages and is unparalleled in the field of computing and data analysis, since the MOSFETs can be scale down to shrinkage its physical size, thereby both lowering its manufacturing cost and lifting its performance at the same time. The famous Moore's Law has been projecting the technological advancement of silicon-based technology correctly over past several decades, thereby making enormous economic benefits to the whole industrial community of Silicon Valley. Nowadays, Si-based large scale integrated (LSIs) or very large scale integrated circuits (VLSIs) [4] are the key components in most of the electrical and electronics systems. It has been relative well-developed and mature for silicon in terms of technology and market. However, silicon has its own limitation in terms of its fundamental physical properties. Some compound semiconductors, particularly III-V semiconductors, such as gallium arsenide (GaAs) and indium phosphide (InP), have been widely adopted and utilized in the high-frequency devices [5] and light-emitting devices [6] application domains. Success in fabricating blue and green light-emitting diodes (LEDs) using gallium nitride (GaN) [7] and indium gallium nitride (InGaN) [8] should be another great milestone in the history of semiconductors or even in modern civilization progress, leading to the technological development of optoelectronics.

As our modern society entering 21st century, the various demands for new functionalities for semiconductors is driving innovations and technologically advancement in the field of electronics. Electronics were usually known as the devices or systems that can process signals and data, which contribute to the information technology (IT) as hardware and infrastructures. However, the concept of Power Electronics, which was introduced by Newell in 1973 [9], has expanded the utility of electronics and semiconductor into the field of managing electrical power and energy. Power electronics involves conversion of electric power using power semiconductor devices and circuits, where the electrical power is regulated and converted so that the power can be supplied to the loads in the most suitable form. In early days of power electronics, Si-based technology are mainly used in form of various devices, such as Schottky Barrier Diode (SBD), MOSFET, Bipolar Junction Transistor (BJT), Insulated Gate Bipolar Transistor (IGBT) , thyristors and etc. Subsequently, those power electronics devices can be further used to compose power electronics sub-systems, including converters (DC to DC), inverters (DC to AC), rectifiers (AC to DC) and cyclo-converters (AC to AC). The key figure of merits of power electronics is the power conversion efficiency. In general, the efficiency of power electronics is limited by the performance of semiconductor devices, capacitors, inductors, and packaging. With current Si-based technology, the efficiency of power conversion is typically around 85% to 95%, which is not high enough, since approximately 10% of the converted electrical power is dissipated into the form of heat, which can induce further problems in terms of thermal management, during every cycle of electrical power conversion. Now that Si power device technology mature and limited by the fundamental physical property of silicon single crystal, it is relative hard to achieve innovative breakthroughs using Si-based technology in the field of power electronics.

Fortunately, we have already a promising semiconductor material solution to develop more advanced power electronics, i.e., Silicon Carbide (SiC), which possesses various superior physical properties that are desirable in the design of power electronics [10]. The author believes that we are currently the dawn of technological revolution in terms of energy utility. An analogy that can be think of is the meaning of advent of Si to the whole information and technology industry. If lucky enough,

we are able to witness and even participate in this energy technological revolution based on the emerging SiC-based semiconductor material, devices and power electronics technology.

In the following sessions of Chapter 1 of this dissertation, the author would like to review briefly in terms of SiC material properties, SiC-based power devices and power electronics, high-temperature power electronics related packaging materials and technology. Finally, the general outline of this dissertation is summarized in end of this introductory chapter.

1.2 Silicon Carbide Material Properties

Silicon Carbide (SiC) is a IV-IV compound material with unique physical and chemical properties. The strong covalent bonding between Si and C atoms, with high bond energy 4.6 eV, renders this particular material a variety of outstanding properties, such as very high hardness, chemical inertness, and high thermal conductivity. As compared with Si, SiC is a wide-band gap semiconductor (WBG) material with superior physical properties that can serve as the basis for the high-voltage, high-temperature, low power loss electronics of the future.

From the crystallographic point of view, SiC the best example of polytypism. Polytypism [11] is the phenomenon that a material can adopt different crystal structures in terms of stacking sequence without changing its chemical stoichiometry. As a matter of fact, SiC crystallizes exhibit a surprisingly large number of polytypes, i.e., more than 200 types, which cause a great difficulty in controlling the process in terms of single crystal semiconductor ingot growth and wafer production and fabrication of SiC single crystal with desirable crystal structure. There are three popular polytypes of SiC of real application interests, i.e., 3C-SiC, 4H-SiC and 6H-SiC, where C stands for cubic and H stands for hexagonal. The major difference of the crystal structures of those polytypes is the crystal plane stacking sequence. 3C-SiC exhibits the repeating sequence of ABC, and 4H-SiC and 6H-SiC can be described as ABCB and ABCACB respectively, where A, B and C are the potentially occupied sites in the close-packed crystal structure (cubic or hexagonal). 4H-SiC and 6H-SiC polytypes are very popular because they exhibit high thermal stability. 3C-SiC is another popular polytype because it can be grown hetero-epitaxially on Si substrates.

All of the SiC polytypes have an indirect band structures, as the same of Si. 3C-SiC has a bandgap of 2.36 eV, 4H-SiC has a bandgap of 3.26 eV and 6H-SiC has a bandgap of 3.02 eV. Among the three polytypes of SiC, 4H-SiC has the largest value of bandgap. Moreover, with higher critical field strength and higher electron mobility along the c-axis (vertical axis of hexagonal crystal), 4H-SiC exhibits significantly higher figure-of-merit (FOM) [12] in terms of high temperature and high power utility, compared with other two. Therefore, 4H-SiC is considered as the most promising and has been almost exclusively employed for power devices and power electronics applications [13]. As a result, the author would like to main discuss the various properties of 4H-SiC in the content of this chapter.

For electrical properties, with a wide bandgap of 3.26 eV, 4H-SiC has an extremely low intrinsic carrier density at room temperature, which has the value as low as 5×10^{-9} cm^{-3} [14]. In comparison, Si has a bandgap of 1.12 eV and intrinsic carrier concentration of 1×10^{10} cm^{-3} at room temperature. The difference of intrinsic carrier concentration at room temperature is on the order of 10^{19}. This is the main reason why SiC electronic devices can operate at very high temperature with low leakage current, thereby enhancing the overall energy conversion efficiency of the power electronics systems. Similar to Si, SiC semiconductor can be readily doped with n-type doping elements, namely, nitrogen (N) and phosphorus (P) and p-type doping elements, namely, aluminum (Al) and boron (B), to increase its conductivity and extrinsic carrier concentration through the process of impurity element ionization. Among wide-bandgap semiconductors, SiC is exceptional because it can be easily doped either with p-type or n-type over a wide range, more than five orders-of-magnitude [15]. In addition, 4H-SiC exhibits electron mobility of 450 $cm^2V^{-1}s^{-1}$ at low electric field at donor density of 2×10^{17} cm^{-3} and its saturated drift velocity is 2.2×10^7 $cm\text{-}s^{-1}$. Si has a similar electron mobility at the same donor concentration with lower saturated drift velocity of $10^7 cm\text{-}s^{-1}$, so that electrons in 4H-SiC are 2.2 times faster than that in Si at high electrical field condition. Furthermore, a semiconductor junction breaks down when the maximum electric field strength reaches a critical value which is inherent to the material. This critical value is called critical electric field strength or breakdown electric field strength. This value is extremely important in the power electronics applications. Breakdown electric field of 4H-SiC is 2.2×10^6 $V\text{-}cm^{-1}$ for perpendicular to c-axis and 2.8×10^6 $V\text{-}cm^{-1}$ for parallel to c-axis [16], which is eight times higher than that of silicon (3×10^5 $V\text{-}cm^{-1}$), meaning that 4H-SiC can

withhold and sustain much higher voltage shot than Si. At last, SiC is the only compound semiconductor whose native oxide is SiO_2, the same insulator as Si. This makes it possible to fabricate the entire family of MOS-based electronics device onto SiC wafer.

As for thermal properties, with its significant contribution from phonons, 4H-SiC has a much higher (more than three times) thermal conductivity (4.9 $W\text{-}cm^{-1}K^{-1}$) than that of Si (1.5 $W\text{-}cm^{-1}K^{-1}$) [17]. 4H-SiC has also high thermal stability, remaining thermally stable at elevated temperature as high as 1900°C [18]. The mechanical properties of SiC are also unique. SiC is one of the hardest known materials, with Mohs Value of 9.5 (Glass 6, Diamond 10) and Knoop value of 2480 (Glass 530, Diamond 7000) where the polytype dependence is small. This make SiC can be more easily handled or solid-state bonded during fabrication if compared with Si. The Young's modulus of 4H-SiC or 6H-SiC is from 390 GPa to 700 GPa [19], which is much higher than Si (160 GPa). SiC has a fracture strength of 21 GPa, which is three times higher than Si (7 GPa). In addition, SiC even retains its high hardness and elasticity at very high temperatures, where its fracture strength is estimated to be 0.3 GPa at 1000°C (Si falls to 0.05 GPa at 500°C) [20]. In summary, those superior electrical, thermal and mechanical properties make 4H-SiC become extremely suitable and the most promising wide bandgap semiconductor material candidate in the field of high-temperature power electronics applications. In the following session, the author would like to give a brief introduction to the high-temperature power electronics, associated with SiC power devices utility.

1.3 High-Temperature Power Devices and Electronics

For a typical traditional power electronics system, the individual power devices are mounted on the heat sink, and the drivers, sensors, and protection circuits are implemented on a printed circuit board (PCB) and mounted near the power devices. In definition, the high-temperature power electronics should be able to have a normal operating temperature at least above 350°C [21]. Nowadays, the high-temperature power electronics have already gained much attention in the fields of real industrial applications, such as oil drilling and natural gas exploration and production, combustion engines in automobiles and in aircrafts, outer-space exploration [22]. In the near future,

a more rapid growth of demands in high-temperature power electronics would be expected from mass production of hybrid electric vehicle (HEV), electric utility vehicle (EUV), electrical power smart grids, solar-based electrical power generation and conversion [10]. However, the fundamental limitation cannot be overcome without a radical change in the design and implementation of power electronics systems. Therefore, many attempts based on the development of SiC technology have been propose in order to bring a technological revolution in the field of high-temperature power electronics, such as the hybrid integration technology [23] or "system-in-a-module" for power electronics [24]. Besides semiconductor power devices, other components in the electronic system need to be also developed in order to meet the requirement of high-temperature or high-power electronics. Therefore, electronic packaging technology can be the limiting and determining factor before fully utilizing the physical advantages offered by SiC or WBG semiconductor materials. Therefore, it is important to develop a whole set of packaging technology, including new packaging material, novel system-level electrical, structural and thermal design and cost-effective manufacturing possess, compatible with SiC semiconductor devices in high temperature utility. Among those mentioned above, die-attachment materials or technology in electronic packaging for the high-temperature utility would be one of the key technologies in terms of the power electronics system integration. In the following session, the author would like to give a further brief review on die-attachment materials used in electronic packaging and potential candidates that could be suitable in the application of high-temperature power electronics.

1.4 Die-attachments in Electronic Packaging

Electronics cannot work with bare chips. They must be interconnected with each other and protected by the packaging structure in order to work together reliably as an integrated system. In the context of textbook [25], the electronic packaging technology should offer five major functions as following: 1. To provide electrical interconnections for integrated circuits (ICs) in order to form a whole electrical system; 2. To provide mechanical fixation for die or chip; 3. To ensure a good heat dissipation path or thermal management; 4. To protect the electronic components from the potential harsh

environments. 5. To ensure the long-term reliability of the system with a predictable life-time. As a matter of fact, the die-attachments materials and technology are closely related to fulfill all of the five major functionality of electronic packaging. Die-attachments can provide the mechanical fixture to mount the chips onto the substrates, and provide electrical interconnection for some chips with vertical structure (I/O terminal at bottom of the chip). Die-attachments materials should have a good conductivity to provide a good thermal dissipation path vertically. Die-attachment materials can also prevent mechanical failure if the electronics device accidently drop and would be one of the determining factors for the overall reliability and life-time of the electronic system. Therefore, die-attachment materials, which connect the chip and device to the rest of the electronic system, play a crucial role to ensure system works consistently. In words, die-attachment materials and technology are extremely important to the development of electronic packaging technology.

High-temperature power electronics, essentially as electronic system, must be electronically packaged as well in order to perform their functions normally and consistently. Therefore, it is a great technological challenge to develop the die-attachment material that is suitable in the high-temperature applications and is compatible with the emerging SiC-based technology. In Table 1.1, it gives a summary of the current popular die-attachment materials available in the market.

Die-attachment Materials (wt. %)	Melting or Degradation Temperature (°C)	Normal Operating Temperature (°C)
Silver filled epoxy	100	75
Eutectic lead-tin solder (Sn63Pb37)	183	92
Lead free solder (SnAgCu)	217	119
High lead solder (Pb97Sn3)	300	185
Eutectic gold-tin (Au80Sn20)	280	170
Eutectic Au-Ge	356	230
Eutectic Au-Si	363	236
Nano-silver particle sintering paste	961	715

Table 1.1 A summary of popular die attachment materials with melting and operating temperatures.

Generally speaking, normal operating temperature of the die-attachment materials, which are compatible with SiC power devices, should be, at least, higher than 350°C, in order to fully harvest those fundamental physical advantages of SiC semiconductor. The normal operating temperature of die-attachment material is usually determined by the 0.8 Th (homologues temperature) of that material. As shown from Table 1.1, it is very clear that none of the popular die-attachment materials that are being widely used by the electronic packaging industry, such as eutectic lead-tin solder [26] (Sn63Pb37), lead-free solder (SnAgCu), or silver particles filled epoxy conductive adhesive, is suitable for high temperature power electronics applications, simply due to their melting or degradation temperatures are usually below 250°C. High lead solder (Pb97Sn3) had been already banned by Restriction of Hazardous Substances (RoHS) in consumable electronic products utility. In literatures, eutectic gold-tin alloy, e.g., Au80Sn20 [27], has been considered as one of the potential candidates for high-temperature applications since it possesses superior corrosion resistance. However, it was reported that eutectic gold-tin alloy had the reliability issues for its microstructural-induced early crack initiation [28] and its melting temperature is only at 280°C. The normal operating temperatures of Au-Ge and Au-Si eutectics are also not high enough to meet the requirement of high temperature power electronics. Moreover, the higher marketing price of gold is actually the determining factor that prevent gold-based alloy from widely accepted in the utility of electronics industry.

On the other hand, silver-based die-attachment materials seemed to be more promising candidates for high-power applications, since silver has the highest electrical and thermal conductivity among all metallic materials. Currently, silver nano-sintering is the most popular die-attach approach for high temperature applications [29]. The molecular dynamics simulation study has shown that isolated silver nanoparticles would have lower melting temperature, down to about 350°C [30]. As a result, it facilities high melting temperature joint forming at relative lower possessing temperature by nano-participles aggregation and agglomeration [31]. Indeed, silver nano-sintering is very attractive emerging die-attachment method for high-power applications. Some reliability issues, such as oxidation [32] and high temperature mechanical degradation [33, 34], associated with the porous

nature of silver nano-sintering due to organic degassing might need to be addressed in the future work.

Our research group, led by Professor Chin C. Lee, has been dedicating on the study of Ag-In binary system for bonding applications over decades [35]. With the idea of transient liquid phase (TLP) bonding, our group had shown that high-temperature Ag-In alloy joint can be formed reliably at low possessing temperature [36]. The previous study had shown that the joint was virtually void-free by examined under scanning acoustic microscopy (SAM). However, it would induce two types of intermetallic compound (IMC) to the resulting joint, namely, Ag2In and AgIn2, which are brittle in their nature, and would detrimental to the overall mechanical behaviors of the resulting bonding structure [37]. Recently, our group had already shown some results of studies previously on successfully converting most of the IMCs into silver-indium solution as bonding medium with several steps of annealing, which resulted in large improvement on the joint bonding strength [38] and can survive after thermal cycling (TC) test of 5000 cycles [39].

Particularly, silver-indium solution phase occurred in the bonding structures was very interesting to our research group at that time. Therefore, our research were considering at that time if we could employ silver-indium solution phase directly as the die-attachment materials for high temperature power electronics, using fluxless solid-state bonding technique. Before utilizing silver-indium solution phase, we must understand this material by studying its various intrinsic material properties, which were not available to the scientific and engineering community at that time. This is the initial motivation of the academic research in the content of this dissertation and how we begin our research journey in probing the nature of Ag-In solid solution. It turns out that the results of the series research have gone far beyond our initial expectations and imaginations, resulting in several meaningful academic findings and eventually contribute to the development of die-attachment materials for the future high temperature power electronics based on SiC technology. So, let's begin our journey in "*Exploring the Mysterious Physical Properties in Silver-Indium Binary System*".

1.5 Dissertation Outline

In the content of this dissertation, the general background of SiC-based high temperature power electronics and high temperature die-attachment materials was introduced in Chapter 1. In Chapter 2, the research methodology used in the dissertation in terms of Material Synthesis and Processing and Material Characterizations will be introduced briefly in principle and detailed in practical, such as vacuum casting, E-beam evaporation deposition and vacuum bonding technique for Material Synthesis and Processing and XRD, XPS, UPS, SEM/EDX, FIB, TEM, AFM for Material Characterizations. In Chapter 3, the mechanical properties of Ag-In solution will be investigated by stress vs. strain characterization, using tensile test. The results of stress vs. strain characterization show that Ag-In solution possess various superior mechanical properties. In addition, an abnormal phenomenon, namely, solid solution softening, has been discovered in Ag-In binary system. In Chapter 4, the author will introduce the discovery that Ag-In solid solution exhibits a great anti-tarnishing property, which could potentially solve the problematic tarnishing issues involved in Ag and its alloy applications, by using a self-designed quantative experimental method. Furthermore, in Chapter 5, a quantitative and theoretical model has been established by the author to explain the underlying anti-tarnishing mechanism within the context of HSAB principle, conceptual DFT formalization and Hammer-Nørskov (HN) d-band model, using an original semi-quantum-mechanical approach. In Chapter 6, solid solution softening, was further studied and discussed in Ag-Al, Ag-Ga, and Ag-Sn binary systems, during which the author has discovered Ag-Ga solid solution exhibits superior mechanical properties as well. In addition, various physical properties of Ag-In alloys, i.e., thermal, electrical and optical properties, have been studied to enable to the multi-physical co-designs, leading to Ag-In alloys potential various applications, and will be introduced in the Chapter 7. In Chapter 8, more importantly, based on the findings of superior physical properties of Ag-In alloys above, an advanced solid-state bonding technology has been proposed by the author using Ag-In solid solution as die-attachment material for high-temperature power electronics applications. Finally, the concluding remarks and future research perspectives will be discussed in Chapter 9, where a unified multi-physical theorem and material co-design principles for electronic packaging could be developed in

the future study. The author hope that the content of this dissertation can be meaningful and contributing some insights to the research and development of high temperature power electronics and packaging technology.

Reference in Chapter 1

1. J. Bardeen and W. H. Brattain, “The transistor, a semi-conductor triode”, Physical Review Letter, vol. 74, No. 230, pp. 230-231, 1948.
2. R. Noyce, US Patent, No. 2981877, “Semiconductor device-and-lead structure”, 1959.
3. D. Kahng, U. S. Patent No. 3,102,230, “"Electric Field Controlled Semiconductor Device", 1960.
4. Y. Taur and T. H. Ning, “Fundamentals of Modern VLSI Devices”, 2nd Edition, Cambridge University Press, 2009.
5. S. Tiwari, “Compound Semiconductor Device Physics”, Academic Press, 1991.
6. E. F. Schubert, “Light-Emitting Diodes”, Cambridge University Press, 2003.
7. J. H. Edger, S. Strite, I. Akasaki, and et al., “Properties, Processing and Applications of Gallium Nitride and Related Semiconductors”, INSPEC, 1999.
8. S. Nakamura and S. F. Chichibu, “Introduction to Nitride Semiconductor Blue Lasers and Light Emitting Diodes”, Taylor & Francis, 2000.
9. R. W. Erickson and D. Maksimovic, “Fundamentals of Power Electronics”, Kluwer Academic Publishers, 2001.
10. T. Kimoto and J. A. Cooper, “Fundamental of Silicon Carbide Technology: Growth, Characterization, Devices and Applications”, John Wiley & Sons, 2014.
11. A. R. Verma and P. Krishna, “Polymorphism and Polytypism in Crystals”, John Wiley & Sons, 1966.
12. B. J. Baliga, “Power semiconductor device figure of merit for high-frequency applications”, IEEE Electron Device Letter, vol. 10, No. 10, pp. 455-457, 1989.
13. J. A. Copper and A. Agarwal, “SiC power-switching devices-the second electronics revolution”, Proceedings of the IEEE, vol. 942, No.6, pp. 956-968.
14. G. Pensl and W. J. Choyke, “Electrical and optical characterization of SiC”, Physica B: Condensed Matter, vol. 185, No. 1, pp. 264-283, 1993.
15. W. Götz, A. Schöner, and G. Pensl, “Nitrogen donors in 4H-silicon carbide”, Journal of Applied Physics, vol. 73, No. 7, pp. 3332-3338, 1993.
16. A. O. Konstantinov, Q. Wahab, N. Nordell, and U. Lindefelt, “Ionization rates and critical fields in

4H silicon carbide", Applied Physics Letter, vol. 71, No. 1, pp. 90-92, 1997.

17. Glen A. Slack, "Thermal conductivity of pure and impure silicon, silicon carbide and diamond", Journal of Applied Physics, vol. 35, No. 12, pp. 3460-3466, 1964.
18. W.S. Yoo and H. Matsunami, "Solid-state phase transformation in cubic silicon carbide", The Japan Society of Applied Physics, vol. 30, No. 3, pp. 545-553, 1991.
19. C. A. Zorman and R. J. Parro, "Micro- and nanomechanical structures for silicon carbide MEMS and NEMS", Basic Solid State Physics, vol. 245, No. 7, pp. 1404-1424, 2008.
20. T. Suzuki, I. Yonenaga, and H. O. K. Kirchner, "Yield Strength of Diamond", Physical Review Letter, vol. 75, No. 19, pp. 3470-3472, 1995.
21. C. Buttay, D. Planson, B. Allard, D. Bergogne, P. Bevilacqua, C. Joubert, M. Lazar, C. Martin, H. Morel, D. Tournier, C. Raynaud, "State of the art of high temperature power electronics", Materials Science and Engineering B, vol. 176. No. 4, pp. 283-288, 2011.
22. H. S. Chin, K. Y. Cheong, and A. B. Ismail, "A review on die attach materials for SiC-based high-temperature power devices," Metallurgical and Materials Transactions B, vol. 41, No.4, pp.824-832, 2010.
23. J. D. Wyk, "Power electronics at the dawn of a new century – past achievements and future expectations", Proceedings of Third IEEE International Power Electronics and Motion Control Conference (IPEMC), pp, 9-20, 2000.
24. F. C. Lee, J. D. Wyk, D. Boroyevich, G. Q. Lu, Z. Liang, and P. Barbosa, "Technology trends toward a system-in-a-module in power electronics", IEEE Circuits and Systems Magazine, vol. 2, No. 4, pp. 4-22, 2002.
25. R. Tummala, "Fundamentals of microsystems packaging", McGraw-Hill, New York 2001.
26. K. N. Tu, "Solder Joint Technology", New York, Springer, 2007.
27. G. S. Matijasevic, C. C. Lee, and C. Y. Wang. "Au-Sn alloy phase diagram and properties related to its use as a bonding medium," Thin Solid Films, vol. 223, No.2, pp. 276-287, 1993.
28. R. R. Chromik, D. N. Wang, A. Shugar, L. Limata, M. R. Notis, and R. P. Vinci, "Mechanical properties of intermetallic compounds in the Au–Sn system," Journal of Materials Research, vol. 20, No.8, pp.2161-2172, 2005.

29. M. Maruyama, R. Matsubayashi, H. Iwakuro, S. Isoda, T. Komatsu, "Silver nanosintering: a lead-free alternative to soldering," Applied Physics A, vol. 93, No. 2, pp. 467-470, 2008.
30. S. J. Zhao, S. Q. Wang, D. Y. Cheng, and H. Q. Ye, "Three distinctive melting mechanisms in isolated nanoparticles," The Journal of Physical Chemistry B, vol. 105, No. 51, pp.12857-12860. 2001.
31. P. Peng, A. Hu, A. P. Gerlich, G. Zou, L. Liu, and Y. N. Zhou, "Joining of Silver Nanomaterials at Low Temperatures: Processes, Properties, and Applications," ACS Applied Materials & Interfaces, vol. 7, No. 23, pp. 12597–12618, 2015.
32. S. Y. Zhao, X. Li, Y. H. Mei and G. Q. Lu, "Study on high temperature bonding reliability of sintered nano-silver joint on bare copper plate," Microelectronics Reliability, vol. 55, No. 12, pp. 2524-2531, 2015.
33. S. A. Paknejad, G. Dumas, G. West, G. Lewis, and S. H. Mannan, "Microstructure evolution during 300° C storage of sintered Ag nanoparticles on Ag and Au substrates," Journal of Alloys and Compounds, vol. 617, pp.994-1001, 2014.
34. S. T. Chua, and K. S. Siow, "Microstructural studies and bonding strength of pressureless sintered nano-silver joints on silver, direct bond copper (DBC) and copper substrates aged at 300° C," Journal of Alloys and Compounds, vol. 687, pp. 486-498, 2016.
35. Yi-Chia Chen, William W. So, and Chin C. Lee, "A fluxless bonding technology using indium-silver multilayer composites", IEEE Transactions on Components, Packaging and Manufacturing technology - Part A, vol. 20, No.1, pp. 46-51, 1997.
36. R. W. Chuang and C. C. Lee, "Silver-indium joints produced at low temperature for high temperature devices," IEEE Transactions on Components and Packaging Technologies, vol. 25, No. 3, pp. 453-458, 2002.
37. Y. Y. Wu, W. P. Lin, and C. C. Lee, "A study of chemical reactions of silver and indium at 180° C. Journal of Materials Science: Materials in Electronics, vol. 23, No. 12, pp. 2235-2244, 2012.
38. Y. Y. Wu and C. C. Lee, "The strength of high temperature Ag-In joins produced between copper by fluxless low-temperature processes," Journal of Electronic Packaging, vol. 136, pp. 61-6, 2014.
39. Y. Y. Wu and C. C. Lee, "Thermal cycling reliability study of Ag–In joints between Si chips and Cu substrates made by fluxless processes", vol. 4, No. 9, pp. 1420-1426, 2014.

Chapter 2

Instrumentations and Experimental Techniques

2.1 Introduction

The research and development of material science and engineering is highly depending on the advancement of instrumentations and experimental techniques. In general, we, material scientists and engineers, have a very useful notion as our research and design guidance, which was known as the triangle of material science and engineering [1], as shown in Fig. 2.1.

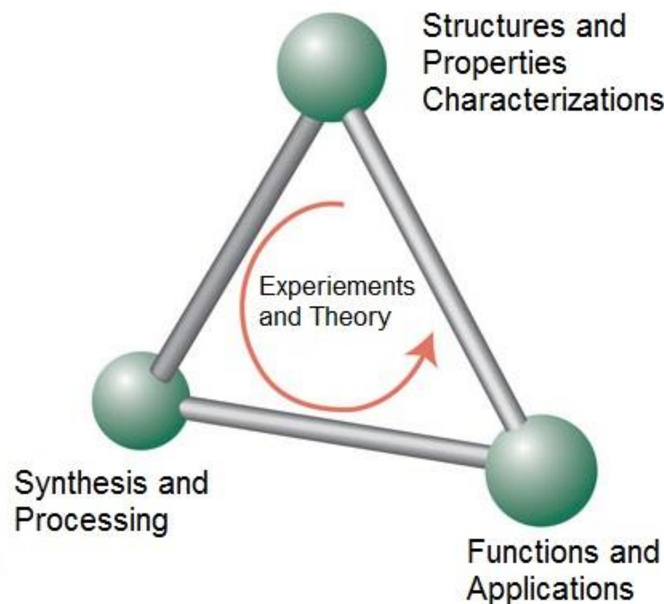

Fig. 2.1 The triangle of material science and engineering.

This particular triangle is composed by three essences of material science and engineering: 1. Synthesis and processing of materials; 2. Characterizations of the structures and properties of materials; 3. Demonstration of the functions of materials for certain applications. Instrumentations and experimental techniques are the back-bones and infrastructures of the first-two essences. In this chapter, the author would like to review the main instrumentations and experimental techniques that were used in both *Material Synthesis and Processing* and *Material Characterizations* in the content of this dissertation.

2.2 Material Synthesis and Processing

2.2.1 Vacuum Casting

Vacuum casting is very useful method to synthesize bulk metallic material for research purposes. The author has developed a whole set of vacuum casting method during the study time period of this dissertation, with joint efforts with colleagues in the laboratory. The vacuum environment is necessary for the casting production of bulk metallic material for reducing the oxidation issues, the number of voids or common defects created by trapped air bubbles. Therefore, a vacuum environment need to be created in the first place, which requires the operation of hydrogen-oxygen gas torch and vacuum sealing. As shown in Fig. 2.2, the hydrogen-oxygen torch operation system is composed of several major parts: torch, hydrogen and oxygen gas cylinders, gas pressure gauges and regulators. In order to control the hydrogen-oxygen torch flame temperature, the ratio of the gas flow of hydrogen and oxygen need to be adjusted carefully. In the application of our laboratory, the adjusted ratio between O_2 and H_2 around 1:4 in order to obtain a stable reducing flame for the torch operation, where the pressures of regulator gauges for hydrogen and oxygen are fixed at 10 psi and 2.5 psi respectively, as shown in Fig. 2.3. At this condition, the color of the flame should be bluish bright white, and resulting flame center temperature is around 3200 ℃.

Quartz tube was selected as the capsule for the vacuum casting method, since it has relative high melting temperature (1700 ℃), and it is chemical inert to most of metallic materials at elevated temperature. As shown in Fig. 2.4, the high purity raw metallic materials shots of desired compositional ratios then can be weighed, uniformly mixed and loaded into the quartz tube with one end closed. Next, as shown in Fig. 2.5, the quartz tube filled with raw metallic materials shots can be connected to a rubber hose linked to a mechanical pump with vacuum level of 50 milli-torr.

When the flame touch the quartz tube, the optical branches of phonons in quartz solid will be excited, resulting in generating a glare bright light, as shown in Fig. 2.5. Therefore, ultraviolet (UV) proved safety gaggles must be worn during this vacuum sealing operation to protect eyes. After the quartz gradually softened and melted, the tube will collapse inwards due to imbalance pressure between atmosphere outside and vacuum inside of the tube. Thus, during the mechanical pumping, the quartz

tube can be melted and sealed at the other end, resulting in forming a closed quartz capsule containing with metallic shots under vacuum.

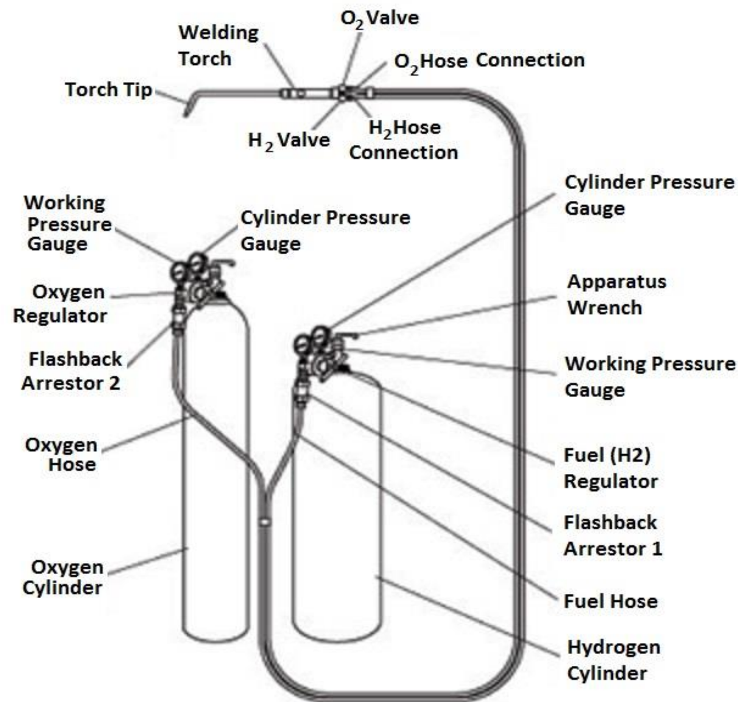

Fig. 2.2 The schematic set-up of hydrogen-oxygen torch operation system.

Fig. 2.3 Normal pressures of gauges for hydrogen cylinder (left) and for oxygen cylinder (right) at working status.

Fig. 2.4 The picture of quartz tube (top) and filled with metallic shots (bottom).

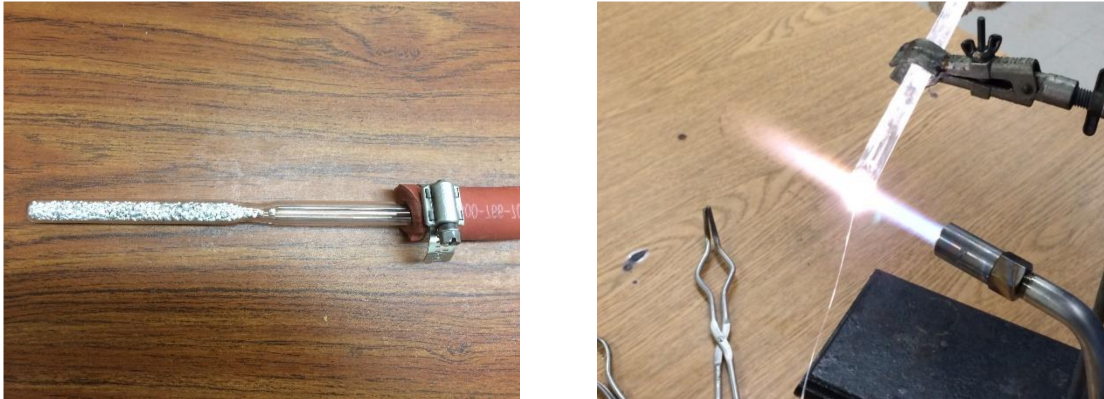

Fig. 2.5 Demonstration of vacuum sealing procedures.

As shown in Fig. 2.6, a specialized capsules holder was designed to accommodate the quartz capsules for following casting procedures. The capsule holder need to be preheated together with convection furnace to the elevated temperature beyond melting temperatures of all metals in the capsules, and then the capsules can be put into the furnace, using a clamp, with swift (taking about 3 seconds) and caution movement in order to ensure all metallic components melt together with each other. Personal protective equipment (PPE) for high-temperature applications, such as fire-retarded clothes, high temperature gloves and safety gaggles, must be worn during this operation.

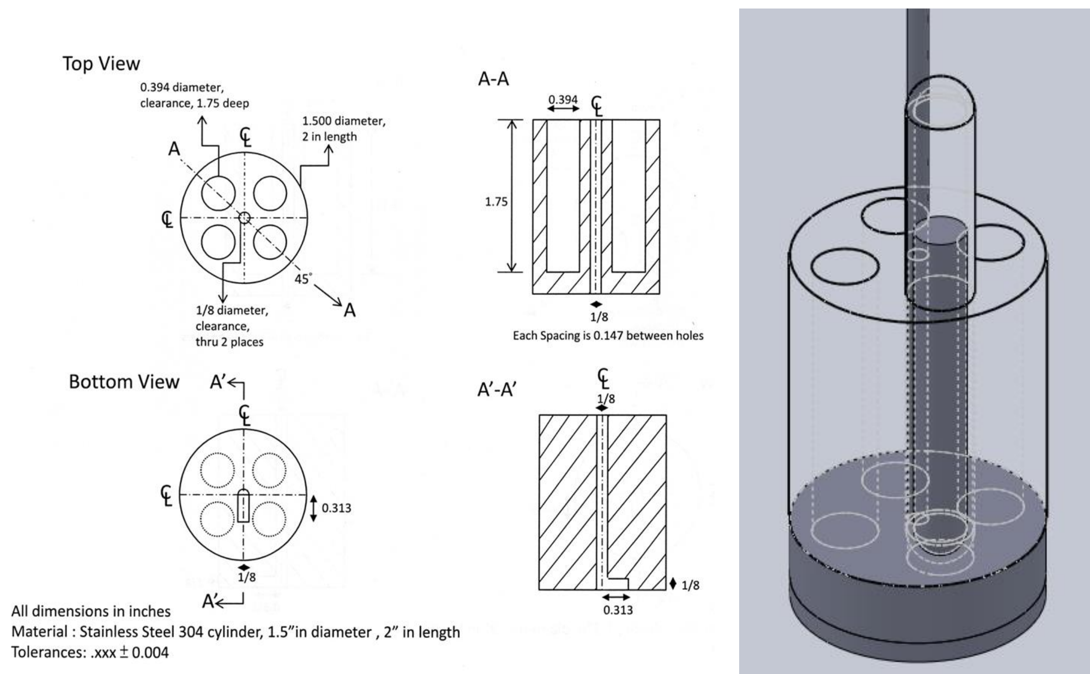

Fig. 2.6 The engineering sketches (left) and 3D model (right) of capsules holder.

After completely melting of the metallic shots, the metal will stay at liquid phase for 30 mins, during which mechanical shaking movement need to be applied to the capsule holder in order to ensure the compositional homogeneity of the metallic liquid phase. Furthermore, specialized step cooling and annealing procedures need to be applied, which allows the material staying at different homologous temperatures for enough length of time. The designed annealing procedure is entirely necessary and important to ensure the compositional homogeneity and uniformity and repeatability in terms of microstructures and grain sizes of the grown ingots. Finally, as shown in Fig. 2.7, the alloy ingots can be thusly grown from the initial metallic shots, using this vacuum casting method described above. Now, this vacuum casting method is well-developed and frequently used in various research activities within our laboratory. The author has been dedicating in the development of this vacuum casting method from scratch with enormous efforts. Personally, I would like to share the credits with and express my gratitude towards Dr. Shou-Jen Hsu and Dr. Yuan-Yun Wu for their help and efforts during this vacuum casting standard operation procedures (SOP) development.

Fig. 2.7 Metal shots before casting (left) and grown ingot (right) after casting.

2.2.2 E-beam Evaporation Deposition

In the content of this dissertation, metallic thin film is one of main research subjects, which usually requires physical vapor deposition (PVD) or chemical vapor deposition (CVD) processes for the sample fabrication. Electron Beam Evaporation, which also commonly referred to as E-beam Evaporation, is a process in which a target material is bombarded with an electron beam given off by a tungsten filament and was redirected by a magnetic field under high vacuum, E-beam evaporation is one of common methods in physical vapor deposition. As shown in Fig. 2.8, the electron beam causes atoms from the target material to evaporate into the gaseous phase. These atoms then precipitate into solid form, coating everything in the vacuum chamber with a thin layer of the source material.

In a high vacuum environment, these metallic gaseous particles have a relatively long mean free path so that they can travel directly to the substrates of deposition without colliding with the background gas. A clear advantage of this process is it permits direct transfer of energy to source during heating and very efficient in depositing evaporated materials in the crucible to substrate, compared with traditional thermal evaporation deposition. In addition, deposition rate in this process can be as low as 1 nm per minute to as high as few micrometers per minute. The material utilization efficiency is high relative to other PVD methods and the process offers structural and morphological control of

films. The deposition rate R_d, can be theoretically estimated by the following equation, as show in Eq. 2.1:

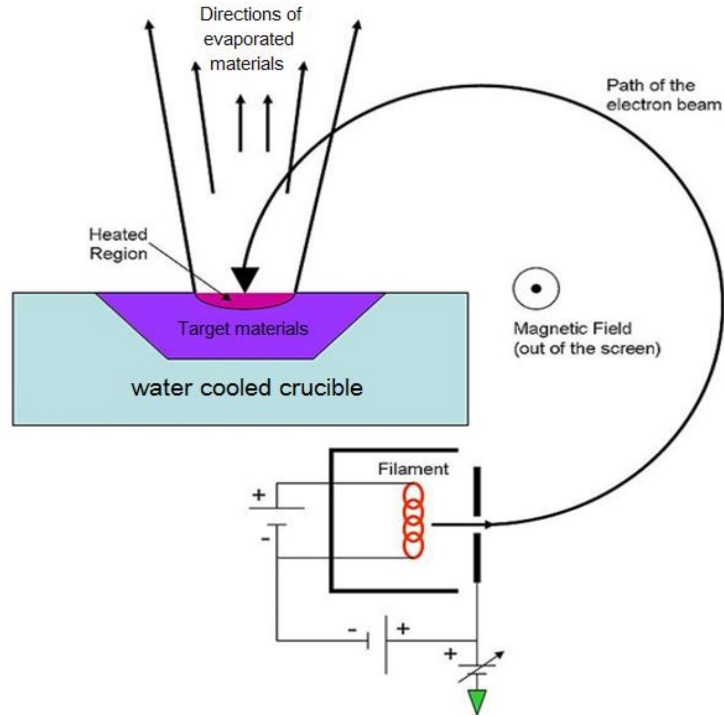

Fig. 2.8 The schematic set-up of E-beam evaporation system in general.

$$R_d = A \times \sqrt{\frac{m}{2\pi k \rho^2}} \times \frac{P_e}{\sqrt{T}} \tag{2.1}$$

, where A is the geometrical factor, m is molar mass, ρ is the mass density of the target material, k is the Boltzmann constant, P_e is partial vapor pressure of the metallic vapor and T is the absolute temperature. Therefore, the E-beam deposition rate is a function of geometry, material properties, and temperature. It is relatively straight forward for pure metal deposition. However, all of these factors need to be accounted in alloy thin film deposition, since its real physical process is rather complicated. The precise control of E-beam deposition rate is crucial to the chemical composition and quality of resulting thin film. The so-called "T-zone" morphology [2] would be desirable to get smooth, dense, high reflectance thin film with small polycrystalline grains in content of this dissertation.

In practice, Angstrom Engineering EvoVac Glovebox Evaporator in Irvine Material Research Institute

(IMRI) was used for the thin film sample preparation of this dissertation, as shown in Fig. 2.9. The evaporation chamber can be pumped down to 2×10^{-8} torr with mechanical-cryogenic two stages pumping system within 1 hour. After turning-on the E-beam source, the sample stage can be protected by E-beam stutter and sample stage stutter during the pre-soaking of target materials. A featured function of this instrument is glancing angle deposition (GLAD) technique, which enable the sample stage rotate at designed speed both in-plane and out-plane to fabricate thin film sample with smooth, high coverage, or even nano-structures. During the E-beam evaporation process, the deposition rate was monitored by quartz crystal microbalance (QCM), and was precisely controlled by an automatic negative feedback system, using proportional–integral–derivative (PID) controller. Thus, this state-of-art instrument ensure the high quality of thin film samples of the research work in the content of this dissertation.

Fig. 2.9 Angstrom Engineering EvoVac Glovebox Evaporator.

2.2.3 Vacuum Bonding Technique

The various bonding techniques that have been developed within our laboratory are great scientific assets to electronic packaging technology research community. Those research works associated with bonding technology development are highly related to the vacuum bonding technique and self-

designed instrument that had been developed in our laboratory, namely, a compact vacuum furnace for scientific research [3]. The structure, function, and design insights of this vacuum furnace are briefly reviewed in this dissertation.

As illustrated in Fig. 2.10, the vacuum furnace consists of a quartz cylinder, two stainless steel plates, a heating platform, and a ceramic post. The quartz cylinder is sandwiched between two steel plates, forming a vacuum chamber. Its inner diameter is 50 mm and height is 200 mm. The quartz cylinder allows us to visibly see the sample during operation. The interface between the cylinder and the steel plate is sealed by an O-ring. Two type-K thermocouples (Chromel$^+$-Alumel$^-$) are used to measure the temperature at two different locations within the chamber. One of the thermocouples is used by a temperature controller as its input, and thus, provides the process value of the controller. The controller switches the electricity applied to the heating platform on and off until the desired set point value is reached. A mechanical pump is employed to bring the chamber to near vacuum conditions during operation.

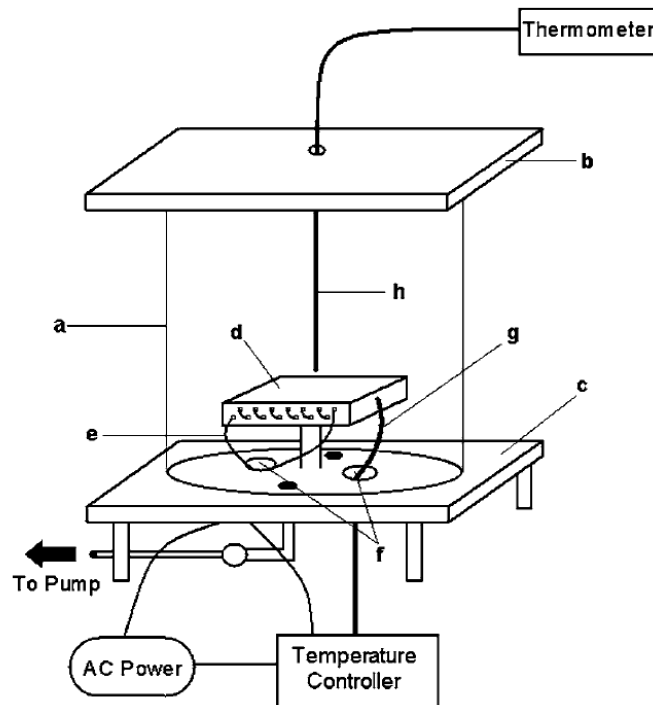

Fig. 2.10 An illustration of the vacuum furnace: (a) quartz cylinder, (b) upper stainless plate, (c) base plate, (d) graphite platform, (e) heating wire, (f) electrical feed-throughs, (g) platform thermocouples and (h) sample thermocouple.

The heating platform is a 75 × 75 × 10 mm^3 graphite block. Many holes were drilled into the platform to allow for resistive heating wire (nickel-chromium alloy) to be looped around and integrated into the body of the block. The wire is electrically insulated from the graphite using ceramic tubes. Graphite was chosen as the material of the platform because it has been experimentally proven that it absorbs 97% of radiation and is a nearly perfect emitter of radiation. Therefore, the platform will absorb a maximum amount of heat given off by the wires. It is also easy to machine and can withstand very high temperature.

Inside the vacuum furnace, the graphite platform is supported by a ceramic poster standing at the center of the base stainless steel plate. A ceramic poster having relatively low thermal conductivity is utilized to support the platform in order to achieve thermal isolation of the platform from the upper and base plates. Once the chamber is pumped down, heat was transferred to the upper and base plates from the platform through radiation. Due to the plates are constructed of stainless steel, are able to reflect and scatter radiation, the plates will not absorb much heat radiation and keep cooled to low. Temperature through natural convection by ambient air. It is designed so that the platform is well thermally isolated from the chamber enclosure that included the cylinder wall and two steel plates. This is a unique feature of the furnace design. It allows for the platform to be heated to high temperatures while the temperature of the rest of the chamber remains relatively low. This is very important as a safety issue allows the chamber to be sealed in vacuum using O-rings. The upper plate is mounted with an ultra-Torr connector to hold the small K-type thermocouple probe for measuring the sample temperature. The base plate contains four ports with National Pipe Thread (NPT). Two of these are occupied with feedthroughs. One feedthrough is for a pair of copper wires to pass into the chamber to connect to the two ends of the heating wire. The other feedthrough is for thermocouple wires. Finally, the third port is used for the vacuum gauge, and the fourth port is for connecting to a mechanical pump. In this design, the chamber is allowed to pump down to 50 milli-torrs and the maximum temperature of the platform is allowed to reach up to 450 ℃. During the solid-state bonding process in the vacuum chamber, the samples were mounted in a stainless steel fixture and applied with a static planar pressure to ensure intimate contact. The assembly was then placed on the graphite platform. Once the vacuum furnace was pumped down and kept at 50 to 100 milli-torrs

to suppress oxidation during solid-state bonding, the temperature controller is turned on to heat up the platform. After reaching the peak temperature and dwell for certain amount of time, the heater was turned off and the assembly was allowed to cool down naturally to room temperature in a vacuum environment. The vacuum bonding furnace described above have been proved to be reliable in controlling the temperature and the vacuum level is good enough for fluxless solid-state bonding. In our laboratory, a number of research works within a decade have been done by using this vacuum bonding furnace, so the design and construction of this vacuum bonding furnace is truly valuable from the scientific perspective.

2.3 Material Characterizations

2.3.1 X-Ray Diffraction

X-ray diffraction (XRD) is a common and important material characterization experimental methodology to study material structures at different dimension levels, from macroscopic to microscopic, as depicted in Fig. 11. Nowadays, XRD is a mature and well-developed experimental technique, and can be used in studying lattice constants, average grain size of power materials, crystallinity, residual stress, crystal quality, epitaxial of thin film and texture or preferred orientation in polycrystalline, and most commonly for phase identification and phase composition determination. In the content of this dissertation, XRD has been heavily used in various research projects.

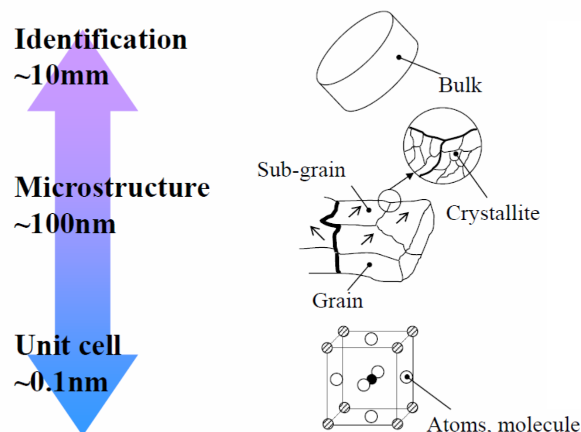

Fig. 2.11 Different level of material structures characterizations of XRD.

In principle, X-ray diffraction is fairly easy to understand by Bragg's Law: the constructive interference happens when the interaction of incident rays and lattice plan satisfy Bragg's equation, as shown in Eq. (2.2):

$$n\lambda = 2d_{hkl}sin\theta \quad (2.2)$$

, where λ is the wavelength of electromagnetic radiation, d is the lattice plane spacing in crystal plane with (h k l) miller index, and θ is the diffraction angle. The detailed principles of X-ray diffraction were well-described in the reference textbook [4]. Therefore, the author would like to focus on the real experimental and instrumental part of XRD in this dissertation.

In practice, Rigaku SmartLab X-ray diffractometer in Irvine Material Research Institute is used for X-ray diffraction characterization. As shown in Fig. 2.12, SmartLab X-ray diffractometer consists of a number of essential parts: 1. A collimated Cu K_{α} line excitation X-ray source, 2. A set of incident-beam optics and receiving-beam optics, 3. A X-Ray detector: count the number of X-rays scattered by the sample, 4. The goniometer and sample stage: the platform that holds and moves sample, optics, detector, and x-ray tube.

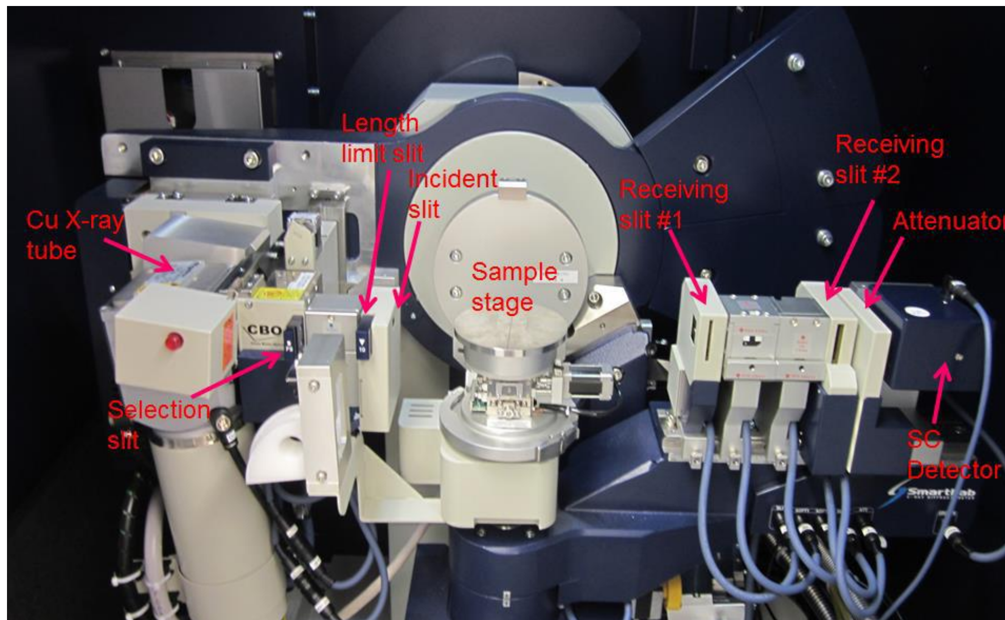

Fig. 2.12 Essential hardware components of Rigaku SmartLab X-ray diffractometer.

In general, two different hardware settings, namely, Bragg–Brentano (BB) and Parallel Beam (PB), can be used in SmartLab diffractometer. Bragg–Brentano optics setting should be used for bulk polycrystalline or power materials characterization, whereas Parallel Beam optics setting usually can be applied to thin film materials characterization. As shown in Fig. 2.13, the upper figure depicted the optics setting inside of Cross Beam Optics (CBO) unit. By changing the selectable slit, the either a focusing beam or a parallel beam can be selected for the usage of BB XRD or PB XRD respectively. In the lower left figure, the focusing beam generated by X-ray gun (XG) can be diffracted by the sample crystal plane and collected by D-tex Ultra X-ray (1D) detector after passing through the receiving slits (RS). In the lower right figure, the parallel beam reflected by the multilayer mirror (single crystal planes) can be diffracted by the sample and collected by scintillation counter (0D) detector after passing through parallel slit analyzer (PSA).

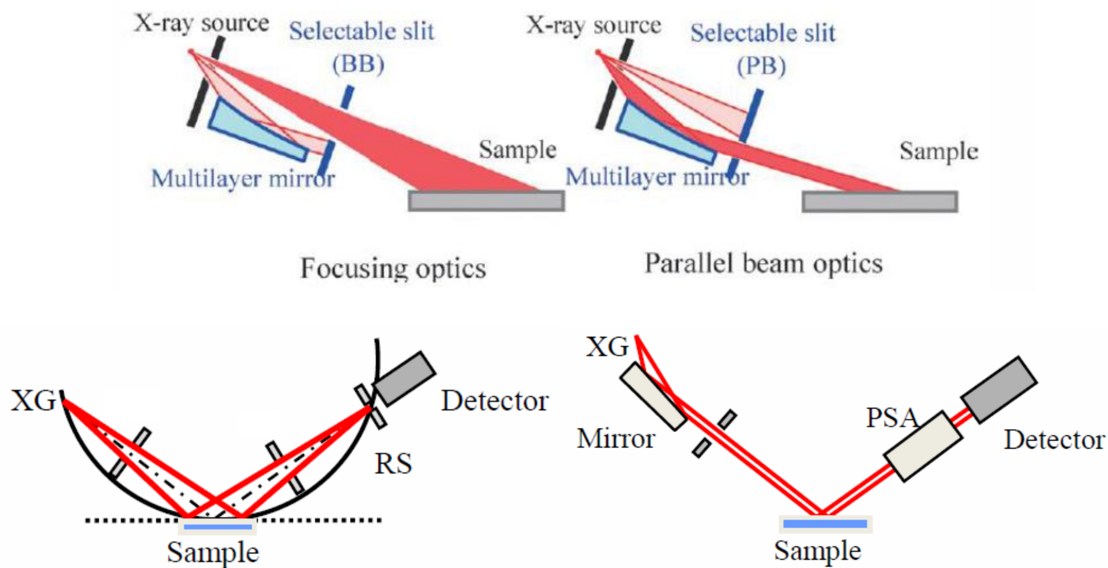

Fig. 2.13 Bragg–Brentano optics setting (left) vs. Parallel Beam optics setting (right).

For BB optics setting, the X-ray penetration depth is around hundreds of microns to several microns, depending on mass absorption coefficient, density, packing factor of the sample material. Within the X-ray penetration depth, as depicted by Fig. 2.14, there will be only a small fraction of material crystallites, namely, whose the lattice planes are parallel to diffraction vector Q, in the sample that are satisfied with diffraction condition and can contribute to X-ray diffraction peak intensity.

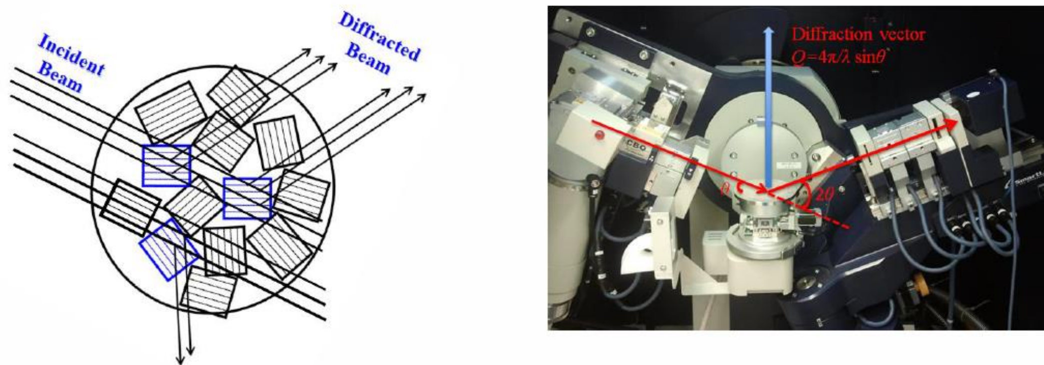

Fig. 2.14 The interactions between X-ray beams and materials in Bragg–Brentano optics setting.

For PB optics setting, it can be further divided into three different modes, as shown in Fig 2.15, namely, out-of-plane, grazing incidence, and in-plane scanning for thin films XRD characterization.

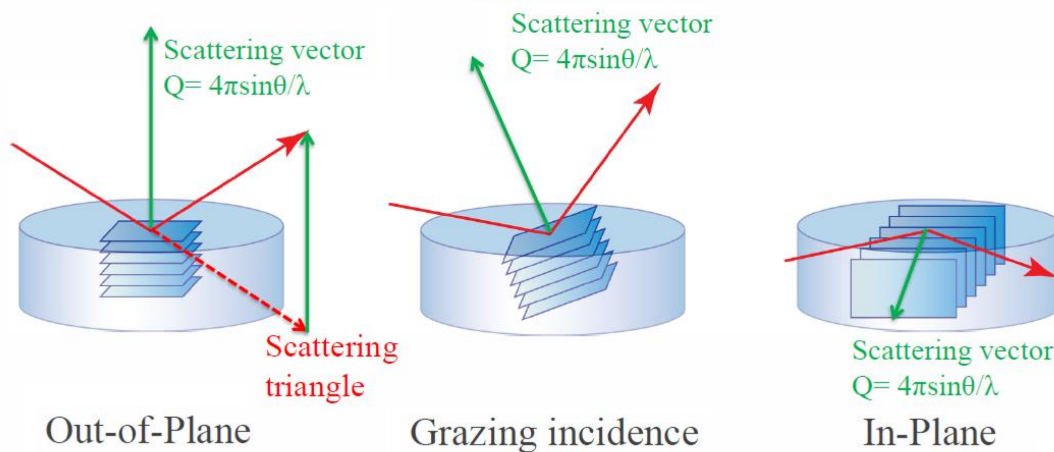

Fig. 2.15 Three different scanning modes in Parallel Beam optics setting.

The out-of-plane scan is similar to BB mode except the X-ray penetration depth is much smaller, usually less than 1 μm, whose X-ray scattering vector is fixed during the measurement. In contrast, as shown in Fig. 2.16, the grazing incidence X-ray diffraction (GIXRD) is quite different from BB mode, whose X-ray scattering vector is tilting and changing during scan, thereby probing grains in all directions during the measurement. As shown in right figure of Fig. 2.16, the incident angle α is set slightly above the critical angle of the film material, at which the total reflection of X-ray beam occurs.

Therefore, the diffracted X-ray signal from substrate of thin film can be suppressed so that the signal contribution from thin film itself can be enhanced, compared to out-of-plane setting.

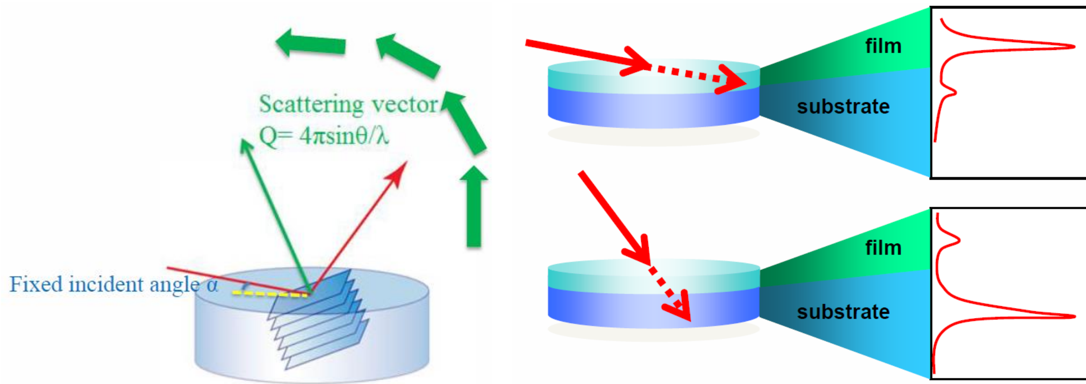

Fig. 2.16 The principle of grazing incidence X-ray diffraction (GIXRD) schematic demonstration, tilting X-ray scattering vector (left) and ratios of signal contribution of GIXRD (upper right) and out-plane setting (lower right).

The third mode of PB optics setting is called in-plane scan, as shown in Fig. 2.17. The X-ray diffraction occurs at the crystal planes within the plane of the sample stage, while the receiving-beam arm and detector move parallel to the surface of that plane. By using this scan setting, second dimension of sample material can be probed by X-ray diffracted beam so that we are be able to construct a 2D pole-figure mapping based on the XRD data of out-of-plane and in-plane scan. Interesting micro or nano structures of thin film materials, such as texture, preferred-orientation and epitaxial directions can be learned from this type of experimental technique.

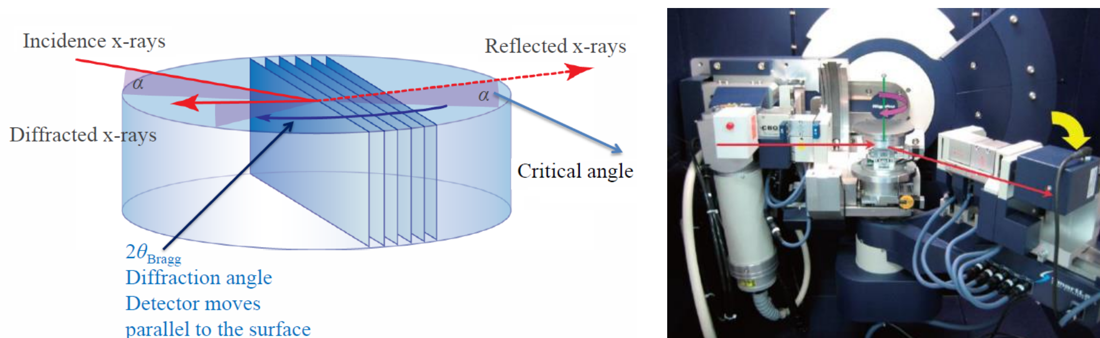

Fig. 2.17 In-plane XRD schematic demonstration (left) and real machine setting (right).

In summary, the principle and experimental details of various XRD techniques that were used in the research and study works during the period of this dissertation are briefly reviewed. Particularly, the BB and PB GIXRD settings were frequently used for material characterizations by the author, and those techniques are very useful and important for bulk material and thin film material characterization. The author would like to express the gratitude towards Dr. Qiyin Lin in teaching how to use and operate Rigaku SmartLab X-ray diffractometer and sharing his expertise in the field of experimental X-ray diffraction characterization techniques.

2.3.2 X-ray and Ultraviolet Photoelectron Spectroscopy

X-ray photoelectron spectroscopy (XPS) and ultraviolet photoelectron spectroscopy (UPS) are very useful material characterization techniques associated with surface science. As depicted by Fig. 2.18, the main difference between bulk, thin film materials and material surface analysis is the physical scale of the dimension. XPS and UPS are such highly surface sensitive experimental techniques due to the fact that 95 percentage of the detected signal is contributed from topmost surface atomic layers within approximately 5 nm. Therefore, XPS and UPS are largely used in characterizing the surface property of materials, associated with the research works on surface science, such as surface diffusion and corrosion related phenomena.

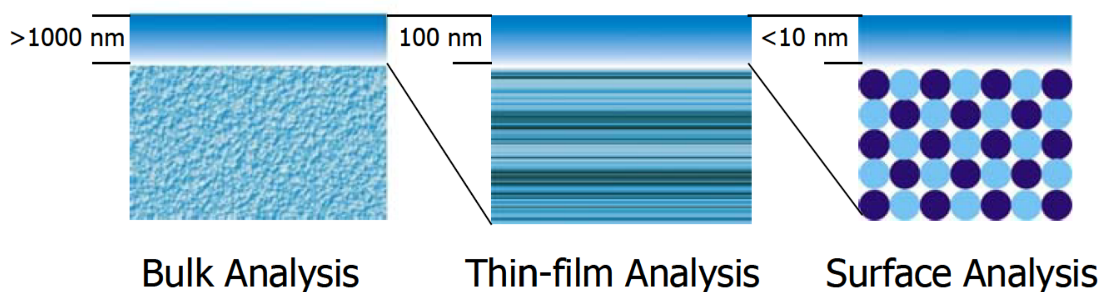

Fig. 2.18 The physical scale of dimension for bulk, thin film materials and material surface analysis.

In principle, XPS and UPS utilized same effects of photoelectric physical process, discovered by Albert Einstein, as shown in Fig 2.19. A incident photon can knock off the inner-core electron of materials, and then generate a photoelectron which can be ejected out of the surface of materials. By the

studying the analysis the kinetics energy of the photoelectron, the binding energies of the inner-core electrons and valence band electrons can be probed experimentally, thereby allowing people to plot such as survey spectrum, region spectrum, valence band spectrum. By using the concept of chemical shift, people can use shifting spectrum of inner-core electrons to testify in chemical states changing. In words, XPS and UPS use physics to interpret chemistry.

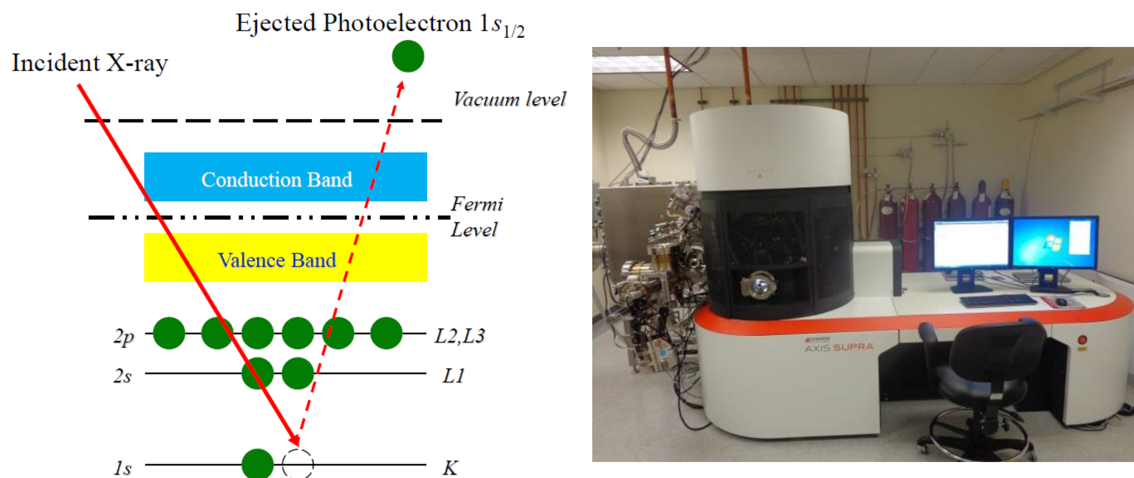

Fig. 2.19 The principle of photoelectric process in X-ray photoelectron spectroscopy (left) and AXIS Supra by Kratos Analytical instrument (right).

In practice, AXIS Supra by Kratos Analytical in IMRI was used for XPS and UPS characterization experiments. The AXIS Supra by Kratos Analytical is a high performance multi-technique surface science instrument combining high-sensitivity X-ray photoelectron spectroscopy (XPS) with Al/Ag monochromatic X-ray source, high resolution Auger electron spectroscopy (AES), ultraviolet photoelectron spectroscopy (UPS). The system is equipped with a multi-mode monatomic Ar^+ and Ar_n^+ gas cluster ion source (GCIS) for state-of-the-art sputter cleaning and depth profiling of any inorganic or organic material, conductive or insulating. The author would like to express the gratitude towards Dr. Ich Tran in teaching how to operate AXIS Supra and basics of XPS and UPS.

2.3.3 Scanning Electron Microscopy

The Scanning Electron Microscopy (SEM) is one of most frequently used experimental techniques, which permit the direct observation and characterization of organic and inorganic materials on micrometer to nanometer scales. The main reasons for the gaining popularity of SEM are ease to use and ease to understand. SEM pictures can be easily understood by people who didn't receive any formal scientific training, so that those pictures can be often used as demonstration to the ordinary audience without further explaining the technical details. In addition, there is no special requirement for the preparing the SEM samples as long as the sample surface is conductive or coated with thin layer of conductive materials to direct the electron to the ground. In principle, SEM can be divided into several main parts: electron filament, electron gun and lenses, scanning coil, camera and electron detectors. Electron filament and gun can use either thermo-emitting or field-emitting effects to generate and accelerate electrons with high voltage. The electron-magnetic lenses can be used to focus electron on the sample, and scanning coil can direct the focused electrons to scan areas in screen with relatively high scanning speed. When the electrons hit the sample, it will result in creation of so called "interaction volume" of SEM. As illustrated in Fig. 2.20, there are various signals that can be generated from the interaction between primary electron beam and sample material, such as auger electrons (AE), secondary electrons (SE), backscattered electrons (BSE), characteristic X-ray, continuum X-ray, secondary fluorescence and etc. Those signals generated from scanned area of the sample can be further collected by various detectors, thereby producing the SEM images of that area with various contrasts for different mechanisms. In the content of this dissertation, the mostly frequent used signal is secondary electrons, resulting in the embodiment of the surface morphology of the sample material. Backscattered electrons can also be used, either generating Z-contrast by the atomic number at low scattering angle or crystallography contrast at high scattering angle, to produce BSE image or electron backscattering diffraction (EBSD) image. Characteristic X-ray can be used as the signatures of different elements, resulting in determining the chemical compositions of the sample within the interaction volume both qualitatively and quantatively. This type of method is known as Energy Dispersive X-ray Spectroscopy (EDX), where some quantative

errors induced by atomic-number (Z) effect, the absorption (A) effect and the fluorescence (F) excitation effect must be accounted and corrected, usually by the so called ZAF correction method. More details on the topic of SEM principle can be found in the reference textbook [5]. The author would like to express the gratitude towards Professor Daniel Mumm in teaching the course, ENGRMSE 264, to provide his insights on the topics of SEM related theorem and principle.

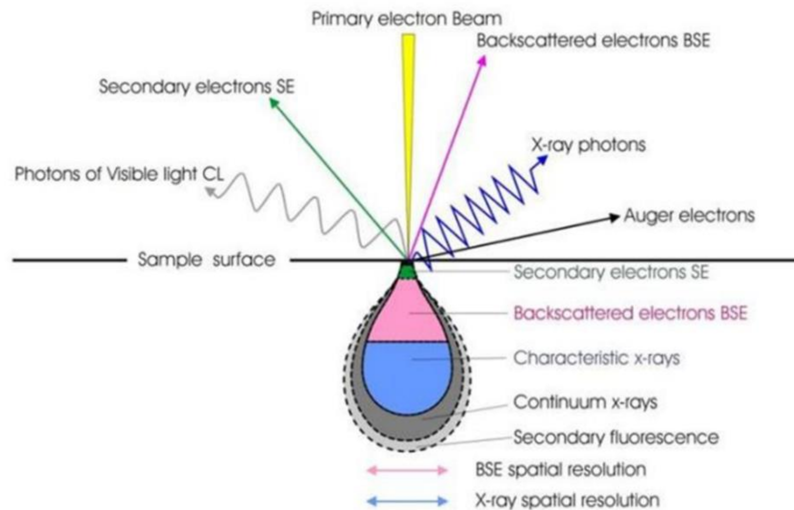

Fig. 2.20 The interaction volume and all of the signals produced by the interaction between the electron beam and sample material.

In practice, as shown in Fig. 2.21, the Philips XL-30 FEG SEM was used for most of SEM imaging in the content of this dissertation. XL-30 is a thermionic field emission SEM which is fully automatic gun configuration controlled by advanced computer technology. The magnification is up to 800,000X with 2nm resolution. It is easy to use for examining and survey the morphology of the nano structures. This XL30 also equipped with EDX detector to provide the composition information. The author would like to express the gratitude towards Dr. Qiyin Lin in teaching how to operate this SEM instrument and recommending the author as the lab assistant in charge of this SEM in conducting training for new users and various individual projects for both academic and industrial customers.

Fig. 2.21 Philips XL-30 FEG SEM.

2.3.4 Focused Ion Beam Technique and Microscopy

Focused Ion Beam (FIB) is a technique used particularly in the semiconductor industry, materials science and increasingly in the biological field for site-specific analysis, deposition, and ablation of materials. In general, FIB is a very flexible technique, allowing people to either cut materials or deposit materials with arbitrarily designed shapes or patterns. In the content of this dissertation, FIB is very useful in making a clean-finishing cross-section, thereby avoiding the "smear" effects usually induced by mechanical polishing. In principle, a FIB setup is a scientific instrument that resembles SEM. However, while the SEM uses a focused beam of electrons to image the sample as discussed previously, the FIB microscopy uses a focused beam of ions instead. FIB can also be incorporated in a system with both electron and ion beam columns, allowing the same feature to be investigated using either of the beams. Most FIB instruments are using liquid metal ion sources (LMIS), especially gallium ion (Ga^+) sources, to generate the ion beams. The gallium primary ion beam hits the sample surface and sputters a small amount of material, which leaves the surface as either secondary ions or neutral atoms. The primary beam also produces secondary electrons. As the primary beam raster-scanning on the sample surface, the signal from the sputtered ions or secondary electrons is collected

to form an image. One should note that FIB with high voltage and large current can largely damage and etch the surface of the materials. Therefore, single frame or integrated frames of FIB images are usually captured instead of viewing FIB imaging alive at screen.

In practice, FEI Quanta 3D FEG Dual Beam SEM/FIB Instrument was used for most of FIB imaging and operation in the content of this dissertation, as shown in Fig. 2.22.

Fig. 2.22 FEI Quanta 3D FEG Dual Beam SEM/FIB Instrument.

A Gas Injection Source (GIS) probe can be inserted into the chamber during SEM/FIB operation, so that FIB-assisted chemical vapor deposition (CVD) can be applied to deposit Pt onto the sample surface. The FIB-assisted can be divided into three sub-steps: 1. Adsorption of the organic-metallic precursor molecules on the sample surface, 2. Focus ion beam induced dissociation of the gas molecules, 3. Deposition on the sample surface atoms and removal of organic ligands. As shown in Fig. 2.23, a strip of Pt layer can be deposited by FIB deposition and viewed by SEM/FIB imaging at same time.

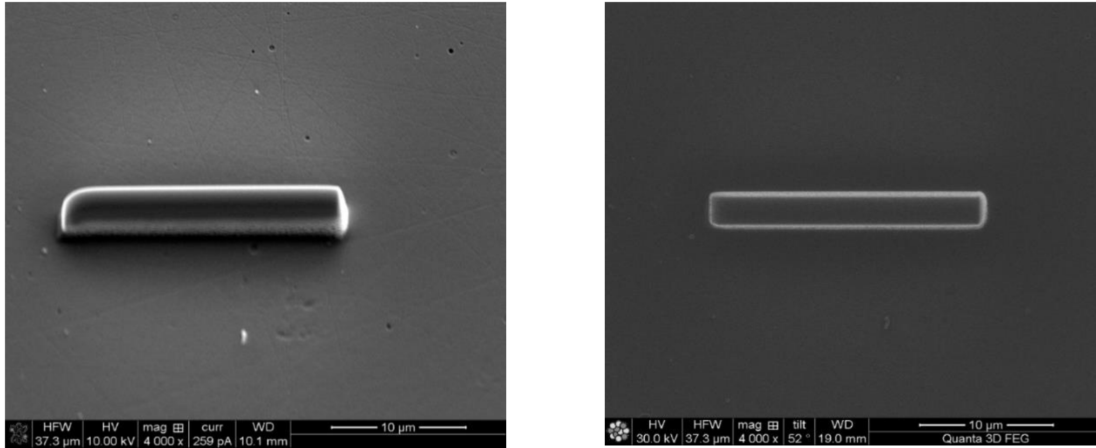

Fig. 2.23 SEM imaging at 52 °(left) and FIB imaging at 0 °(right) of FIB deposited Pt strip layer.

Moreover, the FEI Quanta 3D has also equipped with Omniprobe, which can be used to pick the chopped-off sample in the chamber. By using the FIB deposition, FIB cutting and Omniprobe in combine, a start-of-art way to prepare bulk or cross-sectional transmission electron microscopy (TEM) sample had been enabled and developed. As shown in Fig. 2.24, after a number of sequence of FIB deposition and FIB cutting, the Omniprobe can pick off the tiny TEM sample from the bulk sample surface and further attached to TEM grid for furthering TEM sample thinning by FIB. The type of TEM sample preparation is extremely useful in semiconductor industry for making TEM sample at interfaces without mechanically damaging the original interfaces.

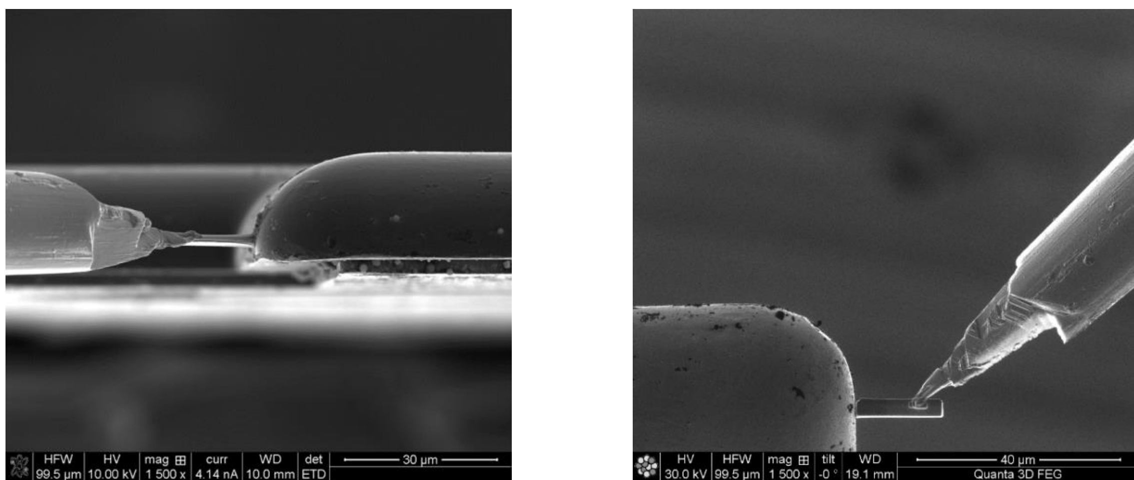

Fig. 2.24 SEM imaging at 0 °(left) and FIB imaging at 52 °(right) of TEM sample attaching TEM grid by using Omniprobe.

The author would like to express the gratitude towards Dr. Jian-Guo Zheng, the operational director of IMRI, in teaching how to operate FEI Quanta 3D for its various functions, especially for the TEM sample preparation techniques by FIB, which was developed by himself. The author has been learning a lot from his great expertise in SEM/FIB/TEM, moreover, his enthusiasm and dedicating spirit towards scientific research.

2.3.5 Transmission Electron Microscopy

Transmission electron microscopy is a microscopy technique in which a beam of electrons is transmitted through a material sample to form an image. The TEM sample is most often an ultrathin section less than 100 nm thick or a suspension on a grid. An image is formed from the interaction of the electrons with the sample as the beam is transmitted and/or diffracted through the material sample. Compared with SEM, TEM imaging is much harder to acquire, especially for making thin TEM sample. In addition, TEM imaging cannot be understand intuitively and need to have relatively complicated physical insights in order to interpret it properly. However, TEM offers a much better spatial resolution, up to single atom (1 Å), and can give much more material structural and crystallographic information than SEM. Therefore, TEM is extremely useful for material and solid-state physics scientific study. Nowadays, TEM related techniques are relative mature and have various modes for different applications, such as bright field (BF), dark field (DF), selected area diffraction (SAD), convergent-beam electron diffraction (CBED), electron energy-loss spectrometry (EELS), high-resolution TEM (HRTEM), high-angle annular dark-field (HAADF) imaging, and more. More details on the topics of TEM physics and principles can be found in the reference textbook [6].
The author would like to express the gratitude towards Professor Xiaoqing Pan, the director of IMRI, in teaching the course, ENGRMSE 259, to provide his insights on various topics of TEM related theorem and principle, for which the author had a chance to audit.

In practice, FEI/Philips CM-20 conventional TEM, as shown in Fig. 2.25, was used in the content of this dissertation. Philips CM 20 TEM with EDX system has accelerating voltage 200 kV that can obtain the image resolution down to 0.27 nm with maximum magnification 750,000X. This CM20 TEM is

equipped with an energy dispersive spectrometer (EDS) that can perform element analysis. The author would like to express the gratitude towards Dr. Jian-Guo Zheng in teaching how to operate CM-20.

Fig. 2.25 FEI/Philips CM-20 conventional TEM.

2.3.6 Atomic Force Microscopy

Atomic force microscopy (AFM) is a type of scanning probe microscopy (SPM), with demonstrated resolution on the order of fractions of a nanometer, more than 1000 times better than the optical diffraction limit. The information is gathered by "feeling" or "touching" the surface with a mechanical probe. Piezoelectric material that facilitate tiny but accurate and precise movements on command enable very precise scanning. The AFM consists of a cantilever with a sharp tip (probe) at its end that is used to scan the specimen surface. When the tip is brought into proximity of a sample surface, forces between the tip and the sample lead to a deflection of the cantilever according to Hooke's law. The AFM can be operated in a number of modes, depending on the application. In general, possible imaging modes are divided into static (also called contact) modes and a variety of dynamic (non-contact or "tapping") modes where the cantilever is vibrated or oscillated at a given frequency. The AFM has three major abilities: force measurement, imaging, and manipulation. In force measurement,

AFMs can be used to measure the forces between the probe and the sample as a function of their mutual separation. This can be applied to perform force spectroscopy. For imaging, the reaction of the probe to the forces that the sample imposes on it can be used to form an image of the three-dimensional shape (topography) of a sample surface at a high resolution (1Å). This is achieved by raster scanning the position of the sample with respect to the tip and recording the height of the probe that corresponds to a constant probe-sample interaction. The surface topography is commonly displayed as a pseudo-color plot. In manipulation, the forces between tip and sample can also be used to change the properties of the sample in a controlled way. Examples of this include atomic manipulation, scanning probe lithography and local stimulation of cells.

In practice, Keysight (formly known as Agilent Technologies) 7500 AFM was used in research of the content of this dissertation, as shown in Fig. 2.26.

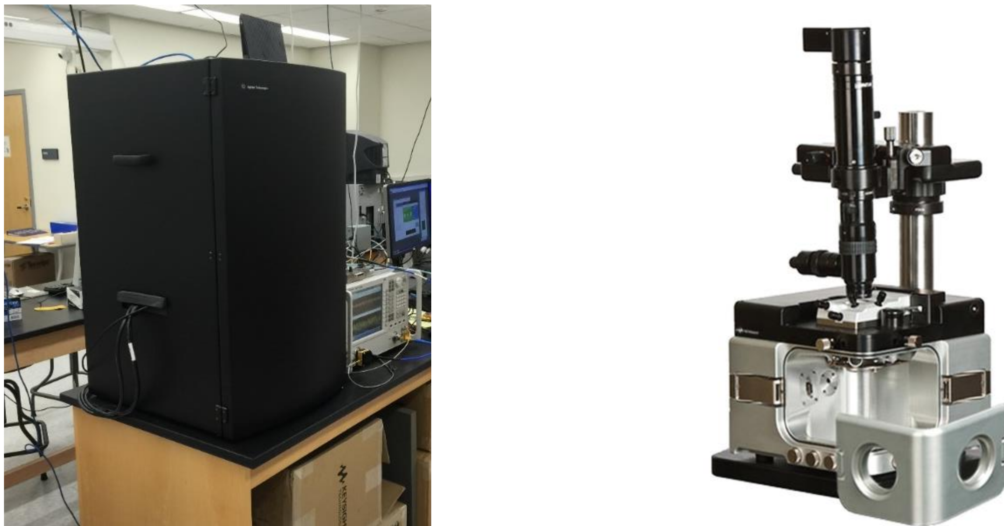

Fig. 2.26 Keysight 7500 AFM.

The Keysight 7500 AFM establishes new performance, versatility, and ease-of-use benchmarks for nano-scale measurement, characterization, and manipulation. The 90 um AFM closed scanner achieves outstanding low noise performance, enabling atomic-resolution imaging. The 7500 is ideal for materials science, life science, polymer science, electrochemistry, electrical characterization, and nanolithography applications. The Keysight 7500 AFM can enable both contact and non-contact modes AFM measurements by changing different types of probes. The author would like to express

the gratitude towards Professor Peter Burke in facilitating the AFM measurement, and Dr. Jinfeng Li in performing the AFM measurement for our group research.

2.4 Summary

In this chapter, the author had reviewed the main instrumentations and experimental techniques that were used in both *Material Synthesis and Processing* and *Material Characterizations* in the content of this dissertation. For materials synthesis and processing, the author introduced the details in vacuum casting, E-beam deposition and vacuum bonding technique. For the material characterizations, the author introduced the basic principles and instrumental details in XRD, XPS/UPS, SEM/EDX, FIB, TEM, and AFM. Some other instrumentations and experimental techniques had been also used in the content of this dissertation, such as optical microscope, sputter coater, mechanical polisher, epoxy mounting technique, slow diamond slow cutting machine, Instron 5500R tensile tester, Dektak XT profilometer, four-point point probe sheet resistance measurement, thermal diffusivity measurement by NETZSCH Laser Flash Analyzers (LFA) 449, optical reflectivity measurement by Perkin Elmer Instruments, Lambda 950. These techniques are rather straightforward or discussed somewhere else in the content of specific following chapters.

Overall, Irvine Materials Research Institute (IMRI) [7] offered a fantastic academic environments for the research work of the author, in terms of instruments hardware and professional and friendly people in there. At last, I would like to give a special thanks to all who had taught and helped me in terms of various Instrumentations and Experimental Techniques described in the content of dissertation.

Reference in Chapter 2

1. P. Yang, and J. M. Tarascon, "Towards systems materials engineering", *Nature Materials*, vol. 11, No. 7, pp. 560-563, 2012.
2. C. R. M. Grovenor, H. T. G. Hentzell, and D. A. Smith, "The development of grain structure during growth of metallic films", *Acta Metallurgica*, vol. 32, No. 5, pp.773-781, 1984.
3. C. C. Lee, D. T. Wang and W. S. Choi, "Design and construction of a compact vacuum furnace for scientific research", *Review of Scientific Instruments*, vol. 77, No. 12, p.125104-1-5, 2006.
4. B. D. Cullity and S. R. Stock, "Elements of X-Ray Diffraction", third edition, Prentice Hall, New Jersey, 2001.
5. J. Goldstein, D. E. Newbury, P. Echlin, D. C. Joy, A. D. Romig Jr, C. E. Lyman, C. Fiori and E. Lifshin, "Scanning electron microscopy and X-ray microanalysis: a text for biologists, materials scientists, and geologists", third edition, Springer Science & Business Media, 2012.
6. B. Fultz and J. M. Howe, "Transmission electron microscopy and diffractometry of materials", fourth edition, Springer Science & Business Media, 2012.
7. Irvine Materials Research Institute, IMRI, website available at: http://www.imri.uci.edu.

Chapter 3

Mechanical Properties of Silver-Indium Solid solution

3.1 Introduction

The material properties of silver and its solid solution had been studied for near a century. In the early days of material and metallurgical science, the lattice constant [1] and elastic constant [2] have been measured and investigated thoroughly for silver primary solid solution, namely, silver solid solution of cadmium, indium, tin, antimony, etc. Solid solution strengthening mechanism is well-known, responsible for increasing the yield strength and hardness of metal which is the result of the interactions between dislocations and solute atoms by following mechanisms: elastic interaction, modulus interaction, stacking-fault interaction, electrical interaction, short-range order and long-range order interaction [3]. Several theoretical models have been proposed for specifically describing the solid solution strengthening mechanisms of silver or FCC crystal structure metal based solid solution [4-6]. However, the research for investigating the mechanical behaviors, especially plasticity of silver based alloy is relatively seldom and underdeveloped, which is possibly due to the fact that silver and its alloy are not major metallic material for structural engineering applications. Recently, silver based alloys have been adopted as a new alternative in interconnection applications [7-8]. Therefore, silver-based solid solution mechanical properties, especially plasticity, would be of a great interest to the electronic devices manufacturing and packaging industry since it is closely related to the manufacturability of the silver alloy based products, and the performance and reliability of electronic components during and after the process of the manufacturing. Stress-strain curve obtained in the tensile test is widely used to provide fundamental information on the strength and mechanical properties for engineering applications. Therefore, the stress-strain curves of silver solid solutions would be very useful and important for the further research and development in this area.

Our research group has been studying the Ag-In system for almost two decades [9], and developed several important fluxless bonding technologies based on the Ag-In binary system. During the previous research, the authors have identified two major intermetallic compound, namely Ag_2In and

$AgIn_2$ [10]. Recently, our research group has successfully converted almost all of those intermetallic compounds into silver-indium solid solution phase [11], which is designated as (Ag)-xxIn in this paper. The experimental results show that the properties of the bonding joint with (Ag)-xxIn phase are intriguingly great. Thus, as following research, we decided to produce (Ag)-xxIn single phase ingots with varied indium concentration to study the properties of this interesting material. The authors have recently reported the great anti-tarnishing property of silver-indium solid solution phase [12]. In this chapter the authors would like to reveal the some details of the material in preparation, and present the characteristic stress-strain curves of silver-indium solid solution with analysis of its mechanical properties.

In the following sections, the authors would like to present the preparation and characterization of (Ag)-xxIn phase material in the polycrystalline form at two different indium compositions with further details. Secondly, the preparation of tensile test samples and the experimental setting of the tensile test are described, followed by the representative results of the tensile test, i.e., stress vs. strain curves, with analysis and discussions. In addition, SEM pictures of the morphology of fractured tensile test samples are presented, following with analysis of the fracture mode and failure mechanism. Lastly, the authors would like to share the vision in terms of the implications of mechanical properties of (Ag)-xxIn solid solution and its potential industrial utility due to its superior intrinsic mechanical behaviors under tensile stress.

3.2 Material Preparation and Characterization

In order to understand Ag-In binary system and produce the single phase (Ag)-xxIn material, it is essential to review the Ag-In binary phase diagram. As shown in silver-indium phase diagram, Fig. 3.1 [13], the maximum solubility of indium element in silver crystal lattice is 20 at. % at room temperature, the silver-indium solid phase with face-centered cubic (FCC) crystal structure is designated as α phase historically. In reference [14], the authors discovered α' phase, which has also cubic crystal structure, at the composition of 25 at. %, and it is correspond to Ag_3In which is transformed from ζ phase at 187℃. It is important to note that material composition may fluctuate

from region to region, which can be caused by various mechanism of segregation effects. Therefore, it is necessary to give enough clearance to the maximum solubility boundary in order to avoid entering the mixture region of α and α' phase in the phase diagram, thereby producing nearly homogeneous single phase silver-indium solid solution. Therefore, (Ag)-xxIn with 19 at. % indium concentration has been chosen as the primary research subject, which is designated as (Ag)-19In in this article. In addition, (Ag)-xxIn with 9.5 at. % indium concentration, which is designated as (Ag)-9.5In, has been also produced and investigated in order to observe the influence of the amount of indium element composition on the properties of (Ag)-xxIn phase. Pure silver has also been grown using the same method as the controlled group for the following experiments.

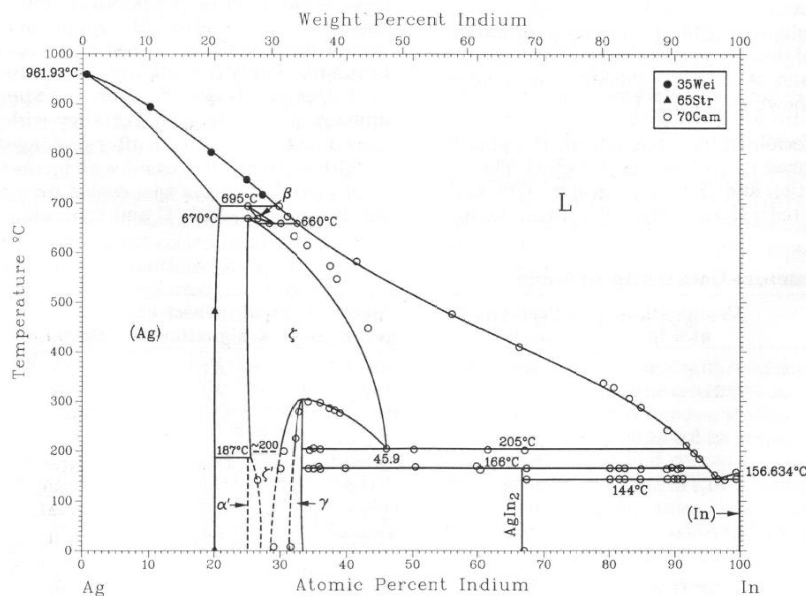

Fig 3.1 Silver-indium binary phase diagram.

The casting method, as described in Chapter 2, was chosen for the production of the material of the interested phase, resulting in the form of ingots. The raw materials of silver and indium shots with 99.99% purity were weighed, uniformly mixed and loaded in quartz tube with one end closed. Since the native oxide forming on the surface of silver and indium metal is negligible thin, there is no treatment required to perform before loading the raw material. While the quartz tube is being pumped by a vacuum pump, the other end of the tube is sealed by hydrogen-oxygen torch operation to form a capsule. The vacuum environment is necessary for the casting production for reducing the

number of voids or common defects created by trapped air bubbles. Next, the capsule was placed into a furnace preheated at 1030 ℃ and stayed there for 30 minutes. The temperature of the furnace was then reduced gradually to room temperature in 7 days in order to obtain the homogenized single phase solid solution at different compositions. This is the preliminary process and optimization requires more time and many growth runs.

After the successful production of (Ag)-xxIn solid solution, the ingots were cut into disk samples, using slow speed diamond saw, for further chemical composition examination. X-ray diffraction (XRD) and scanning electron microscope/energy dispersive X-ray spectroscopy (SEM/EDX) were used in a combination to identify (Ag)-xxIn phase, since their functionality are complementary to each other. While SEM/EDX can provide information about specific chemical composition at local areas within its electron-beam interaction volume, a few micron meters or sub-micron range depending on the electron beam energy and atomic number of the material under examination, XRD is capable of interpreting the crystallography nature of the material by generalizing data generated from macroscopic regions of the samples, thereby identifying the phases of the unknown material precisely and accurately. Before material characterization, the disk samples were prepared by polishing process in the sequence of 120/240/800/1200 grits, using silicon carbide abrasive papers.

FEI/Philips XL-30 FEG SEM in the Laboratory for Electron and X-ray Instrumentation (LEXI) was used for the SEM/EDX examination. Several local areas of the disk samples were randomly chosen to be examined by SEM/EDX. For example, as shown in Fig. 3.2, nine points of interests have been examined by SEM/EDX at 1000× magnification for each (Ag)-9.5In and (Ag)-19In disk samples respectively, and the results of chemical compositions are listed in Table 3.1.

According to the SEM/EDX machine setting, the errors of compositions are ±0.88 at. % and ±0.54 at. % for Ag and In respectively. Therefore, the variation of chemical compositions for the data shown in Table 3.1 is within the range of the error that due to the uncertainty of the SEM/EDX detector, expect for a few points deviation from the intended value.

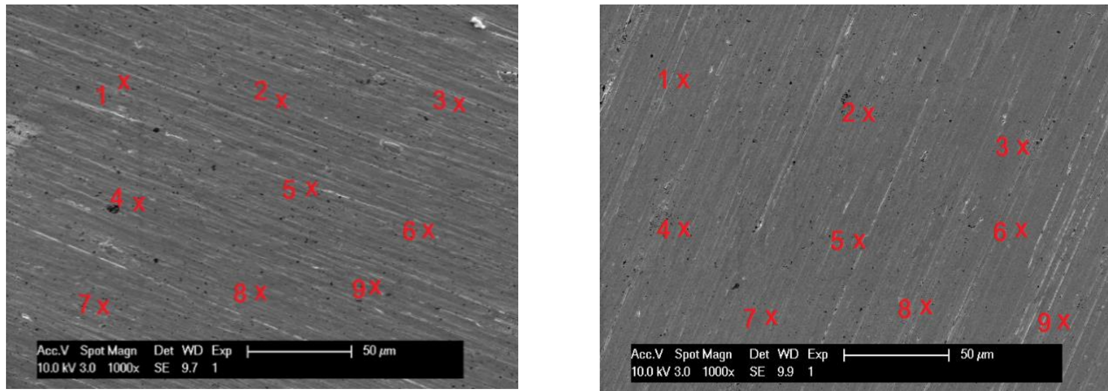

Figure 3.2 (a) (Ag)-9.5In disk SEM/EDX tested region (left), and (b) (Ag)-19In disk SEM/EDX tested region (right).

	(Ag)-9.5 In		(Ag)-19In	
	Ag (at. %)	In (at. %)	Ag (at. %)	In (at. %)
1	90.97	9.03	81.73	18.27
2	90.92	9.08	81.43	18.57
3	91.32	8.68	81.24	18.76
4	91.23	8.77	80.61	19.39
5	92.28	7.72	82.24	17.76
6	90.01	9.99	81.54	18.46
7	90.60	9.40	81.01	18.99
8	90.91	9.09	81.39	18.61
9	90.72	9.28	80.68	19.32

Table 3.1 SEM/EDX results of chemical compositions for (Ag)-9.5In and (Ag)-19In disks in the tested region.

After determination of the chemical composition, Rigaku SmartLab X-ray diffractometer in LEXI was used for further phase identification, using Bragg-Brentano (BB) operation mode with θ-θ diffractometer setting. During XRD examination, the disk sample remains stationary and the detector and X-ray source rotate at the same angular speed. To be more specific, the XRD measurement conditions and parameters are summarized in Table 3.2.

X-Ray Source	40 kV , 44 mA	Scan speed / Duration time	2.0000 deg./min.
Goniometer	None	Step width	0.0200 deg.
Attachment	None	Scan axis	2Theta / Theta
Filter	Cu_K-beta	Scan range	20.0000 - 90.0000 deg.
CBO selection slit	None	Incident slit	2/3 deg
Diffracted beam mono.	None	Length limiting slit	None
Detector	D/teX Ultra	Receiving slit #1	4.000 deg
Scan mode	CONTINUOUS	Receiving slit #2	13.000 mm

Table 3.2 A summary of Rigaku SmartLab X-ray diffractometer measurement conditions and parameters.

The results of XRD examination for (Ag)-9.5In and (Ag)-19In disk samples are shown in Fig. 3.3, with pure Ag disk sample XRD result as reference. The XRD measurement data have been collected and analyzed by PDXL, an integrated powder x-ray analysis software package. The crystallography information for the silver-indium solid solution can be learned thusly from the XRD diffraction, which is listed in Table 3.3.

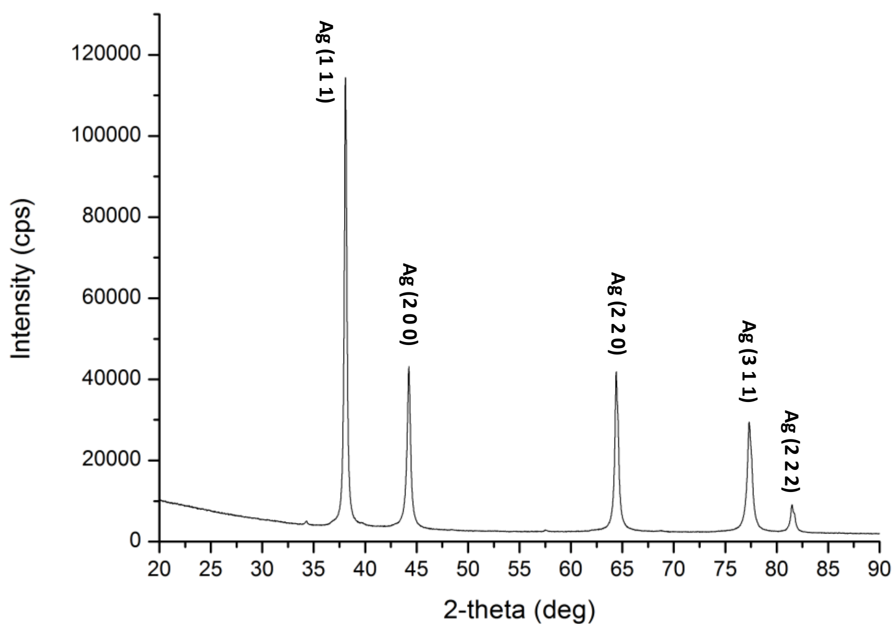

Fig. 3.3 (a) XRD pattern of pure silver disk sample,

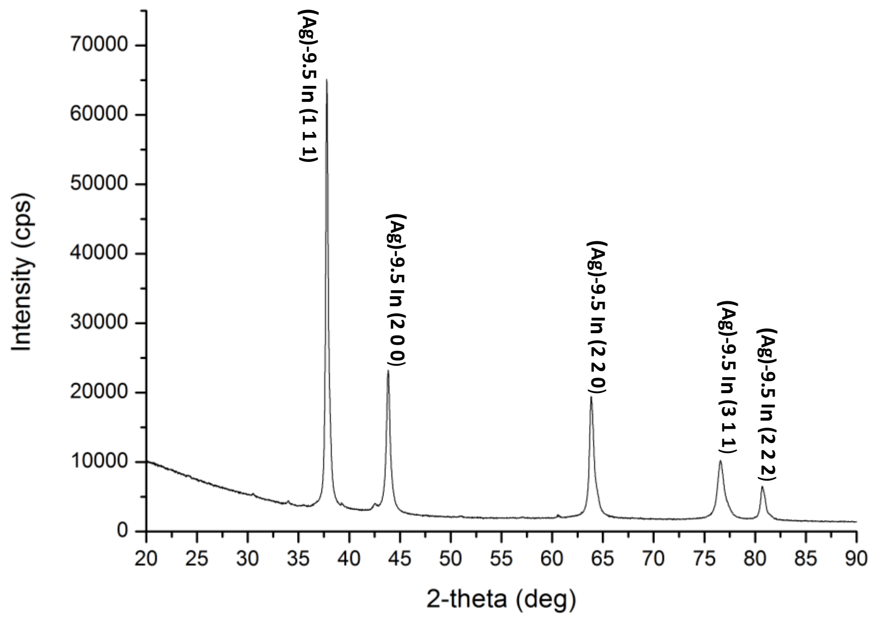

Fig. 3.3 (b) XRD pattern of (Ag)-9.5In disk sample,

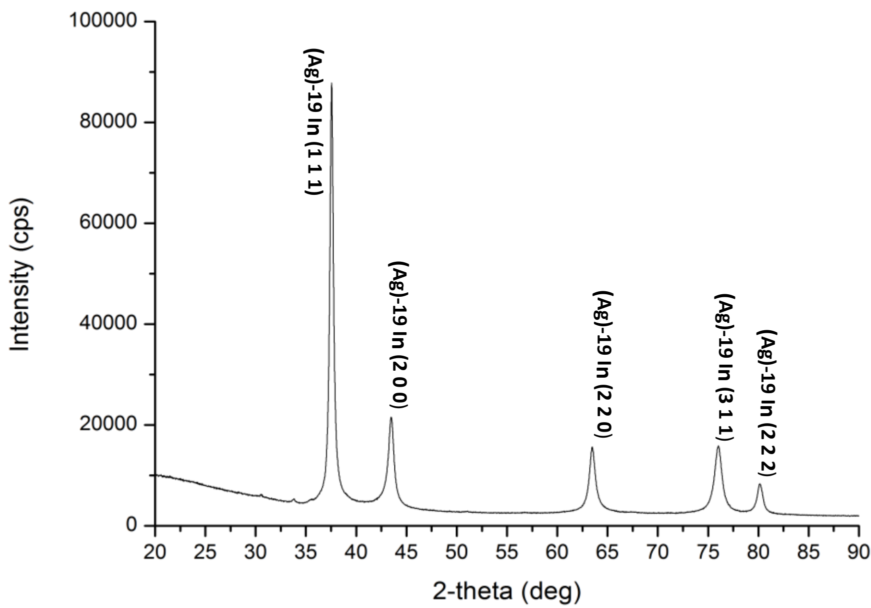

Fig. 3.3 (c) XRD pattern of (Ag)-19In disk sample.

Peaks #	2θ (deg)	**d** (Å)	(h, k, l)	**a** (Å)
1	38.082	2.365	(1 1 1)	4.096
2	44.231	2.048	(2 0 0)	4.096
3	64.378	1.447	(2 2 0)	4.093
4	77.324	1.234	(3 1 1)	4.093
5	81.485	1.181	(2 2 2)	4.091

Table 3.3 (a) A summary of XRD measurement data of pure silver disk sample,

Peaks #	2θ (deg)	**d** (Å)	(h, k, l)	**a** (Å)
1	37.769	2.380	(1 1 1)	4.122
2	43.825	2.067	(2 0 0)	4.134
3	63.816	1.457	(2 2 0)	4.121
4	76.572	1.244	(3 1 1)	4.126
5	80.679	1.191	(2 2 2)	4.126

Table 3.3 (b) A summary of XRD measurement data of (Ag)-9.5In disk sample,

Peaks #	2θ (deg)	**d** (Å)	(h, k, l)	**a** (Å)
1	37.531	2.394	(1 1 1)	4.147
2	43.474	2.082	(2 0 0)	4.164
3	63.423	1.467	(2 2 0)	4.149
4	75.947	1.253	(3 1 1)	4.156
5	80.179	1.197	(2 2 2)	4.147

Table 3.3 (c) A summary of XRD measurement data of (Ag)-19In disk sample after PDXL analysis.

As shown Fig. 3.3, it is very clear that (Ag)-9.5In and (Ag)-19In resemble the crystal structure of pure silver, face-centered cubic (FCC) crystal structure, for its typical systematically peaks absence. In addition, there are no major peaks other the peaks of Ag, (Ag)-9.5In, (Ag)-19In in each XRD patterns. Therefore, it can be safely concluded that the materials in the disk samples are nearly homogeneous and polycrystalline. In Table 3.3, (h, k, l) is the Miller's indices with classic denotation, d is the d-spacing value for corresponding crystal plane, and a is the calculated lattice constant by using the values of each d-spacing. As results, the X-ray diffraction patterns have shifted towards left as the indium element composition increases, which is corresponding to the increasing values of lattice constants from pure Ag, (Ag)-9.5In to (Ag)-19In. The weighted average values for lattice constants are 4.094 Å, 4.126 Å, and 4.153 Å for pure Ag, (Ag)-9.5In, and (Ag)-19In respectively. The trend of increasing values for lattice constants can be explained by reviewing atomic radius for silver and

indium elements. The atomic radius for indium, 167 pm, is larger than that of silver atom, 144 pm, so that if one substitutes silver atoms with indium atoms in the original FCC lattice sites, it would result in the bulge in its crystal structure, thereby increasing the values of the lattice constants as indium element composition increased. In other words, one could reversely determine the indium element composition in (Ag)-xxIn solid solution by examine the lattice constant value using XRD for unknown compositions in the future study. Even though the authors have the awareness of that the radius for silver and indium metallic ions in the metal are different from the values of their atomic radius of solo atoms, the general principle must be plausible for this analysis approach.

The SEM/EDX and XRD results shown above are representatives for disk samples' chemical composition and crystallography examination, and results in general are similar and repeatable for different examined regions, disk samples, and ingots. In conclusion, our research group has been successfully grown the nearly homogeneous and polycrystalline (Ag)-9.5In and (Ag)-19In ingots, using the casting method in a quartz capsule with vacuum pumped and specific annealing profiles within the laboratory and research facility. However, there are still some space for improvement in terms of the ingots growth procedure and annealing profile design.

3.3 Tensile Test

After obtaining nearly homogeneous ingots of (Ag)-9.5In and (Ag)-19In, tensile test samples, conforming with American Society for Testing and Materials (ASTM) standard E8/ E8M- 08 [16], were machined by electrical discharge machining (EDM) which is performed by EDM outsource company. In Fig. 3.4 and Table 3.4, the geometry and dimensions of the tensile test sample are shown respectively. EDM machining can change the surface properties of the work piece, causing the issues such as recasting, heat affected zone (HAZ) grain size enlargement. Therefore, all of the obtained tensile test samples were polished using silicon carbide abrasive papers with 800 grits to remove the HAZ layer on the surface of the tensile test samples. Next, the tensile test samples were put into an oven, annealing at 223°C (homologous temperature T_h = 0.5) for 1 hour, in order to release the residue internal stress induced by the polishing process. After the preparation, all of the tensile test

samples were examined using XRD approach that mentioned previously with the same setting. By comparing the XRD patterns with previous results, the authors can confirm that the tensile test samples have the same composition as the previous disk samples.

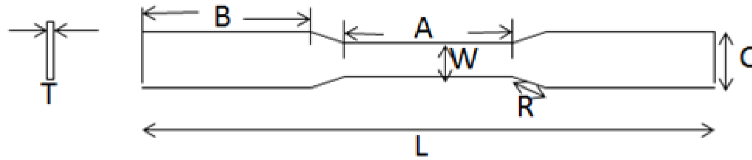

Fig. 3.4 The geometry of tensile test sample, in accordance with ASTM standard E8/ E8M- 08.

The tensile test is performed using the facility, INSTRON 5500R tensile tester, with the deformation rate of 10^{-4} mm/s at controlled software panel setting. Since the real tensile test samples sizes may vary a little bit from its original design, all of the critical dimensions such as the length of the tested region, A, the width of the tested region, W, and the thickness of the sample, T, need to be measured and calibrate at the control software panel. Therefore, the true strain rate is in the vicinity of 10^{-5}/s, which is under the condition of static tension test. During tensile test, the sample is under uniaxial tensile stress initially since the shape of the sample is longitudinal symmetric. The data of engineering stress and strain is recorded, collected, and calculated automatically by the controlled software. (Ag)-9.5In and (Ag)-19In tensile samples were tested with the reference of pure Ag samples in comparison.

unit	W	T	R	L	A	B	C
mm	2.00	1.10	2.00	33.33	10.67	10.00	3.30
inch	0.08	0.04	0.08	1.31	0.42	0.39	0.13

Table 3.4 The dimensions of tensile test sample, in accordance with ASTM standard E8/ E8M- 08.

3.4 Stress vs. Strain Characterization

The true stress and strain can be calculated using the Eq. (3.1) and (3.2) [16]:

$$\sigma = s(e + 1) \tag{3.1}$$

$$\varepsilon = ln(e + 1) \tag{3.2}$$

, where s is the engineering stress, e is the engineering strain, σ is the true stress, and ε is the true strain.

Due to the limitation of the casting method, the ingots may have some defects inside such as cavities and cracks in micron range. In addition, the tensile test samples are from the different locations of the ingots, so that the major orientation of the grains or texture in the each tensile test samples may vary from one to another, and this also applies to the distribution of cavity and cracks in each sample. In Fig. 3.5, three representative results of tensile test for pure Ag, (Ag)-9.5In, and (Ag)-19In are plotted for their engineering stress vs. strain curves.

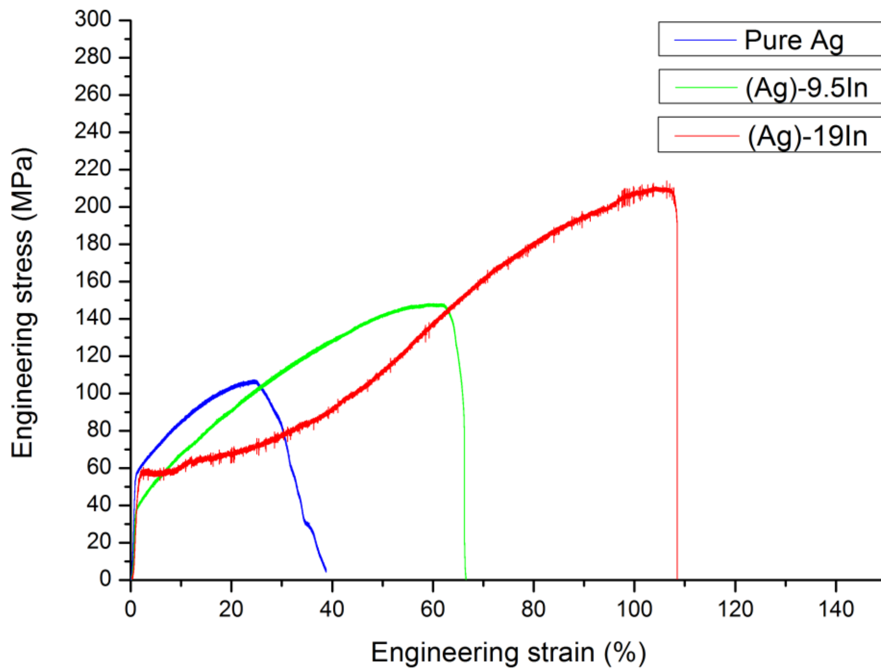

Fig. 3.5 The engineering stress-strain curve of pure silver, (Ag)-9.5In, and (Ag)-19In.

Using the equations (3-1) and (3-2) given above, true stress and strain can be calculated for each data point, thereby plotting true stress vs. strain curves correspondingly, as shown in Fig. 3.6. Mechanical properties of silver-indium solid solution, especially for materials properties of plasticity, such as yield strength, ultimate tensile strength (UTS), true uniform strain and true fracture strain in tension stress status, can be characterized, using the obtained true stress-strain curves. The values of these mechanical properties are summarized and documented in Table 3.5.

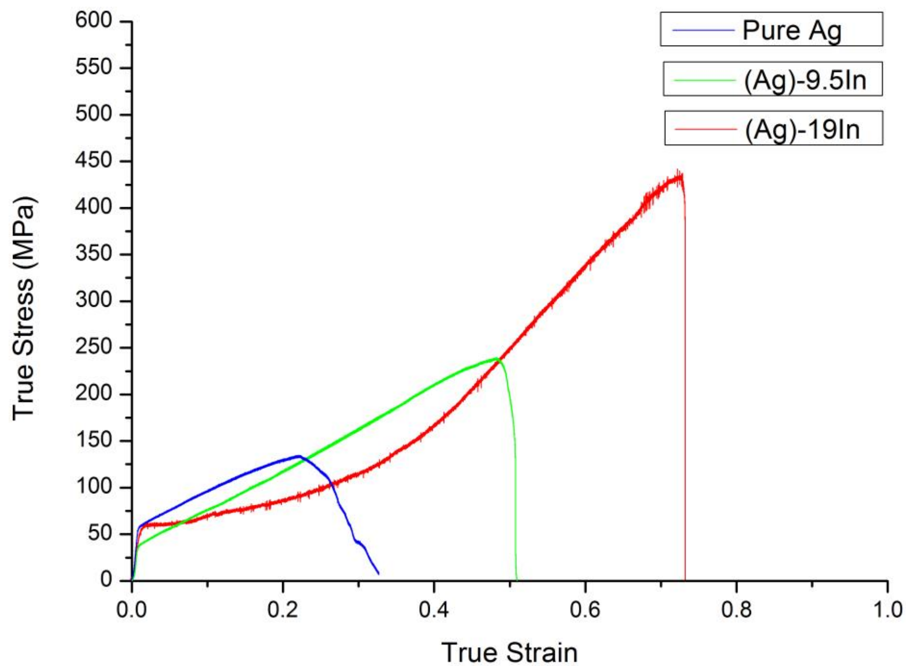

Fig. 3.6 The true stress-strain curve of pure silver, (Ag)-9.5In, and (Ag)-19In.

Typically, as predicted in solid solution strengthening theory, the usual result of solute additions is to raise the yield stress and the level of the stress-strain curve as a whole [16]. However, as shown in Table 3.5, the observation based on the tensile test experiment in silver-indium solid solution system is abnormal to solid solution strengthening theory. The tensile test samples should have similar microstructures due to the fact that the annealing profiles of the ingots growth are similar to each other. Therefore, the major variable here is the solute composition difference. With 9.5 at. % indium element alloying element addition, the yield strength drops from 56 MPa for pure silver to 37 MPa

for 9.5 at. % silver indium solid solution, but it increases back to 53 MPa for 19 at. % indium element alloying. This phenomenon can be referred to as solid solution softening theory [17].

	Yield Strength (MPa)	Ultimate Tensile Strength (MPa)	True Uniform Strain (%)	True Fracture Strain (%)
Pure Ag	56.6	133.9	22.0	32.7
(Ag)-9.5In	37.2	240.1	48.3	50.9
(Ag)-19In	53.2	447.5	72.5	73.4

Table 3.5 A summary of mechanical properties of (Ag)-9.5In and (Ag)-19In with pure Ag in comparison.

According to the reference, solid solution hardening and softening can both occur in the same alloying system depending on several factors such as temperature, solute atom concentration, etc. The solid solution softening mechanism usually occur in substitutional alloy when solute atoms concentrations are relatively high where random distribution of solute atoms would be not be expected. The softening additions are found to locally change the chemical bonding which results in a decrease of the generalized stacking fault energy and atomic row shear resistance with the enhancement of double kink nucleation and dislocation mobility, thereby decreasing the hardness and yield stress of the material. Solid solution softening couples can be commonly found in iron and molybdenum body-centered cubic (BCC) alloying systems [18]. With alloying with high indium solute concentration in silver solid solution, the occurrence of lower yield stress observed in (Ag)-xxIn phase can be partially explained by the solid solution softening theory. However, further research may be needed to investigate the reason behind the increment of yield strength from 9.5 at. % to 19 at. % of indium.

As shown in Fig. 3.6, the shape of the onset of yielding in the stress vs. strain curves of pure Ag and (Ag)-9.5In are similar which both have gradual transition from elastic region to plastic region. The strain hardening rate of pure silver and (Ag)-9.5In are almost constant due to the fact that these two curves have linear shape from yield point to UTS point. As listed in Table V, the ultimate tensile strength, true uniform strain (strain upon UTS point), and true fracture strain (strain upon fracture

point) are increased with 9.5 at. % indium element addition. In other words, the strength and the ductility of the material are simultaneously increased by adding solid solution solute, which usually can be only accomplished by decreasing of the grain size.

However, the shape of stress vs. strain curve of (Ag)-19In has major differences, comparing with that of pure Ag and (Ag)-9.5In. The transition from elastic region to plastic region is quite sharp, followed by a plateau plastic deformation region with relatively low strain hardening rate. The strain hardening rate gradually increases as the material continues to plastically deform, reaching its maximum value at point where true strain equals to 0.45, and then remains to constant value until the material fractures. It is worthwhile to note that the ultimate tensile strength, true uniform, and true fracture strain are much higher than that of pure Ag and (Ag)-9.5In. Base on the information provided by the stress vs. strain curves, it is safe to conclude that both mechanical strength and ductility will increase as the indium alloying element concentration increases in silver solid solution phase.

3.5 Fractography

As shown in Fig. 3.5, the engineering strain of (Ag)-19In at fracture point, i.e., the material elongation is more than 100%, which means it exhibits excellent ductility. To the best knowledge of the authors, the silver and its alloys' elongation usually are within the range from 35% to 50%. Therefore, the high elongation value of silver indium solid solution with high indium concentration is truly remarkable.

In order to confirm the mechanism of deformation and failure mode of (Ag)-19In, the fracture surface morphology of the same tested sample used to plot Fig. 3.5 and Fig. 3.6 curves is examined by using SEM to gain some insights of its microscopic nature. In addition, the fracture surface morphology of the same tested samples for Ag and (Ag)-9.5In used to plot Fig. 3.5 and Fig. 3.6 are shown in Fig. 3.7 and Fig. 3.8 to compare with the fractography of the (Ag)-19In sample.

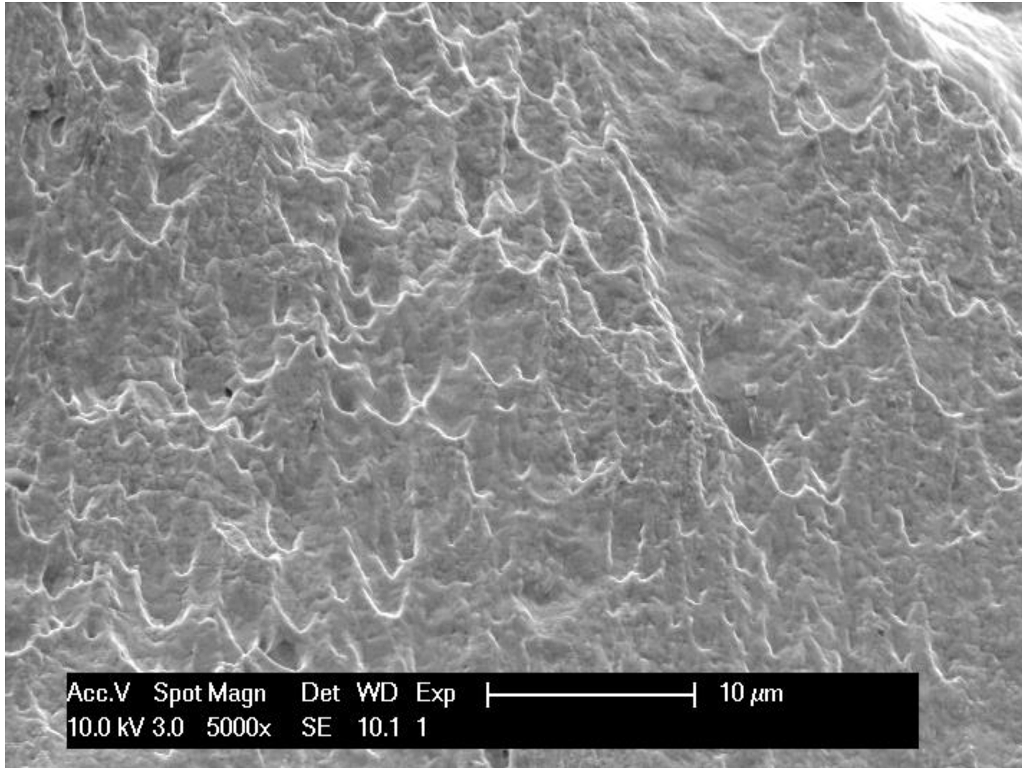

Fig. 3.7 Fractography of Ag tensile test sample, SEM image at 5000× magnification.

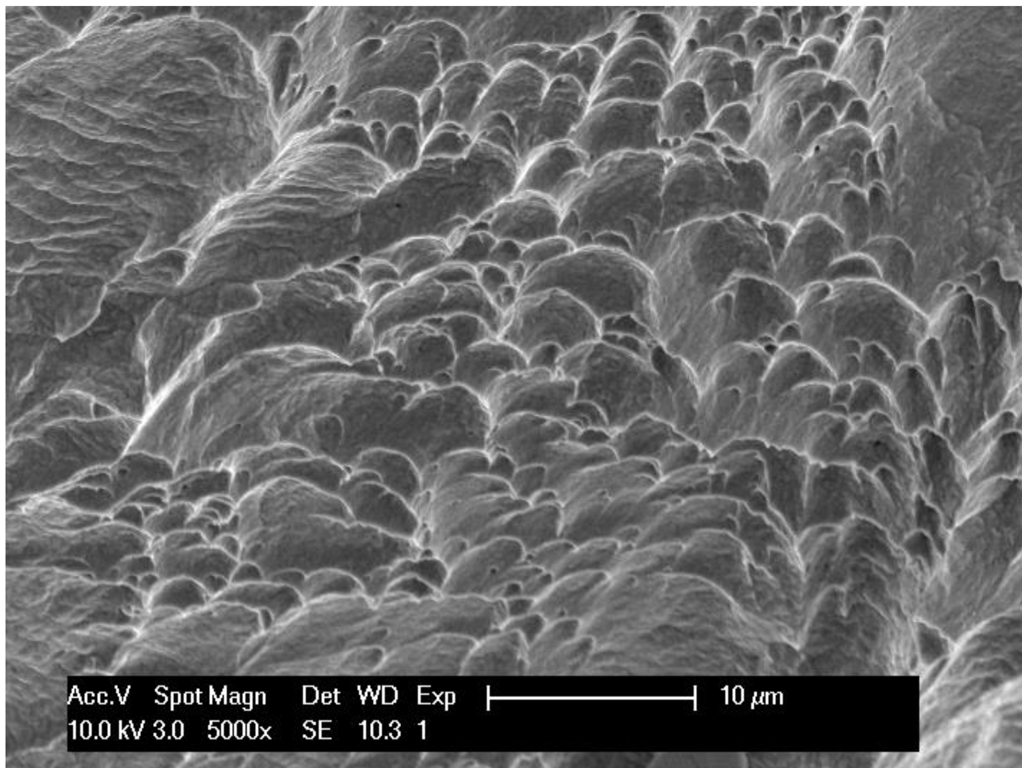

Fig. 3.8 Fractography of (Ag)-9.5In tensile test sample, SEM image at 5000× magnification.

As shown in Fig. 3.9, the surface of fracture is examined at different magnification, and the SEM pictures are shown in a series. A feature of band-like rupture can be clearly seen in these pictures, which means the material has undergone significant plastic deformation before failure. As shown in Fig. 3.10, a representative dimpled rupture can also be easily observed on the fracture surface. This type of fracture surface denotes a ductile mode fracture. Microvoid formation and coalescence during the continued straining and plastic deformation are responsible for this dimpled rupture fractography [19]. Therefore, it can be safely confirmed that (Ag)-19In is truly ductile in its nature from the study of fractography.

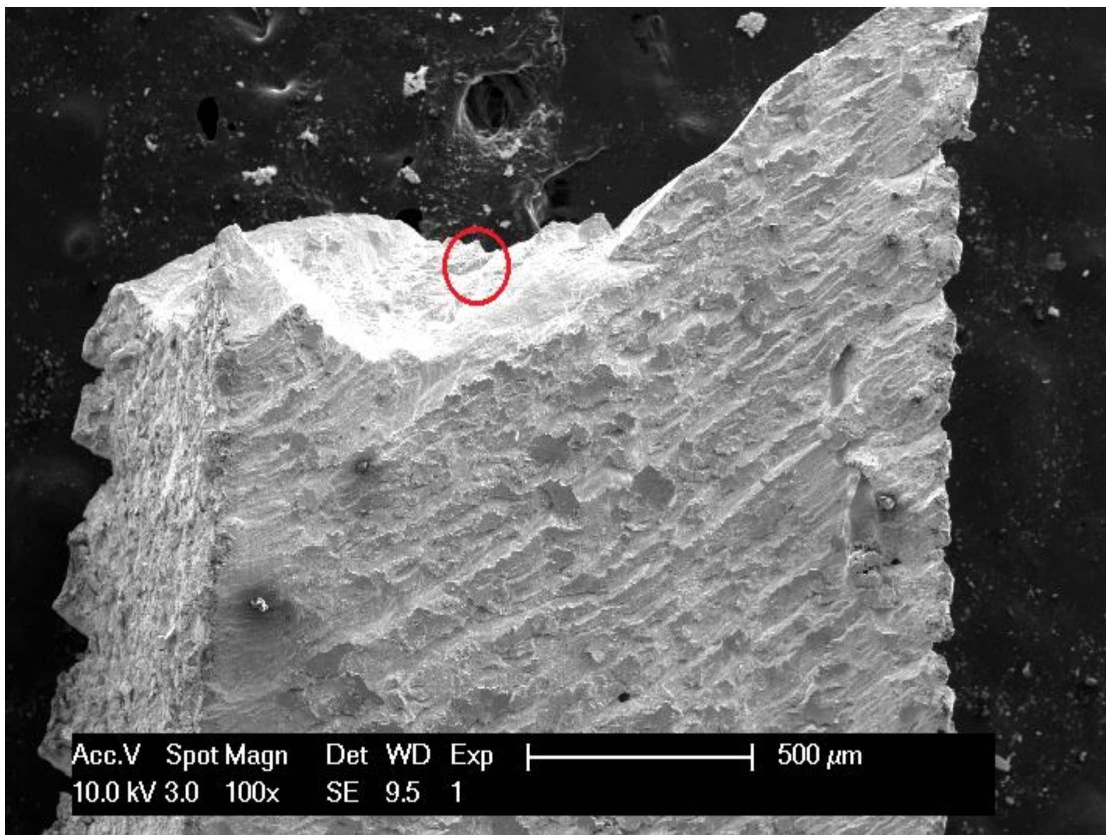

Fig. 3.9 (a) Fractography of (Ag)-19In tensile test sample, SEM image at 100× magnification,

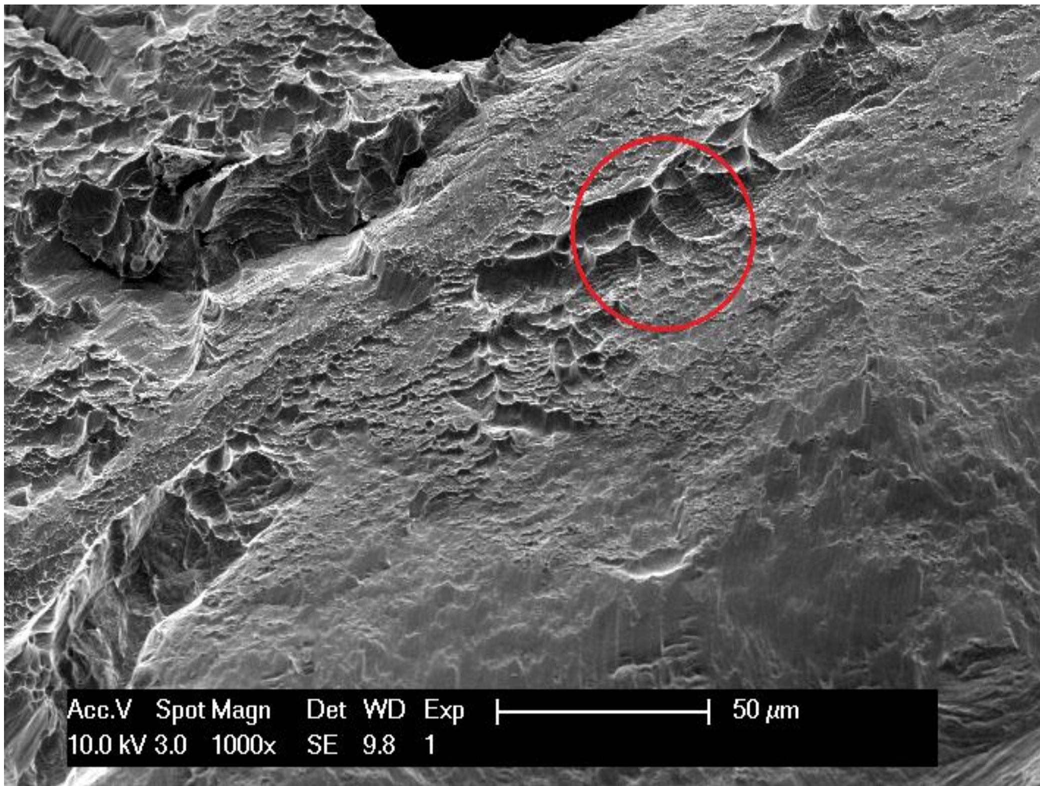

Fig. 3.9 (b) SEM image at 1000× magnification,

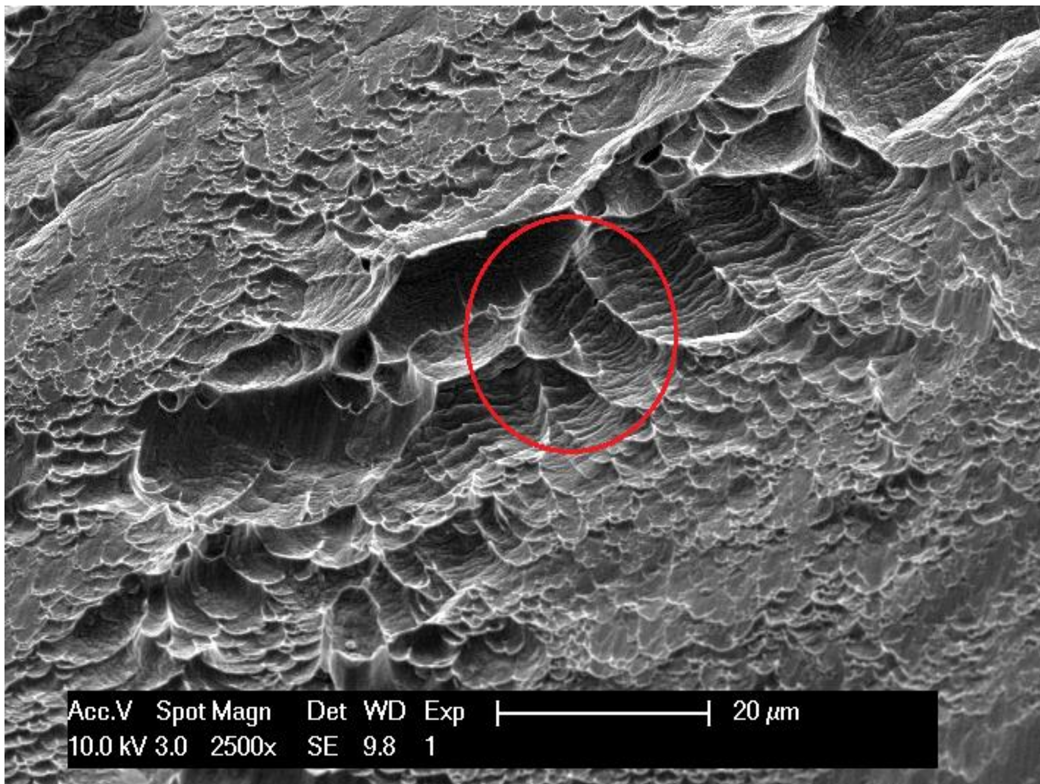

Fig. 3.9 (c) SEM image at 2500× magnification,

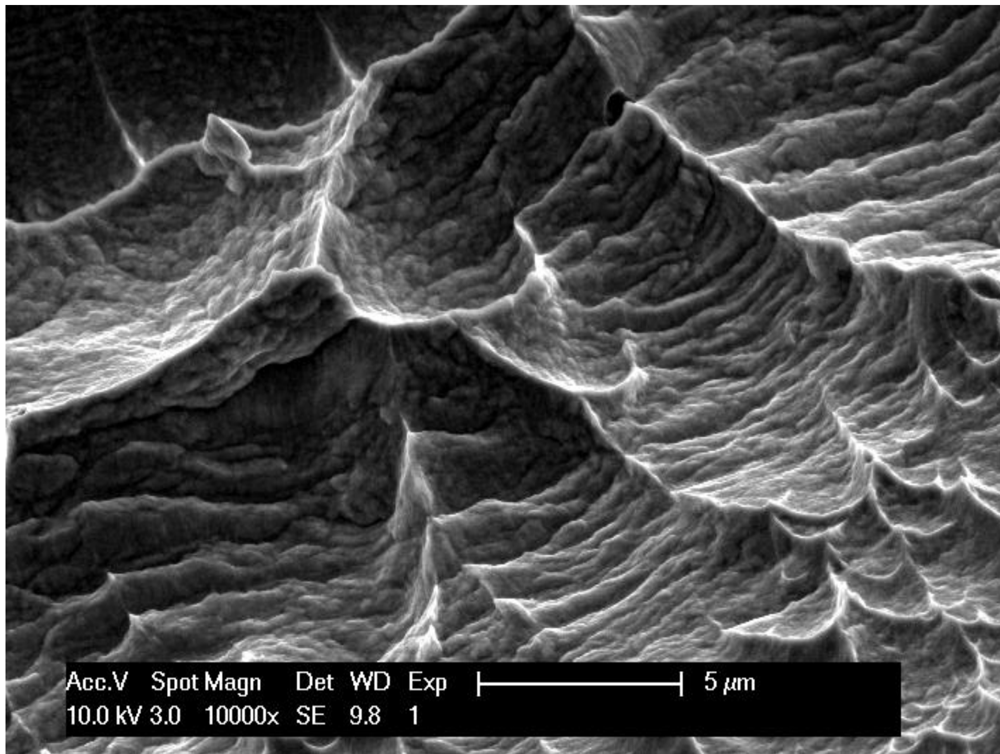

Fig. 3.9 (d) SEM image at 10000× magnification.

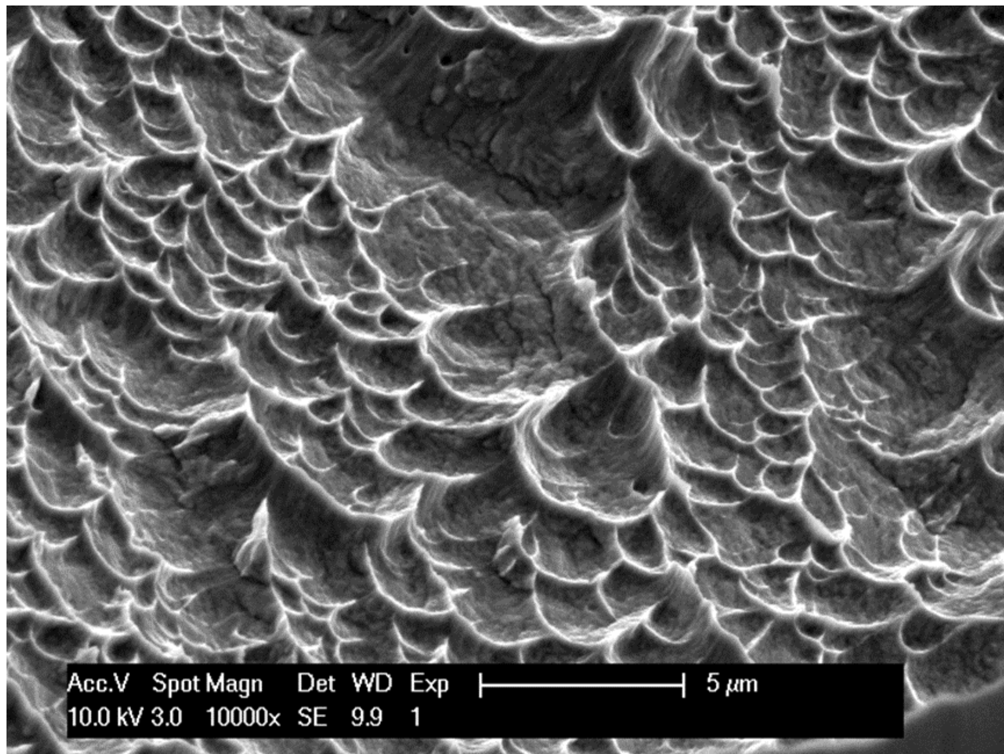

Fig. 3.10 Representative morphology of dimpled rupture on the fracture surface of (Ag)-19In tensile test sample.

In comparison, as shown in Fig. 3.7 and Fig. 3.8, the fractography of Ag and (Ag)-9.5In tensile tested samples are different from the one of (Ag)-19In. The authors can only observe shallow dimpled rupture on the fracture surface of Ag sample, whereas the dimpled rupture of (Ag)-19In shown in Fig. 3.10 is much clearer than that of Fig. 3.7, thereby confirming (Ag)-19In has undergone much more amounts of plastic deformation upon failure than pure Ag tensile test sample. As shown in Fig. 3.8, the authors can observe clear dimpled rupture for (Ag)-9.5In tensile tested sample, but band-like rupture is relatively shallow, comparing with that of (Ag)-19In. Therefore, (Ag)-9.5In is more ductile than pure Ag, but not as ductile as (Ag)-19In.

In conclusion, the result of fractography study is in agreement with previous tensile test data, thereby confirming that the ductility will increase as the indium alloying element concentration increases in silver solid solution phase.

3.6 Conclusion

In this chapter, the materials of silver indium solid solution phase have been grown in the ingot form at two different compositions, (Ag)-9.5In and (Ag)-19In, and characterized by XRD and SEM/EDX methods. Furthermore, the intrinsic mechanical properties of silver solid solution phase with indium, i.e., the stress vs. strain curves, have been presented and analyzed. Due to the large indium alloying concentration, the phenomenon of solid solution softening has been observed. As a result, the yield stress of the silver indium solid solution phase at two different composition, (Ag)-9.5In and (Ag)-19In, are lower than that of pure silver. In addition, the silver indium solid solution phase exhibits superior ductility, especially for (Ag)-19In, since the its ultimate tensile strength is 3.3 times of that of pure silver, and its elongation upon fracture are 2.2 times of that of pure silver. With the preliminary study of the mechanical properties, the silver indium solid solution phase is a promising candidate for interconnection applications in electronic industries. As interconnection medium, the lower hardness and yield stress would be desirable [20] since it induce less internal stress to the die or bonding pad underneath. With the superior ductility, forming of silver indium solid solution phase is better than that of pure silver, so that it is suitable for being forged into various forms of industrial

products. The documentation of the stress vs. strain curves of silver indium solid solution phase would be valuable for further research and investigation for this material. For example, mechanical finite element analysis (FEA) [21] regarding to silver indium solid solution phase can be readily performed with the availability of this material mechanical properties such as yield stress, UTS, and stress vs. strain curves. Further work may be continued to study the other interesting properties of silver solid solution phase with indium.

Reference in Chapter 3

1. W. Hume-Rothery, G. F. Lewin, and P. W. Reynolds. "The lattice spacings of certain primary solid solutions in silver and copper." Proceedings of the Royal Society of London. Series A, Mathematical and Physical Sciences, vol. 157.890, pp. 0167-0183, Oct 1936.
2. R. Bacon, and C. S. Smith. "Single crystal elastic constants of silver and silver alloys." Acta Metallurgica, vol. 4.4, pp. 337-341, 1956.
3. R. W. K. Honeycombe. "The plastic deformation of metals." First edition, Edward Arnold Ltd., Cambridge, 1968.
4. P. Jax, P. Kratochvil, and P. Haasen. "Solid solution hardening of gold and other fcc single crystals." Acta Metallurgica, vol. 18.2, pp. 237-245, 1970.
5. C. B. Alcock, K. T. Jacob, and T. Palamutcu. "Thermodynamics of α-solid solutions of silver with indium and tin." Acta Metallurgica, vol. 21.7, pp.1003-1009, 1973.
6. H. Suga and T. Imura. "Solid Solution Hardening of Silver Single Crystals by Indium, by Tin and by Antimony." Japanese Journal of Applied Physics, vol. 14.8, pp. 1253-1254, 1975.
7. T. H. Chuang, C. H. Tsai, H. C. Wang, C. C. Chang, C. H. Chuang, J. D. Lee, H. H. Tsai. "Effects of annealing twins on the grain growth and mechanical properties of Ag-8Au-3Pd bonding wires." Journal of Electronic Materials, vol. 41.11, pp. 3215-3222, 2012.
8. T. H. Chuang, H. C. Wang, C. H. Chuang, H. J. Lin, J. D. Lee, H. H. Tsai. "Surface Reconstruction of an Annealing Twinned Ag-8Au-3Pd Alloy Wire Under Current Stressing." Metallurgical and Materials Transactions A, vol. 44.11, pp. 5106-5112, 2013.
9. Y. C. Chen, W. W. So, and C. C. Lee. "A fluxless bonding technology using indium-silver multilayer composites." Components, Packaging, and Manufacturing Technology, Part A, IEEE Transactions, vol. 20.1, pp. 46-51, 1997.
10. Y. Y. Wu, W. P. Lin, and C. C. Lee. "A study of chemical reactions of silver and indium at 180° C." Journal of Materials Science: Materials in Electronics, vol. 23.12, pp. 2235-2244, 2012.
11. Y. Y. Wu and C. C. Lee. "The Strength of High-Temperature Ag–In Joints Produced Between Copper by Fluxless Low-Temperature Processes." Journal of Electronic Packaging, vol. 136.1, pp.

0110061-6, March 2014.

12. Y. Huo, and C. C. Lee. "Anti-tarnishing evaluations of silver solid solution phase with indium." Electronic Components and Technology Conference (ECTC), 2015 IEEE 65th. IEEE, pp. 2180-7, 2015.
13. M.R. Baren, Indium Alloys and their Engineering Applications, ed. C.E.T. White and H. Okamoto (Materials Park, OH: ASM Intl., 1993), p. 15.
14. A. N. Campbell, R. Wagemann, and R. B. Ferguson. "The silver-indium system: thermal analysis, photomicrography, electron microprobe, and X-ray powder diffraction results." Canadian Journal of Chemistry, vol. 48.11, pp. 1703-1715, 1970.
15. ASTM standard E8/ E8M- 08, "Standard test methods for tension testing of metallic materials," ASTM International, West Conshohocken, PA, 2008, DOI: 10.1520/E0008_E0008M-08, www.astm.org.
16. G. E. Dieter, "Mechanical Metallurgy." Third Edition, Mc Graw Hill, NY, 1986.
17. A. K. I. K. A. Z. U. Sato, and M. Meshii. "Solid solution softening and solid solution hardening." Acta Metallurgica, vol. 21.6, pp. 753-768, 1973.
18. N. I. Medvedeva, Y. N. Gornostyrev, and A. J. Freeman. "Solid solution softening in bcc Mo alloys: Effect of transition-metal additions on dislocation structure and mobility." Physical Review B, vol. 72.13, pp. 134107, 2005.
19. R. H. Van Stone, T. B. Cox, J. R. Low, Jr and J. A. Psioda. "Microstructural aspects of fracture by dimpled rupture." International Metals Reviews, vol. 30.1, pp. 157-179, 1985.
20. Z. W. Zhong, H. M. Ho, Y. C Tan, W. C. Tan, H. M. Goh, B. H. Toh, and J. Tan. "Study of factors affecting the hardness of ball bonds in copper wire bonding." Microelectronic engineering, vol. 84.2, pp. 368-374, 2007.
21. S. Elangovan, S. Semeer, and K. Prakasan. "Temperature and stress distribution in ultrasonic metal welding — An FEA-based study." Journal of materials processing technology, vol. 209.3, pp. 1143-1150, 2009.

Chapter 4

Anti-tarnishing Property of Silver-Indium Solid Solution

4.1 Introduction

Silver possesses the title of champion for its highest thermal conductivity, electrical conductivity, and reflectivity among any known metal elements. Dry silver does not form a significant surface oxide at ambient temperature and pressure [1], so it is relatively chemical inert to oxidation under normal atmosphere. However, silver is very sensitive to the presence of sulfur-containing corrosive gases such as sulfur vapor, hydrogen sulfide, sulfur dioxide, and carbonyl sulfide, etc. Typically, the concentrations of those corrosive gases are very low, ranging from less than 1 parts per billion (ppb) under normal atmosphere to hundreds of ppb in heavy industrial environment [2]. However, the corrosion phenomenon can be commonly observed from silver used in electronics. The corrosive reaction product is silver sulfide which can be the killer of electronic products in several aspects. First of all, silver sulfide has poor mechanical strength, so it can be detached and crumbled from its substrate easily. In addition, the resistivity of silver sulfide is 7 to 10 order of magnitude higher than that of silver [3], so the overall resistivity will continue to increase with the formation of silver sulfide. Silver sulfide also poses a threat to circuits because its dendritic growth nature might result in the formation of silver sulfide whiskers [4]. This could lead to the occurrence of short circuit since silver sulfide is not a good insulating material either. Furthermore, the reflectance of silver mirror surface used in LEDs would drop significantly with corrosive degradation, resulting in light output power reduction [5].

In order to understand the nature of silver sulfurization, extensive research has been conducted over the decades. Several experiments, using various corrosive gases, such as sulfur vapor [6], hydrogen sulfide [7], sulfur dioxide [8], and organic sulfur [9], have been performed to see the influence on the rate of silver tarnishing. Other environmental parameters, such as temperature, relative humidity [10], illumination [8], and silver surface state [11], have also been studied to explore the silver tarnishing mechanism, thereby searching possible scientific and engineering solutions for anti-

tarnishing purposes. In literatures, some surface treatments for silver using different coating methods or coating materials such as metallic coating by electroplating [12], sputter-applied coatings [13], oxide coating [14], organic coating [15], chromate conversion coating [16], etc. However, such thin layer of coating material can be worn off very easily after a short period of time. Another approach to improve the anti-tarnishing property of silver is by alloying. Alloying with copper can strengthen silver, but it will make silver less tarnish resistant to corrosive gases [17]. It has been reported that adding other elements such as palladium [18], silicon [19], tin [20], germanium [21], and zinc [22], would have, more or less, increased anti-tarnishing effects compared with sterling silver. However, to the knowledge of the authors, there is no standard test method existing to quantify the capability of anti-tarnishing for different silver alloy.

Recently, the authors had presented some preliminary anti-tarnishing results of the silver solid solution phase with indium [23]. In the study of this chapter, we have designed a new quantitative test method and performed the reaction experiments with well-controlled and repeatable environments. The authors hope to establish this method as a standard anti-tarnishing test method for silver-based alloys.

Argentium silver is one of commercially available sterling silver with claimed good anti-tarnishing property [21]. Germanium is used as alloying element to protect the silver by forming a thin layer of germanium oxide on the surface of this silver alloy. Argentium silver was purchased from local vendor in sheet form, and then cut into disk samples. The compositions of the Argentium silver are 93.5 at. % of Ag, 5 at. % of Cu, and 1.5 at. % of Ge in average, according to the vendor material data sheet and our EDX data. In this research, Argentium silver was used as reference controlled group to compare with (Ag)-xxIn solid solution in the following experiments.

Silver solid solution phase with indium, designated as (Ag)-xxIn, are produced in polycrystalline ingot form at two different compositions. After examining their chemical composition using SEM/EDX and XRD, the prepared samples are tested in the designed sulfurization experiment. The disk samples preparation were the same as described in Chapter 3. The details of the design of the sulfurization test experiment have been described. Experimental results are reported, analyzed, and discussed. Finally, a summary is then given.

4.2 Design of Sulfurization Experiment

In measuring anti-tarnishing property of silver and its alloys, we have not been able to find a standard test method or a repeatable test method in literature. We have thusly designed a set of experiments to quantitatively study the chemical reaction between sulfur-containing corrosive gas and (Ag)-xxIn solid solution and other silver-based alloys. Since sulfur is the element essentially responsive to the corrosive behavior of silver tarnishing, sulfur vapor (S_n) and hydrogen sulfide gas (H_2S) would be plausible corrosive gas candidates for this experiment. In literature [24], the reaction between silver and hydrogen sulfide as shown in equation (4.1) is endothermic, where the change of enthalpy is ΔH = +10 kJ/mol. In ambient environment, the hydrogen sulfide can corrode silver as in equation (4.2). However, it cannot react with silver without heating or oxidizing agent.

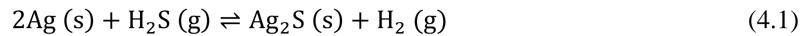

$$2Ag\ (s) + H_2S\ (g) \rightleftharpoons Ag_2S\ (s) + H_2\ (g) \tag{4.1}$$

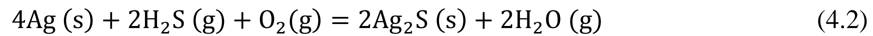

$$4Ag\ (s) + 2H_2S\ (g) + O_2(g) = 2Ag_2S\ (s) + 2H_2O\ (g) \tag{4.2}$$

$$2Ag\ (s) + S\ (g) = Ag_2S\ (s) \tag{4.3}$$

On the other hand, the reaction between silver and sulfur vapor shown in equation (4-3) is exothermic, where the change of enthalpy is ΔH = -32 kJ/mol. The sulfur vapor can corrode silver without heating or other gases involved. It is much easier to control on the concentration of one species of vapor than two species in the experiment system. In addition, the reaction between the sulfur vapor and silver is thermodynamically preferable, so corrosion environment of sulfur vapor is more severe than that of hydrogen sulfide gas. Accordingly, the authors selected the sulfur vapor as the corrosive gas for the design of this accelerated quantitative corrosion test experiment.

In the following steps, pure silver, Argentium silver, (Ag)-9.5In and (Ag)-19In disk samples were prepared by polishing using 800 and 1200 grits abrasive paper. Finally, the disk samples preparation finished with mirror surface using 0.5 micron diamond suspension polishing process.

In order to evaluate the rate of chemical reaction between sulfur and silver quantitatively, the amount of resultant, i.e., silver sulfide, need to be measured. Therefore, the authors designed a technique to measure the thickness of silver sulfide layer by creating a sharp step (boundary)

between reacted region and untouched region on the samples. First of all, all of the samples were evaluated in terms of surface roughness using the Dektak XT profilometer in Integrated Nanosystems Research Facility (INRF). The Dektak XT is a profilometer that provides quantitative data about sample's surface by using a contact measurement technique. Measurements are made by a diamond tipped stylus moving laterally in contact with a sample across a specified distance with a specified force with a resolution of 0.5nm across a variety of surfaces. Typical root-mean-square (RMS) values of surface roughness are on the order of 50 nm. Next, the authors coated a layer of photoresist, AZ 4620, on half of the sample surface, followed by baking the samples at 120°C for 10 minutes and baking the samples at 140°C for 5 minutes. The resulting photoresist layer blocks the sulfur vapor from reaching the sample surface. An experiment was conducted to confirm that it was indeed the case.

As shown in Fig. 4.1, a closed system was designed to conduct the sulfurization experiment. The reaction chamber is a glass jar of 1L volume having lid sealed with rubber which can also be tightened up, thereby ensuring no leakage of sulfur vapor to the outside environment during experiment. Precipitated sulfur S595-500 was used as the sulfur vapor source. The melting temperature of sulfur 115.21°C, so 120°C is enough to completely melt the sulfur into liquid phase, thereby generating sulfur vapor through thermal evaporation.

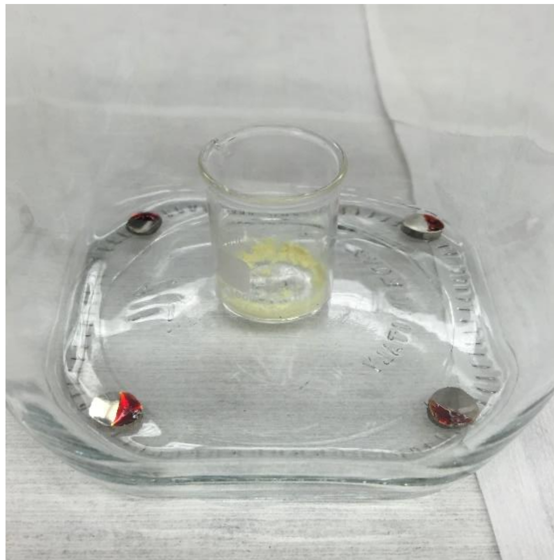

Fig. 4.1 The configuration of the designed closed system for sulfurization experiment.

As shown in Fig. 4.2 [25], most of sulfur vapor molecules would be in the form of S_8, so the total sulfur vapor pressure at thermal equilibrium is almost equal to partial vapor pressure of S_8. After calculation using ideal gas law, if supplied with 5 mg sulfur element in weight, it would be enough for the sulfur vapor to reach the saturation point of vapor pressure at 120°C. Considered the sulfur gas could be consumed continually during the reactions, the authors decided to oversupply the amount of precipitated sulfur in order to ensure that sulfur vapor concentration remains as a constant during the sulfurization experiment. As a result, 100 mg of precipitated sulfur was placed inside a small beaker which sit at the center of the reaction chamber during reaction.

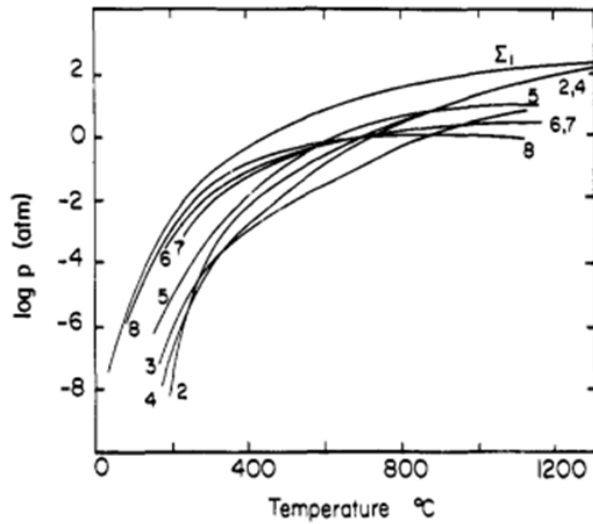

Fig. 4.2 Equilibrium pressure of sulfur, Σ_i is the total pressure, $2 \leq n \leq 8$, are partial pressures of S_n.

For one around of sulfurization experiment, disk samples of pure silver, argentium silver, (Ag)-9.5In and (Ag)-19In were put inside of the reaction chamber and evenly distributed near the sulfur containing beaker. After sulfurization experiment, the photoresist was removed by soaking into AZ 400T stripper at 70°C for 2 mins, leaving silver sulfide layer untouched. A separate experiment was conducted to confirm that the stripper did not attack the silver sulfide layer. After removing the photoresist, a step of silver sulfide layer was formed between the untouched and reacted regions. Finally, the step height was measured using Dektak XT profilometer. For example, the result has been illustrated for the profilometer measurement of the step height of silver sulfide layer on pure silver

disk sample after 60 mins sulfurization experiment. As shown in Fig. 6, the total length of profilometer scanning is 300 μm, and the sharp step of the silver sulfide layer is placed near the center of the scanning profile. The silver sulfide layer is not as smooth as the mirror finished silver surface due to the nature of silver sulfide film growth. Therefore, it is necessary to use statistical approach to evaluate the average film thickness. As a result, using the controlling software of Dektak XT profilometer, the RMS height values of selected red region (reacted region) and green region (protected region) can be evaluated upon the measurement, where the typical length of selected area is from 50 μm to 60 μm. Thus, the difference between RMS values of reacted region and protected region can be determined, and then recorded as the step height value of the profilometer measurement.

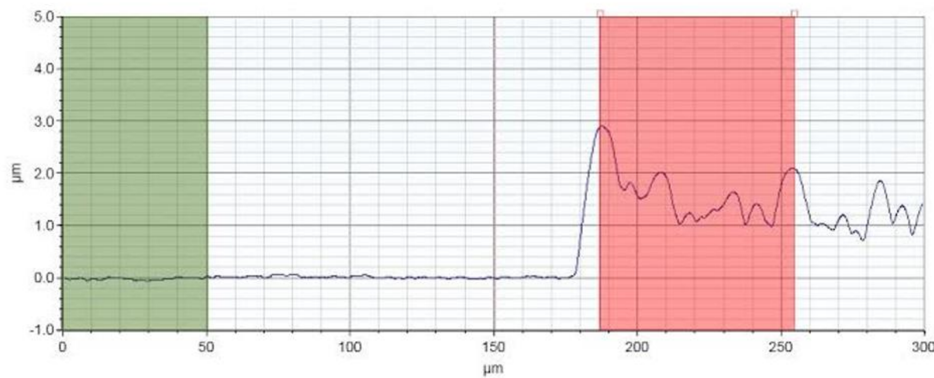

Fig. 4.3 Dektak XT Profilometer measurement profile of silver sulfide layer on pure silver sample.

4.3 Experimental Results and Discussions

The purpose of the sulfurization experiment in this research is to evaluate the anti-tarnishing property of (Ag)-9.5In and (Ag)-19In, compared with pure silver and Argentium silver quantitatively. The authors studied the growth rate of silver sulfide layer, i.e., the thickness of silver sulfide layer varying with time. Based on the assumption that the material medium is continuous and the law of mass conservation, the authors can calculate that the thickness of silver sulfide layer is 2.5 times of the value of measured step height that obtained from profilometer measurement, considering the silver sulfide layer growth is bidirectional at the initial solid-gas interface. The time length of the

sulfurization experiments have set as 15 mins, 30 mins, 45 mins, and 60 mins respectively. After the experiments, the top-view images of the steps between the protected region and reacted region were taken, using the digital optical microscope. The images were taken at 500× magnification using 50× objective lens. At this magnification, the depth of focus of the objective is in the range of ± 0.3μm. As shown in Fig. 4.4, the surface of pure silver, Argentium silver, (Ag)-9.5In, and (Ag)-19In samples were observed under optical microscope after 15 mins sulfurization experiment. It is clear that the color of right hand side of the samples are still silvery, which means the applied photoresist protect the samples surface very well, so that the protected area of the samples remain inert to sulfur gas during the sulfurization. Furthermore, the author can observe left hand side of pure silver sample surface has been already blackened by the sulfur gas, even if the experiment time is only 15 mins, as a result of the severity of corrosion environment of the designed experiment. The grains of silver sulfide can be clearly observed on the surface of pure silver sample, shown in Fig. 4.4 (a). As shown in Fig. 4.4 (b), Argentium silver reacted with sulfur vapor, resulting in forming the silver sulfide in islands form. The average size of islands of silver sulfide is about 5 μm, and RMS value of the thickness of the islands is 0.45 μm. Therefore, Argentium silver exhibits anti-tarnishing property to some extent if compared with pure silver, since it didn't form the continuous silver sulfide layer as pure silver did. In contrast, as shown in Fig. 4.4 (c), the color of the surface of (Ag)-9.5In sample is gray, meaning the formation of silver sulfide layer is much thinner than pure silver. Remarkably, as shown in Fig. 4.4 (d), the appearance of the (Ag)-19In sample is still silvery, even though a little bit of yellowish color in combine. As shown in Fig. 4.5, the pure silver and (Ag)-9.5In samples have been corroded further by the sulfur gas, as the experimental time increases to 30 mins, since the color of reacted regions is darker than the previous ones. The authors can observe that a continuous film of silver sulfide start to form on the surface of (Ag)-9.5In sample. As shown in Fig. 4.5 (b), the Argentium silver sample surface preserved the island-like morphology after reacting with sulfur vapor for 30 mins, and the average size of silver sulfide islands increases to 10 μm, and RMS value of the thickness of the islands has increased to 1.30 μm. In contrast, as shown in Fig. 4.5 (d), the reacted region of (Ag)-19In still remains yellowish, but darkened a little bit compared with the one in the 15 mins experiment. When the experimental time increases to 60 mins, the trend of corrosion for pure silver and (Ag)-9.5In

samples continues, as opposed to the (Ag)-19In samples remains relatively inert to sulfur gas corrosion, as shown in Fig. 4.6 As shown in Fig. 4.6 (b), the island-like morphology on the argentium silver sample surface has changed, which means the islands of silver sulfide have been grown and coalesce with each other, resulting in forming the continuous film of silver sulfide. Therefore, through the direct observation of optical microscope image, the authors can conclude that silver indium solid solution exhibits a great anti-tarnishing property, and the ability of anti-tarnishing increases with the indium element concentration. As compared with Argentium silver, the (Ag)-19In exhibits better anti-tarnishing property.

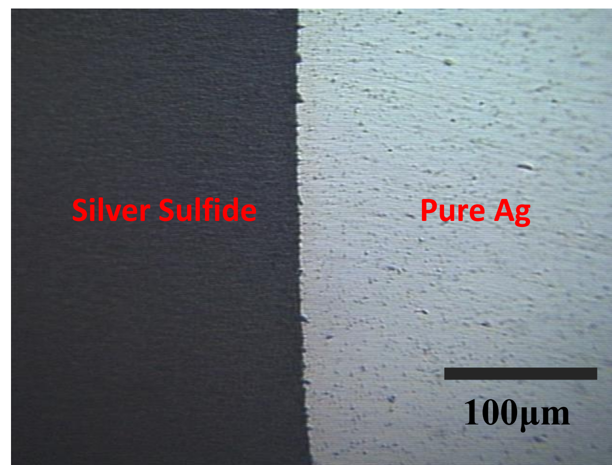

Fig. 4.4 (a) The top-view optical microscope image of pure silver disk sample,

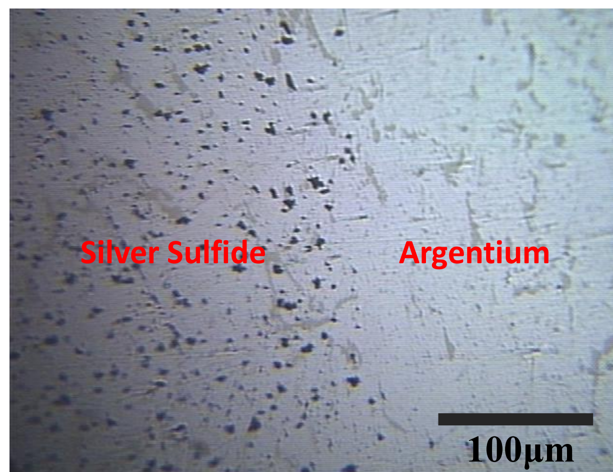

Fig. 4.4 (b) The top-view optical microscope image of Argentium silver disk sample,

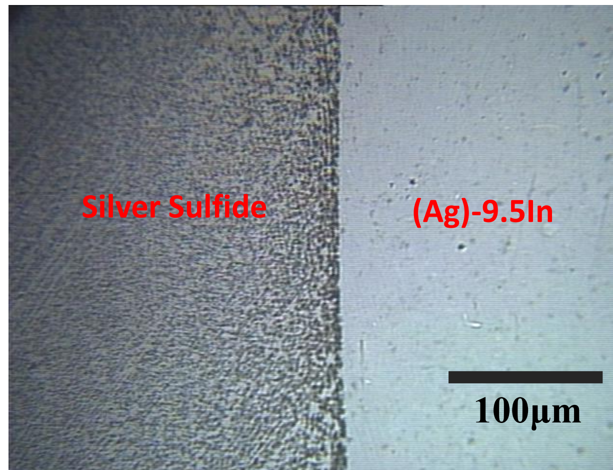

Fig. 4.4 (c) The top-view optical microscope image of (Ag)-9.5In disk sample,

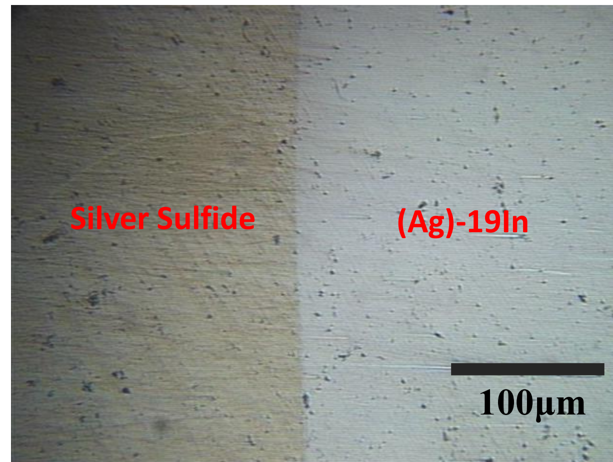

Fig. 4.4 (d) The top-view optical microscope image of (Ag)-19In disk sample after 15 mins sulfurization experiment.

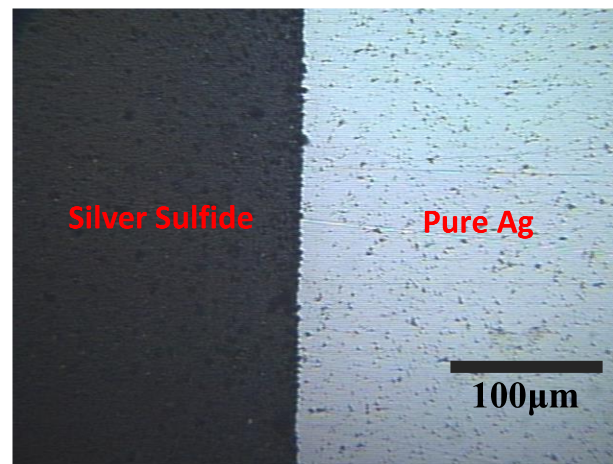

Fig. 4.5 (a) The top-view optical microscope image of pure silver disk sample,

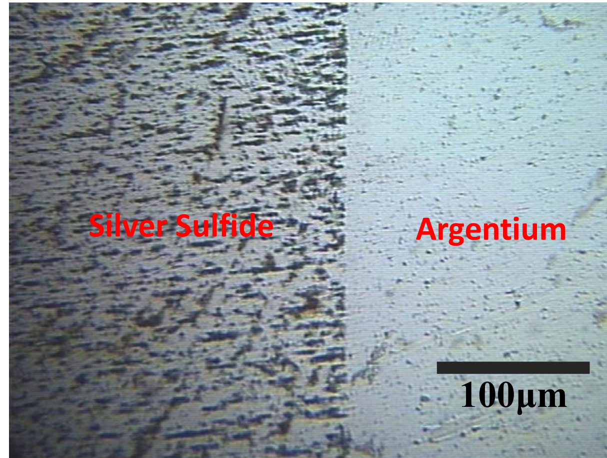

Fig. 4.5 (b) The top-view optical microscope image of Argentium silver disk sample,

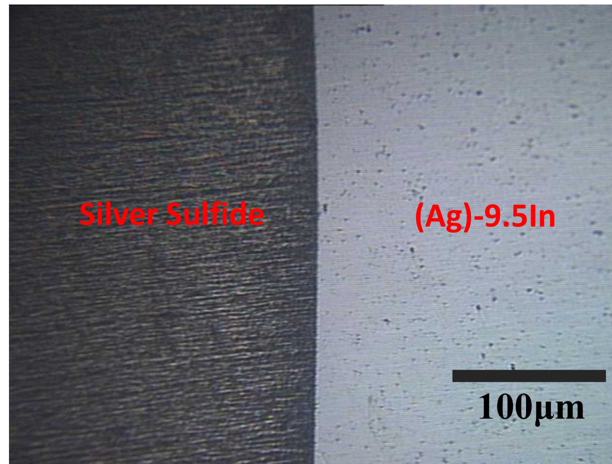

Fig. 4.5 (c) The top-view optical microscope image of (Ag)-9.5In disk sample,

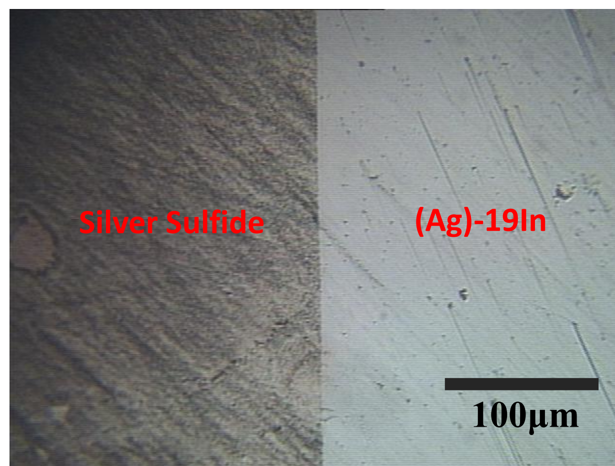

Fig. 4.5 (d) The top-view optical microscope image of (Ag)-19In disk sample after 30 mins sulfurization experiment.

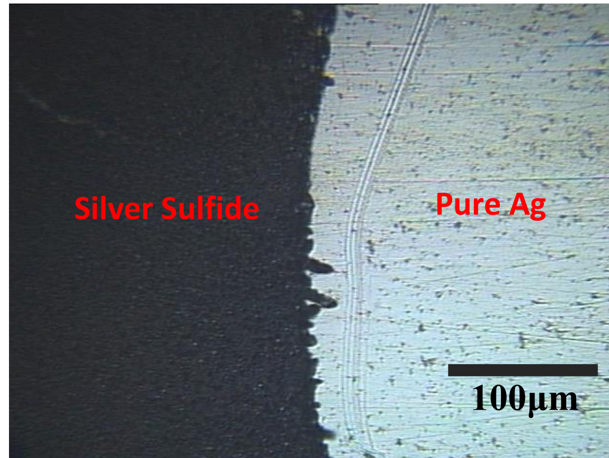

Fig. 4.6 (a) The top-view optical microscope image of pure silver disk sample,

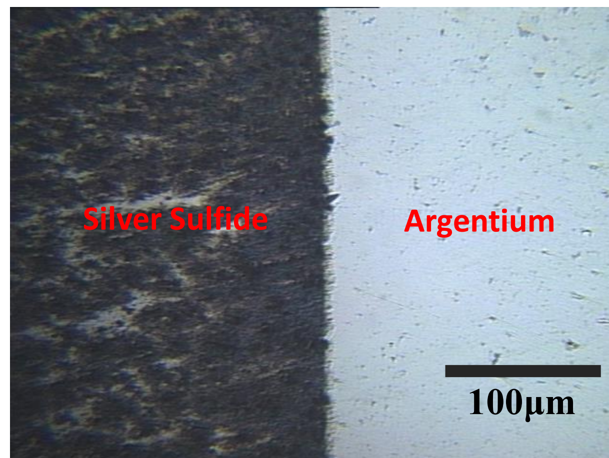

Fig. 4.6 (b) The top-view optical microscope image of Argentium silver disk sample,

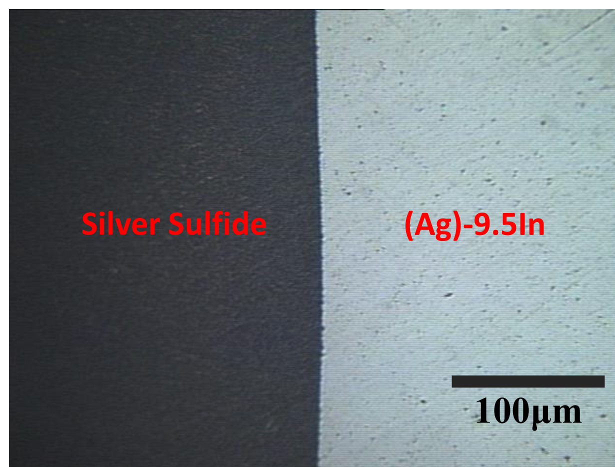

Fig. 4.6 (c) The top-view optical microscope image of (Ag)-9.5In disk sample,

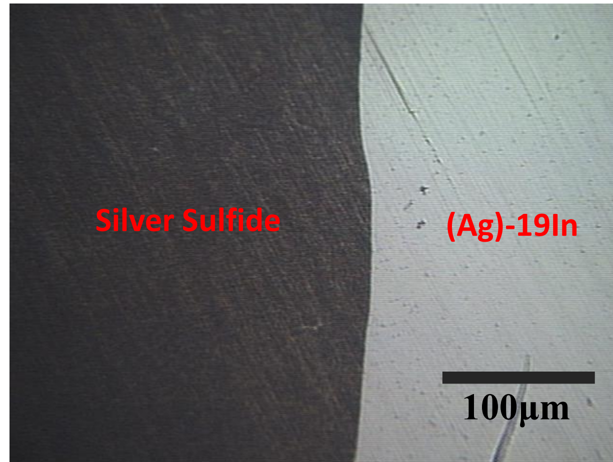

Fig. 4.6 (d) The top-view optical microscope image of (Ag)-19In disk sample after 60 mins sulfurization experiment.

After measuring by Dektak XT profilometer, the RMS values of the step height were recorded, so that the corrosion film thickness, i.e., the thickness of silver sulfide layer, can be calculated. The experimental data of the sulfurization test are collected and summarized in Table 4.1.

	Time	Pure Ag	Argentium	(Ag)-9.5In	(Ag)-19In
Measured step height (µm)	15 mins	0.34	0.18	0.15	0.04
	30 mins	0.72	0.52	0.27	0.05
	45 mins	1.20	1.09	0.39	0.07
	60 mins	1.61	1.60	0.48	0.08
Film thickness (µm)	15 mins	0.85	0.45	0.38	0.10
	30 mins	1.80	1.30	0.68	0.13
	45 mins	3.01	2.73	0.98	0.18
	60 mins	4.03	4.01	1.20	0.20
Corrosion rate (µm/s)		1.14×10^{-3}	7.25×10^{-4} 1.50×10^{-3}	3.33×10^{-4}	5.00×10^{-5}

Table 4.1 A summary of sulfurization experimental results of Argentium silver, (Ag)-9.5In and (Ag)-19In with pure silver in comparison.

In the literature [26], the reaction between silver and sulfur-based corrosion gas has a linearly time dependent relationship. Our experimental data of pure silver, (Ag)-9.5In and (Ag)-19In agrees with this linear relationship, and can be fit well into linear curves, as shown in Fig. 4.7. The slope of the linear curves are the corrosion rates in the environment of the designed sulfurization experiment for pure silver, (Ag)-9.5In and (Ag)-19In. After calculation, the corrosion rate of pure silver is 1.14×10^{-3} μm/s. The corrosion phenomenon in Argentium deviate from this linear assumption. The data of argentium silver can be fit into two piecewise-linear curve. The initial corrosion rate is 7.25×10^{-4} μm/s when the samples exhibit island-like morphology. After the coalescence of the islands, the corrosion rate accelerated to 1.50×10^{-3} μm/s, which is even higher than pure silver. Silver and copper can hardly be dissolved in to each other crystal lattice at room temperature [27]. Therefore, the Argentium silver is essentially two phase alloy, which has Ag-rich phase and Cu-Ge rich phase [28]. It would explain why the argentium silver samples exhibit island-like morphology for short-term sulfurization reaction. Upon the coalescence of the islands, the silver sulfide layer become continuous, then continuous film morphology will be exhibited. On the other hand, our grown (Ag)-xxIn solid solutions have only single phase, so they would follow the linear growth behavior during sulfurization experiment. The corrosion rate of (Ag)-9.5In is 3.3×10^{-4} μm/s, which is 3.4 times slower than that of pure silver and 2.2 times slower than that of initial stage of argentium. Significantly, the corrosion rate of (Ag)-19In disk samples is only 5×10^{-5} μm/s, which is 22.8 times slower than of pure silver, 14.5 times slower than of initial stage of Argentium silver and 6.6 times slower that of (Ag)-9.5 In.

Using the corrosion rates obtained above, an exponential equation (4.4) can be extrapolated from the experimental data to describe the correlation of growth rate of silver sulfide film and indium concentration of (Ag)-xxIn solid solution:

$$K = A * \exp(-x/t) + b \tag{4.4}$$

, where the K is the corrosion reaction rate (Å/s), x is the indium concentration (at. %) of (Ag)-xxIn solid solution, A is the pre-exponential factor, which has the value of 12.55 Å/s, and t and b are both fitting constants, which have the numerical values of 9.07 and -1.13 respectively, and their units agree with x and K in the equation (4.4).

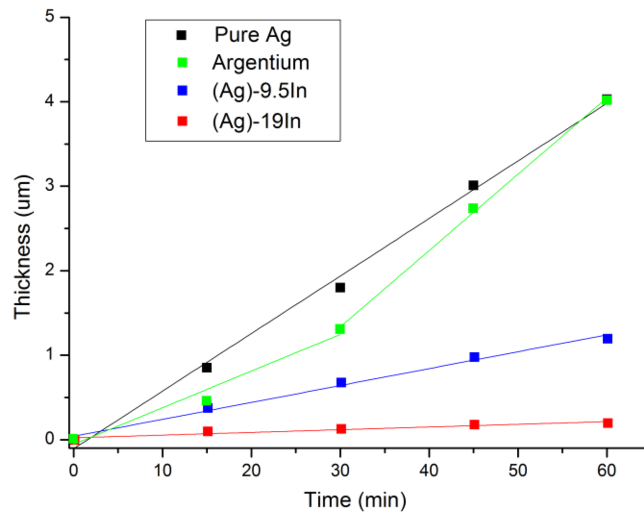

Fig. 4.7 The plot of silver sulfide layer thickness vs. time after sulfurization experiments for pure silver, Argentium silver, (Ag)-9.5In, and (Ag)-19In disk samples.

Therefore, as shown in Fig. 4.8, the corrosion reaction rate of the (Ag)-xxIn solid solution with sulfur vapor is exponentially decrease with the increase of indium concentration. In other words, the anti-tarnishing proper of (Ag)-xxIn solid solution is exponentially increasing with indium alloying concentration.

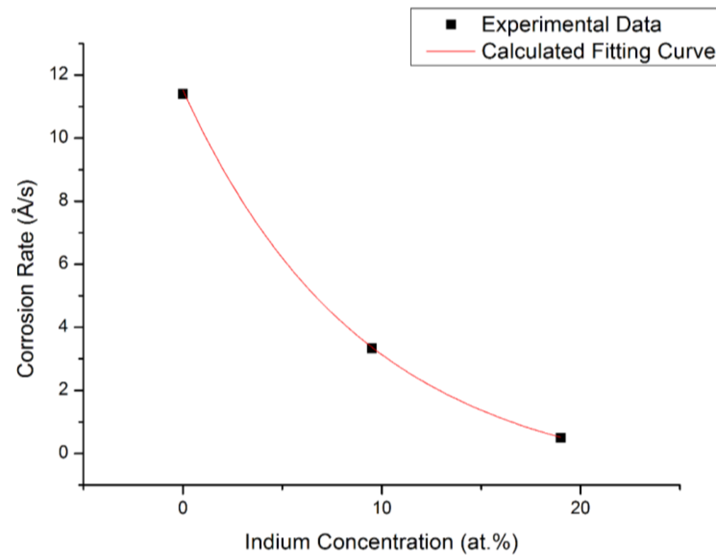

Fig. 4.8 The plot of silver sulfide growth rate vs. indium concentration of (Ag)-xxIn solid solution.

In conclusion, through this quantitative study of the sulfurization experiment, the sulfur gas corrosion reaction rate of pure silver, Argentium silver, (Ag)-9.5In and (Ag)-19In have been determined. The experimental results quantitatively confirm that the conclusion of previous observation under optical microscope. The correlation between the growth rate of silver sulfide and indium concentration have been made. Remarkably, (Ag)-19In exhibits fantastic anti-tarnishing property with repeatable experimental evidences.

4.4 Summary

In this chapter, an accelerated quantitative corrosion test experiment has been designed to study the tarnishing reaction between silver-based alloy and sulfur vapor. Previously, the anti-tarnishing property of silver-based alloy was used to be qualitatively described by the color or the reflectance of the tarnished surface of the sample. Details and insights of the design of experiment have been explained, and the results of testing experiment are accurate and repeatable. The qualitative observations under optical microscope are in agreement with quantitative measurement results, which can confirm the validity of the designed method. Therefore, this accelerated quantitative corrosion test experiment can potentially be used to develop standard test to evaluate anti-tarnishing property of silver-based alloy. In addition, the results of the sulfurization experiment of pure silver, Argentium, (Ag)-9.5In and (Ag)-19In have shown that (Ag)-xxIn solid solution exhibits excellent anti-tarnishing property, and the ability of anti-tarnishing exponentially increases with the indium element concentration. Significantly, the sulfurization reaction rate of (Ag)-19In is 22.8 times slower than of pure silver, 14.5 times slower than of Argentium silver. With the superior anti-tarnishing property, (Ag)-19In can be potentially used as the material in making jewelry, mirrors, and reflecting layers in LEDs devices.

Reference in Chapter 4

1. F. A. Cotton and G. Wilkinson, "Inorganic Chemistry," 4th Edition, John Wiley, New York, 1980.
2. C. Hillman, J. Arnold, S. Binfield, J. Seppi, "Silver and Sulfur: Case Studies, Physics and Possible Solutions," Proceedings of SMTA International, Orlando, FL. October, 2007.
3. M. H. Hebb, "Electrical conductivity of silver sulfide." The Journal of Chemical Physics, vol. 20, No.1, pp. 185-190, 1952.
4. D. Minzari, M. S. Jellesen, P. Moller, R. Ambat, "Morpholofical study of silver corrosion in highly aggressive sulfur environments.", Engineering Failure Analysis, vol. 18, No.8, pp. 2126-2136, July 2011.
5. G. Mura, G. Cassanelli, F. Fantini, and M. Vanzi, "Sulfur-contamination of high power white LED." Microelectronics Reliability, vol. 48, No. 8, pp. 1208-1211, 2008.
6. B. T. Reagor and J. D. Sinclair. "Tarnishing of silver by sulfur vapor: film characteristics and humidity effects." Journal of the Electrochemical Society, vol. 128, No.3, pp. 701-705, 1981.
7. H. Kim, "Corrosion process of silver in environments containing 0.1 ppm H2S and 1.2 ppm NO2." Materials and Corrosion, vol. 54, No.4, pp. 243-250, 2003.
8. X. Y. Mao, and K. S. Tian. "Tarnish mechanism of silver plating and anti-tarnish process." Electroplating and Pollution Control, vol. 15, No.1, pp. 8-12, 1995.
9. J. D. Sinclair, "Tarnishing of silver by organic sulfur vapors: rates and film characteristics." Journal of the Electrochemical Society, vol. 129, No.1, pp. 33-40, 1982.
10. T. E. Graedel, "Corrosion mechanisms for silver exposed to the atmosphere." Journal of the Electrochemical Society, vol. 139, No.7, pp. 1963-1970, 1992.
11. C. J. Yang, C. H. Liang, and X. Liu. "Tarnishing of silver in environments with sulphur contamination." Anti-Corrosion Methods and Materials, vol. 54, No.1, pp. 21-26, 2007.
12. R. R. Benham, "Silver plating." Anti-Corrosion Methods and Materials, vol. 10, No.2, pp. 31-35, 1963.
13. R. Bond, R. P. Stanek and W. Hoffman. "Silver infrared reflective film, metal oxide dielectric film, silicon nitride protective coating; for windshields, windows." U.S. Patent, No. 5834103, issued

Nov. 10, 1998.

14. L. Paussaa, L. Guzmana, E. Marina, N. Isomakib, L. Fedrizzia. "Protection of silver surfaces against tarnishing by means of alumina/titania-nanolayers." Surface and Coatings Technology, vol. 206, No. 5, pp. 976-980, 2011.
15. C. Liang, C. Yang, and N. Huang. "Tarnish protection of silver by octadecanethiol self-assembled monolayers prepared in aqueous micellar solution." Surface and Coatings Technology, vol. 203, No. 8, pp. 1034-1044, 2009.
16. J. Randin, "Chromated layer as an Anti-tarnish protection of AuAgCu alloys." Materials and Corrosion, vol. 43, No.4, pp. 172-176, 1992.
17. A. Butts, "Silver Economics Metallurgy and Use", R.E. Krieger Pub, Huntington, 1967, pp. 123-136.
18. J. Nielsen and J. Tuccillo. "Tarnish resistant alloy." U.S. Patent, No. 3767391, issued Oct. 23, 1973.
19. Sirirut, N. and Ekasit, N., "The anti-tarnishing, microstructure analysis and mechanical properties of sterling silver with silicon addition", Journal of Metals, Materials and Minerals, vol. 12, No.2, pp. 13-18, 2003.
20. K. F. Edward, "Silver alloy." U.S. Patent, No. 1970319, issued Aug. 14, 1934.
21. P. Johns, "Silver ternary alloy." U.S. Patent, No. 20070009375 A1, issued Jan. 11, 2007.
22. D. Davitz, "Alloy for jewelry with zinc, copper and silicon." U.S. Patent, No. 5882441, issued Mar. 16, 1999.
23. Y. Huo, and C. C. Lee. "Anti-tarnishing evaluations of silver solid solution phase with indium." Electronic Components and Technology Conference (ECTC), 2015 IEEE 65th. IEEE, pp. 2180-7, 2015.
24. S. Lilienfeld and C. E. White, "A study of the reaction between hydrogen sulfide and silver", Journal of American Chemical Society, vol. 52, No.3, pp. 885-892, 1930.
25. M. Beat, "Elemental Sulfur", Chemical Reviews, vol. 76, No.3, pp. 367-386, 1976.
26. D. W. Rice, P. Peterson, E. B. Rigby, P. B. P. Phipps, R. J. Cappell and R. Tremoureux. "Atmospheric Corrosion of Copper and Silver", Journal of the Electrochemical Society, vol. 128, No. 2, pp. 275-284, 1981.

27. P. R. Subramanian, J. H. Perepezko, “The Ag-Cu (silver-copper) system”, Journal of Phase Equilibria, vol. 14, No. 1, pp. 62-75, February 1993.

28. A. Cusma, M. Sebastiani, D. D. Felicis, A. Basso and E. Bemporad, “Study on the Correlation between Microstructure Corrosion and Wear Resistance of Ag-Cu-Ge Alloys”, Coatings, vol. 5, No. 1, pp. 78-94, March 2015.

Chapter 5

Anti-tarnishing Mechanism in Silver-Indium Binary System

5.1 Introduction

Silver is a truly amazing material as it has been already used in forging coins in ancient Lydia around 700 BC, but still can keep fitting in brand-new special niches of technological applications, such as silver thin films [1-3], silver nano-particles [4-8], and silver nano-sintering [9, 10], even in the modern days of 21st century. This is actually quite understandable since silver possesses superior material properties, such as the highest electrical conductivity of any element, the highest thermal conductivity and reflectivity among metals, with reasonable price and truly remarkable aesthetic value.

However, silver has its own Achilles' heel for being very chemical sensitive to the presence of sulfur-containing corrosive gases such as sulfur vapor [11], hydrogen sulfide [12], sulfur dioxide [13], and organic sulfur vapors [14], etc., even for very low concentrations ranging from less than 1 parts per billion (ppb) in normal atmosphere to hundreds of ppb under heavy industrial environment. Therefore, pure silver can easily get tarnished and form silver sulfide after a period of time, resulting in degradation of original electrical [15] or optical performance [16] or rendering long-term reliability [17] of its products at stake.

In order to understand the nature of silver sulfurization, a number of research have been conducted over the decades. For example, several environmental parameters, such as temperature, relative humidity [18], illumination [13], and surface states [19], have been studied to explore the silver tarnishing mechanism based on electrochemical models. In order to search possible scientific and engineering anti-tarnishing solutions, some surface treatment techniques for silver have been proposed, using different coating methods or coating materials, such as metallic coating by electroplating [20], sputter-applied coatings [21], oxide coating [22], organic coating [23], chromate conversion coating [24]. However, such thin layer of coating material can be worn out very easily after a period of time. Another approach to address tarnishing issues for silver is by alloying. It has

been reported that adding other elements such as palladium [25], silicon [26], tin [27], germanium [28], and zinc [29], can be effective, more or less, for anti-tarnishing purposes.

In the previous chapter, the author had demonstrated a designed experimental method to quantitatively study the tarnishing reactions of pure silver and silver-indium solid solutions with sulfur vapor (S_8) [30]. The experimental results had shown that silver-indium solid solutions exhibited a superior anti-tarnishing property, which could be meaningful to various fields of silver applications which have been suffering from the tarnishing issues, such as jewelry, catalyst, welding, electronics, and optics. However, the anti-tarnishing nature of silver-indium solid solutions was not fully understood yet by the authors at that time, so we did not discuss or speculate its underlying mechanism in the content of that paper.

In this chapter, the author would like to reveal the anti-tarnishing mechanism in silver-indium binary system in a theoretical and systematical manner. Essentially, silver tarnishing is a corrosion phenomenon which is largely related to solid-gas interfacial reactions. Therefore, anti-tarnishing should be one of the intrinsic properties of silver-indium solid solutions surface. Accordingly, it is appropriate to study its fundamental physical-chemistry with surface sensitive techniques. X-ray photoelectron spectroscopy (XPS) and ultraviolet photoelectron spectroscopy (UPS) are such desired experimental techniques whose capabilities can fulfill the tasks for probing physical-chemical properties determined by core-level electrons and valence band electronic structures.

In the following sessions, the author first presents the preparation and characterization of Ag-In thin film samples in details. Following, the nature of metallic surfaces of silver-indium alloy will be unveiled by the XPS and UPS experimental results. Next, the authors have conducted a systematic review for Hard and Soft Acids and Bases (HSAB) principle, its conceptual Density Functional Theory (DFT) formalization, and Molecular Orbital Theory (MOT). Furthermore, the experimental results will be further discussed within the framework of HSAB principle. During the discussion, the authors have proposed an alternative methodology, which is incorporated with the Hammer-Nørskov d-band model, to calculate HSAB parameters for bulk metals. Finally, the authors would like to propose a physical-chemical model to explain the anti-tarnishing mechanism in silver-indium binary system, based on solid experimental evidences and self-contained theoretical analysis.

5.2 Material Preparation and Characterization

5.2.1 E-beam Evaporation Process

In the previous chapter, the author has shown the methods to grow ingots of silver-indium solid solution phase bulk material for characterizing its mechanical properties [31]. The sequence of polishing process, which are regularly and necessarily performed in bulk material sample preparation, would actually largely damage and contaminate samples surface, and eventually alter the original material surface properties. However, XPS and UPS are highly surface sensitive experimental techniques due to the fact that 95 percentage of the detected signal is contributed from topmost surface atomic layers within approximately 5 nm. Therefore, bulk material samples might not be suitable to the current study. As consequence, high quality thin film samples of silver-indium solid solution phase (α phase) with same compositions of our previous study is indeed needed.

E-beam evaporation was chosen for the preparation of thin film samples of pure silver, silver-indium solid solution phase, Ag_9In_4 intermetallic compound (IMC) in Ag-In binary system. The raw materials of pure silver and indium shots with 99.99 wt. % purity were weighed, uniformly mixed and loaded in a graphite crucible for the following E-beam evaporation. In this study, the compositions of starting raw materials were carefully adjusted in order to obtain the desired composition of Ag-In alloys thin film samples. 1 inch × 1 inch squares of fused quartz with 1 mm thickness were mounted on the substrate stage of the evaporator as the deposition substrates of the thin film samples. The evaporation chamber was pumped down to 2×10^{-8} torr before turning-on the E-beam source, and then materials in crucible were pre-soaked for 5 mins with swirling pattern of E-beam in order to completely melt the target materials. During the E-beam evaporation process, the deposition rate was monitored by quartz crystal microbalance (QCM), and was precisely settled at 1 Å/s within ± 5% error of tolerance, using proportional–integral–derivative (PID) controller. The substrate stage was in-plane rotating constantly at 60 °/s during the deposition to ensure the uniformity of the resulting thin film samples. The resulting thickness of silver-indium thin film samples was 100 nm within ± 5% error of tolerance.

5.2.2 Grazing Incidence X-ray Diffraction Characterization

Next, the fabricated thin film samples were further examined with Rigaku SmartLab X-ray diffractometer, using parallel beam (PB) mode to perform grazing incidence X-ray diffraction (GIXRD). The grazing angle of incidence (Ω) is optimized at 0.65 °in order to achieve optimal intensity of GIXRD signal. The GIXRD is performed from 20 ° to 90 ° at scanning speed of 1 °/min, using collimated Cu Kα line excitation X-ray source. After GIXRD measurement, the collected data were analyzed by PDXL, an integrated powder X-ray analysis software package, and compared with The International Centre for Diffraction Data (ICDD) standard card. As a result, the GIXRD pattern of pure silver, silver-indium solid solutions with different compositions, and Ag_9In_4 IMC thin film samples have been plotted in Fig. 5.1. In this study, the intended values of indium concentration of the silver-indium solutions thin film samples were 5 at. %, 9.5 at. % and 19 at. %, which were nominally designated as (Ag)-5In, (Ag)-9.5In and (Ag)-19In, in order to correlate with the tarnishing experimental reaction rates measured in our previous study [30].The weighted average values for lattice constants are 4.082 Å, 4.094 Å, 4.109 Å and 4.145 Å for pure silver and each silver-indium solid solutions thin film samples. In addition, silver-indium binary system should obey Vegard's Law [32]. As shown in Fig. 5.2, the calculated average lattice constants of bulk samples in previous study and of thin film samples in this study are plotted together with ICDD standard powder samples of silver and silver-indium solid solutions. The lattice constants of silver-indium solid solutions of bulk material samples data were measured in our previous study [33], and they increase linearly with the increase of indium concentration. As shown in Fig. 5.2, the linear fitting curve of bulk material lattice constants is nearly parallel and above the linear curve determined by ICDD data points. Next, we used the nominal indium concentration values of silver-indium solid solutions thin samples to plot another curve in Fig. 5.2. As a result, resulting lattice constants data points of thin samples fitted well with the increasing linear relationship, and their linear fitting curve is also nearly parallel but under the linear curve of ICDD powder samples. Thus, we can safely confirm that nominal indium concentrations were near true values of silver-indium solid solutions thin film samples. Additionally, if ICDD powder samples were considered stress-free samples, the bulk materials grown in house

should exhibit macroscopic residual tensile stress, and the thin film samples should exhibit macroscopic residual compressive stress to explain the reason why their linear curves shifted upwards and downwards, respectively, in Fig. 5.2.

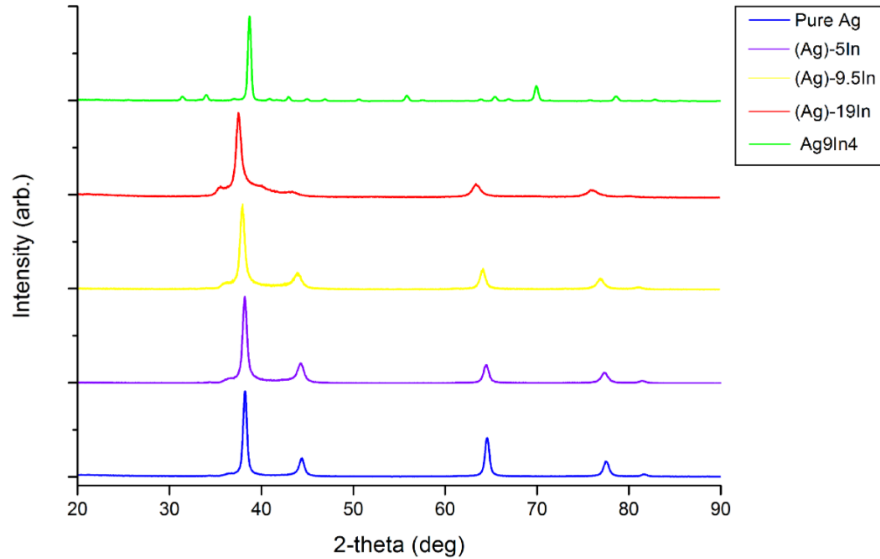

Fig 5.1 GIXRD patterns of the Ag-In thin film samples.

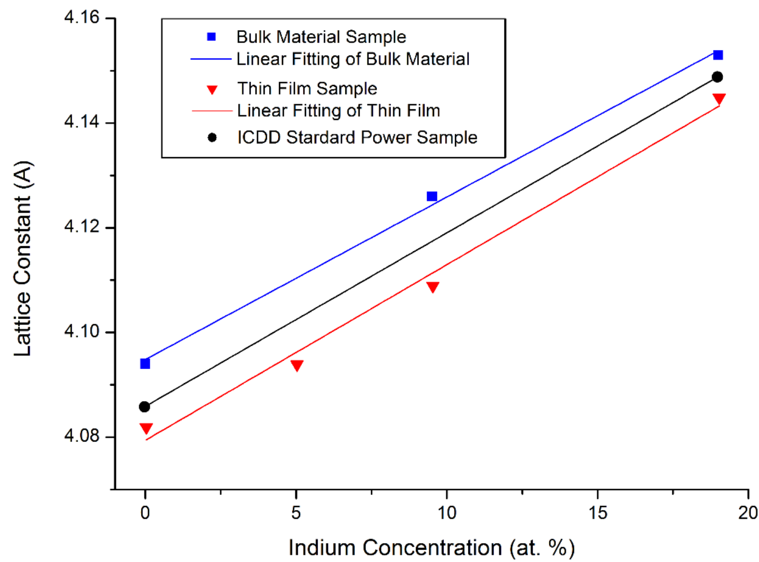

Fig. 5.2 The plot of calculated average lattice constants of Ag-In bulk samples, thin film samples and ICDD standard powder samples with linear fitting curves.

For Ag_9In_4 IMC sample, 24 peaks in GIXRD pattern were recognized by PDXL, 23 peaks among them were identified with Ag_9In_4 phase except for the one minor peak. Ag_9In_4 IMC exhibits complex crystal structure in cubic system with P-43m space group symmetry. The most intensive peak is centered at 38.69 °, which corresponds to (3 3 0) crystal plane, according to ICDD standard card No. 01-071-0128. Therefore, the authors can safely confirm that the resulting Ag_9In_4 IMC thin film is single phase material, without any other phases in silver-indium binary system.

In summary, pure silver, silver-indium solid solutions and Ag_9In_4 IMC thin film samples have been successfully fabricated for further XPS/UPS study, with the confirmation of GIXRD phase identification. It is worthwhile noticing that several minor peaks in GIXRD patterns of native metallic oxides have been also identified, and it will be discussed in the following section.

5.3 Experimental Results

The AXIS Supra by Kratos Analytical at the UC Irvine Materials Research Institute (IMRI) was used to perform the experimental XPS/UPS characterization for the resulting thin film samples. X-ray photoelectron spectra (XPS) were recorded with a monochromatized Al K_α radiation source ($\hbar\omega$ = 1486.6 eV) under ultra-high vacuum (UHV) operated below 1×10^{-8} torr. The analyzed spot size was 300 μm × 700 μm, with an analyzer pass energy of 20 eV. All of the XPS survey spectra were obtained by scanning of the analyzer using step of 1 eV with a dwell time of 300 ms, and the recorded survey spectra can be used for quantification analysis. The XPS regions spectra were obtained by using scanning step of 0.05 eV with dwell time of 300 ms, and a sufficiently large number of sweep for each regions was recorded to achieve reasonable signal-to-noise ratio (SNR). The gas cluster ion source (GCIS) system inside the AXIS Supra enables the authors to clean the sample surface with Ar+ ions in order to remove any form of surface contamination and native oxide while maintaining at UHV, thereby preventing the surface from any further contamination or oxidation after the surface cleaning. After quantification analysis of CasaXps, the cleaned surface composition of the samples can be precisely determined with sensitivity as high as 0.01 at. %, using intensity and areas of survey spectral peaks in Ag 3d and In 3d regions. The results showed that the indium concentration were

5.32 at. %, 9.86 at. %, 19.70 at. % and 32.43 at. % for each Ag-In solid solutions and Ag_9In_4 IMC respectively. Therefore, it is conclusive to confirm that the thin film samples compositions were well-controlled within 1 at. % error of tolerance, verifying that nominal notations for the thin film samples were indeed valid.

5.3.1 X-ray Photoelectron Ag 3d Regions Spectra Results

As shown in Fig. 5.3, Ag 3d region spectra were measured, recorded and plotted for all of the cleaned thin film samples. All of measured spectral peaks positions were calibrated against the pure Ag 3d 5/2 peak at Eb = 368.30 eV, which is the reference level from the instrument manufacturer for monochromatic Al K_α X-ray source excitation, and the spectral intensities were normalized with the highest peak in each spectra. The Ag 3d region peaks were labeled in each spectra, and the peak position were recorded and summarized in Table 5.1. As shown in Fig. 5.3 (a), the Ag 3d 3/2 and 5/2 peaks exhibits typical Doniach-Sunjic asymmetric lineshape [33] with unchanged spin-orbit splitting energy of 6.0 eV for all thin film samples, which is in agreement with the high energy resolution results of pure Ag 3d regions spectra in the literature [34].

Compositions	Ag 3d 3/2 (eV)		Ag 3d 5/2 (eV)		Chemical Shift (eV)
	BE	FWHM	BE	FWHM	
Pure Ag	374.30	0.60	368.30	0.58	-
(Ag)-5In	374.35	0.62	368.35	0.60	0.05
(Ag)-9.5In	374.35	0.63	368.35	0.62	0.05
(Ag)-19In	374.40	0.67	368.40	0.64	0.10
Ag_9In_4	374.55	0.69	368.55	0.67	0.25

Table 5.1 A summary of Ag 3d regions spectral peaks position, FWHM and chemical shift of Ag-In thin film samples.

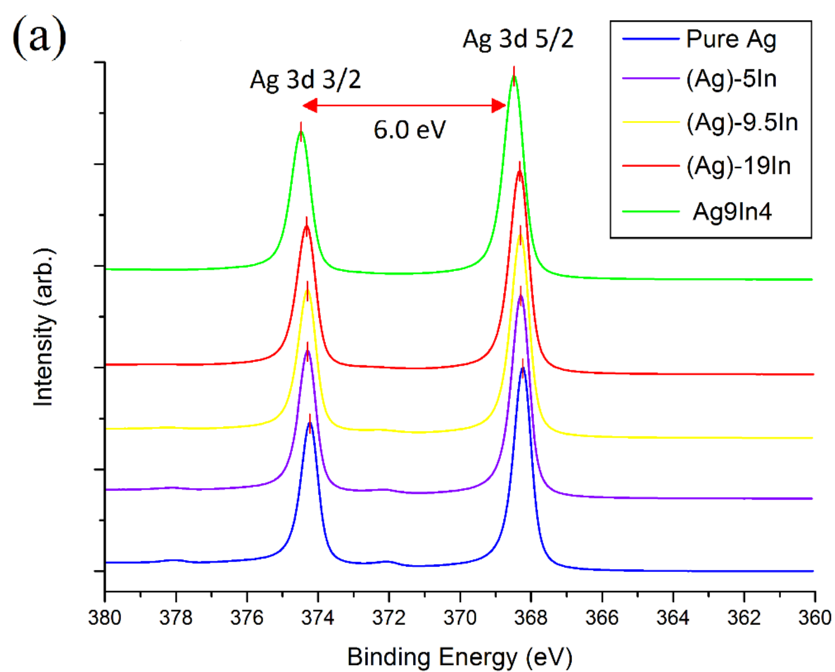

Fig. 5.3 (a) X-ray photoelectron spectra of Ag 3d region,

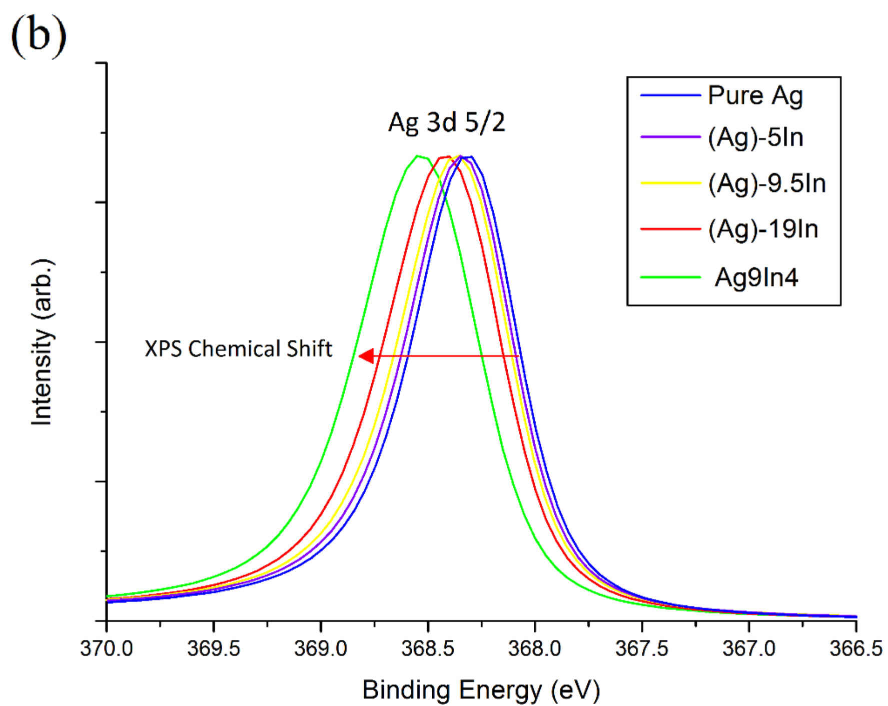

Fig. 5.3 (b) Chemical shift of Ag 3d 5/2 peaks of Ag-In thin film samples.

As shown in Table 5.1, the peaks position of Ag 3d 3/2 and 5/2 have both shifted to higher binding energy, and the full width at half maximums (FWHMs) of both peaks have increased with the increase of indium concentration of the thin film samples. As illustrated in Fig. 5.3 (b), we can clearly observe the continuous trend of peak shifting in Ag 3d 5/2 peaks regions of silver-indium solid solutions and Ag_9In_4 IMC, where (Ag)-5In, (Ag)-9.5In and (Ag)-19In exhibit small chemical shift of 0.05 eV and 0.10 eV, respectively, with respect to pure Ag. The measured chemical shift of Ag_9In_4 IMC is 0.25 eV, which is relatively large compared to that of silver-indium solid solutions. This is understandable since its crystallography has changed from FCC to complex cubic superlattice crystal structure, so that the chemical environment of Ag atoms in the IMC would be altered drastically.

In the literature [35], the chemical shift measured by XPS was also referring as core-level shift (CLS) measured by electron spectroscopy for chemical analysis (ESCA), which is different from the shift of the core-electron eigenstates (initial state CLS) by the amount of the core hole relaxation energy (ΔE_R). The core hole relaxation process will contribute to the shift from the remaining electrons as they were screened by the charge imbalance caused by the core hole, and it is often known as final state effects. However, in many cases, the final state effects are often assumed to be independent of the chemical environment, and therefore do not contribute to the core-level chemical shift. A more detailed approach in analyzing core-level chemical shift can be rationalized by using the calculation scheme through Born-Haber cycle [36]. Several important physical and thermodynamic properties of alloys, such as cohesive energy [37], heat of mixing [38], the segregation energy [39], etc. can be estimated from core-level chemical shift analysis of this approach. However, the authors would not explore further but to conclude that the Ag 3d core-level electrons of silver-indium alloy exhibited typical core-level electrons character, and were well-screened from outside environment.

5.3.2 X-ray Photoelectron O 1s Region Spectra Results

It is also of great importance to understand the natural oxidation state of the original silver-indium alloy surface, since it is largely correlated with the various interfacial chemical reactions. Therefore, XPS O 1s region spectra were measured for the as-deposited thin film samples without Ar+ ion

cleaning. The resulting XPS O 1s region measured spectra were plotted with solid lines, and fitted with Gaussian lineshape using dot-lines for each major peaks for all thin film samples in Fig. 5.4, with intensity normalized against the highest peak in each spectra. As shown in Fig. 5.4 (a), the O 1s region spectra for as-deposited pure silver thin film sample has one major peak at Eb = 530.4 eV, which is corresponding to atomic oxygen with Ag-O bonding character [40]. It is clear that a hump start to show up at lower binding energy side of original major peak in the O 1s region spectra of (Ag)-5In thin film sample, and the original major peak of O 1s has shifted towards higher binding energy side to Eb = 530.9 eV. After deconvolution and fitting with Gaussian lineshape, the peak position and relative intensity of the emerging peak can be determined, which is at Eb = 529.1 eV and of 26 % intensity of original major peak. The major characteristic O 1s peak of pure In_2O_3 is known at Eb = 529.5 eV, and peak position would shift if other doping elements involved [41]. Therefore, this emerging O 1s might be corresponding to In-O bonding character with Ag element involved in its local chemical environment. Accordingly, as shown in Fig. 5.4 (b), the trend continues as the indium concentration of the thin film samples increases: the relative intensity of In-O bonding character O 1s peak increases; both Ag-O and In-O bonding character peak positions shift towards higher bonding energy. It is worthwhile noticing that the shift of Ag-O bonding character from (Ag)-9.5In to (Ag)-19In is negligible, meaning the chemical environment of atomic oxygen with Ag-O bonding character remains almost the same for silver-indium solid solutions with high indium concentration. In addition, the amount of peak shift from solid solutions to IMC is relatively large so that the chemical environment of atomic oxygen is quite different from solid solutions to IMC surfaces. In Table II, the peak position, relative intensity, and energy splitting of two major peaks were summarized. Based on the experimental results above, it is clear that atomic oxygen experiences two different chemical environment, namely, Ag-rich and In-rich, in the naturally formed oxide layers of silver-indium solid solutions and IMC, and the percentage of In-rich oxide increases with the indium concentration of the alloy increases, reaching about the same level of Ag-rich oxide for Ag_9In_4 IMC thin film sample.

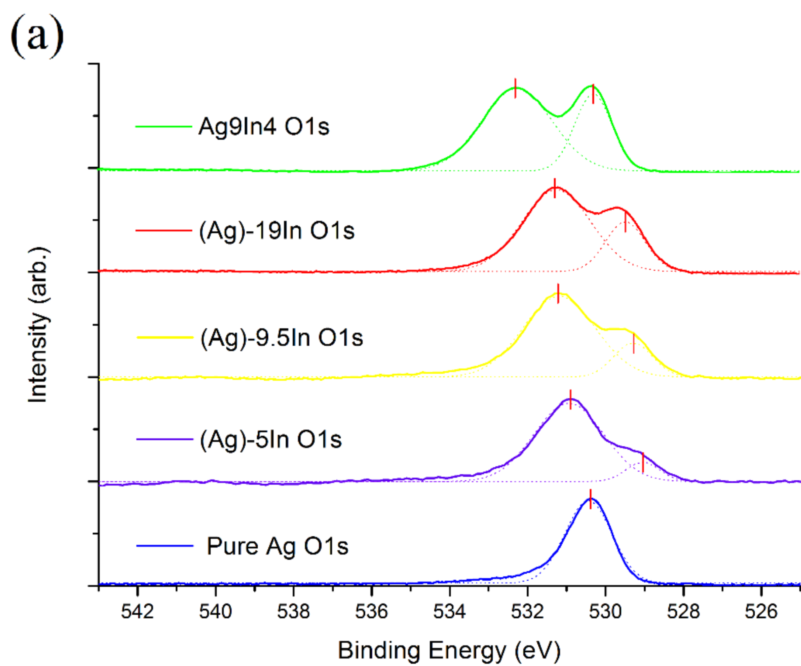

Fig. 5.4 (a) X-ray photoelectron spectra of O 1s region,

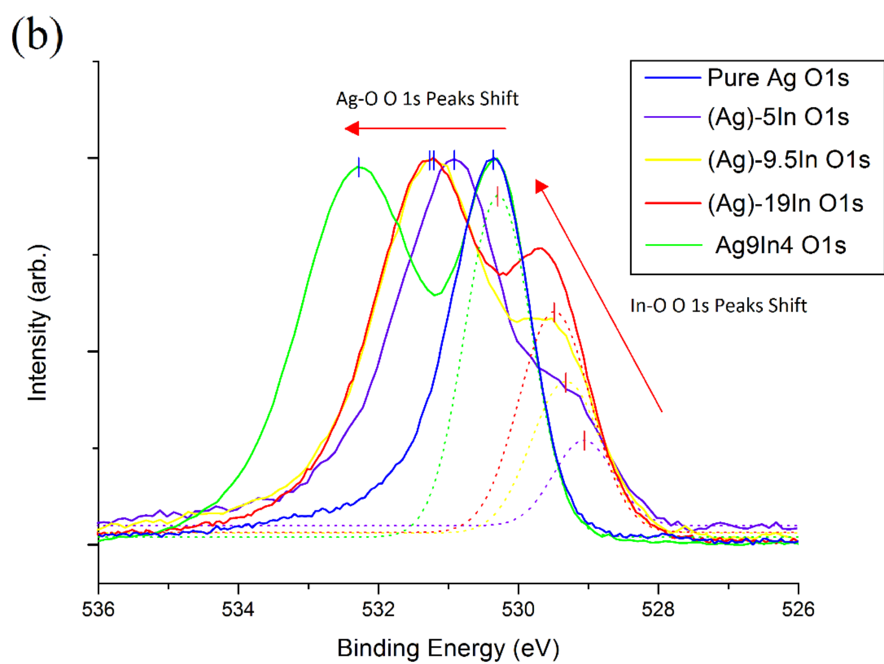

Fig. 5.4 (b) The trend of O 1s region major peaks shift of Ag-In thin film samples.

Binding Energy (BE)	Ag-O (eV)	Relative Intensity (%)	In-O (eV)	Relative Intensity (%)	Doublet Splitting (eV)
Pure Ag	530.4	100 %	-	-	-
(Ag)-5In	530.9	100 %	529.1	26 %	1.8
(Ag)-9.5In	531.2	100 %	529.3	43 %	1.9
(Ag)-19In	531.2	100 %	529.5	60 %	1.7
Ag_9In_4	532.3	100 %	530.3	88 %	2.0

Table 5.2 A summary of O 1s regions spectral peaks position of Ag-In thin film samples.

5.3.3 Ultraviolet Photoelectron Spectra Results of Valence Bands

It is crucial to visualize silver-indium alloys valence band electronic structures in order to understand the mechanism behind dramatic lowering of the chemical reactivity with sulfur gas molecule (S_8) in our previous tarnishing experiment. Ultraviolet photoelectron spectroscopy (UPS) is one of the well-established powerful tools to investigate electronic structures of valance bands, since it offers higher photoionization cross sections and inherently fourfold higher energy resolution compared to XPS [42]. Although UPS spectral shapes are often incident photon energy dependent, the spectra generally converge to the same one and start to resemble the occupied density of states (DOS), i.e., electronic density distribution, of the measured valance bands for photon energy $\hbar\omega > 40$ eV. Accordingly, the monochromatized resonance radiation source from He II ($\hbar\omega$ = 40.8 eV) of the AXIS Supra was chosen to conduct the UPS experimental measurement on the silver-indium alloy valance bands structure. The analyzer energy resolution was set as high as 0.01 eV, and a sufficiently large number of sweep for each spectra was recorded to achieve good SNR for the measurement data. The inherent energy resolution of the UPS measurement was 0.095 eV, which was determined from the width of the Fermi edge of pure Ag thin film sample. The raw data of the measurement were smoothed by 10 adjacent point averaging algorithm, thereby not significant lowering the UPS inherent energy resolution.

In the literature [43], indium had an s2p1 outer valence shell electronic configuration, and it was reported that In 4d spectral peaks (Eb = 16 - 18 eV) exhibited core-level electron character. The charge transfer between In 4d energy level and Ag 4d-band is negligibly small, so that the In 4d

energy level is well-separated from the Ag valence bands. Therefore, we have chosen the energy scanning range from Eb = 15.8 eV to Fermi energy level for our UPS valence bands measurement. Accordingly, as shown in Fig. 5.5 (a), the smoothed UPS spectra of thin film samples were plotted and their binding energy started from 11 eV, beyond which no features showed up other than inelastic scattering background. Each Ag valence 4d-band UPS spectra of Ag-In thin film samples could be divided into two parts, which were designated as primary 4d-bands and secondary 4d-bands in this paper. The authors observed several features directly from the UPS smoothed spectra. First of all, the Ag overall 4d-bands moved to higher binding energy, which agreed with the general trend in Ag-In binary system UPS spectra described in literature [44]. Secondly, the indium 5s valence level signal showed up at higher binding energy end of spectra and they were well-separated from Ag 4d-bands. The Fermi energy edges and Ag 5s-bands were clearly observed and labelled in the UPS spectra.

It is essential to remove the background signal of inelastic scattering and obtain normalized UPS spectra for further quantitative study. In bulk Ag, Ag 5s electrons mixed with 4d electrons to a large extent in valence band, which began at Eb = 7.5 eV and extended all the way to the edge of Fermi energy. In literature [45], the distribution of Ag 5s electrons exhibited a shallow terrace form, and their contributions to valence band were negligible small. In addition, it is also hard to distinguish 5s valence electrons apart from inelastic electrons. Therefore, the authors decided to remove Ag 5s-bands together with the inelastic background, thereby investigating Ag 4d-bands exclusively for each spectra. By discarding s-band and considering only the d-band electrons, it turns out to be largely in accordance with the valence band data treatment method in Hammer-Nørskov (HN) d-band model [46, 47]. In HN d-band model, for the transition metals (TMs) the s-band is half-full, and correspondingly the reactivity of TMs is given by the position of the d-band. It has been proved that Hammer-Nørskov d-band model is very useful and effective theoretical quantum-mechanical modelling method in predicting noble and late transition metallic catalysts behaviors.

Furthermore, each spectra was normalized against total number of electrons in valence bands. As shown in Fig. 5.5 (b), the normalized Ag valence 4d-bands were plotted with primary and secondary 4d-bands peaks and band-widths labelled. The features of normalized UPS spectra, namely, primary and secondary 4d-band peak positions, front edges and rear edges of Ag valence 4d-bands and band-

widths, were listed in Table 5.3. As the data shown in Table 5.3, the front edges of Ag valence 4d-bands shifted away from Fermi energy level with the increase of indium concentration. Moreover, primary 4d-bands peaks exhibited even larger amount of shifting. In contrast, not only the amount of secondary 4d-bands peaks shift was relatively small, but also the rear edges of the Ag valence 4d-bands were almost pinned, therefore largely narrowing the band-widths. In addition, in term of normalized intensity, its d states were localized at the top of the valence band for pure Ag [34], which could be directly confirmed with Fig. 5.5 (b). However, the normalized intensities of primary 4d-bands were dropping for Ag-In solid solutions spectra as indium concentration increased, whereas secondary 4d-bands intensity were boosted by indium solutes adding. Therefore, the occupied valence states become less localized at the top of valence band, and a prominent charge transfer phenomenon, from primary bands to secondary bands, occurred. In conclusion, the electronic distribution of Ag 4d-bands were largely affected by adding indium solutes into original silver crystal lattice, and would further lead to a great impact on chemical behaviors. In the following section, the authors would like to discuss the correlation between the Ag-In valance bands electronic structures to their chemical behaviors within the framework of HSAB principle.

Binding Energy (eV)	Primary 4d-band Peak	Secondary 4d-band Peak	Front Edge	Rear Edge	Band Width	Primary 4d-band Peak Shift	Front Edge Shift
Pure Ag	4.10	6.19	3.84	7.06	3.22	-	-
(Ag)-5In	4.17	6.21	3.87	7.07	3.20	0.07	0.03
(Ag)-9.5In	4.49	6.33	3.92	7.09	3.17	0.39	0.08
(Ag)-19In	4.91	6.33	4.01	7.10	3.09	0.81	0.17
Ag_9In_4	5.52	6.56	4.68	7.10	2.42	1.42	0.84

Table 5.3 A summary of normalized UPS spectra characteristic information of Ag-In thin film samples.

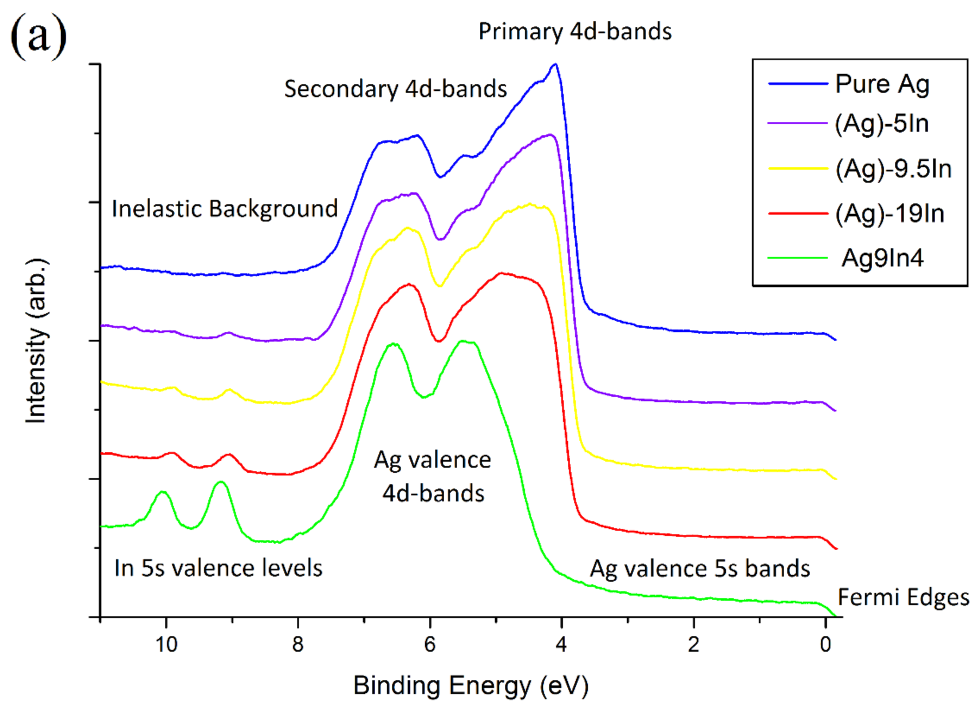

Fig 5.5 (a) Ultraviolet photoelectron spectra of valence bands,

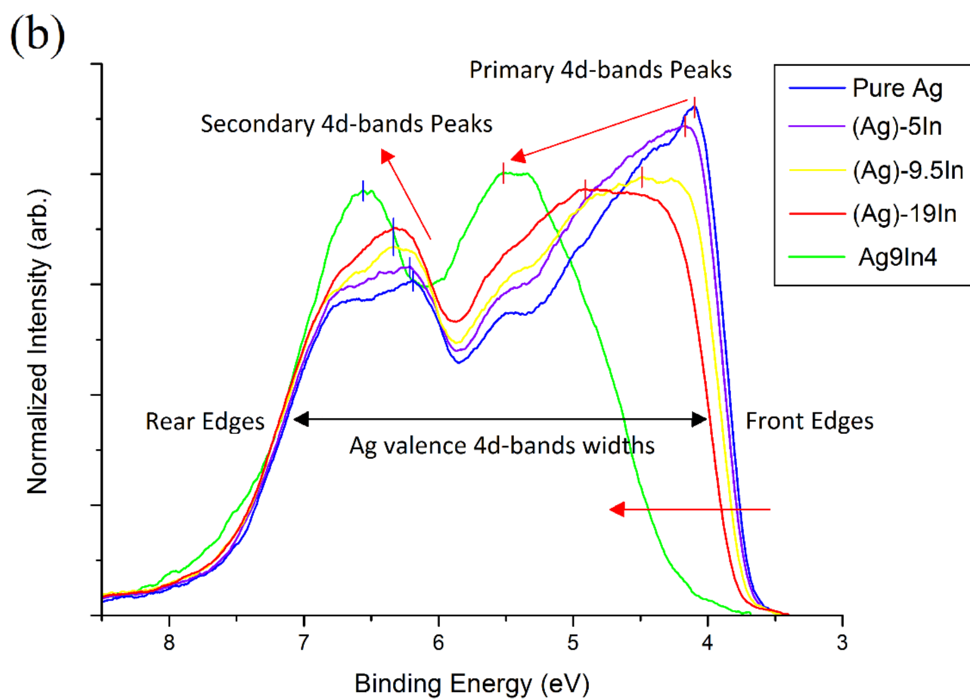

Fig. 5.5 (b) Normalized spectra of Ag valence 4d-bands of Ag-In thin film samples.

5.4 HSAB Principle and Discussions

5.4.1 HSAB Principle and its Conceptual DFT Formalization

In early days, R.G. Pearson had categorized Lewis acids and bases as either hard or soft, and established hard and soft acids and bases (HSAB) principle based on experimental facts: ***hard acids react preferentially with hard bases, and soft acids react preferentially with soft bases*** [48]. This statement refers to the generalized acid-base reaction shown in Eq. (5.1), where A is the Lewis acid, electron acceptor or electrophile, B is the Lewis base, electron donor or nucleophiles, and A:B is an acid–base complex, an adduct, or a coordination compound. It is worthwhile noticing that one reactant could act as Lewis acid in one chemical reaction and act as Lewis base in another chemical reaction, depending on whether it would accommodate electrons or donate electrons in that particular chemical reaction.

$$A + :B \rightarrow A:B \qquad (5.1)$$

HSAB principle has been proved to be useful in inorganic [49] and organic chemistry [50]. One of the great successes of HSAB principle is to rationalize the experimental fact that silver (soft base) is relatively chemical inert to oxygen (hard acid) in the atmosphere, but can be easily tarnished by sulfur element containing gases (soft acids), whereas classic reduction–oxidation (redox) theories failed to interpret those phenomena appropriately. In essence, HSAB principle is phenomenological in its nature, which means that there should be underlying theoretical reasons to explain the chemical facts which this principle summarizes. Intuitively, the ionic–covalent theory would be able to give qualitative explanations for HSAB principle: hard acids and hard bases tend to form ionic character (coulomb attraction) molecular bonding, whereas soft acids and soft bases tend to form covalent character (orbitals hybridization) molecular bonding in their resulting acid–base complex respectively. Those hard–hard or soft–soft chemical interactions are generally more favored energetically, so that their acid–base complex is also chemically and thermally stable. Particularly, some transition metals with loosely held outer d-orbital electrons, especially Ag, are willing to share its valence electrons with empty outer orbitals available on other basic atoms, such as sulfur and iodine, to form covalent bonding and lower its orbital energy by d-p hybridization of their molecular

orbitals [51]. Above statements had been supported by the π-bonding theory of Chatt [52] and d-p orbital hybridization mechanism proposed by Mulliken [53]. On the other hand, for example, silver oxide (Ag_2O) has much lower melting temperature (300 ℃) compared to most metal oxides and it would even decompose at 200 ℃. Thus it is clearly not thermally nor chemically stable. Because silver oxide is essentially a hard acid–soft base complex, its molecular bonding is at transition state between ionic character and covalent character, which results in energetically non-favorable electronic configuration.

However, HSAB principle was criticized earlier because of the lack of a strict mathematical deduction or parameters to quantify this kind of material property described by HSAB principle. Fortunately, Parr has introduced quantifiable parameters into HSAB principle scheme, namely, chemical hardness and softness [54]. In addition, Kohn and Sham (K-S) have developed the density functional theory (DFT) [55] as a computational quantum-mechanical modelling method, thereby allowing people to describe and explain HSAB phenomena in a more mathematically rigorous and systematical manner. Within the K-S framework of DFT, one would be able to compute with a set of self-consistent equations, and acquire calculated results of electron density distribution, n(r), total number of electron, N[n(r)], and total ground state electronic energy, E[n(r)], for a chemical system of finite atomic number (100-200). Generally, the resulting E vs. N plots are usually convex upward curves, and their slopes and curvatures represent two parameters of substantial importance, electronic chemical potential (μ) and chemical hardness (η), as shown in Eq. (5.2) and Eq. (5.3):

$$\mu = (\partial \mathrm{E}/\partial \mathrm{N})_v = -\chi_M \tag{5.2}$$

$$\eta = (\partial^2 \mathrm{E}/\partial \mathrm{N}^2)_v = (\partial \mu/\partial \mathrm{N})_v \tag{5.3}$$

$$\sigma = (\partial \mathrm{N}/\partial \mu)_v = 1/\eta \tag{5.4}$$

, where v is the potential due to the nuclei, uniquely determined by n(r). The definition of chemical softness, σ, is given by Eq. (5.4), which is the reciprocal of chemical hardness.

The electronic chemical potential characterizes the escaping tendency of electrons from the equilibrium system [56], and it is exactly negative value of the absolute electronegativity in Mulliken scale (χ_M). In the Lewis acid–base reaction (Eq. (5.1)), the total energy (E) and chemical potentials (μ) of the acid (A) and base (B) reactants can be expanded into Taylor series respectively. The resulting

equations, Eq. (5.5) and (5.6), can be derived then if let chemical potentials of A and B, i.e., $\mu_A = \mu_B$, equal to each other.

$$\Delta N = \frac{(\mu_{B^0} - \mu_{A^0})}{(\eta_A + \eta_B)} = \frac{(\chi_{A^0} - \chi_{B^0})}{(\eta_A + \eta_B)} \tag{5.5}$$

$$\Delta E = -\frac{1}{2}(\mu_{B^0} - \mu_{A^0})\Delta N = -\frac{1}{2}\frac{(\mu_{B^0} - \mu_{A^0})^2}{(\eta_A + \eta_B)} = -\frac{1}{2}\frac{(\chi_{A^0} - \chi_{B^0})^2}{(\eta_A + \eta_B)} \tag{5.6}$$

, where the superscript zero refers to the original reactants states and the total number of charge transfer is $\Delta N = N_A - N_{A^0} = N_{B^0} - N_B$ and total energy change due to charge transfer $\Delta E = (E_A - E_{A^0}) + (E_B - E_{B^0})$. When chemical potentials of A and B are equal to each other, the thermo-equilibrium state can be reached and net charge transfer process between two reactants will stop. Historically, above discussions had been done by Parr [54] and were known as the conceptual DFT formalization for HSAB principle.

Obviously, the acid must be more electronegative than the base to drive the electron transfer process, and total energy of the system will be lower as a result of electron charge transfer. Physically, the chemical hardness can be regarded as the resistance to electron charge transfer process. If both acid and base are soft, then the denominator, $\eta_A + \eta_B$, would be a small number. If they have also a reasonable difference in electronegativity, e.g. sulfur and silver, the resulting ΔN and ΔE in Eq. (5.5) and Eq. (5.6) would be substantial, which mathematically demonstrates that soft acid–soft base interactions facilitate the electron charge transfer to form covalent bonding and substantially lowering total energy of the system. For hard acid–hard base combination, the electron charge transfer should be small, but it can stabilize system by energy-favorable electrostatic interactions, namely, ionic bonding.

However, the derivatives of Eq. (5.2) and (5.3) were historically ill-defined [57] due to the "integer discontinuities" [58]. Thus, people usually calculate the electronic chemical potential and chemical hardness for practical applications by using finite-difference approximation, shown in Eq. (5.7) and Eq. (5.8), where I is ionization potential and A is the electron affinity.

$$\mu = -\frac{I + A}{2} < 0 \tag{5.7}$$

$$\eta = I - A \geq 0 \tag{5.8}$$

It is also important to correlate HSAB principle with molecular orbital theory (MOT) since it is one of well-established theories and has been accepted and widely used by most of the chemists. One can establish the bridge by Eq. (5.9), according to Koopmans' theorem:

$$-\varepsilon_{HOMO} = I, \qquad -\varepsilon_{LUMO} = A \tag{5.9}$$

, where $\varepsilon_{\text{HOMO}}$ is the frontier orbital energy of highest occupied molecular orbital (HOMO) and $\varepsilon_{\text{LUMO}}$ is the frontier orbital energy of lowest unoccupied molecular orbital (LUMO). Combing Eqs. (5.7) - (5.9), it is easy to see that electronic chemical potential is the midpoint of energy HOMO and LUMO frontier orbitals, and chemical hardness is the energy gap between HOMO and LUMO. Note that Koopmans' theorem is only valid within the Hartee-Fock theory so that DFT calculated $\varepsilon_{\text{HOMO}}$ and $\varepsilon_{\text{LUMO}}$ are rather poor approximations for -I and -A. In summary, HSAB principle has been proven to be self-contained and can be quantatively and theoretically formalized using conceptual DFT. Therefore, HSAB principle and its DFT conceptual formalization should be valid and useful in explaining or predicting most of molecular or aqueous based chemical reactions.

5.4.2 HSAB Parameters Calculation for Bulk Metals

For all bulk metals, the authors have noticed that they seemed to have the same chemical hardness, $\eta = 0$, since their ionization potential equals to electron affinity (I = A). Historically, this I = A, which leads to $\eta = 0$, was well-known and had been often acknowledged in literature [54]. In solid state physics, the corresponding term of HOMO–LUMO gap is the band gap between valence band and conduction band. For bulk metals, the valence band overlaps with conduction band, so the band gap would be zero, which is equal to the chemical hardness of bulk metals. However, we cannot overlook the experimental facts that large difference exists in terms of chemical reactivity in reactions with soft acids (e.g. sulfur element containing gases) for different bulk metals, even for those with similar electronegativity (e.g. silver vs. copper). Therefore, it would be questionable whether the finite-

difference approximation is still suitable for chemical hardness calculation of bulk metals within the HSAB and its conceptual DFT framework. In literature, Yang and Parr [59] had showed that when temperature is at absolute zero (T= 0 K), the chemical hardness, η, of bulk metals was actually related to the inverse of their density of states at Fermi energy, which was an extremely small number. More recently, some attempts had been made to establish HSAB models for bulk metals and surfaces, incorporating work functions and Fermi energy for parameterization [60, 61]. The established HSAB model [61] is valid in predicting the charge transfer and reaction between bulk metal and reactive atomic adsorbates (strong Lewis acids), namely, N, O, and Cl. However, as matter of fact, S element and sulfur molecules were not mentioned in that model. Therefore, in this research, the authors would like to go back to the original definitions of electronic chemical potential and chemical hardness, given by Eq. (2) and Eq. (3), to establish a theoretical model based on HSAB and conceptual DFT by using a different approach, namely, incorporating with Hammer-Nørskov d-band model.

As an alternative method to the DFT quantum-mechanical computation, people are able to experimentally acquire the information of electronic distribution for valence bands through high-precision instrumental measurement. From our previous XPS regions spectra, we can clearly see that the core-level electrons are well-screened and separated from outside environment, so their influence on chemical reactions in terms of charge transferring would be negligible small. Therefore, the authors would only consider the valence band electrons for HSAB parameters calculation.

With normalized UPS measurement data of Ag valence 4d-bands, i.e., the density-of-states (DOS) of the 4d-bands, $n_d(\varepsilon)$, at hands, the total ground state electronic energy in 4d-bands, $E_d[\varepsilon]$, and total number of electrons in 4d-bands, $N_d[\varepsilon]$, can be readily calculated through the approach of numerical integration of the experimental data by using Eq. (5.10) and Eq. (5.11):

$$N_d(\varepsilon) = \int_{-\infty}^{\varepsilon} n_d(\varepsilon')d\varepsilon' \approx \sum_i n_d(\varepsilon_i)w \tag{5.10}$$

$$E_d(\varepsilon) = \int_{-\infty}^{\varepsilon} \varepsilon' n_d(\varepsilon')d\varepsilon' \approx \sum_i \varepsilon_i n_d(\varepsilon_i)w \tag{5.11}$$

, where w is the step width of the numerical integration, and ε_i is the local electronic energy, which is equal to negative value of the binding energy of valence band electrons. The Eq. (5.10) is known as the integrated-density-of-states, and the Eq. (5.11) is known as the moment of the d-band. These two equations together have been used to calculate the center of the d-band by integrating over the whole d-band within the scheme of Hammer-Nørskov d-band model. This calculation approach is in agreement with the local density approximation (LDA) in DFT framework.

By using this approach, we have assumed that the UPS spectra approximately resemble the nature of electronic distribution in their corresponding valence bands, which should be valid in our case. This methodology should be more accurate than finite-difference approximation in calculating electronic chemical potential and chemical hardness for bulk transition metals. In spite of the UPS spectra being measured from thin film samples, thermodynamically, those thin film samples should still be considered as bulk metals, as compared with molecules or nanoclusters. In addition, we must be careful when computing E vs. N curves for HSAB consideration, since not all of the electrons in Ag valence 4d-bands would contribute to the hybridization process in forming covalent bonding with soft acids molecular orbitals. As a result, the authors have chosen the primary Ag valence 4d-bands to construct the E vs. N curves due to fact that those electrons are at higher energy states (lower binding energy) and most likely to participate in the acid–base reactions, i.e., hybridizing with LUMOs of molecules of sulfur element containing gases to form covalent bonds.

As shown in Fig. 5.6, the total electronic energy vs. total number of electrons in 4d-bands, E vs. N, curves of thin film samples were computed and plotted, using the methodology described above, and the calculated HSAB quantifiable parameters, i.e., absolute electronegativity, chemical hardness, and chemical softness, were listed in Table 5.4. In Fig. 5.6, the energies are all negative with zero energy high up on top, and numerical integration values for total number of electrons are the same for all curves. Since the numerical integration values of total number of electrons and total electronic energy are correlated, the averaged slopes and curvatures of curves are invariants to the normalization constant, which has guaranteed the resulting HSAB quantifiable parameters are exact as defined in Eq. (5.2) and Eq. (5.3). First of all, as listed in Table 5.4, all of the resulting chemical hardness have small but non-zero positive values, which demonstrates that the results are in

consistent with earlier non-zero estimation of chemical hardness for bulk metals [59]. The chemical hardness values are larger than previous results due to the fact that the authors discarded s-band electrons and considered d-band electrons only in UPS data post-possessing. Secondly, as depicted in Fig. 5.6, the change of E vs. N curves from pure Ag to (Ag)-5In is negligible small, so the difference in terms of electro-negativity is only 0.02 and calculated chemical hardness and softness of (Ag)-5In remain as the same values of pure Ag, which indicates that dilute concentration of indium element solutes would not significantly alter the original valence band electronic structure of silver, nor the thermodynamic properties. In contrast, the trend of increasing electronegativity and chemical hardness with the increase of indium concentration is prominent for heavily doped silver-indium solid solutions, (Ag)-9.5In and (Ag)-19In. Significantly, there is a tremendous increase in terms of absolute electronegativity and chemical hardness for Ag_9In_4 IMC, so that one would expect a fundamental change of its thermodynamic and chemical property. In the following session, the authors would demonstrate that the correlation between the HSAB parameters and anti-tarnishing property in silver-indium binary system.

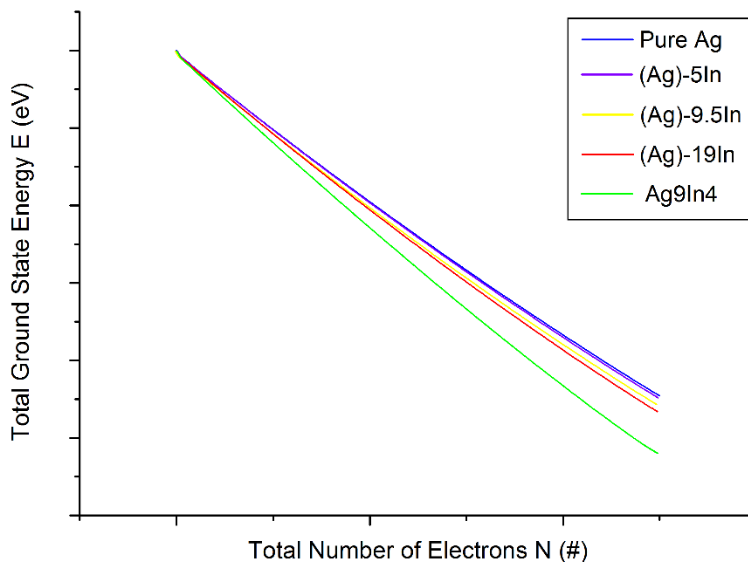

Fig. 5.6 The plot of total ground state energy vs. total number of electrons curves in 4d-bands of Ag-In thin film samples.

	χ_M (eV)	η (eV)	σ (eV^{-1})
Pure Ag	5.03	0.24	4.1
(Ag)-5In	5.05	0.24	4.1
(Ag)-9.5In	5.21	0.26	3.8
(Ag)-19In	5.33	0.27	3.6
Ag_9In_4	6.00	0.32	3.1
S_2	5.51	3.85	0.26
H_2S	4.20	6.20	0.16
O_2	6.30	5.90	0.17

Table 5.4 A summary of absolute electronegativity, chemical hardness, and chemical softness of Ag-In thin film samples and molecular gases.

5.5 Anti-Tarnishing Mechanism

In literature [49], absolute electronegativity and chemical hardness of S_2, H_2S, and O_2 molecular gases were calculated by using finite-difference approximation, and were also listed in Table 5.4. We can immediately make several qualitative theoretical predictions by making comparisons with our calculated values of absolute electronegativity. First of all, oxygen molecule can oxidize all thin film samples since its absolute electronegativity is higher, and this has been experimentally proved by our previous GIXRD and XPS experimental results. Secondly, the absolute electronegativity of hydrogen sulfide molecule is lower than that of pure Ag, so it predicts that H_2S molecular gases cannot spontaneously react with pure Ag or Ag-In alloy alone. This is also an experimental fact which has been demonstrated in early days by several chemists [62], showing that H2S gases will not tarnish Ag without the help of moisture and oxidizing agents. Importantly, the authors have noticed that the value of absolute electronegativity of S_2 molecules sits between that of (Ag)-19In and Ag_9In_4 IMC, so it predicts that sulfur gases can still slightly tarnish Ag-In solid solutions, but will not tarnish Ag_9In_4 IMC at all. By plugging values in Table 5.4 into Eq. (5.5), the calculated result of ΔN for Ag_9In_4 should be larger in magnitude than that of (Ag)-19In, but it has a negative value. The negative value of ΔN implies that the charge transfer would flow reversely, namely, from HOMOs of sulfur molecules to Ag 4d-band of Ag_9In_4. However, the Ag 4d-band has been already completely filled, therefore, the

electrons in sulfur element or molecules cannot flow into 4d-band in order to form stable covalent bonds. This implies that the roles of Lewis acid and Lewis base in the reaction between S molecules and Ag-In alloy cannot interchange in order to form stable acid–base complex. Therefore, the authors considered that the reaction rate between Ag_9In_4 IMC and S molecules would be zero. Note that above arguments should be only valid for noble metals with full-filled d-bands. The authors were curious about whether this theoretical prediction was correct or not, so we had conducted a separated tarnishing experiment to confirm, using Ag_9In_4 thin film sample and exactly the same experimental setup and parameters with 60 mins duration as described in our previous paper [30]. Under such serve tarnishing environment, pure Ag would definitely grow a thick black layer of Ag_2S and Ag-In solid solutions would be blacken slightly on the surface. It turns out that the prediction is astonishing accurate, i.e., Ag_9In_4 thin film sample is completely anti-tarnishing, showing exactly the same shining silvery mirror surface as before the tarnishing experiment. All of above experimental facts are highly in agreement with our theoretical predictions. Therefore, the authors have been fully convinced that our methodology in calculating absolute electronegativity and chemical hardness for bulk metals is accurate and consistent with the scale of previous calculated HSAB parameters.

In previous study, the authors had reported that the tarnishing rates of (Ag)-9.5In and (Ag)-19In were 3.5 times and 22.8 times, respectively, slower than that of pure Ag in the reaction experiment with sulfur vapor (S_8) within a closed system. With those values of electronegativity and chemical hardness at hands, it is easy to calculate nominal total number of charge transfer, ΔN, and total energy lowering, ΔE, of chemical reactions between sulfur vapor and Ag, Ag-In solid solutions and Ag_9In_4 IMC by using Eq. (5.5) and Eq. (5.6). Note that the authors set $\chi_M - \chi_{S2}$ to zero if $\chi_M > \chi_{S2}$ so that ΔN and ΔE would be both equal to zero. The reason to justify this treatment was given above previously. As a result, the calculated values of ΔN and ΔE in reactions with S_2 molecule were listed, together with experimental reactions rates with S_8 molecule, in Table 5.5, normalized with data value of pure silver. Those calculated values exhibited highly non-linear characters from which logistic functions can be extrapolated, and they were plotted as logistic fitting curves in Fig. 5.7. As shown in Fig. 5.7 (a), tarnishing reactions rates, total number of charge transfer and total amount of energy lowering are dropping all together immensely with the increase of indium concentration. It is clear

that the trend of decrease for tarnishing reaction rates and energy lowering is highly correlated, therefore the drop of energy lowering in the process of charge transfer should be the underlying reason for the anti-tarnishing property in Ag-In binary system. The calculation results are largely in agreement with the theoretical predictions given by Hammer-Nørskov d-band model. Hammer-Nørskov d-band model essentially says that the lower is the center of the d-band (ε_d), the less reactive is the surface, which is evident from Fig. 5.5(b). Remarkably, the data points of energy lowering can be perfectly fitted into the following logistic function, shown in Eq. (5.12):

$$\Delta E(x) = \frac{100}{1 + \left(x/t\right)^{k}} + 0.11 \tag{5.12}$$

, where x is the indium concentration (at. %) of Ag-In thin film samples and t and k are both fitting constants which have the numerical values of 8.57 and 4.42 respectively.

	ΔN (%)	ΔE (%)	R (%)
Pure Ag	100	100	100
(Ag)-5In	95.8	91.8	-
(Ag)-9.5In	62.2	38.8	28.6
(Ag)-19In	37.2	3.4	4.4
Ag_9In_4	0	0	0

Table 5.5 A summary of calculated total charge transfer and energy lowering of reactions with S_2 molecule and experimental reactions rates with S_8 molecule.

As depicted in schematic diagrams, shown in Fig. 5.7, the author would like to summary and conclude the most fundamental tarnishing and anti-tarnishing mechanism in Ag-In binary system as following: As shown in Fig. 5.7 (b), when silver crystal is exposed to environment containing the sulfur vapor (S_8), the sulfur molecules (adsorbates) can be brought into intimate contact with the surface of silver (adsorbent) through the process of chemical absorption, during which original sulfur molecules might dissociate into smaller ones (S_2-S_7) or even elemental form (S). Upon the moment of the contact, a strong tendency of electron charge transfer would occur from the top of valence band of Ag solid to empty outer orbitals of sulfur element, i.e., LUMOs, which results in forming the Ag-S covalent

bonds by orbital hybridization process and in substantially lowering overall energy of the system. When $\Delta E > 0$, the forward reaction is thermodynamically favorable. The amount of energy released by the orbital hybridization process can be contributed to overcoming the energy barrier of the growth of Ag_2S, thereby facilitating breaking original chemical bonds, nucleation, atomic migration and rearrangement. Therefore, the silver can be easily tarnished by sulfur vapor and the sulfurization reaction is both energetically and kinetically favorable.

On the contrary, as shown in Fig. 5.7 (c), when silver formed a solid solution with indium solute, the valence electrons become less localized at top of valence band. The electronic valence band structures keep on changing and contracting inwards with the increase of indium solute concentration, which results in increasing its absolute electronegativity and chemical hardness. During the sulfurization reaction, the tendency of electron charge transfer from valence band to LUMOs is largely reduced and total amount of energy lowering become much smaller. The change of ΔE will affect the chemical process in terms of overcoming the energy barrier of the chemical reaction, thereby affecting the reactivity and kinetics of the sulfurization reaction. Therefore, even though the sulfurization reaction is still thermodynamic favorable, the tarnishing rates of Ag-In solid solutions are substantially suppressed due to the fact that much less energy releases from the electron charge transfer process. In other words, the tarnishing reaction become less kinetically favorable, which leads to much less tarnishing rates of Ag-In solid solutions. The prediction of the reactivity of Ag-In metal surface is essentially in agreement with Hammer-Nørskov d-band model.

Furthermore, as shown in Fig. 5.7 (d), when silver-indium has formed intermetallic as indium concentration increases, it has fundamentally changed the crystallography and thermodynamic properties. The valence electrons of IMC are much less localized at the top of valence band and the band structure are further contracted inwards, which result in its absolute electronegativity value become even higher than sulfur vapor molecules. Even though the majority atoms in Ag_9In_4 lattices are still silver, there is a very limited tendency of electron charge transfer between the LUMOs of sulfur molecules and the Ag 4d-band of Ag_9In_4, due to the resulting modified Ag valence band structure. When the $\Delta E \leq 0$, the change in terms of Gibbs free energy of the forward reaction should be greater than zero, so that the reaction cannot proceed spontaneously. Therefore, the tarnishing

reaction has become thermodynamically unfavorable, so that Ag_9In_4 IMC is completely anti-tarnishing to sulfur vapor.

Above arguments conclude the fundamental anti-tarnishing mechanism in Ag-In binary system, but we still have to keep in minds that very thin atomic layer metallic oxide exists on the surfaces of bulk metal in reality. As seen in our previous XPS results, the fact of O 1s core-level shifting towards higher binding energy indicates that metallic oxide on the surface becomes more chemically stable and the percentage of In-rich metallic oxide is also increasing with indium concentration in the bulk metal. Since indium oxide will not react with sulfur vapor, it is natural to think that the thin metallic oxide layers could also contribute to the anti-tarnishing property. However, in our previous tarnishing experiment, the silver sulfide layers grown on both pure Ag and Ag-In solid solutions exhibit linear growth characteristic, which implies that those sulfurization processes are kinetically limited only by the reaction rate at the growth sites, so it is reaction-controlled rather than diffusion-controlled. Therefore, the authors would consider that no continuous metallic oxide layer forms to act as passivation layer or diffusion barrier to shield the silver from tarnishing gases and correlate metallic oxide with anti-tarnishing mechanism at this point, or at least, it is not the determining factor for the anti-tarnishing mechanism in Ag-In binary system.

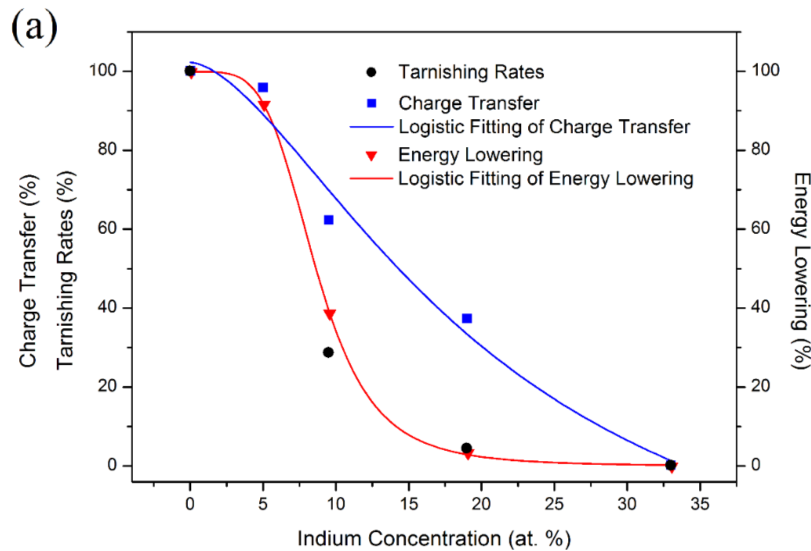

Fig. 5.7 (a) The plot of logistic fitting curves for calculated total charge transfer and energy lowering of reactions with S_2 molecule and experimental reactions rates with S_8 molecule,

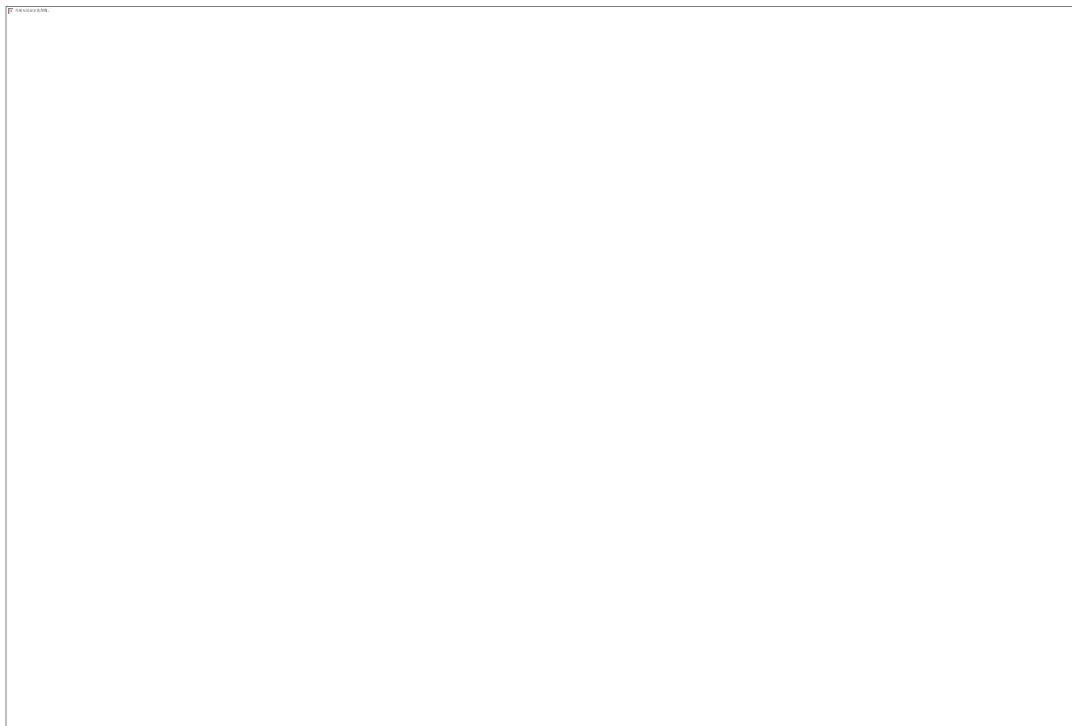

Fig. 5.7 (b) Schematic diagram of Ag tarnishing mechanism,

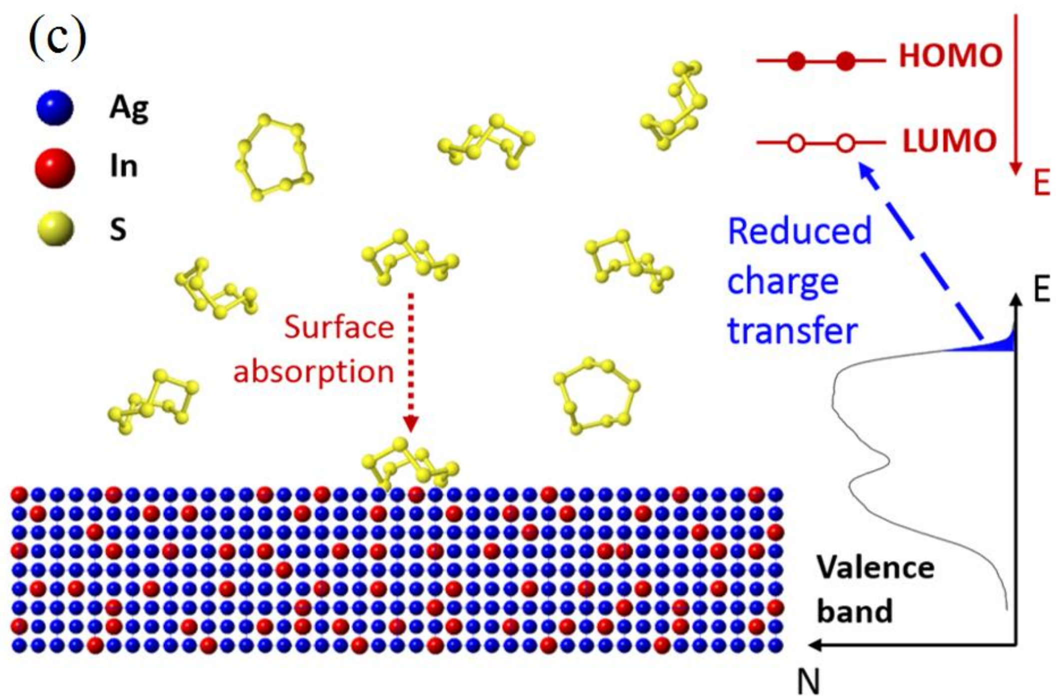

Fig. 5.7 (c) Ag-In solid solution anti-tarnishing mechanism,

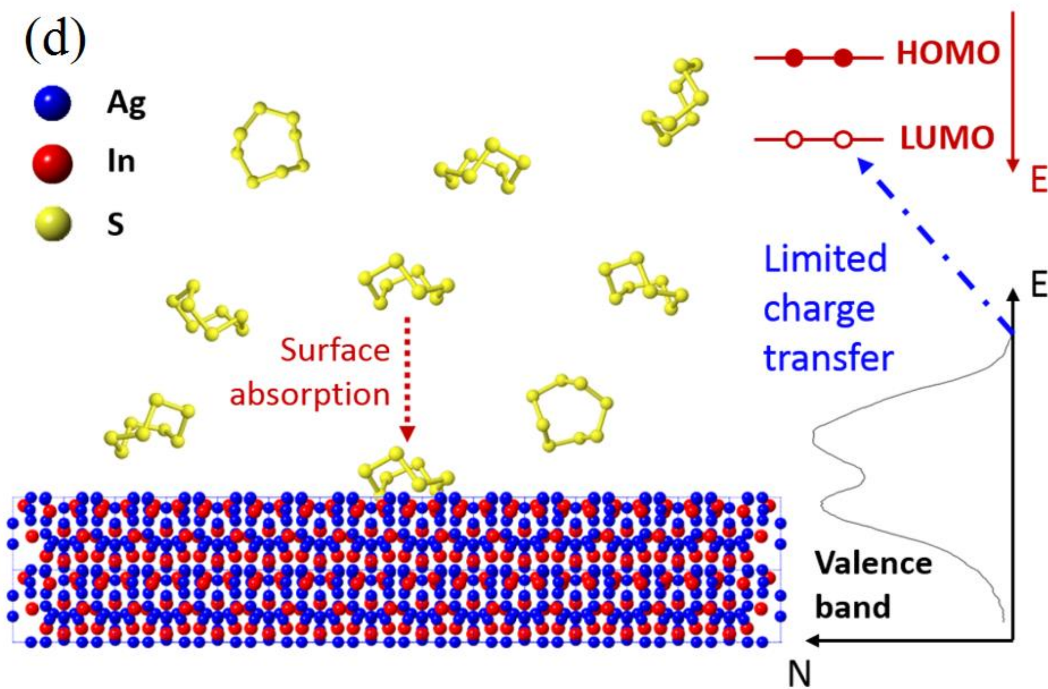

Fig. 5.7 (d) Ag_9In_4 IMC anti-tarnishing mechanism.

5.6 Concluding Remarks

In summary, the authors have systematically explored and discovered the anti-tarnishing mechanism in silver-indium binary system by fabricating and experimental characterization of thin film samples using GIXRD, XPS and UPS techniques. Importantly, the authors have introduced an alternative method to calculate the absolute electronegativity and chemical hardness for bulk metals within the framework of HSAB principle and its conceptual DFT formalization, using measured UPS spectra data of valence band structures. The results have shown that the absolute electronegativity and chemical hardness are both increasing in Ag-In binary system as the indium concentration increases, which fundamentally explain the underlying anti-tarnishing mechanism in terms of soft acid–soft base electron charge transfer and energy lowering process. The calculation results are highly in accordance with the theoretical predictions of reactivity of metal surface given by Hammer-Nørskov d-band model. Essentially, this methodology is a semi-quantum-mechanical approach which would be able to conduct theoretical thermodynamic calculations while using experimental data obtained

from metallic valence bands measurement. Therefore, it is an experimentally driven quantum-mechanical investigation, rather than computationally model driven. However, the HSAB calculation recipe proposed by the authors can be readily used for the DFT computational software calculated DOS. The authors considered that it could be further developed and generalized to apply to other metallic systems for noble and transition metals, since it largely correlated with Hammer-Nørskov d-band model. It would also have potential applications in the field of valence-band engineering [63-66] for corrosion resistant alloys design. In other words, this semi-quantum-mechanical methodology should be meaningful and valuable to the whole chemistry and materials science communities as an alternative application to HSAB principle chemical analysis in calculating, explaining, and predicting thermodynamic and reactivity behaviors for metallic materials.

In conclusion, the anti-tarnishing mechanism in silver-indium has been explored and investigated, and the understanding towards the nature of tarnishing and anti-tarnishing phenomena has been advanced. It could be one step further towards the development of ultimate remedy for silver tarnishing issues and meaningful for corrosion inhibitor design. With the scientific knowledge of anti-tarnishing mechanism, it could serve as a design guidance in principle for the practical applications of Ag-In alloy bulk or thin film materials into various fields, such as electrical and mechanical interconnections of SiC/GaN-based power electronics, GaN-based LED reflector, giant astronomical telescope array of mirrors construction and etc.

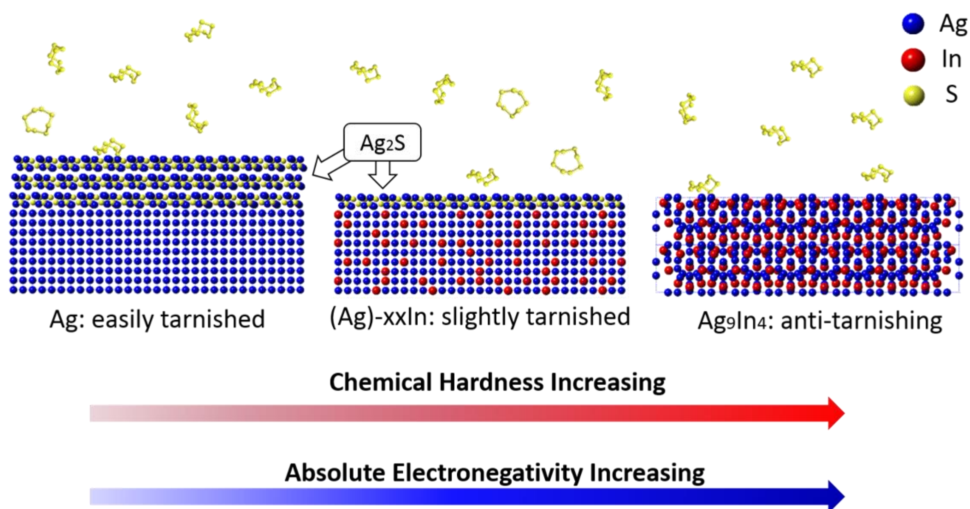

Fig. 5.8 Anti-tarnishing mechanism in Ag-In binary system from HSAB principle point of view.

Reference in Chapter 5

1. L. Ke, S. C. Lai, H. Liu, C. K. N. Peh, B. Wang, and J. H. Teng, "Ultrasmooth Silver Thin Film on PEDOT:PSS Nucleation Layer for Extended Surface Plasmon Propagation", ACS Applied Materials & Interfaces, vol. 4, No. 3, pp. 1247-1253, 2012.
2. Y. Wu, Y. Li, and B. S. Ong, "A Simple and Efficient Approach to a Printable Silver Conductor for Printed Electronics", Journal of the American Chemical Society, vol. 129, No. 7, pp. 1862-1863, 2007.
3. C. Yu, J. D. Baek, C. Su, L. Fan, J. Wei, Y. Liao, and P. Su, "Inkjet-Printed Porous Silver Thin Film as a Cathode for a Low-Temperature Solid Oxide Fuel Cell", ACS Applied Materials & Interfaces, vol. 8, No. 16, pp. 10343-10349, 2016.
4. K. Awazu, M. Fujimaki, C. Rockstuhl, J. Tominaga, H. Murakami, Y. Ohki, N. Yoshida, and T. Watanabe, "A Plasmonic Photocatalyst Consisting of Silver Nanoparticles Embedded in Titanium Dioxide", Journal of the American Chemical Society, vol. 130, No. 5, pp. 1676-1680, 2008.
5. S. Dunn, P. M. Jones, and D. E. Gallardo, "Photochemical Growth of Silver Nanoparticles on c- and c+ Domains on Lead Zirconate Titanate Thin Films", Journal of the American Chemical Society, vol. 129, No. 28, pp. 8724-8728, 2007.
6. G. V. Ramesh and T. P. Radhakrishnan, "A Universal Sensor for Mercury (Hg, HgI, HgII) Based on Silver Nanoparticle-Embedded Polymer Thin Film", ACS Applied Materials & Interfaces, vol. 3, No. 4, pp. 988–994, 2011.
7. A. Dabirian, and N. Taghavinia, "Theoretical Study of Light Trapping in Nanostructured Thin Film Solar Cells Using Wavelength-Scale Silver Particles", ACS Applied Materials & Interfaces, vol. 7, No. 27, pp. 14926–14932, 2015.
8. Y. Chen, T. Yang, H. Pan, Y. Yuan, L. Chen, M. Liu, K. Zhang, S. Zhang, P. Wu, and J. Xu, "Photoemission Mechanism of Water-Soluble Silver Nanoclusters: Ligand-to-Metal–Metal Charge Transfer vs Strong Coupling between Surface Plasmon and Emitters", Journal of the American Chemical Society, vol. 136, No. 5, pp. 1686–1689, Jan. 2014.

9. P. Peng, A. Hu, A. P. Gerlich, G. Zou, L. Liu, and Y. N. Zhou, "Joining of Silver Nanomaterials at Low Temperatures: Processes, Properties, and Applications", ACS Applied Materials & Interfaces, vol. 7, No. 23, pp. 12597–12618, 2015.
10. M. Maruyama, R. Matsubayashi, H. Iwakuro, S. Isoda, T. Komatsu, "Silver nanosintering: a lead-free alternative to soldering", Applied Physics A, vol. 93, No. 2, pp. 467-470, 2008.
11. B. T. Reagor and J. D. Sinclair, "Tarnishing of silver by sulfur vapor: film characteristics and humidity effects", Journal of the Electrochemical Society, vol. 128, No.3, pp. 701-705, 1981.
12. H. Kim, "Corrosion process of silver in environments containing 0.1 ppm H2S and 1.2 ppm NO2", Materials and Corrosion, vol. 54, No. 4, pp. 243-250, 2003.
13. X. Y. Mao, and K. S. Tian, "Tarnish mechanism of silver plating and anti-tarnish process", Electroplating and Pollution Control, vol. 15, No. 1, pp. 8-12, 1995.
14. J. D. Sinclair, "Tarnishing of silver by organic sulfur vapors: rates and film characteristics", Journal of the Electrochemical Society, vol. 129, No. 1, pp. 33-40, 1982.
15. M. H. Hebb, "Electrical conductivity of silver sulfide." The Journal of Chemical Physics, vol. 20, No. 1, pp. 185-190, 1952.
16. G. Mura, G. Cassanelli, F. Fantini, and M. Vanzi, "Sulfur-contamination of high power white LED", Microelectronics Reliability, vol. 48, No. 8, pp. 1208-1211, 2008.
17. D. Minzari, M. S. Jellesen, P. Moller, R. Ambat, "Morpholofical study of silver corrosion in highly aggressive sulfur environments", Engineering Failure Analysis, vol. 18, No. 8, pp. 2126-2136, July 2011.
18. T. E. Graedel, "Corrosion mechanisms for silver exposed to the atmosphere", Journal of the Electrochemical Society, vol. 139, No. 7, pp. 1963-1970, 1992.
19. C. J. Yang, C. H. Liang, and X. Liu, "Tarnishing of silver in environments with sulphur contamination", Anti-Corrosion Methods and Materials, vol. 54, No. 1, pp. 21-26, 2007.
20. R. R. Benham, "Silver plating", Anti-Corrosion Methods and Materials, vol. 10, No. 2, pp. 31-35, 1963.

21. R. Bond, R. P. Stanek and W. Hoffman, "Silver infrared reflective film, metal oxide dielectric film, silicon nitride protective coating; for windshields, windows", U.S. Patent, No. 5834103, issued Nov. 10, 1998.
22. L. Paussaa, L. Guzmana, E. Marina, N. Isomakib, L. Fedrizzia, "Protection of silver surfaces against tarnishing by means of alumina/titania-nanolayers", Surface and Coatings Technology, vol. 206, No. 5, pp. 976-980, 2011.
23. C. Liang, C. Yang, and N. Huang, "Tarnish protection of silver by octadecanethiol self-assembled monolayers prepared in aqueous micellar solution", Surface and Coatings Technology, vol. 203, No. 8, pp. 1034-1044, 2009.
24. J. Randin, "Chromated layer as an Anti-tarnish protection of AuAgCu alloys", Materials and Corrosion, vol. 43, No. 4, pp. 172-176, 1992.
25. J. Nielsen and J. Tuccillo, "Tarnish resistant alloy", U.S. Patent, No. 3767391, issued Oct. 23, 1973.
26. N. Sirirut and N. Ekasit, “The anti-tarnishing, microstructure analysis and mechanical properties of sterling silver with silicon addition”, Journal of Metals, Materials and Minerals, vol. 12, No. 2, pp. 13-18, 2003.
27. K. F. Edward, "Silver alloy", U.S. Patent, No. 1970319, issued Aug. 14, 1934.
28. P. Johns, "Silver ternary alloy", U.S. Patent, No. 20070009375 A1, issued Jan. 11, 2007.
29. D. Davitz. "Alloy for jewelry with zinc, copper and silicon", U.S. Patent, No. 5882441, issued Mar. 16, 1999.
30. Y. Huo, S. W. Fu, Y. L. Chen, C. C. Lee, “A reaction study of sulfur vapor with silver and silver-indium solid solution as a tarnishing test method”, Journal of Materials Science: Materials in Electronics, vol. 27, No. 10, pp. 10382-10392, Oct. 2016.
31. Y. Huo and C. C. Lee, “The growth and stress vs. strain characterization of the silver solid solution phase with indium”, Journal of Alloys and Compounds, vol. 661, pp. 372-379, March 2016.
32. W. Hume-Rothery, G. F. Lewin, and P. W. Reynolds, "The lattice spacings of certain primary solid solutions in silver and copper”, Proceedings of the Royal Society of London. Series A, Mathematical and Physical Sciences, vol. 157.890, pp. 0167-0183, Oct. 1936.

33. S. Doniach and M. Sunjic, “Many-electron singularity in X-ray photoemission and X-ray line spectra from metals”, Journal of Physics C: Solid State Physics, vol. 3, No. 2, pp. 285-291, 1970.
34. A. Barrie and N. E. Christensen, “High-resolution x-ray photoemission spectra of silver”, Physical Review B, vol. 14, No. 6, pp. 2442-2447, Sept. 1976.
35. I. A. Abrikosov, W. Olovsson, and B. Johansson, “Valence-band hybridization and core level shifts in random Ag-Pd alloys”, Physical Review Letters, vol. 87, No. 17, pp. 176403-1-4, Oct. 2001.
36. B. Johansson and N. Martensson, “Core-level binding-energy shifts for the metallic elements”, Physical Review B, vol. 21, No. 10, pp. 4427- 4457, May 1980.
37. P. Steiner and S. Hufner, “Thermochemical data of alloys from photoelectron spectroscopy”, Acta Metallurgica, vol. 29, No. 11, pp. 1885 – 1898, 1981.
38. A. Rosengren and B. Johansson, “Surface heat of segregation from surface core-level binding-energy shifts”, Physical Review B, vol. 23, No. 8, pp. 3852- 3858, April 1981.
39. U. Gelius, “Binding Energies and Chemical Shifts in ESCA”, Physica Scripta, vol. 9, No. 3, pp. 133-147, 1974.
40. A. I. Boronin, S. V. Koscheev, G. M. Zhidomirov, “XPS and UPS study of oxygen states on silver”, Journal of Electron Spectroscopy and Related Phenomena, vol. 96, No. 1-3, pp. 43-51, 1998.
41. C. Donley, D. Dunphy, D. Paine, C. Carter, K. Nebesny, P. Lee, D. Alloway, and N. R. Armstrong, “Characterization of Indium-Tin Oxide Interfaces Using X-ray Photoelectron Spectroscopy and Redox Processes of a Chemisorbed Probe Molecule: Effect of Surface Pretreatment Conditions”, Langmuir, vol. 18, pp. 450-457, 2002.
42. C. S. Fadley and D. A. Shirley, “Electronic Densities of States from X-Ray Photoelectron Spectroscopy”, Journal of Research of the Natianal Bureau of Standards, vol. 74A, No.4, 1970.
43. M. Trzcinskia, A. Bukaluka, M. Bürgenerb, and A. Goldmannb, “Alloy formation of ultrathin indium and silver layers on W (1 1 0): A photoemission study”, Surface Science, vol. 589, No. 1-3, pp. 192-200, Sep. 2005.
44. J.D. Riley, R. C. G. Leckey, J. G. Jenkin, J. Liesegang, and R. T. Poole, “Ultraviolet photoelectron spectra of the outer d bands of Ag-In and Ag-Cd alloys”, Journal of Physics F: Metal Physics, vol. 6, No. 2, pp. 293-301, 1976.

45. G Panaccione, G. Cautero, M. Cautero, A. Fondacaro, M. Grioni, P. Lacovig, G. Monaco, F. Offi, G. Paolicelli, M. Sacchi, N. Stojic, G. Stefani, R. Tommasini and P. Torelli, "High-energy photoemission in silver: resolving d and sp contributions in valence band spectra", Journal of Physics: Condensed Matter, vol. 17, No. 17, pp. 2671-2679, April 2005.

46. B. Hammer and J. K. Nørskov, "Theoretical surface science and catalysis—calculations and concepts", Advances in Catalysis, vol. 45, pp. 71-129, 2000.

47. B. Hammer, "Special Sites at Noble and Late Transition Metal Catalysts *Topics*", Topics in Catalysis, vol. 37, No. 1, pp. 3-16, 2006.

48. R.G. Pearson, "Hard and Soft Acids and Bases", Journal of the American Chemical Society, vol. 85, No. 22, pp. 3533-3539, Nov. 1963.

49. R.G. Pearson, "Absolute Electronegativity and Hardness: Application to Inorganic Chemistry", Inorganic Chemistry, vol. 27, No. 4, pp. 734-740, Feb. 1988.

50. T. Ho, "The Hard Soft Acids Bases (HSAB) Principle and Organic Chemistry", Chemical Reviews, vol. 75, No. 1, Feb. 1975.

51. R. G. Pearson, "Hard and soft acids and bases, HSAB, part II: Underlying theories", Journal of Chemical Education", vol. 45, No. 10, pp. 643-648, 1968.

52. J. Chatt and L. M. Venanzi, "Olefin Complexes of Rhodium", Nature, vo. 177, No. 4514, pp. 852-853, May 1955.

53. R. S. Mulliken, "Structures of the Halogen Molecules and the Strength of Single Bonds", Journal of the American Chemical Society, vol. 77, No. 4, pp. 884-887, 1955.

54. R. G. Parr and R. G. Pearson, "Absolute Hardness: Companion Parameter to Absolute Electronegativity", Journal of the American Chemical Society, vol. 105, No. 26, pp. 7512-7516, Dec. 1983.

55. W. Kohn, A. D. Becke, and R. G. Parr, "Density Functional Theory of Electronic Structure", Journal of Physical Chemistry, vol. 100, No. 31, pp. 12974-12980, Aug. 1996.

56. R. G. Parr, R. A. Donnelly, M. Levy and W. E. Palke, "Electronegativity: The density functional viewpoint", The Journal of Chemical Physics, vol. 68, No. 8, pp. 3801-3807, 1978.

57. M. H. Cohen and A. Wasserman," On the Foundations of Chemical Reactivity Theory", The Journal of Physical Chemistry A, vol. 111, No. 11, pp. 2229-2242, 2007.
58. J. P. Perdew, R. G. Parr, M. Levy and J. L. Balduz, "Density-functional theory for fractional particle number: derivative discontinuities of the energy", Physical Review Letters, vol. 49, No. 23, pp. 1691-1694, 1982.
59. W. Yang and R. G. Parr, "Hardness, softness, and the fukui function in the electronic theory of metals and catalysis", Proceedings of the National Academy of Sciences, vol. 82, No. 20, pp. 6723-6726, 1985.
60. L. Lee, "Relevance of the density-functional theory to acid-base interactions and adhesion in solids", Journal of Adhesion Science and Technology, vol. 5, No. 1, pp. 71-92, 1991.
61. A. Kokalj, "On the HSAB based estimate of charge transfer between adsorbates and metal surfaces", Chemical Physics, vol. 393, No. 1, pp. 1-12, 2012.
62. S. Lilienfeld and C. E. White, "A study of the reaction between hydrogen sulfide and silver", Journal of the American Chemical Society, vol. 52, No. 3, pp. 885-892, 1930.
63. L. Zhao, J. He, S. Hao, C. Wu, T. P. Hogan, C. Wolverton, V. P. Dravid, and M.G. Kanatzidis, "Raising the Thermoelectric Performance of p-Type PbS with Endotaxial Nanostructuring and Valence-Band Offset Engineering Using CdS and ZnS", Journal of the American Chemical Society, vol. 134, No. 39, pp. 16328-16336, 2012.
64. G. Tan, L. Zhao, F. Shi, J. W. Doak, S. Lo, H. Sun, C. Wolverton, V. P. Dravid, C. Uher, and M. G. Kanatzidis, "High Thermoelectric Performance of p-Type SnTe via a Synergistic Band Engineering and Nanostructuring Approach", Journal of the American Chemical Society, vol. 136, No. 19, pp. 7006-7017, 2014.
65. G. Tan, F. Shi, S. Hao, H. Chi, T. P. Bailey, L. Zhao, C. Uher, C. Wolverton, V. P. Dravid, and M. G. Kanatzidis, "Valence Band Modification and High Thermoelectric Performance in SnTe Heavily Alloyed with MnTe", Journal of the American Chemical Society, vol. 137, No. 35, pp. 11507-11516, 2015.

66. A. Banik, U. S. Shenoy, S. Saha, U. V. Waghmare, and K. Biswas, “High Power Factor and Enhanced Thermoelectric Performance of SnTe-AgInTe2: Synergistic Effect of Resonance Level and Valence Band Convergence”, Journal of the American Chemical Society, vol. 138, No. 39, pp. 13068–13075, 2016.

Chapter 6

Solid Solution Softening Phenomenon in Ag-based Solid Solutions

6.1 Introduction

In early days of metallurgical science, silver solid solutions with various solute elements were the subjects of research study to learn their material properties, such as the lattice constants [1] and elastic constants [2]. Solid solution strengthening or hardening is a well-known mechanism to explain the increase of yield strength and hardness of alloys due to the interactions between dislocations and solute atoms. Generally speaking, the types of interactions can be qualitatively classified into the following categories: elastic interaction, modulus interaction, stacking-fault interaction, electrical interaction, short-range order (SRO) and long-range order (LRO) interaction [3]. In literature [4-6], some scholars have been trying to establish theoretical models and quantitative parameters, such as solute size misfit [6], change of the shear modulus (η), stacking fault energy (γ) and stacking fault density (α), to get a better picture of the nature of silver and face centered cubic (FCC) dilute solid solution mechanical behaviors. However, the results of those attempts were rather ambiguous and disappointing since the theoretical predictions were often inconsistent with each other or contradicted to experimental facts. Therefore, the underlying mechanism of silver solid solution mechanical behavior is rather complicated and hard to apply to quantitative interpretation, even though it has relatively simple crystal structure. On the other hand, presumably due to the fact that silver and its alloys were not major metallic materials for structural engineering applications, the fundamental research and study on the mechanical properties of silver-based alloys was rather rare and limited. With the fast development of integrated circuit (IC) industries, electronic manufacturing and packaging activities have already grown into a global market of hundreds of billions of dollars per year. Recently, silver-based alloys have been considered as an alternative of interconnection materials in various applications, such as die-attachment pads [7, 8] and bonding wires [9, 10], for electronic and photonic products. Therefore, the fundamental study of mechanical properties, especially plasticity, of silver-based alloys would be very meaningful to the

real industrial applications since it is largely correlated with manufacturability of silver-based alloy products and long term mechanical reliability of whole electronic systems which contain silver-based alloys.

In the previous chapter, our research group has studied and reported the stress vs. strain characterization of silver-indium (Ag-In) solid solutions [11] and silver-zinc (Ag-Zn) solid solutions [12] at various solute compositions, obtained from tensile test under static tension. The author discovered that both Ag-In and Ag-Zn solid solutions exhibited excellent mechanical properties. Importantly, (Ag)-9.5In (alloying with 9.5 at. % of In) and (Ag)-15Zn (alloying with 15 at. % of Zn) both show abnormal mechanical material behavior versus the classic solid solution strengthening theory because the yield strength of solid solutions decreases compared to that of pure Ag. Similar phenomenon had also been reported in other metallic systems [13], which was known as solid solution softening. The property of lower yield strength is very desirable in applications associated with solid-state bonding in electronics manufacturing, since it allows the bonded structures to curtail the stresses induced by coefficient of thermal expansion (CTE) mismatch with easier plastic deformation, thereby preventing electronic devices from cracking and mechanical failure [14]. With more than two-decade research experience on bonding technology in our group, the authors consider the combination of low yield strength, large elongation, and high UTS as an ideal case in terms of material mechanical properties for electronic joining applications. In this chapter, the author would like to further investigate on phenomenological nature of mechanical behaviors of Ag-based solid solutions by studying the stress vs. strain curves of silver-aluminum (Ag-Al), silver-gallium (Ag-Ga), and silver-tin (Ag-Sn).

In the following sessions, the author will first briefly report the growth and characterization for Ag-Al, Ag-Ga, and Ag-Sn solid solutions with X-ray diffraction (XRD) and scanning electron microscope/energy dispersive X-ray spectroscopy (SEM/EDX). Next, tensile test sample preparation and experimental setting are described. Representative stress vs. strain curves and various mechanical properties for Ag-Al, Ag-Ga, and Ag-Sn solid solutions are presented. Furthermore, the fractography of samples tested is evaluated under SEM with analysis and discussions. Finally, a

generalized summary of mechanical behaviors of Ag-based solid solutions are given, followed with comments and suggestion on potential utility in electronic industries.

6.2 Material Preparation and Characterization

Initially, the author discovered the solid solution softening phenomenon in Ag-In binary system. A question was raised naturally: does this solid solution softening mechanism exist only in Ag-In binary system or in other Ag-based solid solutions as well? Since our research starting point is Ag solid solution phase with In solute, the authors decided to choose common metallic elements in the IIIA column of periodic table, same as In, namely, Al and Ga, as potential candidates of solute elements. In addition, Sn was chosen as it is the next element after In. Cadmium (Cd), the element before In, was seriously considered but not chosen because it is one of the banned elements by Restriction of Hazardous Substances (RoHS) in electronic products utility.

It is constructive to review Ag-Al, Ag-Ga, and Ag-Sn binary phase diagrams before preparing each single phase Ag solid solutions in these three systems. According to Ag-Al, Ag-Ga, and Ag-Sn binary phase diagrams [15-17], as shown in Fig. 6.1, the maximum solubility of Al, Ga and Sn elements in silver crystal lattice at room temperature are about 10 at. % (2.6 wt. %), 10 at. % (6.6 wt. %), and 8 at. % (8.7 wt. %), respectively. In literature [13], the solid solution softening usually occurs in solid solutions with high concentration of solute element, which is exactly true in Ag-In binary system. Therefore, the authors decided to grow Ag-Al and Ag-Ga solid solution ingots with solute concentration near 10 at. %, and Ag-Sn solid solution ingots with solute concentration near 8 at. %, using the vacuum casting method that was described in our previous paper [11], which are nominally designated as (Ag)-10Al, (Ag)-10Ga, and (Ag)-8Sn in this paper, respectively. Raw materials with 99.99% purity of Ag shots together with Al, Ga, Sn shots, respectively, were weighed, uniformly mixed and loaded in quartz tubes with one end closed. There is no special treatment performed before loading the raw materials. While the quartz tube is being pumped by a vacuum pump, the other end of the tube is sealed by hydrogen-oxygen torch operation to form a capsule. The vacuum environment is essential for the casting production to reduce material oxidation, the number of voids,

and common defects created by trapped air bubbles. It is worthwhile to mention that aluminum reacts with inner side of quartz tube during the occurrence of molten materials, resulting in formation of a small amount of aluminum silicate on the surface of ingots. Therefore, the ratio of initial raw element materials for growing (Ag)-10Al ingots was carefully adjusted to compensate of Al loss in that reaction. Next, the capsules were placed into a furnace preheated at 1030 ℃ and stayed there for 30 minutes. The temperature of the furnace was then reduced gradually to room temperature in 7 days in order to obtain the homogenized single phase Ag-Al, Ag-Ga, and Ag-Sn solid solutions at designed compositions. After successful production of (Ag)-10Al, (Ag)-10Ga, and (Ag)-8Sn ingots, they were cut into disk samples using slow speed diamond saw and polished by the sequence of 120/240/800/1200 grits of silicon carbide abrasive papers for further chemical composition examinations and crystal structure evaluations.

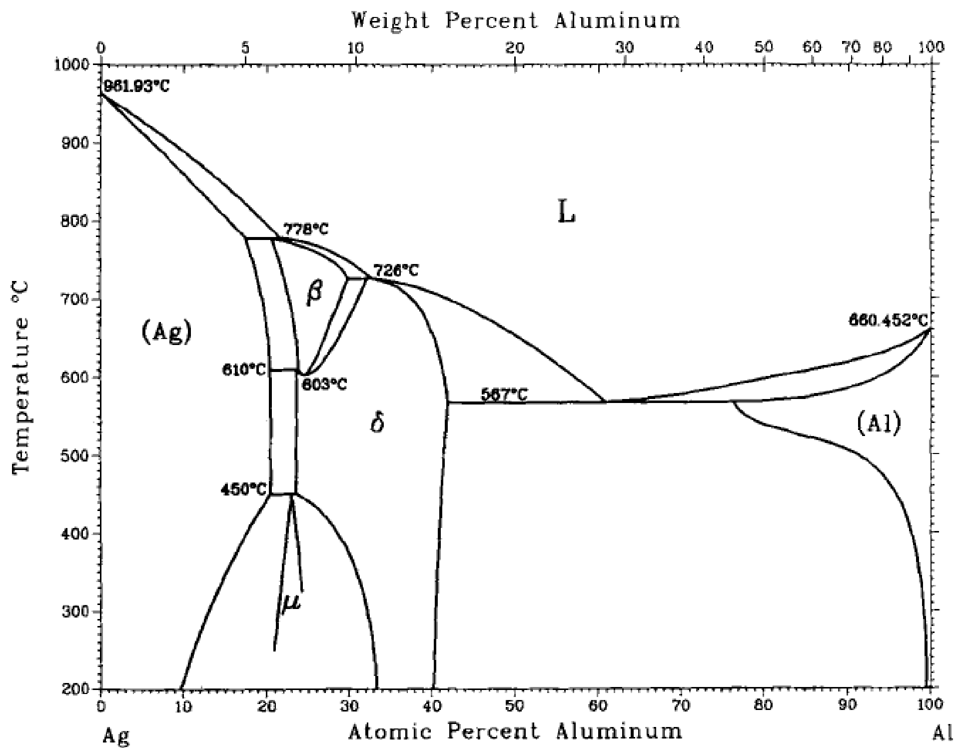

Fig 6.1 (a) Silver-Aluminum binary phase diagram,

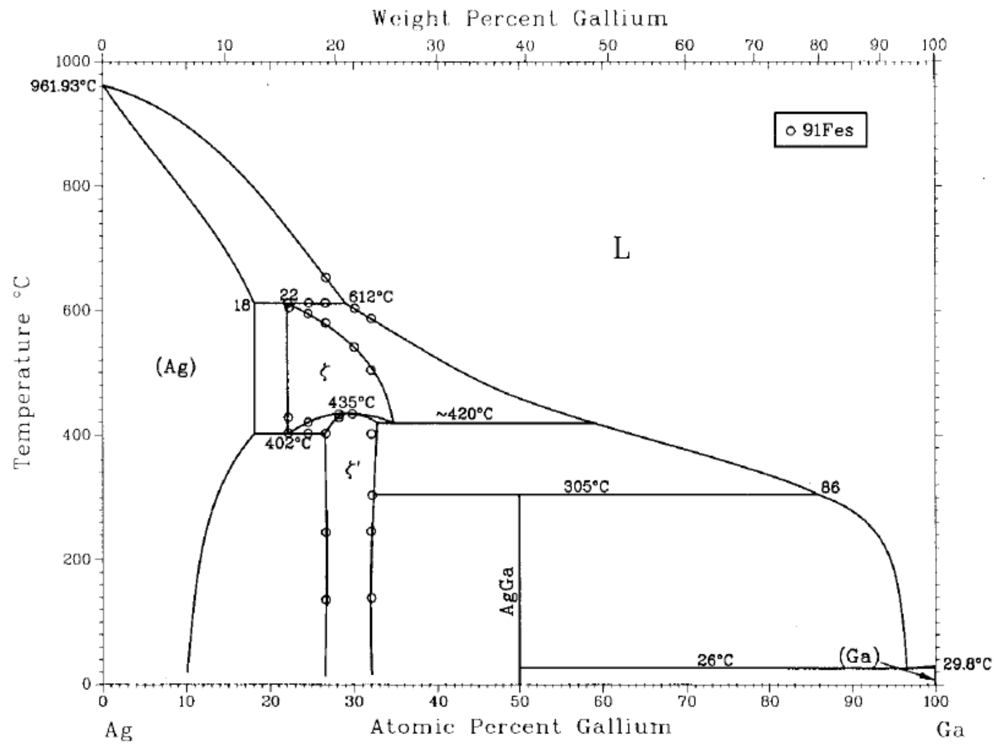

Fig 6.1 (b) Silver-Gallium binary phase diagram,

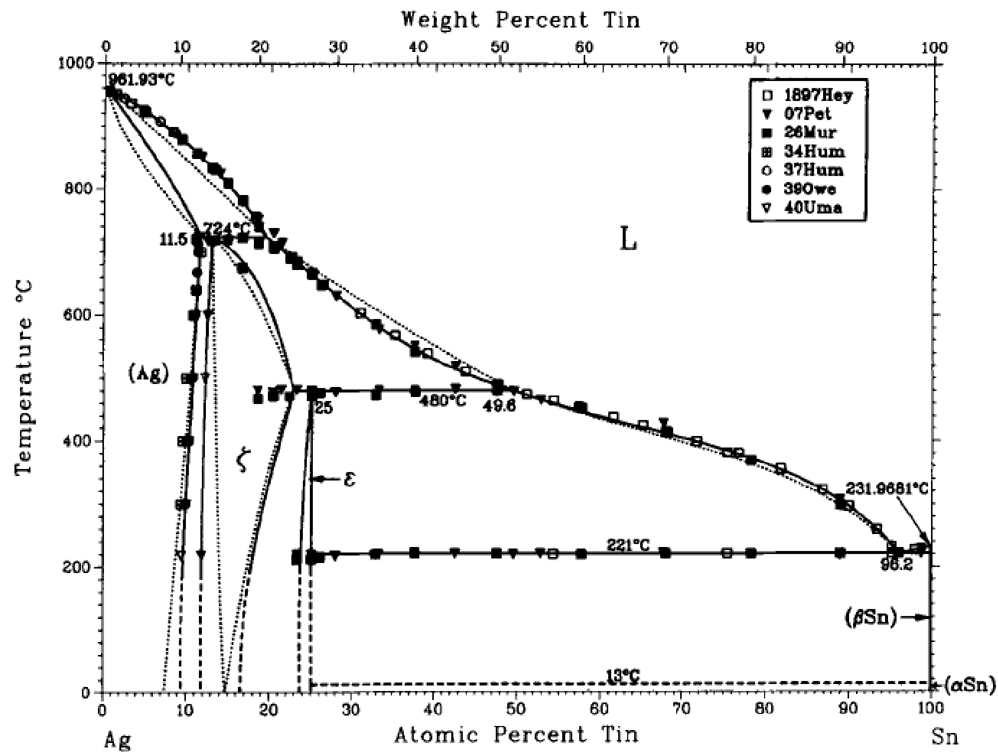

Fig. 6.1 (c) Silver-Tin binary phase diagram.

XRD and SEM/EDX were used in a combination to identify the phases and chemical compositions of the grown ingots. Rigaku SmartLab X-ray diffractometer in Irvine Material Research Institute (IMRI) was used for phase identification, using Bragg-Brentano (BB) operation mode with θ-θ diffractometer setting. Bragg-Brentano optics setting was chosen since the disk samples from ingots were bulk polycrystalline materials. The XRD is performed from 30 ° to 90 ° at scanning speed of 2 °/min with scanning step width of 0.02 °, using collimated Cu K_{α} line excitation X-ray source, with a filter removing Cu K_{β} line. After XRD measurement, the collected data were analyzed by PDXL, an integrated powder X-ray analysis software package, and compared with The International Centre for Diffraction Data (ICDD) standard card. As results, the crystallography information of (Ag)-10Al, (Ag)-10Ga and (Ag)-8Sn disk samples was listed and summarized in Table 6.1, and their XRD patterns were plotted in Fig. 6.2 respectively. As shown Fig. 6.2, it is very clear that (Ag)-10Al, (Ag)-10Ga and (Ag)-8Sn resemble the crystal structure of pure silver, FCC structure, for their typical systematically peaks absence. In addition, there are no peaks other than the peaks of (Ag)-10Al, (Ag)-10Ga and (Ag)-8Sn in each XRD patterns. Therefore, it can be safely concluded that the materials in the disk samples are single phase, nearly homogeneous and polycrystalline. In Table 6.1, (h, k, l) is the Miller's indices with classic denotation, d is the d-spacing value for corresponding crystal plane, and a is the calculated lattice constant by using the values of each d-spacing. The weighted average values for lattice constants are 4.084 Å, 4.088 Å and 4.129 Å for (Ag)-10Al, (Ag)-10Ga and (Ag)-8Sn, respectively. For the reference, the lattice constant of pure Ag has the value of 4.094 Å, using the similar ingot growth method. Therefore, as shown in Fig. 6.2, the XRD patterns of (Ag)-10Al and (Ag)-10Ga have shifted towards right as compared to that of pure Ag, which means that replacing Ag atoms with Al and Ga solutes will result in dent in its original crystal lattice. On the other hand, the XRD pattern of (Ag)-8Sn has shifted towards left, showing the substitution of Ag atoms with Sn solute will bulge its original crystal lattice. These two types of distortion of crystal structure were referred as solute size misfit, which would affect the distribution of Peierls potential [18], i.e., the self-energy of the dislocation changes periodically as the dislocation glides along its slip plane, thereby possibly further altering the mechanical properties and plastic deformation curves.

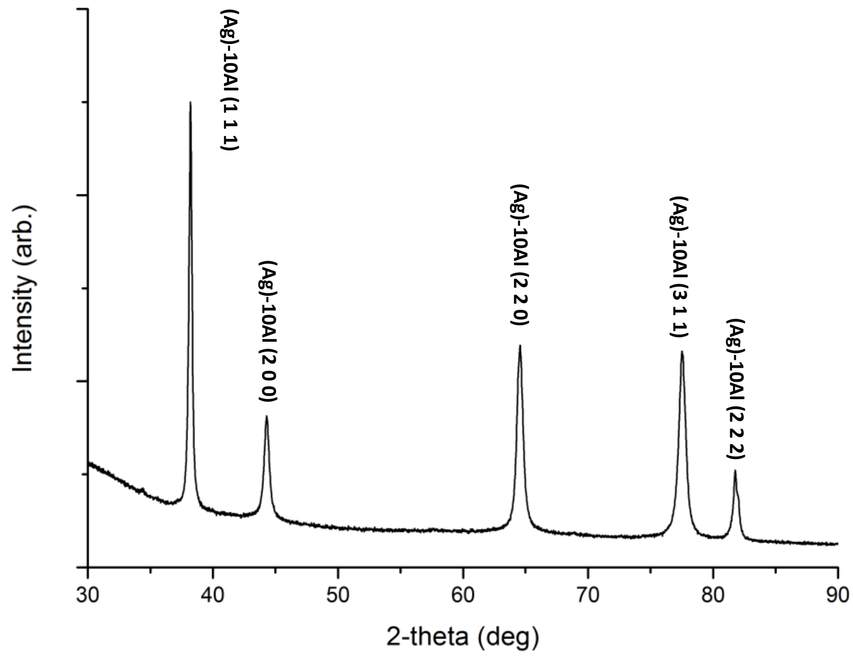

Fig. 6.2 (a) XRD pattern of (Ag)-10Al solid solution disk sample,

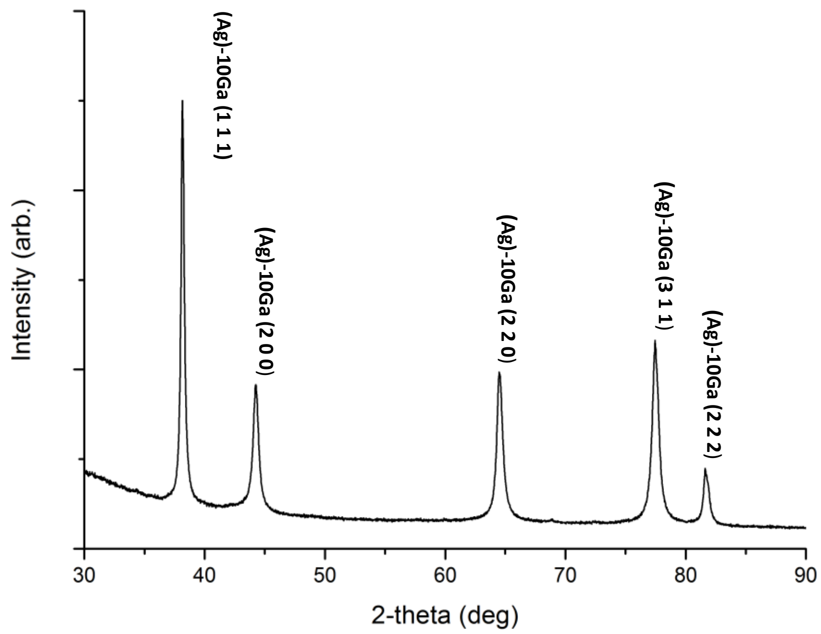

Fig. 6.2 (b) XRD pattern of (Ag)-10Ga solid solution disk sample,

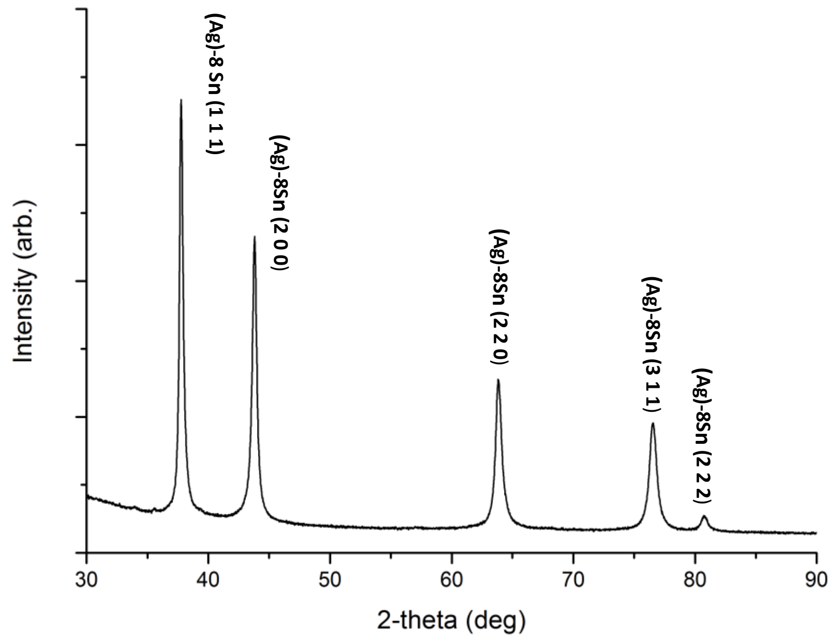

Fig. 6.2 (c) XRD pattern of (Ag)-8Sn solid solution disk sample.

Peaks #	2θ (deg)	**d** (Å)	(h, k, l)	**a** (Å)
1	38.206	2.356	(1 1 1)	4.080
2	44.267	2.045	(2 0 0)	4.090
3	64.499	1.445	(2 2 0)	4.086
4	77.513	1.231	(3 1 1)	4.084
5	81.770	1.178	(2 2 2)	4.080

Table 6.1 (a) A summary of XRD measurement data of (Ag)-10Al solid solution disk sample,

Peaks #	2θ (deg)	**d** (Å)	(h, k, l)	**a** (Å)
1	38.132	2.360	(1 1 1)	4.088
2	44.253	2.046	(2 0 0)	4.092
3	64.486	1.445	(2 2 0)	4.087
4	77.418	1.233	(3 1 1)	4.088
5	81.598	1.179	(2 2 2)	4.087

Table 6.1 (b) A summary of XRD measurement data of (Ag)-10Ga solid solution disk sample,

Peaks #	2θ (deg)	**d** (Å)	(h, k, l)	**a** (Å)
1	37.735	2.384	(1 1 1)	4.129
2	43.784	2.068	(2 0 0)	4.135
3	63.816	1.458	(2 2 0)	4.126
4	76.474	1.246	(3 1 1)	4.131
5	80.701	1.191	(2 2 2)	4.125

Table 6.1 (c) A summary of XRD measurement data of (Ag)-8Sn solid solution disk sample.

After confirmation of the phase of the disk samples, their chemical compositions were further examined with SEM/EDX with FEI XL-30 FEG SEM in IMRI. Multiple local areas of the disk samples were randomly chosen to be examined by SEM/EDX. EDX spectrum mapping mode was used with ZAF correction method at 20 kV e-beam voltage and 33.7 °take-off angle. The quantification results of SEM/EDX spectrum mapping were summarized in Table 6.2 with the information of average concentration and machine error. As shown in Table 6.2, the average chemical compositions of (Ag)-10Al, (Ag)-10Ga and (Ag)-8Sn were very close to the nominal compositions with very small systematic machine errors caused by the uncertainty of the SEM/EDX detector. Therefore, it can be safely concluded that the grown ingots of (Ag)-10Al, (Ag)-10Ga and (Ag)-8Sn were single phase, polycrystalline, and nearly homogeneous at the designed solute concentrations, as supported by XRD and SEM/EDX experimental results, thereby, proving that the initial nominal designations were indeed valid.

	(Ag)-10Al		(Ag)-10Ga		(Ag)-8Sn	
	Ag (at. %)	Al (at. %)	Ag (at. %)	Ga (at. %)	Ag (at. %)	Sn (at. %)
Average concentration	90.3	9.7	90.1	9.9	91.7	8.3
Machine error	0.40	0.10	0.30	0.10	0.30	0.10

Table 6.2. SEM/EDX spectrum mapping quantification results of chemical compositions for (Ag)-10Al, (Ag)-10Ga and (Ag)-8Sn disk samples.

6.3 Tensile Test

After obtaining nearly homogeneous ingots of (Ag)-10Al, (Ag)-10Ga and (Ag)-8Sn, tensile test samples, conforming with American Society for Testing and Materials (ASTM) standard E8/ E8M- 08 [19], were produced using electrical discharge machining (EDM) by an EDM outsource company. In Fig. 6.3 and Table 6.3, the geometry and dimensions of the tensile test sample are shown, respectively. EDM process can change the surface properties of the workpiece, causing the issues such as recasting, heat affected zone (HAZ) grain size enlargement. Therefore, all resulting tensile test samples were polished using silicon carbide abrasive papers with 800 grits to remove the HAZ layer. Next, the tensile test samples were put into an oven and annealed at 200°C for an hour to release the residue internal stresses induced by the polishing process. After the preparation, all tensile test samples were examined using XRD approach mentioned previously with the same setting. By comparing the XRD patterns with previous results, the authors can confirm that the tensile test samples have the same compositions as the previous disk samples used in XRD and SEM/EDX analysis.

The tensile test was performed using Instron model 5500R tensile tester with the deformation speed of 10^{-4} mm/s at controlled software panel setting. Since the real tensile test samples sizes may vary a little bit from its original design, all of the critical dimensions such as the length of the tested region, A, width of the tested region, W, and the thickness of the sample, T, were measured and calibrated at the control software panel. Therefore, the true strain rate is in the vicinity of 10^{-5}/s, which is within the condition of static tension test range. During tensile test, the sample was under uniaxial tensile stress initially since the sample had longitudinal symmetric shape. Accordingly, (Ag)-10Al, (Ag)-10Ga, and (Ag)-8Sn test samples were tested, and the data of engineering stress and strain were recorded, collected, and calculated automatically by the controlled software for the following data analysis.

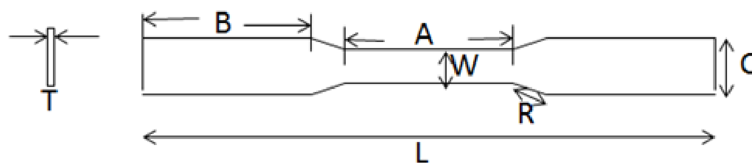

Fig. 6.3 The geometry of tensile test sample, in accordance with ASTM standard E8/ E8M- 08.

unit	W	T	R	L	A	B	C
mm	2.00	1.10	2.00	33.33	10.67	10.00	3.30
inch	0.08	0.04	0.08	1.31	0.42	0.39	0.13

Table. 6.3 The dimensions of tensile test sample, in accordance with ASTM standard E8/ E8M- 08.

6.4 Experimental Results and Discussions

The true stress and strain can be calculated using the Eq. (6.1) and (6.2) [20]:

$$\sigma_T = s(e + 1) \tag{6.1}$$

$$\varepsilon_T = ln(e + 1) \tag{6.2}$$

, where s is the engineering stress, e is the engineering strain, σ_T is the true stress, and ε_T is the true strain.

Due to the random distribution of micron defects, such as cavities and cracks, and the fact that the test samples were cut from different locations of the ingots, the quality of the tensile test sample may vary a little bit from each other. As a consequence, representative data of stress vs. strain characterization results were selected and plotted as the engineering stress-strain curves in Fig. 6.4, together with curves of pure Ag and (Ag)-9.5In obtained previously. By using equations (6.1) and (6.2), the true stress and strain can be calculated for each data point, and the true stress vs. strain curves were plotted accordingly, as shown in Fig. 6.5. Mechanical properties of (Ag)-10Al, (Ag)-10Ga and (Ag)-8Sn can be further determined from the true stress vs. strain curves, namely, yield strength, ultimate tensile strength (UTS), true uniform strain and true fracture strain in tension stress status, summarized in Table 6.4 with pure Ag and (Ag)-9.5In data for comparison.

In plastic deformation region, the true stress can be also expressed mathematically in terms of yield stress and true plastic strain, which was depicted by Ludwik's equation [21], as shown in Eq. (6.3) below. With the data provided in Fig. 6.5, the strain hardening index, n, can be calculated, using Eq. (6.4), by examining the slope of $\log \sigma_p - \log \varepsilon_p$ curve. In addition, the local strain hardening rate, R, for each stress vs. strain curve can be determined by using Eq. (6.5).

$$\sigma_T = \sigma_y + K\varepsilon_p^n \tag{6.3}$$

$$n = \frac{dlog\ \sigma}{dlog\ \varepsilon} = \frac{\varepsilon}{\sigma}\frac{d\sigma}{d\varepsilon} \tag{6.4}$$

$$R = \frac{d\sigma}{d\varepsilon} = n\frac{\sigma}{\varepsilon} \tag{6.5}$$

, where σ_T is the true stress, σ_y is the yield stress, K is strength coefficient, $\varepsilon_p = \varepsilon_T - \varepsilon_e$ is the true plastic strain, ε_T is the true strain, ε_e is the true elastic strain and n is the strain hardening index. As a result, the calculated strain hardening indexes for (Ag)-10Al, (Ag)-10Ga and (Ag)-8Sn were also collected in Table 6.4, and the local strain hardening rates were plotted at each strain value, as shown in Fig. 6.6.

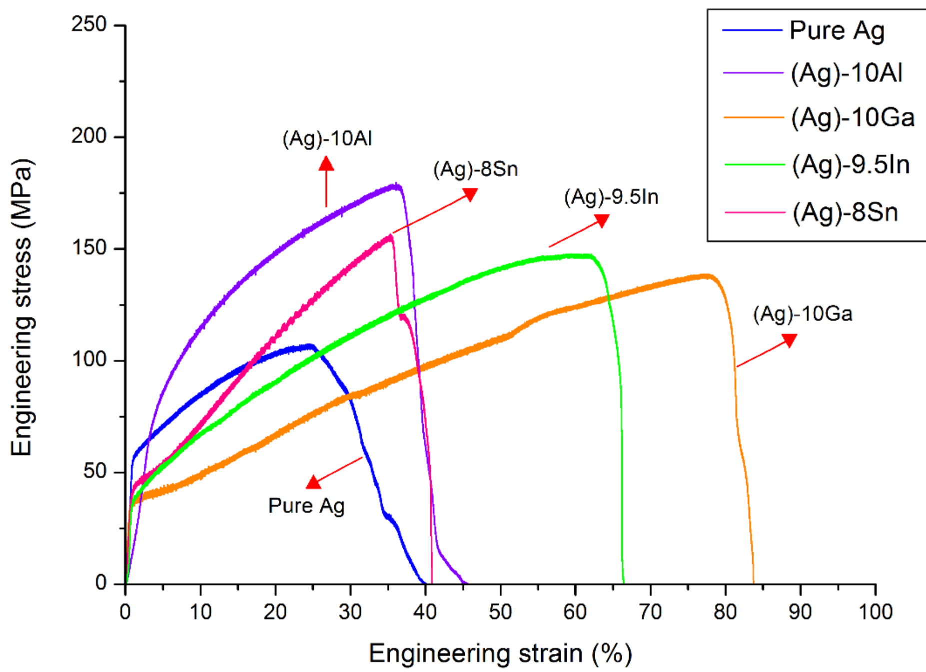

Fig. 6.4 The representative engineering stress-strain curves of (Ag)-10Al, (Ag)-10Ga, (Ag)-9.5In and (Ag)-8Sn with that of pure Ag in comparison.

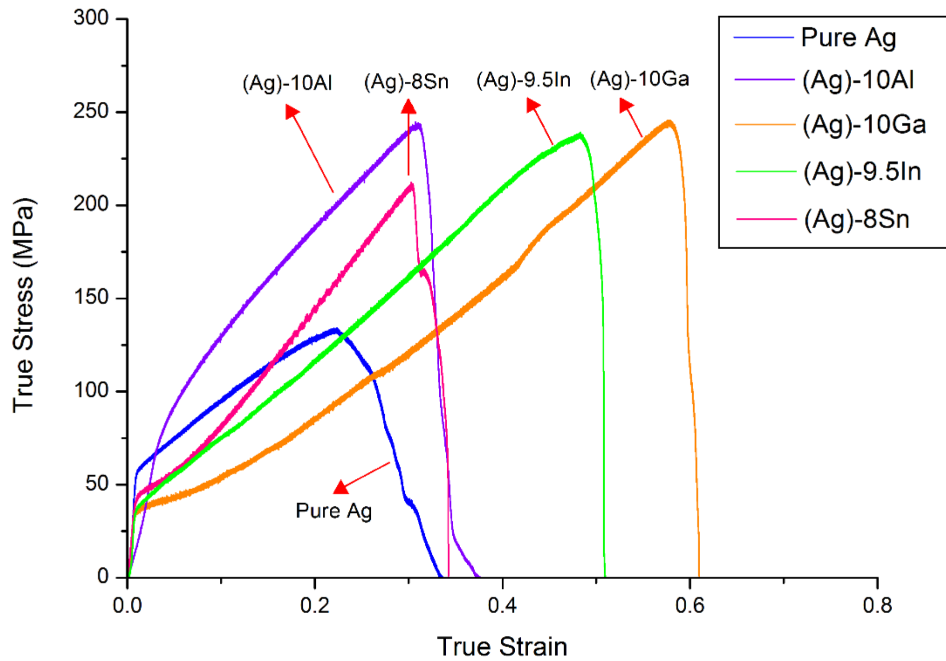

Fig. 6.5 The representative true stress-strain curves of (Ag)-10Al, (Ag)-10Ga, (Ag)-9.5In, and (Ag)-8Sn with that of pure Ag in comparison.

	Yield Strength (MPa)	Ultimate Tensile Strength (MPa)	True Uniform Strain (%)	True Fracture Strain (%)	Strain Hardening Index
Pure Ag	56.6	133.9	22.0	32.7	0.81
(Ag)-10Al	75.1	245.0	30.8	37.4	0.78
(Ag)-10Ga	34.5	246.1	57.5	60.8	1.32
(Ag)-9.5In	37.2	240.1	48.3	50.9	0.99
(Ag)-8Sn	42.3	212.6	30.2	34.2	1.27

Table 6.4 A summary of mechanical properties of (Ag)-10Al, (Ag)-10Ga, (Ag)-9.5In and (Ag)-8Sn with pure Ag in comparison.

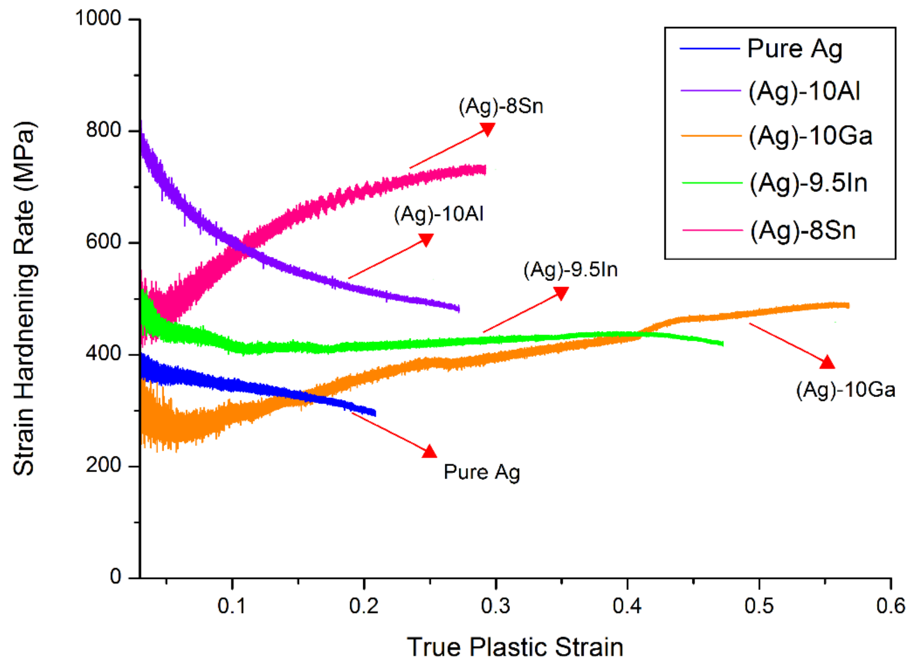

Fig. 6.6 The graphs of strain hardening rates of pure Ag, (Ag)-10Al, (Ag)-10Ga, (Ag)-9.5In, and (Ag)-8Sn.

It is worthwhile to note that all tensile test samples should have similar microstructures with relative large grain size in several micron range, since similar annealing profiles have used in during ingot growth. In addition, the solute concentrations for different solid solutions are close to each other. Therefore, the only variable here would be the difference of the solute element. As shown in Fig. 6.5, although (Ag)-10Al, (Ag)-10Ga, (Ag)-9.5In, and (Ag)-8Sn possess close solute concentrations with the same crystal structure, the stress vs. strain curves are quite different from each other. As predicted by solid solution strengthening theory, the yield strength of (Ag)-10Al increases to 75.1 MPa from 56.6 MPa of pure Ag. Its stress vs. strain curve has very smooth transition from elastic region to plastic deformation stage. In the view of traditional solid solution strengthening theory, the lattice distortion induced by the solute atoms has created a local hydrostatic stress field which can behave as an obstacle for gliding movement of dislocations, thereby postponing the onset of material yielding point and resulting in larger yield strength. However, as the authors had seen in Ag-In solid

solution, the phenomenon of solid solution softening has been observed again in Ag-Ga and Ag-Sn solid solutions in current study, as shown in Fig. 6.5. The yield strengths of (Ag)-10Ga and (Ag)-8Sn decrease to 34.5 MPa and 42.3 MPa, respectively. Their stress vs. strain curves have relatively sharp elastic-to-plastic transitions. Especially, the yield strength of (Ag)-10Ga is even lower than that of (Ag)-9.5In previously observed, and it is the lowest among the five different solid solutions discussed in current study. In addition, (Ag)-10Ga has the sharpest elastic-to-plastic transition, followed by the onset of plastic deformation region with the lowest strain hardening rate, around 300 MPa, as depicted in Fig. 6.6. In literature [22], similar phenomenon had been interpreted as the interaction between dislocation and short range order (SRO) of solute element in solid solution. From statistical point of view, one would not expect to observe absolute random distribution of solute atoms in a substitutional solid solution with relatively high solute concentration. Rather, short range order of arrangement of solute atoms would exist in the local area, even though the solid solution still is disordered in the long range. Since SRO could be an obstacle for dislocation gliding, once the leading dislocation had started to glide, the SRO would be destroyed and could not be restored, resulting in easier dislocation gliding in the crystal plane and relatively low strain hardening rate [23]. The above argument was expected to be valid for all Ag-based solid solutions with similar concentrations. But our experimental facts show otherwise, as depicted in Fig. 6.6, where different strain hardening behaviors have been observed for Ag solid solutions with different solute elements. As shown in Fig. 6.6, the strain hardening rates for pure Ag and (Ag)-9.5In almost remain near constant, about 350 MPa and 430 MPa in average, respectively, at various plastic strain values. The strain hardening rate of (Ag)-10Al has decreased with plastic strain, from the highest initial value among the five material, about 800 MPa to 500 MPa. In contrast, the strain hardening rates of (Ag)-10Ga and (Ag)-8Sn have increased with plastic strain, respectively, from around 300 MPa and 500 MPa to around 450 MPa and 700MPa. Therefore, the authors believe that the previous theoretical interpretations are not entirely conclusive in explaining the strain hardening phenomenon here, and might need further investigation in order to understand the discrepancy between existing theoretical interpretations and observed experimental phenomena.

Ultimate tensile strength (UTS) describes how strong the material is under tension. The true uniform strain (ε_u) is the true strain at the maximum load (strain upon UTS point), which is often useful in estimating the formability of metals. It is noticeable that the UTS values of all Ag solid solutions studied are nearly the same, most of them above 240 MPa, which are 1.8 times of that of pure Ag. However, the values of true uniform strain are quite different from each other. (Ag)-10Al and (Ag)-8Sn have similar true uniform strain values, about 1.4 times of that of pure Ag. Significantly, (Ag)-10Ga has the largest value of true uniform strain among all Ag solid solutions with similar solute concentrations, which is 2.6 times of that of pure Ag. Therefore, the authors have discovered that (Ag)-10Ga possesses the material properties with most desirable combination for electronic device bonding applications, i.e., lowest yield strength, largest elongation and highest UTS among all Ag solid solutions with similar solute concentrations in this study. Thus, it is safe to conclude that both mechanical strength and ductility of Ag can be increased by alloying with the Ga solute element.

The authors believe that this particular combination of mechanical properties could be highly correlated with the solid solution softening phenomenon. Thus, it is essential to review and study the solid solution softening mechanism in order to gain some insight of the underlying reasons behind the shape forming of those stress vs. strain curves. The solid solution softening phenomenon had been extensively studied in body centered cubic (BCC) transition metal alloys [13], and also was found in intermetallics [24], semiconductors [25], ceramic [26], etc., i.e., in those materials whose dislocation mobility is controlled and enhanced by the double kinks nucleation and propagation processes at point defects [5]. This was referred as the intrinsic solid solution softening mechanism, and the elastic stress induced by solute atoms was considered as a reason for the double kinks nucleation. However, it is very clear that, as seen in our XRD results, adding Al and Ga solute atoms would result in compressive stress cores in Ag crystal lattice, while adding In and Sn solute atoms would result in dilating stress cores. From experimental results of current research, it is safe to conclude that the difference of atomic radii between solute and matrix atoms would barely have any correlation to their corresponding mechanical behaviors. As a matter of fact, the strongest interaction between point defect and dislocation actually occurs inside the dislocation core. Therefore, continuum elasticity model that was used by the previous theorem become incorrect.

Instead, chemical or valence electronic (quantum-mechanical) mechanisms may play a more dominant role in increasing the dislocation mobility by promoting the double kinks nucleation and propagation processes, which was supported by the ab initio calculation results. It had been shown that two influential parameters of atomic row displacement (ARD) energy and generalized stacking fault (GSF) energy were the determining factors associated with solid solution softening mechanism within BCC crystal structure scheme. However, the solid solution softening mechanism was rarely studied within FCC crystal structure scheme, therefore, whether the underlying mechanism would be similar to or different from that of BCC model still remains inconclusive at this point. Although Al, Ga and In are elements all from IIIA column, the effective valence electron contributions to the mixing valence bands of solid solutions could be much different from each other. Therefore, the authors would consider that quantum-mechanical mechanism may also play a very important role in explaining the solid solution softening phenomenon occurred in Ag-based or FCC solid solutions. In other words, further studies need to be conducted in order to fully understand solid solution softening mechanisms in Ag-based or FCC solid solutions.

6.5 Fractography

Topography of fracture surfaces of samples tested can provide some additional information and qualitatively described the deformation behaviors of materials. Therefore, the fractography of representative tensile test samples of (Ag)-10Al, (Ag)-10Ga and (Ag)-8Sn were examined under SEM at various fracture regions and different magnifications, in order to gain some insight of the deformation history from a microscopic point of view. As shown in Fig. 6.7, the morphology of fracture surface of (Ag)-10Al exhibits a feature called tear-ridges, which should be corresponding to quasi-cleavage fracture mode. This type of fracture mode denotes that some but limited amount of plastic deformation has occurred before failure, so (Ag)-10Al was at transition state from brittle to ductile. In addition, the morphology of fracture surface of (Ag)-8Sn exhibits fibrous features in its appearance, as shown in Fig. 6.8 (a), and some shallow dimpled rupture, shown in Fig. 6.8 (b), which testify that (Ag)-8Sn was actually ductile in its nature. The elongations before failure of (Ag)-10Al

and (Ag)-8Sn tested samples were all around 0.35, therefore, the opposite strain hardening histories may explain the existing differences between their fractography. As shown in Fig. 6.9, the morphology of fracture surface of (Ag)-10Ga exhibits highly ductile character, since a large amount of necking and many deep elliptical dimpled ruptures have been observed. Microvoid formation and coalescence during the continued straining and plastic deformation are responsible for this dimpled rupture morphology [27], and shape of the dimples are depending on the local stress status during the tensile test. As we have seen in Fig. 6.4, the engineering strain of (Ag)-10Ga at fracture point is more than 80%, showing the truly remarkable elongation. The topography of fracture surface of (Ag)-10Ga has testified that a large amount of plastic deformation has occurred before final failure, therefore, confirming that (Ag)-10Ga is indeed highly ductile in its nature. The high values of elongation and ductility of (Ag)-10Ga could possibly be related to solute segregation at grain boundaries, resulting in the formation of amorphous type of complexions [28], which have been proven to be the responsible mechanism in the ductility enhancement of certain alloys [29].

In conclusion, the results of fractography study are very consistent with previous tensile test data and can provide additional experimental evidences at microscopic level for the future solid solution softening mechanism study and quantitative modeling.

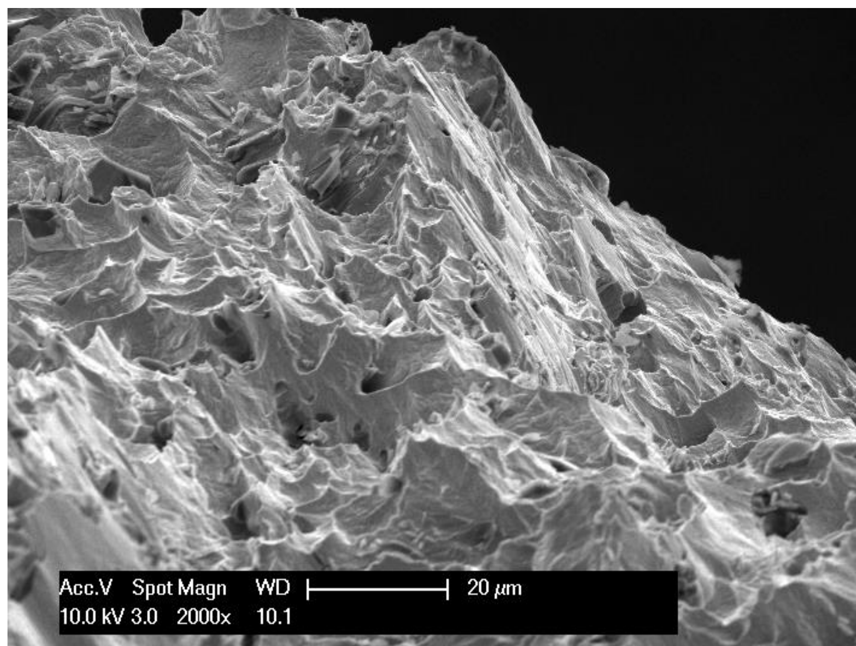

Fig. 6.7 (a) Fractography of (Ag)-10Al representative tensile test sample, SEM image at 2000×,

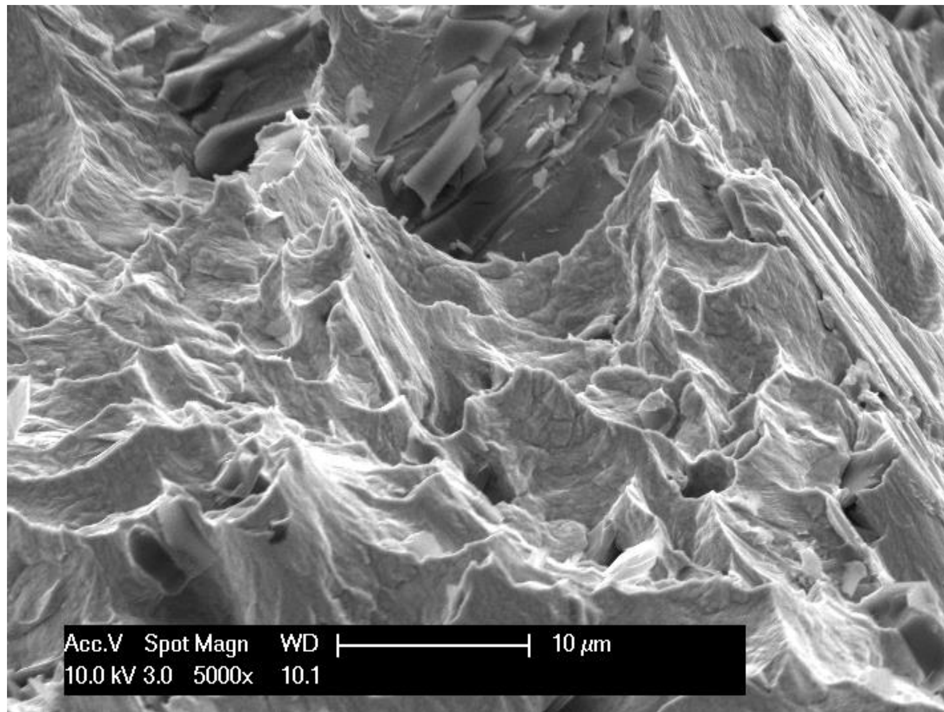

Fig. 6.7 (b) SEM image at 5000× magnification.

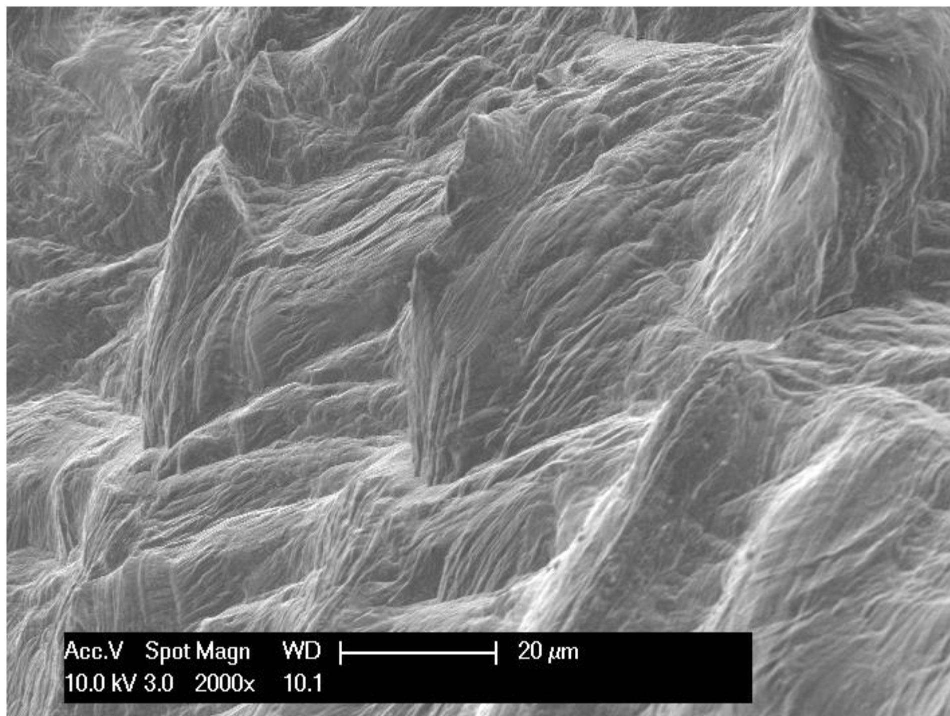

Fig. 6.8 (a) Fractography of (Ag)-8Sn representative tensile test sample, SEM image at 2000× magnification,

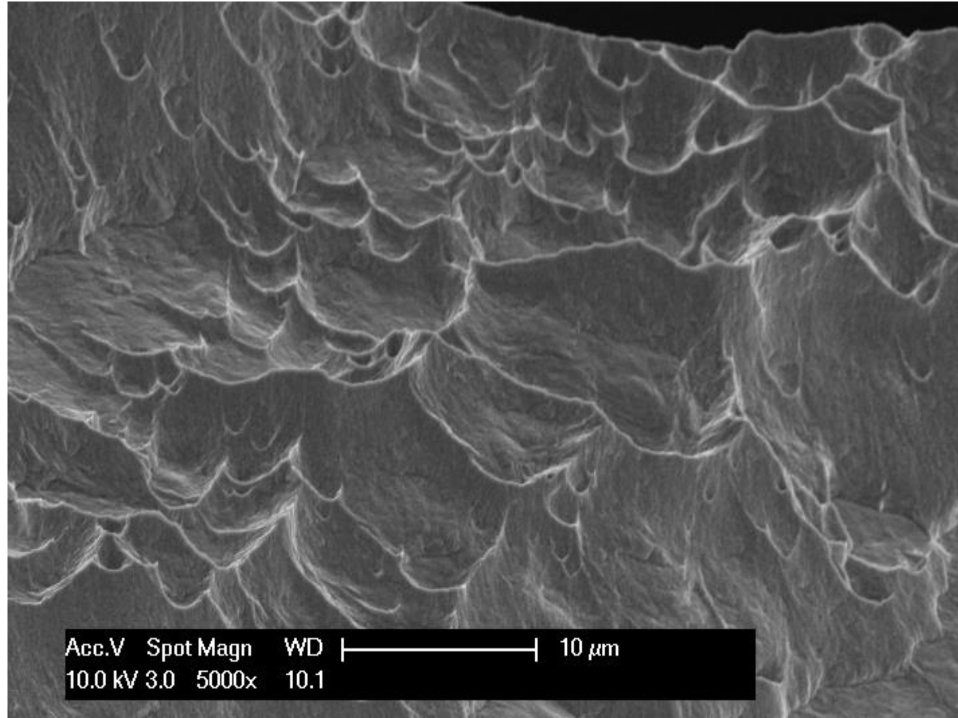

Fig. 6.8 (b) SEM image at 5000× magnification.

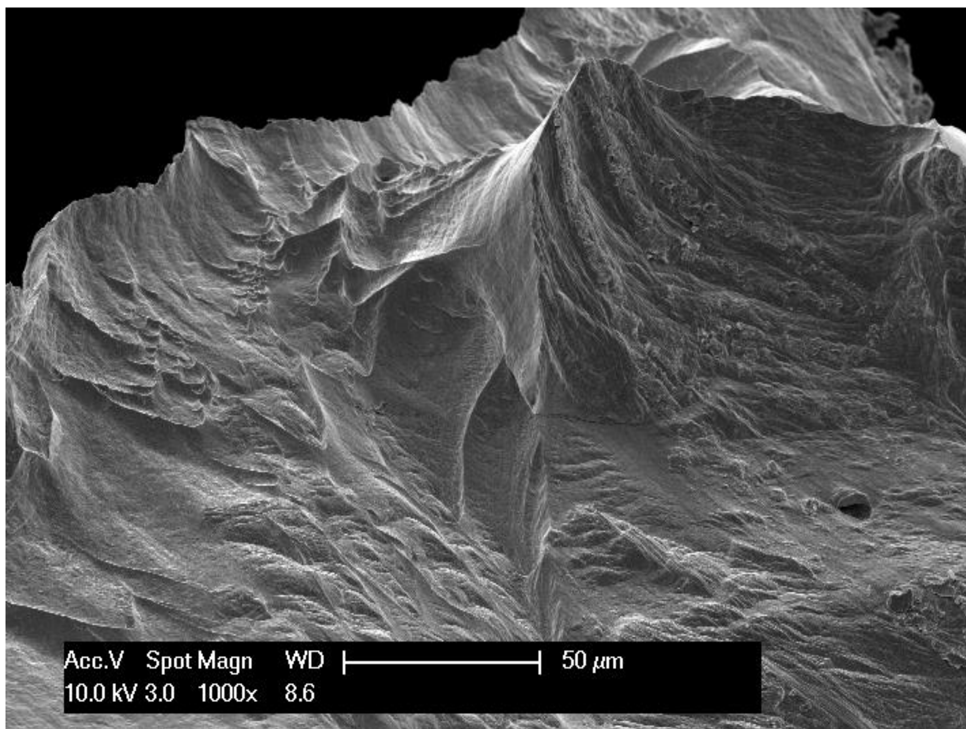

Fig. 6.9 (a) Fractography of (Ag)-10Ga representative tensile test sample, SEM image at 1000× magnification,

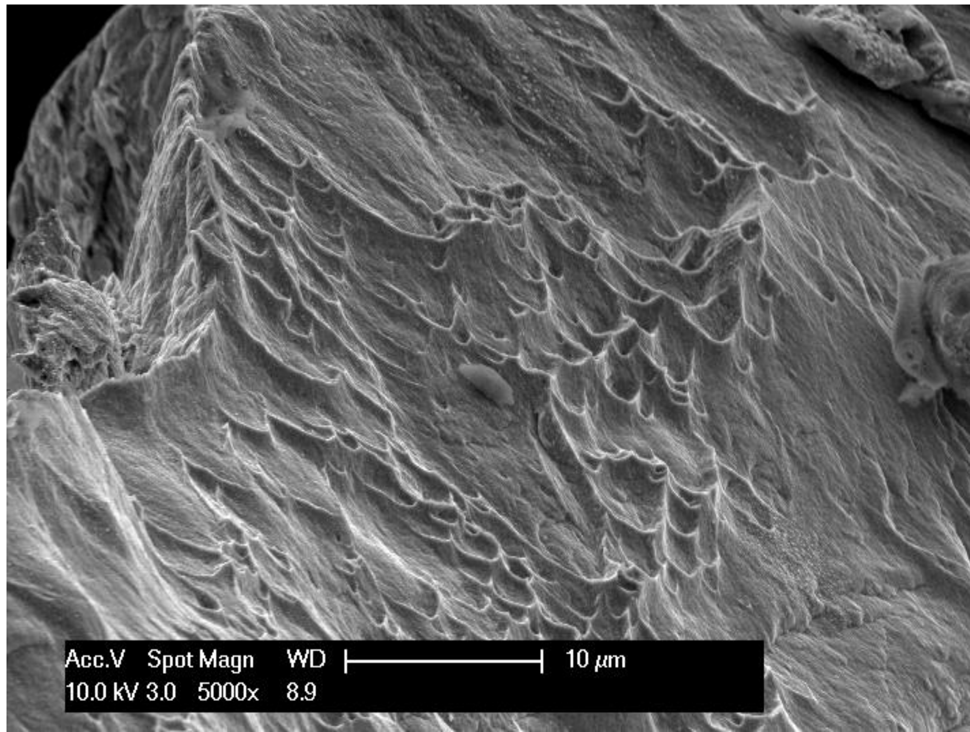

Fig. 6.9 (b) SEM image at 5000× magnification,

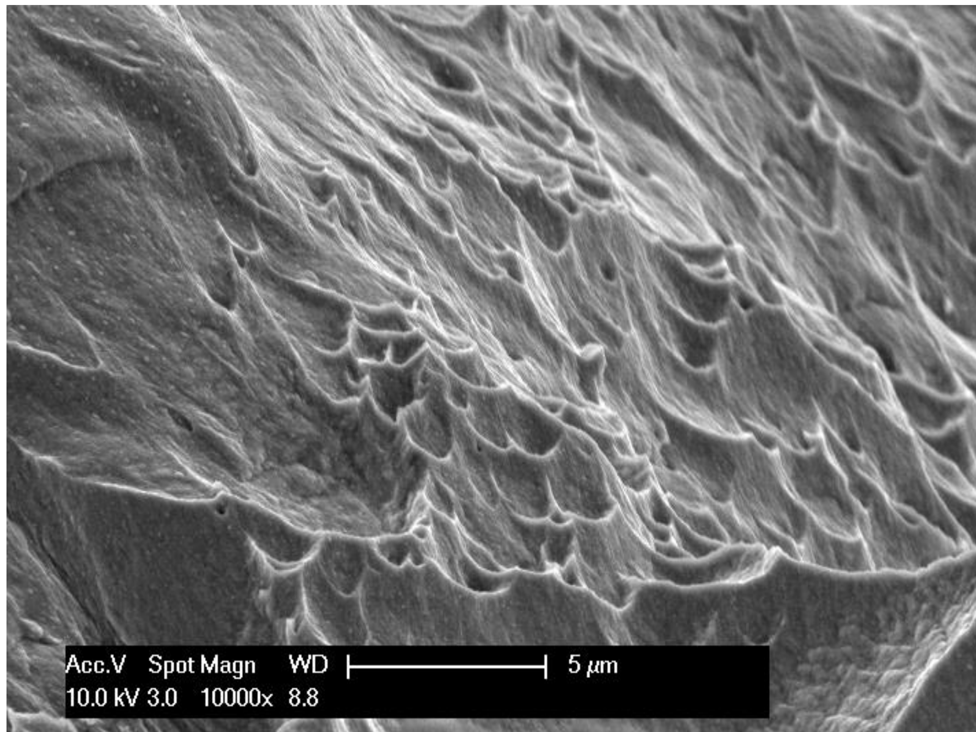

Fig. 6.9 (c) SEM image at 10000× magnification.

6.6 Concluding Remarks

In this chapter, materials of Ag-based solid solutions with solute elements Al, Ga, and Sn have been successfully prepared in ingot form at similar concentrations. Under uniaxial tensile stress status, the (Ag)-10Al has shown typical solid solution strengthening mechanical behaviors, while solid solution softening phenomenon have been observed in (Ag)-10Ga and (Ag)-8Sn's mechanical behaviors. Especially, the authors have discovered that (Ag)-10Ga exhibits superior mechanical properties with low yield stress, large elongation and high UTS, compared with pure Ag and other Ag-based solid solutions. In semiconductor manufacturing, low hardness and yield strength would be highly desirable [30] for the selection of interconnecting materials, since it induces less internal stress to the areas underneath wire-bond pads on integrated circuit (IC) chips. With high degree of ductility, it can also better accommodate the CTE mismatch induced stress and strain by the plastic deformation process. In addition, Ga has extremely low melting temperature, at 29.8 ºC, and Ag-Ga eutectic temperature is even lower, at 25 ºC. Therefore, it can be considered as a new alternative method as transit liquid phase (TLP) bonding technique, using Ag-Ga binary system, which can possibly achieve the fantastic goal for room temperature (RT) bonding. In current research, the authors have proved that Ag-Ga binary system is indeed a promising candidate for the further development of TLP and solid-state bonding techniques due to Ag-Ga solid solution phase exhibiting such an ideal combination of mechanical properties. The documentation of the stress vs. strain curves and strain hardening rates of (Ag)-10Al, (Ag)-10Ga, and (Ag)-8Sn would also be of interest to those researchers and engineers in the electronics industry and community in terms of its scientific and engineering values. For example, finite element analyses (FEA) for electronics mechanical, manufacturing and reliability designs [31, 32] can be readily performed with the availability of mechanical properties and stress vs. strain curves of those Ag-based solid solutions. Further investigations on the solid solution softening phenomenon and mechanism in Ag-based and FCC solid solutions will continue in our future research activity.

Reference in Chapter 6

1. W. Hume-Rothery, G. F. Lewin, and P. W. Reynolds. “The lattice spacings of certain primary solid solutions in silver and copper.” *Proceedings of the Royal Society of London. Series A, Mathematical and Physical Sciences*, vol. 157.890, pp. 0167-0183, Oct 1936.
2. R. Bacon, and C. S. Smith. “Single crystal elastic constants of silver and silver alloys.” *Acta Metallurgica*, vol. 4, No.4, pp. 337-341, 1956.
3. R. W. K. Honeycombe. “The plastic deformation of metals.” First edition, Edward Arnold Ltd., Cambridge, 1968.
4. P. Jax, P. Kratochvil, and P. Haasen. “Solid solution hardening of gold and other fcc single crystals." *Acta Metallurgica*, vol. 18, No. 2, pp. 237-245, 1970.
5. A. Sato, and M. Meshii. "Solid solution softening and solid solution hardening.” *Acta Metallurgica*, vol. 21.6, pp. 753-768, 1973.
6. L. Delehouzee, and A. Deruyttere. “The stacking fault density in solid solutions based on copper, silver, nickel, aluminium and lead.” *Acta Metallurgica*, vol. 15, No. 5, pp. 727-734, 1967.
7. J. G. Bai, J. Yin, Z. Zhang, G. Q. Lu, and J. D. van Wyk, “High-temperature operation of SiC power devices by low-temperature sintered silver die-attachment.” *IEEE Transactions on advanced packaging*, vol. 30, No. 3, pp. 506-510, 2007.
8. Y. Y. Wu and C. C. Lee. "The strength of high-Temperature Ag–In joints produced between copper by fluxless low-temperature processes." *Journal of Electronic Packaging*, vol. 136, No. 1, pp. 0110061-6, 2014.
9. T. H. Chuang, C. H. Tsai, H. C. Wang, C. C. Chang, C. H. Chuang, J. D. Lee, H. H. Tsai. “Effects of annealing twins on the grain growth and mechanical properties of Ag-8Au-3Pd bonding wires.” *Journal of Electronic Materials*, vol. 41, No. 11, pp. 3215-3222, 2012.
10. T. H. Chuang, H. C. Wang, C. H. Chuang, H. J. Lin, J. D. Lee, H. H. Tsai. “Surface reconstruction of an annealing twinned Ag-8Au-3Pd alloy wire under current stressing.” *Metallurgical and Materials Transactions A*, vol. 44, No.11, pp. 5106-5112, 2013.
11. Y. Huo and C. C. Lee, “The growth and stress vs. strain characterization of the silver solid solution

phase with indium", *Journal of Alloys and Compounds*, vol. 661, pp. 372-379, 2016.

12. J. Wu, and C. C. Lee, "The growth and tensile deformation behavior of the silver solid solution phase with zinc." *Materials Science and Engineering: A*, vol. 668, pp. 160-165, 2016.
13. N. I. Medvedeva, Y. N. Gornostyrev, and A. J. Freeman. "Solid solution softening in bcc Mo alloys: Effect of transition-metal additions on dislocation structure and mobility." *Physical Review B*, vol. 72, No. 13, pp. 134107-1-9, 2005.
14. A. R. Dhamdhere, A. P. Malshe, W. F. Schmidt, and W. D. Brown, "Investigation of reliability issues in high power laser diode bar packages." *Microelectronics Reliability*, vol. 43, No. 2, pp.287-295, 2003.
15. A. J. McAlister, "The Ag-Al (Silver-Aluminum) System", *Bulletin of Alloy Phase Diagrams*, vol. 8 No. 6, pp. 527-533, 1987.
16. I. Karakaya and W. T. Thompson, "The Ag-Sn (Silver-Tin) System", *Bulletin of Alloy Phase Diagrams*, vol. 8 No. 4, pp. 340-347, 1987.
17. M. R. Baron, "The Ag-Ga (Silver-Gallium) System", *Bulletin of Alloy Phase Diagrams*, vol. 11 No. 4, pp. 334-339, 1990.
18. R. Peierls, "The size of a dislocation". *Proceedings of the Physical Society*, vol. 52, No. 1, pp. 34-37, 1940.
19. ASTM standard E8/ E8M- 08, "Standard test methods for tension testing of metallic materials" ASTM International, West Conshohocken, PA, 2008, DOI: 10.1520/E0008_E0008M-08, www.astm.org.
20. G. E. Dieter, "Mechanical Metallurgy", Third Edition, Mc Graw Hill, NY, 1986.
21. P. Dadras and S. Majlessi, "Plastic bending of work hardening materials", *Journal of Engineering for Industry (Transactions of the ASME)*, vol. 104, No. 3, pp. 224-230, 1982.
22. J. C. Fisher, "On the strength of solid solution alloys", *Acta Metallurgica*, vol. 2, No. 1, pp. 9-10, 1954.
23. N. Clement, D. Caillard and J. L. Martin, "Heterogeneous deformation of concentrated Ni-Cr F.C.C. alloys: Macroscopic and microscopic behavior", *Acta Metallurgica*, vol. 32, No. 6, pp. 961-975,

1984.

24. A. A. Sharif, A. Misra, and T. E. Mitchell, "Deformation mechanisms of polycrystalline $MoSi_2$ alloyed with 1 at. % Nb", *Materials Science and Engineering: A*, vol. 358, No. 1, pp. 279-287, 2003.
25. K. Maeda, and S. Takeuchi, "Enhancement of dislocation mobility in semiconducting crystals by electronic excitation", Dislocations in Solids, edited by F. R. N. Nabarro, vol. 10, pp. 443-504, North-Holland, Amsterdam, 1996.
26. T. E. Mitchell, "Dislocations and mechanical properties of $MgO-Al_2O_3$ spinel single crystals", *Journal of the American Ceramic Society*, vol. 82, No. 12, pp. 3305-3316, 1999.
27. R. H. Van Stone, T. B. Cox, J. R. Low, Jr and J. A. Psioda. "Microstructural aspects of fracture by dimpled rupture" *International Metals Reviews*, vol. 30.1, pp. 157-179, 1985.
28. P. R. Cantwell, M. Tang, S. J. Dillon, J. Luo, G. S. Rohrer, and M. P. Harmer, "Grain boundary complexions", *Acta Materialia*, vol. 62, No. 152, pp. 1-48, 2014.
29. A. Khalajhedayati, Z. Pan, and T. J. Rupert, "Manipulating the interfacial structure of nanomaterials to achieve a unique combination of strength and ductility", *Nature Communications*, vol. 7:10802, pp. 1-8, 2016.
30. Z. W. Zhong, H. M. Ho, Y. C Tan, W. C. Tan, H. M. Goh, B. H. Toh, and J. Tan. "Study of factors affecting the hardness of ball bonds in copper wire bonding", *Microelectronic Engineering*, vol. 84, No. 2, pp. 368-374, 2007.
31. S. Elangovan, S. Semeer, and K. Prakasan. "Temperature and stress distribution in ultrasonic metal welding — An FEA-based study", *Journal of Materials Processing Technology*, vol. 209.3, pp. 1143-1150, 2009.
32. Y. Lin, W. Liu, and F. G. Shi, "Laser welding induced alignment distortion in butterfly laser module packages: Effect of welding sequence", *IEEE transactions on advanced packaging*, vol. 25, No. 1, pp. 73-78, 2002.

Chapter 7

Thermal, Electrical and Optical Properties of Ag-In Solid Solution

7.1 Introduction

In the previous chapters, the author has investigated the mechanical properties and anti-tarnishing property of Ag-In solid solution. In order to fulfill our initial goal of the research, namely, developing the die-attachment material for high temperature power electronics, further physical properties need to be studied as well. Thermal conductivity and diffusivity of die-attachment materials are important parameters that will directly affect the overall performance of the power electronics system, in terms of thermal management. Electrical conductivity is important to the high-frequency electronics since it can affect the RC delay of the system. To power electronics, electrical conductivity of the interconnection materials need to be high enough so that the resistance thermal dissipation of interconnection would be negligible to the switching loss, thereby not affecting the overall system level energy conversion efficiency. Moreover, the author has discovered the anti-tarnishing property and mechanism in Ag-In binary system, thereby leading to potential optical applications, such as GaN-based LED reflector and giant astronomical telescope array of mirrors construction. Therefore, it would be interesting to study the optical reflectivity of Ag-In alloy thin film sample. In the following sessions, the author would like to study the multi-physical properties of Ag-In solid solution and IMC in Ag-In binary system, using experimental methods.

7.2 Thermal Property of Ag-In Solid Solution

Pure Ag has the highest thermal conductivity among all of the metals, which has the value of 429 W/m-K. The high value of thermal conductivity is desirable in the electronic application. However, by alloying with indium solutes to form solid solution, the author would expect that the value of thermal conductivity will decrease with the concentration of indium solutes. In principle, the reason behind this dropping of the thermal conductivity is mainly due to the scattering effects induced by the solutes element. The solutes element will distort the original perfect lattice of the pure silver, so that

the probability of phonons and electrons scattering can be increased due to the defect sites and stress/strain field. The question remains here is how much the value of dropping in terms of thermal conductivity will be. From engineering design principle, it is acceptable if the thermal conductivity of the die-attachment material is comparable to solder, which is one of the most frequently used die-attachment materials in the electronics packaging industry.

For the thermal conductivity measurement, steady-state and transient experimental methods can be used to measure the thermal conductivity directly and indirectly. The author has tried both methods and it turns out that the transient methods can give better a more precise and accurate values of thermal conductivity, as we used pure Ag sample as the reference. As a result, standard test method for thermal diffusivity by the flash method, ASTM E1461 [1], was used in this study. In this method, as depicted in Fig. 7.1, a small, thin disk specimen is subjected to a high intensity short duration radiant energy pulse. The energy of the pulse is absorbed on the front surface of the specimen and the resulting rear face temperature rise (thermal curve) is recorded. The thermal diffusivity value is calculated from the specimen thickness and the time required for the rear face temperature rise to reach a percentage of its maximum value. When the thermal diffusivity of the specimen is to be determined over a temperature range, the measurement must be repeated at each temperature of interest. Thermal diffusivity values ranging from 0.1 to 1000 $mm^2\ s^{-1}$ are measurable by this test method from about 75 to 2800 K, so this method is suitable for our sample measurement. As shown in Eq. (7.1), thermal diffusivity, α, of a solid material—the property is given by the thermal conductivity divided by the product of the density and heat capacity per unit mass. It measures the ability of a material to conduct thermal energy relative to its ability to store thermal energy. It has the SI unit of mm^2/s.

$$\alpha = \frac{\lambda}{\rho C_p} \tag{7.1}$$

, where λ is thermal conductivity, $W/\ m \cdot K$, ρ is density, kg/m^3, C_p is specific heat capacity, $J/\ kg \cdot K$. The typical value for thermal diffusivity of silver is 165.63 $mm^2\ s^{-1}$.

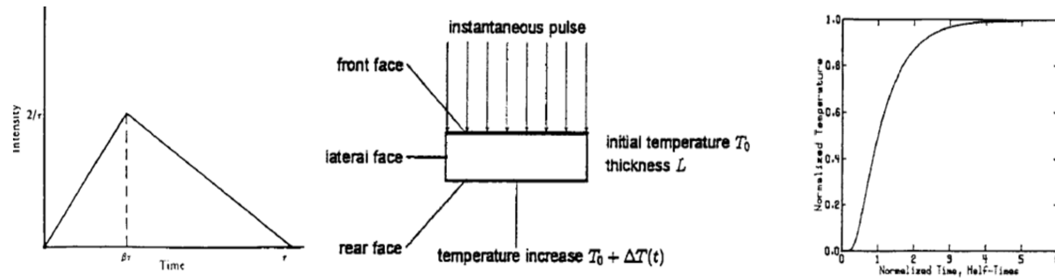

Fig. 7.1 Flash method for thermal diffusivity measurement, laser pulse shape (left), schematic of the flash method (middle), characteristic thermal curve for the flash method (right).

Specific heat capacity and density will not change much from pure Ag to Ag-In alloy. Therefore, after the measurement of thermal diffusivity, the author can calculate the corresponding thermal conductivity by using Eq. (7.1). In practice, Laser Flash Analyzers (LFA), NETZSCH LFA 449, was used to measure thermal diffusivity, with ASTM E1461. Ag-Al, Ag-Ga, and Ag-Sn solid solutions, described in chapter 6, are also measured by this flash method to get their values of thermal diffusivities. As results, the thermal diffusivities and thermal conductivities of Ag-In, Ag-Al, Ag-Ga and Ag-Sn solid solutions are listed in Table 7.1, using bulk disk samples described in previous chapters.

	Thermal Diffusivity (mm^2/s)	Thermal Conductivity (W/ m · K)
Pure Ag	164.25	414.70
(Ag)-9.5In	30.70	76.97
(Ag)-19In	21.04	52.97
(Ag)-10Al	15.56	39.17
(Ag)-10Ga	15.43	38.85
(Ag)-8Sn	12.95	32.60

Table 7.1 The summary of thermal diffusivity measurement results and calculated thermal conductivity results for pure Ag, Ag-In, Ag-Al, Ag-Ga, and Ag-Sn solid solutions.

As shown in Table 7.1, the values of thermal diffusivity and thermal conductivity of all of the Ag-based solid solutions decrease a lot from the value of pure silver, as expected. Among all of studied Ag-based solid solutions, (Ag)-9.5In has highest value of thermal conductivity. As reference, the value of thermal conductivity of pure Sn solder is 66.8 W/ m · K, and typical values of SnPb eutectic solder and SnAgCu lead free solder are around 50 W/ m · K. Therefore, Ag-In solid solution still has a better thermal property if compared with traditional solder for die-attachment applications, and should be acceptable by the electronic packaging industry.

7.3 Electrical Property of Ag-In Solid Solution

In the context of solid state physics, the Wiedemann-Franz law [2], as shown in Eq. (7.2), states that for metals at not too low temperatures the ratio of thermal conductivity to the electrical conductivity is directly proportional to the temperature, with the value of the constant of proportionality independent of the particular metal. This result was important in the history of the theory of metals, for it supported the picture of an electron gas as the carrier of charge and energy.

$$\frac{\mathrm{K}}{\sigma T} = \frac{\pi^2}{3}(\frac{k_B}{e})^2 = L \tag{7.2}$$

, where K is the thermal conductivity, σ is the electrical conductivity, T is temperature is absolute scale, k_B is the Boltzmann constant, e is the electron charge, and the proportional constant L is called the Lorenz Number.

In the electronics applications, the electrical conductivity of the interconnection material is also important. Initially, the author used Eq. (7.2) to estimate the electrical conductivity of the Ag-In solid solution. Unlike measuring the resistance of electrical resistors, the resistance of metallic conductor is usually very small so that it requires highly sensitive instrument to conduct the measurement. However, the thin film sample of Ag-In samples on quartz substrate that were described in chapter 5, the author would be able to directly measure the electrical conductivity or electrical resistivity by the experimental approach. With the help from Dr. Jinfeng Li, the sheet resistance of Ag-In alloy thin films can be directly measured by the four-point probe method.

As shown in Fig. 7.2, the four-point probe measurement was conducted by using the square set-up, which can ensure that the contact resistance induced by the probe itself can be diminished during the sheet resistance measurement. The electrical resistivity can be calculated by using Eq (7.3). The calculated results of the electrical resistivity for the Ag-In alloy thin film samples were listed in Table 7.2.

$$\rho = R_s \times t \tag{7.3}$$

, where ρ is the electrical resistivity, R_s is the measured sheet resistance of thin film sample and t is the thickness of the thin film.

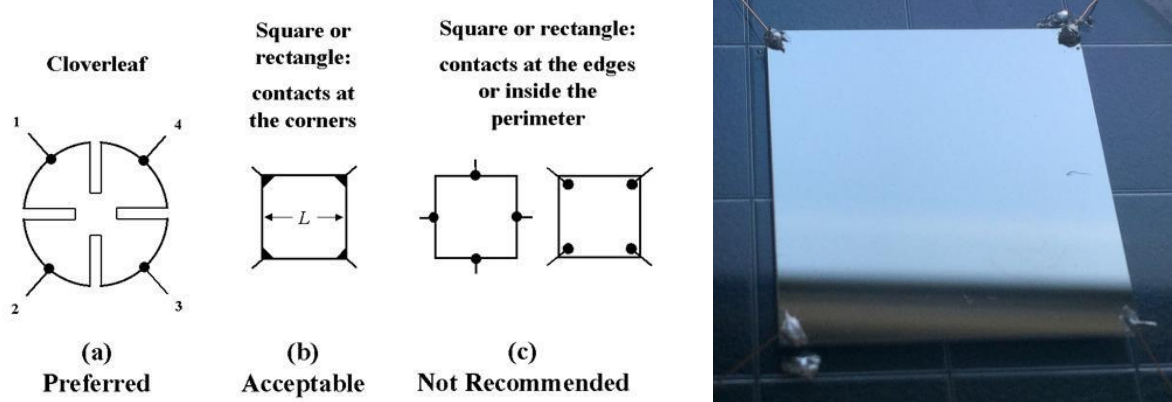

Fig. 7.2 The requirement of the sample for the four-point probe electrical sheet resistance measurement (left) and a picture of real thin film sample during the measurement (right).

	Electrical Resistivity (10^{-8} Ω ·m)	Relative Electrical Conductivity (% of Ag)	Relative Thermal Conductivity (% of Ag)
Pure Ag	4.92	100	100
(Ag)-5In	11.36	43.3	-
(Ag)-9.5In	14.40	34.2	18.6
(Ag)-19In	26.20	18.8	12.8
Ag_9In_4	45.50	10.8	-

Table 7.2 Electrical resistivity, relative electrical conductivity and relative thermal conductivity of the Ag-In alloy thin film samples.

As shown in Table 7.2, the change of electrical resistivity and electrical conductivity of Ag-In exhibits highly non-linear character with the increase of solute concentration. Moreover, the ratios of between relative electrical conductivity and relative thermal conductivity are not a fixed constant, as predicted by Wiedemann-Franz law. In other words, Ag-In solid solution remain more electrical conductive than thermal conductive. Therefore, the Ag-In solid solution should be good enough to be used as die-attachment material or interconnecting materials as an alternative method to conventional solder. The reason behind non-corrected prediction of Wiedemann-Franz law towards the Ag-In alloy thin film need to further study in order to understand.

7.4 Optical Property of Ag-In Solid Solution

Apart from die-attachment, Ag-In solid solution can be also applied as reflective material since it exhibited the great anti-tarnishing property as the described by the previous chapters. Therefore, the author has also conducted the experiments to measure the optical reflectivity of Ag-In alloy thin film samples. The author used the visible-infrared spectrometer, Lambda 950 Perkin Elmer Instruments, ranging from 300 nm to 2500 nm in terms of the light wavelength with incident angle of 8 degree and resolution of 4 nm. The resulting optical reflectivity of Ag-In alloy thin film under visible and infrared (IR) spectrum is shown in Fig. 7.3. As shown in Fig 7.3, the optical reflectivity of pure Ag is very good and the plasma frequency and the cut-off can be clearly seen from the curve. According to the results, the pure silver spectrum is almost identical to the published data, with 316 nm cutoff wavelength. The reflectivity remains as high as 99% for IR range and stay above 95 % for most of the visible range. For (Ag)-19In sample, the reflectivity remains as high as around 95% for IR range, but drop to about 80% for the visible spectrum. However, major scratches and spot can be observed on the surface of the sample due to handling. Therefore, the result might need to be measured again in order to confirm the accuracy of the optical reflectivity values. For Ag_9In_4 sample, the reflectivity is around 85% at IR range, and drop to 80% for visible spectrum. Its reflectivity on UV light is 75% which is the highest among those measured samples. Both Ag-In solid solution and IMC sample exhibited a left-shifting plasma frequency. This is only a preliminary result of the optical reflectivity study for Ag-In.

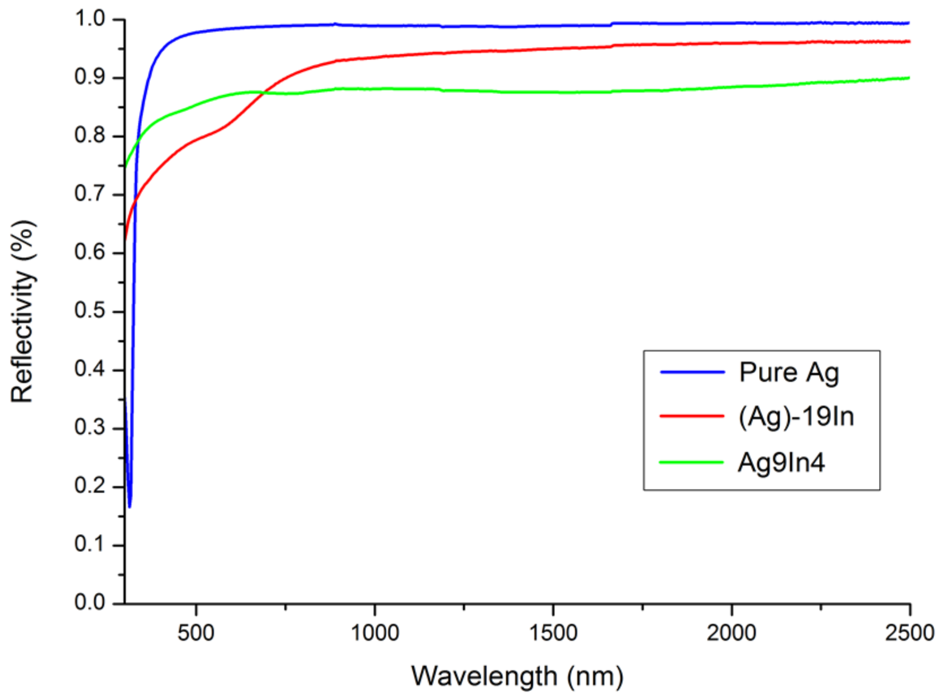

Fig. 7.3 Optical reflectivity spectrum of Ag-In alloy thin film under the visible and infrared range.

The optical reflectivity is highly affected by the quality of the reflector. Therefore, the author has also investigated the quality of our fabricated Ag-In thin film sample on quartz substrate by using AFM. Keysight 7500 AFM was used to conduct the AFM measurement in contact mode. The AFM measurement results are shown in Fig. 7.4, Fig. 7.5 and Fig. 7.6.

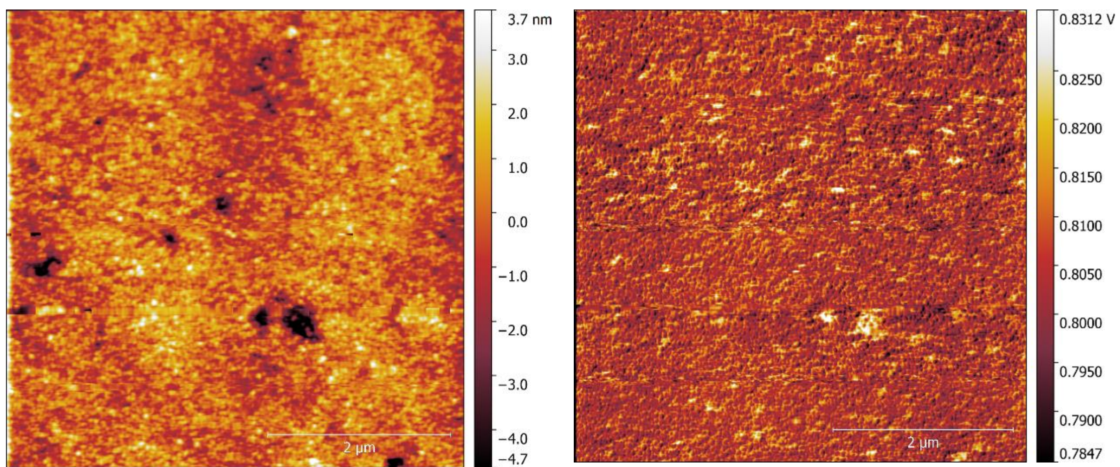

Fig. 7.4 AFM measurement results of Ag-In thin film sample on quartz substrate with 5μm × 5μm measured area size, topography AFM image (left) and friction AFM image (right).

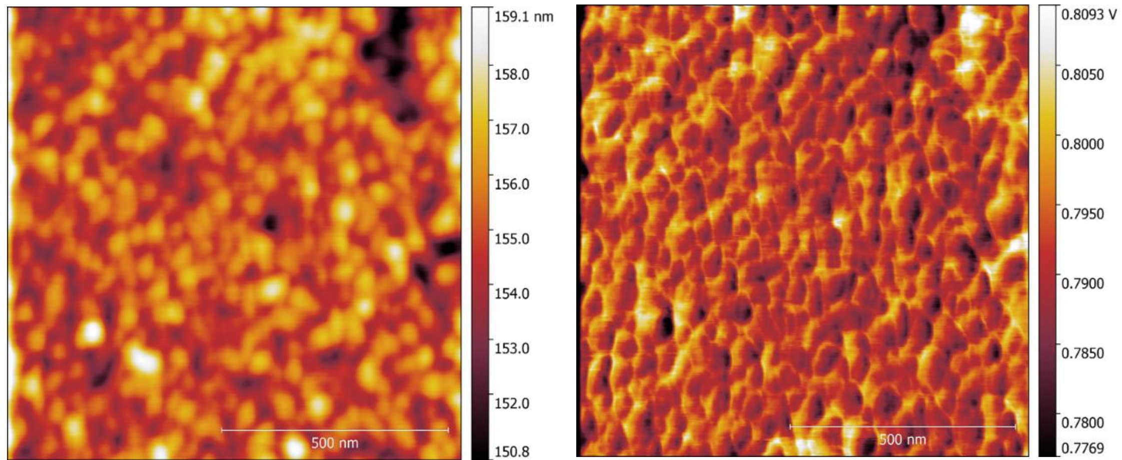

Fig. 7.5 AFM measurement results of Ag-In thin film sample on quartz substrate with 1μm × 1μm measured area size, topography AFM image (left) and friction AFM image (right).

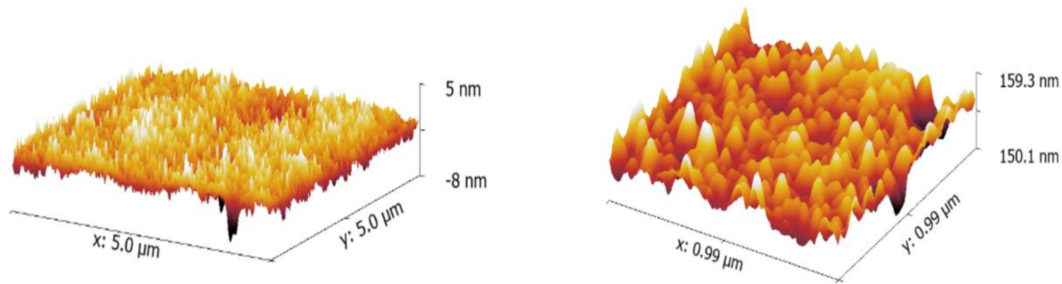

Fig. 7.6 3D Topography AFM Image Ag-In thin film sample on quartz substrate with 5μm × 5μm measured area size (left) and 1μm × 1μm measured area size (right).

As shown in the AFM result, our E-beam deposited Ag-In thin film is indeed within "T-zone" of deposited thin film with grain size about tens of nanometers. The surface roughness is only about ±5 nm, which is half size of the grains. Therefore, the quality of thin film sample fabrication process is confirmed with AFM measurement. More AFM investigations for Ag-In thin film maybe conduct in our group future study in order to fully understand the correlation with optical properties and surface nano-structure of thin film.

7.5 Summary

In summary, the thermal, electrical and optical properties have been studied in this chapter. With thermal and electrical properties of Ag-In solid solution, the author would like to conclude that it is indeed suitable as an alternative die-attachment material in the high-temperature power electronics application. However, the conduct of the measurement of those multi-physical properties is inter-disciplinary in its nature. Therefore, it is relative hard for the author to finish all of study in a very comprehensive way within the limited time of graduate study. The author would like to point out that those study are only preliminary results for thermal, electrical and optical properties in the Ag-In binary system. Further study for those subjects maybe needed in our group future research activities.

Reference in Chapter 7

1. Standard, ASTM, E1461, "Standard Test Method for Thermal Diffusivity by the Flash Method," ASTM International, West Conshohocken, PA, 2007.
2. C. Kittel. "Introduction to solid state". 8th Edition, John Wiley & Sons, 2005.

Chapter 8

Bondable Copper Substrates with Silver Solid Solution Coating for High-Temperature Power Electronic Applications

8.1 Introduction

As researchers and engineers, we are thrilled to study in the era upon the dawn of a new generation of technological revolution, namely, energy revolution. With the advent and development of wide bandgap (WBG) semiconductor material, i.e., silicon carbide (SiC) and gallium nitride (GaN), the figure of merits of power electronics have been largely improved by breaking the physical boundaries of traditional silicon-based semiconductor devices, thereby allowing power electronics sub-systems such as, inverters and converters, to operate at higher temperature, higher voltage with higher energy efficiency [1].

However, electronic packaging technology could be the limiting and determining factor before fully utilizing the physical advantages offered by WBG semiconductor materials. Generally speaking, the operating temperature of WBG semiconductor power electronic device can be even higher than 350°C [2]. Therefore, it is important to develop a whole set of packaging technology, including new packaging material, novel system-level electrical, structural and thermal design and cost-effective manufacturing possess, compatible with WBG semiconductor devices in high temperature utility.

Substrates and die-attachment technology would naturally to be considered as key components in the packaging technological advancement for WBG-based power electronics system. Apparently, traditional materials for die-attachment, such as lead-tin (SnPd) solder, lead-free solder (SnAgCu), and conductive adhesive, are not suitable for high-power and high-temperature applications, simply due to the fact that their melting or degradation temperatures are usually below 250°C [3]. Eutectic gold-based alloy, e.g. Au-Sn, could be one of the potential candidates for high-power applications since it possesses superior corrosion resistance [4]. However, it was reported that eutectic gold-based alloy had the reliability issues for its microstructural-induced early crack initiation [5]. In addition, it required higher possessing temperature and not really cost-effective for manufacturing

due to higher market pricing of gold.

On the other hand, silver-based die-attachment materials seemed to be more promising candidates for high-power applications, since silver has the highest electrical and thermal conductivity among all metallic materials. The most popular approach is silver nano-sintering for die-attachment [6]. The molecular dynamics simulation study has shown that isolated silver nanoparticles would have lower melting temperature, down to about 350°C [7]. As a result, it facilities high melting temperature joint forming at relative lower possessing temperature by nano-participles aggregation and agglomeration [8]. Indeed, silver nano-sintering is very attractive emerging die-attachment method for high-power applications. Some reliability issues, such as oxidation [9] and high temperature mechanical degradation [10, 11], associated with the porous nature of silver nano-sintering due to organic degassing might need to be addressed in the future work.

Our research group has been dedicating on the study of Ag-In binary system for bonding applications over decades [12]. With the idea of transient liquid phase (TLP) bonding, our group had shown that high-temperature Ag-In alloy joint can be formed reliably at low possessing temperature [13]. The previous study had shown that the joint was virtually void-free by examining under scanning acoustic microscopy (SAM). However, it would induce two types of intermetallic compound (IMC) to the resulting joint, namely, Ag2In and AgIn2, which are brittle in their nature, and would detrimental to the overall mechanical behaviors of the resulting bonding structure [14]. Recently, our research group has discovered that the mechanical properties of silver-indium solid solution phase, which is designated as (Ag)-xxIn, are intriguingly great [15] due to the experimental fact that it exhibits lower yield strength and much higher values of elongation and ultimate tensile strength (UTS), if compared with pure Ag. Moreover, the authors have also discovered that silver-indium solid solution phase exhibits superior anti-tarnishing property by using quantitative experimental study approach [16], which potentially resolved the tarnishing issues associated with silver applications. Therefore, silver-indium solid solution could be one of the potential suitable material candidates for high-power devices die-attachment application. Our group had already shown some results of studies previously on successfully converting all IMCs into single phase silver-indium solution as bonding medium with

several steps of annealing [17, 18], which resulted in large improvement on the joint bonding strength.

In this chapter, the author would like to introduce an alternative method to fabricate a layer of homogeneous single phase thin film of silver-indium solid solution phase directly on Cu substrate by E-beam evaporation deposition, without the help of any further annealing steps. The resulting coated Cu substrate can be used as bondable substrate for high-temperature power electronics applications. In the following sections, the authors would like to first present E-beam evaporation deposition process in fabricating the bondable substrate, followed with the experimental results of grazing incidence X-ray diffraction (GIXRD) and X-ray photoelectron spectra (XPS) in order to characterize the phase, crystallography and surface composition of resulting thin film. Next, the experimental bonding results between silicon chips and the bondable Cu substrates will be discussed after examining the cross-sectional images of optical microscope (OM) and scanning electron microscope (SEM) respectively. The preliminary bonding results of fabricated bondable Cu substrate indicated that a low temperature and cost-effective possess could be developed with solid-state bonding technology, using silver-indium solid solution as bonding medium layer. Finally, the implications and potential applications will be addressed, which could be meaningful and interesting to those researchers and engineers in the community of high-power electronics and electronic packaging technology.

8.2 Experimental Process

8.2.1 Bondable Substrate Fabrication

According to Ag-In binary phase diagram [19], the maximum solubility of indium atoms in silver lattice is 20 at. %. In order to be consistent with our previous studies [15, 16], the initial intended values of indium concentration in silver-indium solid solution phase thin film were 9.5 at. % and 19 at. %, and were designated as (Ag)-9.5In and (Ag)-19In respectively. E-beam evaporation was chosen for the deposition silver-indium solid solution thin film layer on Cu substrates, using Angstrom Engineering evaporator in Irvine Materials Research Institute (IMRI).

The authors have selected commercial available 1/4 hard Cu sheet with 1 mm thickness as the starting point of the fabrication of bondable Cu substrate. It is well known that Cu can be easily oxidized after exposed to air after a period of time, and the resulting the copper oxide layer on the surface will prevent further solid state bonding from success. Therefore, one of the initial motivations to coat a layer of silver-indium solid solution on the surface of copper is to prevent Cu oxidation, while less suffering from tarnishing issues induced by pure silver. The initial Cu sheet was polished on one-side with mirror finish, and protected with a layer of peel-off polymer film. The Cu sheet was firstly cut into the size of 10 inch × 7.5 inch (25.4 mm × 19 mm), and then mounted on the substrate stage of the E-beam evaporator with the polished side facing up. It is crucial that only peel off the protective polymer layer on Cu substrate upon the moment before loading the sample substrate stage into the E-beam evaporation chamber, in order to prevent Cu from oxidation. The raw materials of pure silver and indium shots with 99.99 wt. % purity were weighed, uniformly mixed and loaded into a graphite crucible for the following E-beam evaporation. Different ratios of amount of silver and indium shots need to be carefully adjusted in order to achieve the intended indium concentration values of silver-indium solid solutions thin films. The E-beam chamber is ready to conduct the deposition after pumping down to the high vacuum level to 2×10^{-8} torr. The raw material in the crucible need to be pre-soaked with E-beam swirling pattern in order to achieve complete melting, and the loaded Cu substrates can be protected by a shutter during pre-soaking process. During the real E-beam evaporation process, the deposition rate is monitoring all the time by quartz crystal microbalance (QCM), and can be precisely controlled by using proportional–integral–derivative (PID) controller with a negative feedback mechanism. The substrate stage was in-plane rotating constantly at 60º/s during the deposition to ensure the uniformity and homogeneity for different areas and different samples. As a result, the deposition rate of the silver-indium solid solution is precisely set at 1 Å/s within ± 5% error of tolerance. The intended thickness of the silver-indium solid solution coating layer is about 200 nm. The authors would like to note that this value is only a preliminary one, and further study need to be done in order to optimize the thickness of the coating layer for the bondable copper substrates fabrication.

8.2.2 Grazing Incidence X-ray Diffraction Characterization

fter the fabrication of bondable Cu substrates, the samples need to be further characterized with GIXRD in order to study and confirm the phase and crystallography of coating thin film layer on the substrates. The GIXRD experiments were conducted with Rigaku SmartLab X-ray diffractometer in IMRI using collimated Cu Kα line excitation X-ray source and parallel beam (PB) mode. The grazing angle of incidence (Ω) was optimized at 0.75 °in order to achieve optimal intensity of GIXRD signal from thin film layer, while maintaining a certain level of signal intensity from the underneath Cu substrate. The collected GIXRD data were analyzed by PDXL, an integrated powder X-ray analysis software package, and matched with The International Centre for Diffraction Data (ICDD) standard card, No. 03-065-9808 and No. 03-065-9743 for phase identification respectively.

As a result, the GIXRD patterns for bondable substrate coated with (Ag)-9.5In and (Ag)-19In were plotted and shown in Fig. 8.1, and crystallographic information of silver-indium solid solutions was summarized in Table 8.1 for further analysis. In Table 8.1, (h, k, l) is the Miller's indices with classic denotation, d is the d-spacing value for corresponding crystal plane, and a is the calculated lattice constant by using the values of each d-spacing.

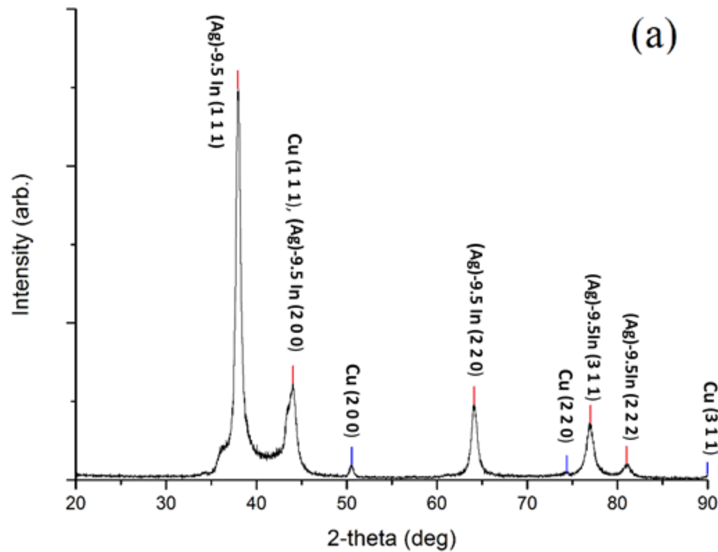

Fig. 8.1 (a) GIXRD patterns of (Ag)-9.5In on Cu substrate,

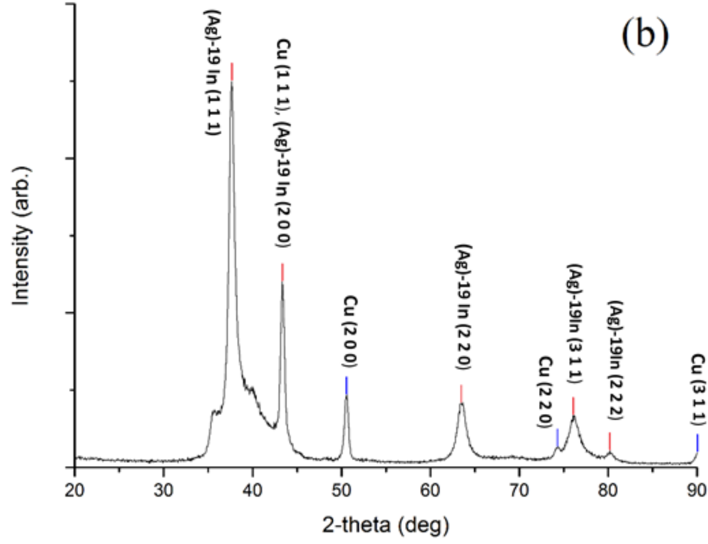

Fig. 8.1 (b) GIXRD patterns of (Ag)-19In on Cu substrate.

2θ (deg)	**d** (Å)	(h, k, l)	**a** (Å)
37.914	2.371	(1 1 1)	4.107
43.991	2.057	(2 0 0)	4.114
64.067	1.452	(2 2 0)	4.107
76.881	1.239	(3 1 1)	4.109
80.925	1.187	(2 2 2)	4.112

Table 8.1 (a) Crystallographic information of silver-indium solid solutions of (Ag)-9.5In film,

2θ (deg)	**d** (Å)	(h, k, l)	**a** (Å)
37.582	2.394	(1 1 1)	4.146
43.312	2.079	(2 0 0)	4.158
63.502	1.465	(2 2 0)	4.144
75.954	1.253	(3 1 1)	4.155
79.994	1.199	(2 2 2)	4.155

Table 8.1 (b) Crystallographic information of silver-indium solid solutions of (Ag)-19In film.

As shown in Fig. 8.1, the peaks of GIXRD pattern were labelled with red and blue color, which were corresponding to silver-indium solid solutions coating and copper substrate respectively. It is very clear that (Ag)-9.5In and (Ag)-19In resemble the crystal structure of pure silver, face-centered cubic (FCC) crystal structure, since their major peaks are showing typical systematically peaks absence. As shown in Table 8.1, the weighted average values for lattice constants are 4.110 Å and 4.152 Å for (Ag)-9.5In and (Ag)-19In thin film coating, which obey Vegard's Law and are consistent with our previous study. Therefore, it is confirmed that the compositions of E-beam evaporated thin film coatings on the Cu substrates are indeed within silver-indium solid solution phase range.

8.2.3 X-ray Photoelectron Survey Spectral Results

After confirmation the phase of silver-indium solid solutions coating with GIXRD, the indium concentration of films still need to be examined quantitatively and to be determined precisely for further study. Since the thin film is as thin as 200 nm, the traditional test method for bulk materials, such as energy dispersive X-ray spectroscopy (EDX) with SEM is not suitable for the characterization of this type of sample due to the fact that interaction volume is too large. X-ray Photoelectron Spectroscopy (XPS) is highly surface sensitive experimental techniques due to the fact that 95 percentage of the detected signal is contributed from topmost surface atomic layers within approximately 5 nm. Therefore, XPS is the ideal experimental characterization method to quantitatively study the surface compositions of our silver-indium solid solutions coating films.

The AXIS Supra by Kratos Analytical in IMRI was used for XPS quantification of the silver-indium solid solutions coating film. The XPS characterization experiments were performed with a monochromatized Al Kα radiation source ($\hbar\omega$ = 1486.6 eV) under ultra-high vacuum (UHV) operated below 1×10^{-8} torr. XPS survey spectra were obtained by scanning of the analyzer using step of 1 eV with a dwell time of 300 ms, and the recorded survey spectra can be used for the following quantification analysis. The gas cluster ion source (GCIS) system inside the AXIS Supra was used to clean the surface to remove native oxide and surface contamination with Ar+ ions. After quantification by the XPS analytical software, CasaXps, the cleaned surface compositions of the

samples can be precisely determined with sensitivity as high as 0.01 at. %, using intensity and areas of survey spectral peaks in Ag 3d and In 3d regions. The relative sensitive factors (R.S.F.) used for the quantification were 18.04 and 22.54 for Ag and In respectively. As results, the measured survey spectra were recorded and plotted in Fig. 8.2, and all of show-up peaks were labelled properly in the figures. As shown in Fig. 8.2, the quantification results of the indium concentration in the coating films were 9.86 at. % and 19.70 at. % for (Ag)-9.5In and (Ag)-19In respectively, within 1 at. % error tolerance from intended values.

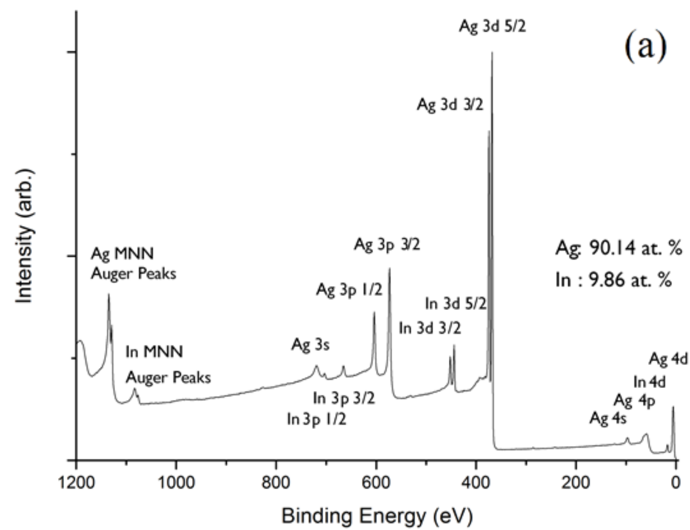

Fig. 8.2 (a) XPS survey quantification results of (Ag)-9.5In film coating,

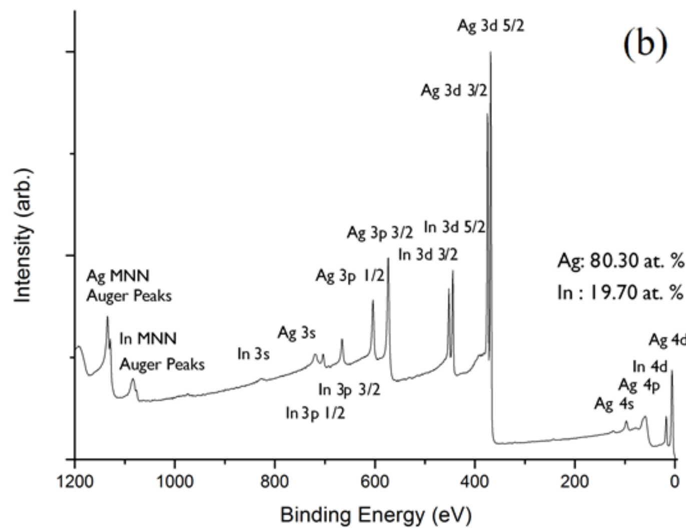

Fig. 8.2 (b) XPS survey quantification results of (Ag)-19In film coating.

Therefore, with experimental data support from GIXRD and XPS results, it is conclusive to confirm that the compositions of E-beam coated films of silver-indium solid solutions on Cu substrates were the intended values of initial design within acceptable error of tolerance, and should be good enough for further bonding experimental study.

In words, the bondable Cu substrates with silver-indium solid solutions coating with various compositions have been successfully fabricated with phase and surface composition confirmed with GIXRD and XPS experimental methods.

8.3 Solid-State Bonding Experimental Results and Discussions

8.3.1 Solid-state Bonding Experimental Parameters

Essentially, the bondable copper substrates were designed and fabricated for the high-power electronics semiconductor die-attachment utility. Due to the fact that price of single crystal WBG semiconductor wafer, such as SiC and GaN, is still really high, the authors would like to firstly demonstrate the bondability of fabricated bondable copper substrates with silicon dummy chips as a good starting point. The silicon wafer was coated with back-side metallization layers of Cr/Au (30 nm/100 nm), and then diced into the sized of 5 mm × 5 mm silicon dies with a thickness of 250 μm for the subsequent bonding experiments. In this paper, the authors have chosen bondable Cu substrates with (Ag)-9.5In coating as the primary bonding experimental study subjects.

The bonding experiments between Si chips and bondable Cu substrates were performed in the laboratory with a vacuum bonding furnace well-descripted in the reference paper [20]. The authors have applied 1000 psi (6.9 MPa) static pressure on the silicon chips with 300 °C under intermediate level of vacuum (0.1 Torr) to achieve solid-state bonding. With preliminary qualitative shear test by tweezers, it has shown that a strong bonding between Si chip and bondable Cu substrate has been achieved. After the solid-state bonding, the bonded samples were mounted into epoxy molding compound, and then further cut by slow diamond saw to reveal the cross-sectional bonding interfaces. Lastly, the bonded samples were polished with sequence of silicon carbide clothes, and

mirror-surface finished with diamond suspension particles fine-polishing. The resulting cross-sectional bonding interfaces can be further examined and studied under OM and SEM.

8.3.2 Optical Microscope Imaging Results

As shown in Fig. 8.3, the cross-sectional bonding interfaces were observed under optical microscope for initial bonding quality evaluations at various magnifications. As shown in Fig. 8.3 (a), the global cross-sectional view at lower magnification of bonded sample exhibited that silicon chip was well sit on the copper substrate without visible damages or die-lifting issues induced by coefficient of thermal expansion (CTE) mismatch between silicon die and copper substrate. However, the bonding interface can be barely seen at 100× magnification. If we increase the magnification by ten times and focus on the bonding interface, as shown in Fig. 8.3 (b), then a distinct dark line across the entire bonding interface will be seen clearly. However, the authors cannot identify whether the dark line is the bonding medium, i.e., silver-indium solid solution layer or simply a straight long micro-crack at the bonding interface because it has already reached the resolution limitation of optical microscope. Since the bonding structure has shown a good bonding strength initially, the authors would expect that the dark line is corresponding to the bonding layer rather than a micro-crack. As a result, bonded samples must be further examined under SEM with higher magnification and resolution to offer better imaging of the cross-sectional bonding interface.

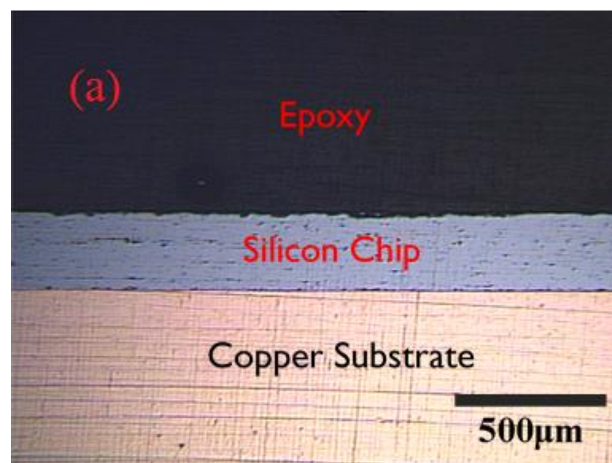

Fig. 8.3 (a) Optical microscope images of solid-state bonding results between (Ag)-9.5In coated bondable substrate and silicon chip at 100× magnification,

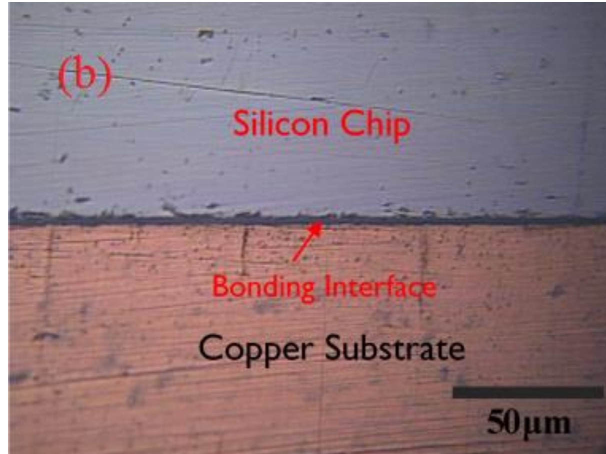

Fig. 8.3 (b) Optical microscope images of solid-state bonding results between (Ag)-9.5In coated bondable substrate and silicon chip at 1000× magnification.

8.3.3 Scanning Electron Microscope Imaging Results

The Philips XL-30 SEM in IMRI was used for the SEM imaging and the cross-sectional bonding interface was observed at various magnifications. As shown in Fig. 8.4, the author can still observe the dark line at the bonding interface clearly at relative low magnification. With the SEM imaging zoomed-in further with higher magnification, the bonding interface become much clearer so that the authors can safely confirm that the original dark line is the bonding medium layer. In other words, the sample was truly well-bonded.

If observed more carefully, we can easily find out that the surface roughness of original Cu substrate without coating is about hundreds of nanometers, even though it was fine-polished by the manufacturer. The most fundamental underlying mechanism of solid-state bonding other than inter-diffusion is to achieve atomic-level intimate contact in the first place [21].With such large surface roughness and oxidation issues, it is relatively hard to directly bond the Cu substrate with silicon chip using solid-state bonding, because the most of bonding areas cannot reach the atomic-level intimate contact distance, rendering the bonding structure with a relatively poor strength or simply not bonded at all.

On the other hand, the bondable Cu substrate was coated with a layer of silver-indium solid solution so that it can be well-bonded with silicon chip using solid-state bonding. The role of silver-indium

solid solution layer is to prevent Cu substrate from oxidation from the initial design point of view. After observed with SEM, it can also improve the quality of the bonding surface roughness. With the solid solution softening mechanism in silver-indium solid solution, the (Ag)-9.5In has exhibited much lower yield strength compared with pure Ag so that it can be deformed plastically, thereby accommodating the different profiles of bonding interfaces with its bonding pair in order to achieve atomic-level intimate contact. Furthermore, (Ag)-9.5In has exhibited much longer elongation and UTS at same time so that it can also accommodate large deformation and strain energy generated during the solid-state bonding and CTE mismatch induced stress and strain during the period of cooling down to room temperature without breakage. The bonding medium layer in the SEM picture is very uniform and dense, so that the authors expect that it would have good mechanical strength and good thermal reliability. After SEM/EDX measurement and analysis, the major elements in bonding medium layer are Au, Ag, In and small amount of Cr. Therefore, the resulting bonding medium layer should be corresponding to Au-Ag-In ternary phase. The thickness of the bonding medium layer is larger than our expectation and will be further investigated in the future work.

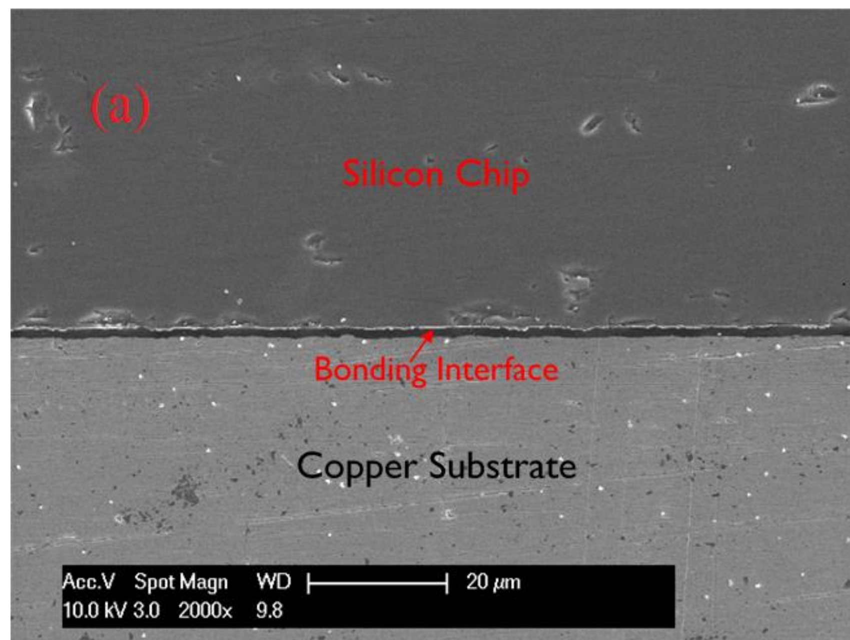

Fig. 8.4 (a) Scanning electron microscope image of solid-state bonding results between (Ag)-9.5In coated bondable substrate and silicon chip at 2000 × magnification,

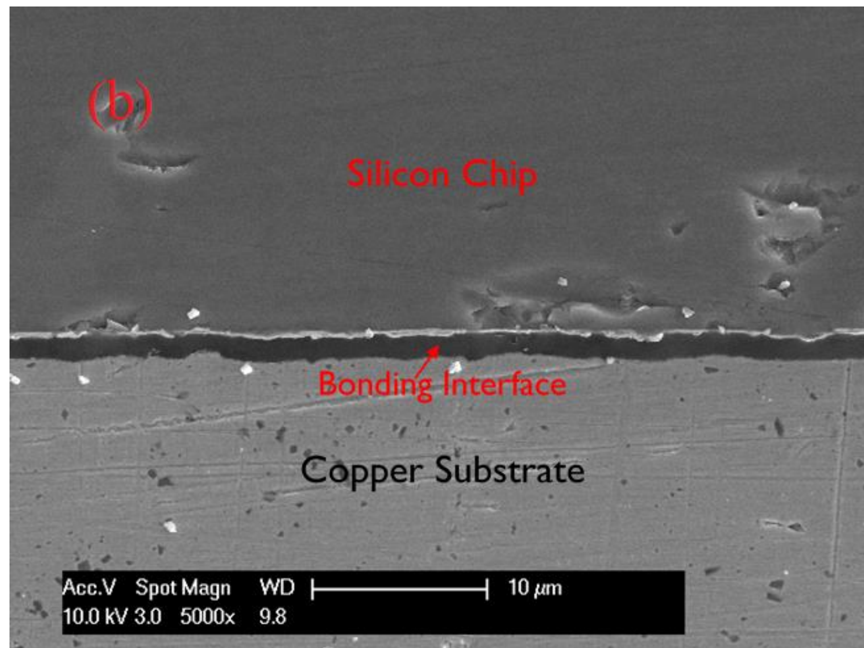

Fig. 8.4 (b) Scanning electron microscope image of solid-state bonding results between (Ag)-9.5In coated bondable substrate and silicon chip at 5000 × magnification,

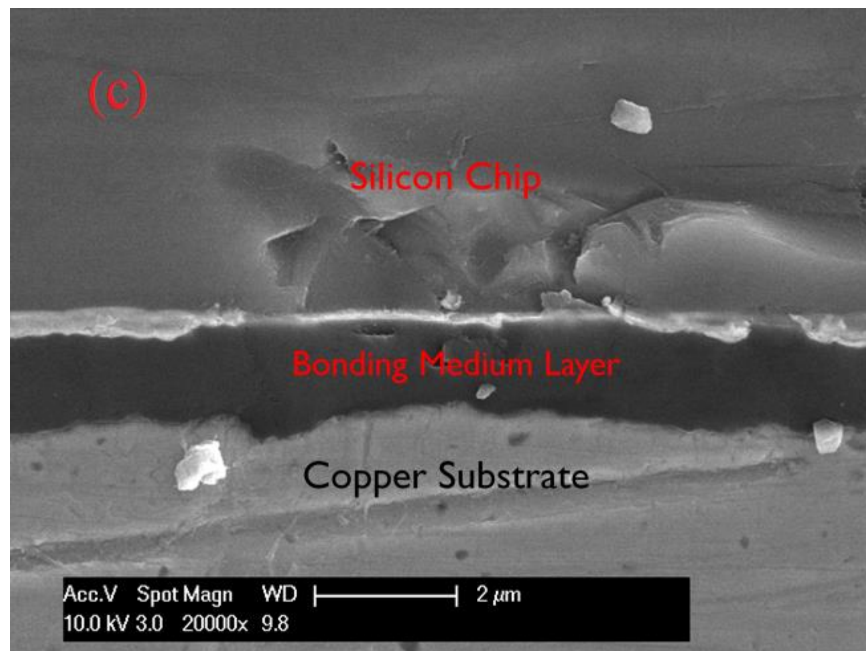

Fig. 8.4 (c) Scanning electron microscope image of solid-state bonding results between (Ag)-9.5In coated bondable substrate and silicon chip at 20000 × magnification,

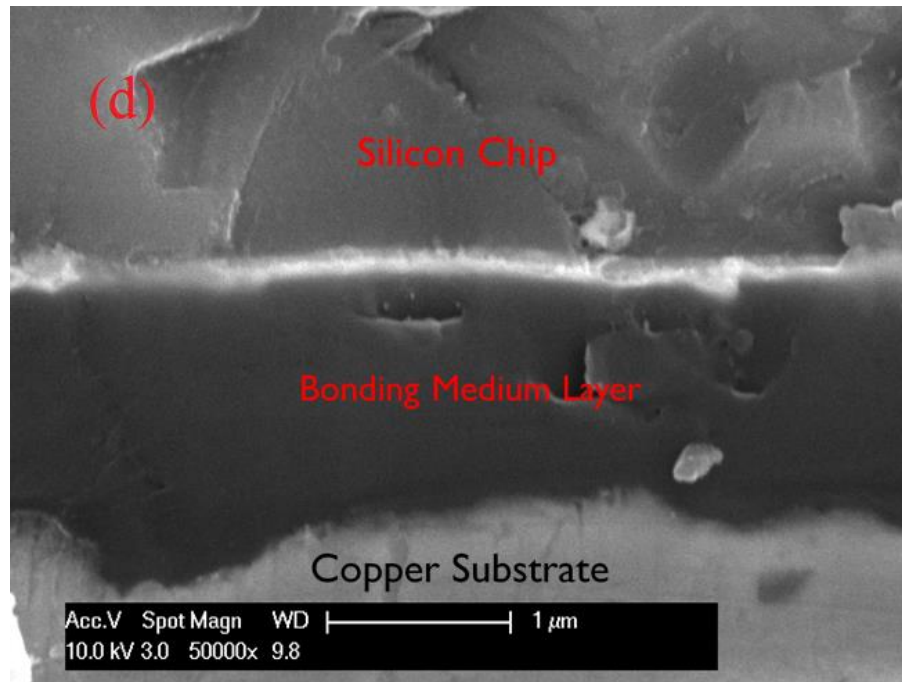

Fig. 8.4 (d) Scanning electron microscope image of solid-state bonding results between (Ag)-9.5In coated bondable substrate and silicon chip at 50000 × magnification.

In summary, the preliminary results of solid-state bonding between silicon chips and bondable Cu substrate have shown a great bondability with its low-yield strength and smooth bonding surface. Therefore, the author would like to share this qualitatively promising result with electronic packaging research community. Future works, such as shear test, thermal cycling (TC) and high temperature storage (HTS), will be addressed in order to the quantitatively study the bonding strength and reliability for the fabricated bondable Cu substrates.

8.4 Bondable Copper Substrates Quality Evaluations

To the experience of the author, the solid-state bonding is highly related to the quality of the bonding interfaces in terms of surface roughness, surface flatness, oxidation and contamination conditions, and etc. Therefore, it is crucial to evaluate the quality of our fabricated bondable copper substrates with Ag-In solid solution coating. In addition, the thickness of the coating layer need to be confirmed with more direct measurement method. As results, a global view of the surface of bondable Cu

substrate is shown in Fig. 8.5. The surface roughness of Cu substrate can be clearly seen from the SEM image, where the E-beam deposited (Ag)-9.5In conform to original morphology of the Cu substrate. Furthermore, with FIB techniques that were described in chapter 2, the author would be able to have a clear view of the cross-sectional imaging of the bondable substrate with coating layer. The main advantage of FIB cutting to prepare cross-sectional sample is avoiding the "smear effect" induced by mechanical polishing for the regular cross-sectional sample preparation. After Pt protection layer deposition, the sample was cut with FIB and fine-cleaning in order to reveal its cross-section without smear or deformation. As a result, as shown in Fig. 8.6, the damage free cross-sectional imaging of the bondable substrate with coating layer can be used as a direct measurement method to determine the thickness of the coating layer. In the batch, the author has increased the thickness of (Ag)-9.5In coating of the bondable substrate to 300 nm. The thickness measurement result of (Ag)-9.5In thin film is 388.7 nm under SEM with 52 degree tilt angle. With the reference of 2 μm Pt FIB deposition layer, the thickness can be calibrated to conduct tilted correction, resulting in 313.5 nm. The result shows that the E-beam deposition rate was well-controlled, a little bit higher than 300 nm as intended.

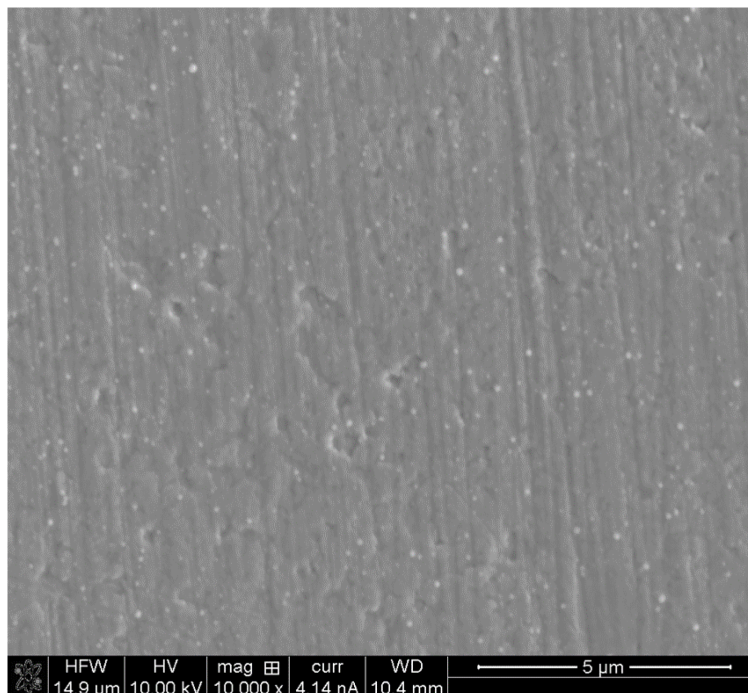

Fig. 8.5 The SEM image of the surface of bondable Cu substrate.

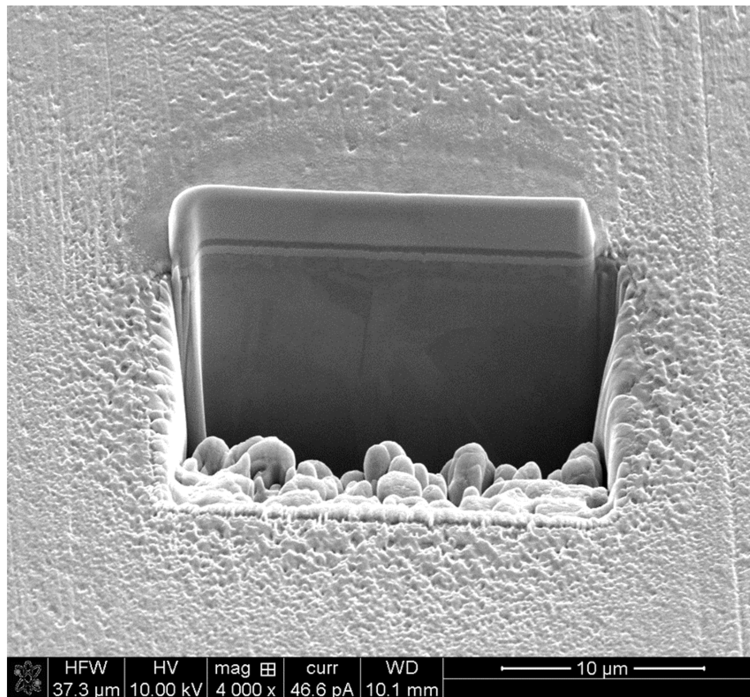

Fig. 8.6 (a) The SEM cross-sectional image of bondable Cu substrate after Pt deposition and FIB cutting,

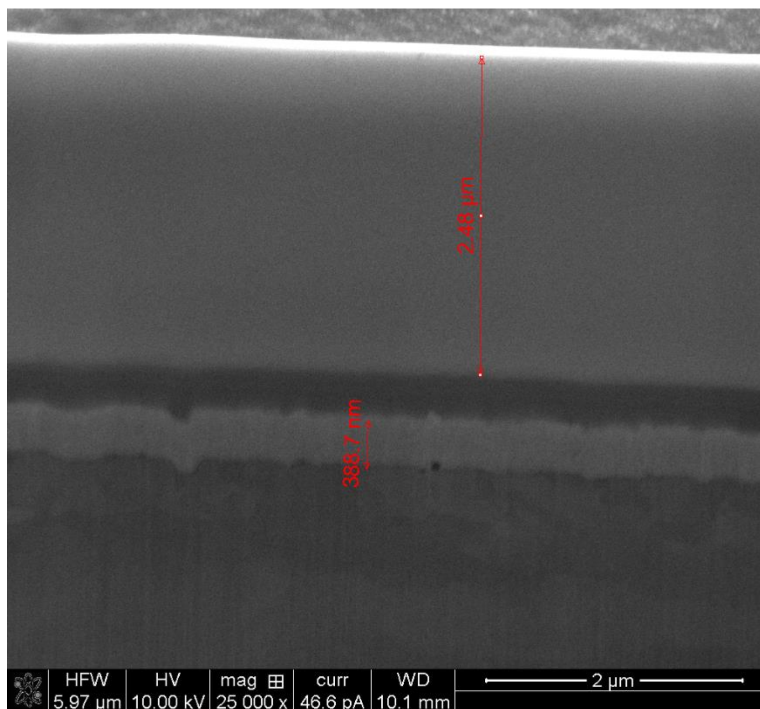

Fig. 8.6 (b) Zoomed-in SEM cross-sectional image of bondable Cu substrate after Pt deposition and FIB cutting with direct measurement of the (Ag)-9.5In coating layer.

Since the surface roughness of the bonding interfaces are crucial to the solid-state bonding technique, a direct surface roughness measurement is indeed needed and can be readily done by AFM method which was described in chapter 7. As a result, the Keysight 7500 AFM was used to conduct the AFM measurement in contact mode. The AFM measurement results are shown in Fig. 8.7, Fig. 8.8 and Fig. 8.9.

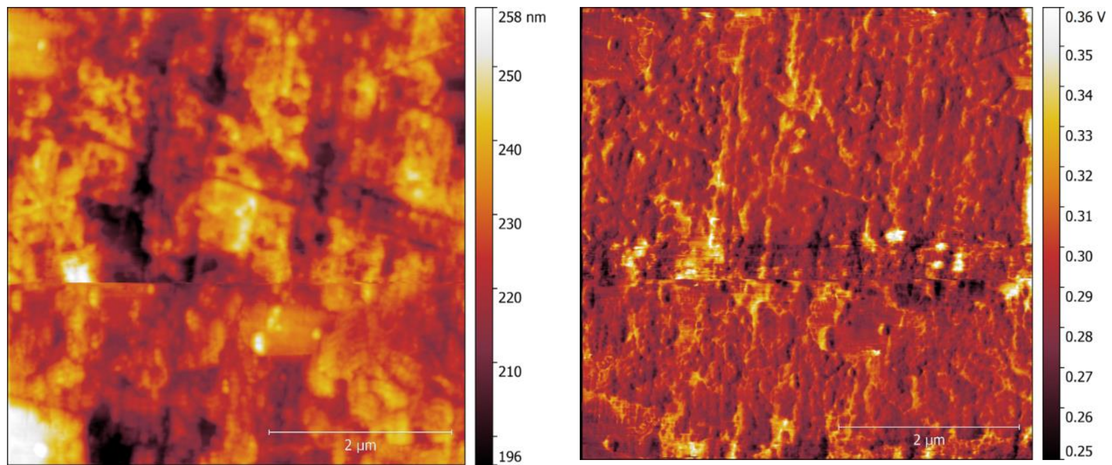

Fig. 8.7 AFM measurement results of (Ag)-9.5In coating layer of bondable copper substrate sample with 5µm × 5µm measured area size, topography AFM image (left) and friction AFM image (right).

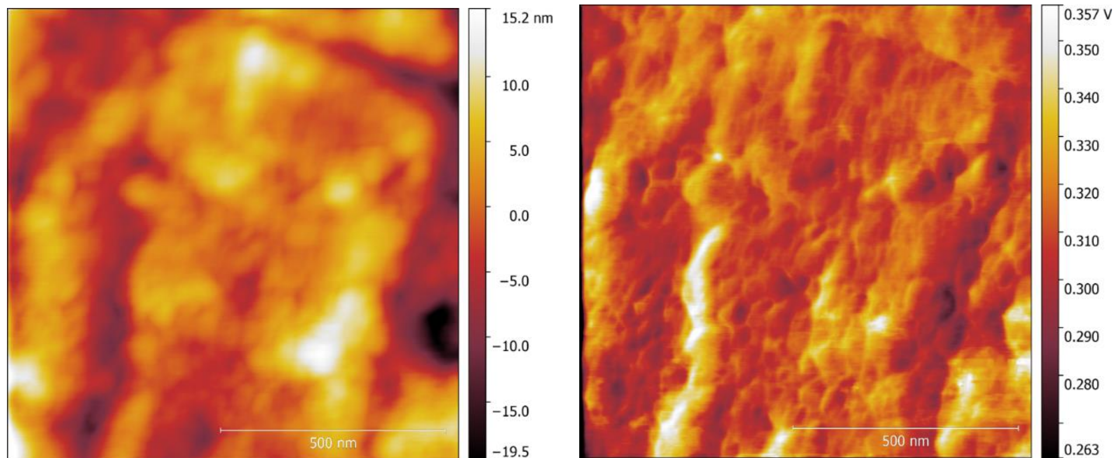

Fig. 8.8 AFM measurement results of (Ag)-9.5In coating layer of bondable copper substrate sample with 1µm × 1µm measured area size, topography AFM image (left) and friction AFM image (right).

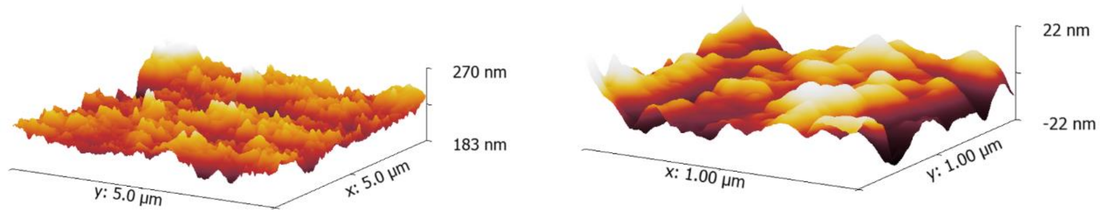

Fig. 8.9 3D Topography AFM Image of (Ag)-9.5In coating layer of bondable copper substrate with 5μm × 5μm measured area size (left) and 1μm × 1μm measured area size (right).

As shown in the AFM result, (Ag)-9.5In coating layer of bondable copper substrate exhibits larger surface roughness that previous E-beam deposited Ag-In thin film on quartz substrate, with global surface roughness around ±40 nm and local surface roughness around ±20 nm. Therefore, the surface roughness of the coating layer can be affected by the original substrate. Since our preliminary solid-state bonding results indicate that a good jointing has been achieved, the author would like to tentatively conclude that the surface roughness of resulting bondable substrate is good enough for solid-state bonding purposes. Further study might be needed in order to optimize the parameters such as the thickness of coating layer and surface roughness of the original substrates.

8.5 TEM Evaluation of 4H-SiC Chip with Cr/Au Metallization Layers

The purpose of the research and development of bondable copper substrate is eventually providing a compatible electronic packaging technology for the SiC-based high-temperature power electronics utility. Therefore, it is essential to study the 4H-SiC chip and its metallization layers for the development of its die-attachment and substrates materials and technology. Fortunately, the author would be able to get some 4H-SiC wafers from II-VI Incorporated, knowing that single crystal 4H-SiC wafers is still extremely expensive right now. As results, 2-inch (50.8 mm) single crystal n-type 4H-SiC wafers were deposited with metallization layers of 30 nm chromium (Cr) and 100 nm Au sequentially using electron beam evaporation system in Integrated Nanosystems Research Facility (INRF), which was done by our research previous members. The Cr layer acts as the adhesion layer since it exhibited good interfacial bonding strength to most of semiconductor. The Au layer can

protect Cr from oxidation when exposed to air and act as the electroplating seed layer for the following process. After metallization, the wafers were further diced into 8 mm × 8 mm 4H-SiC dies.

Transmission Electron Microscopy (TEM) can offer much higher spatial resolution and magnifications than SEM, therefore, it is very suitable for the study of 4H-SiC chip and its metallization layers evaluation. The cross-sectional TEM sample can be prepared by the FIB lift-off process. This FIB cut/lift-off TEM sample preparation method can save a lot of time and get a better damage-free TEM sample as compared with traditional grinding and dimpling method (usually takes a few days to prepare one TEM sample). The general procedure of this FIB cut/lift-off TEM sample preparation can be divided into ten major steps, which are listed as following:

1. Load-in the bulk sample and TEM grids into SEM/FIB dual beam system chamber.
2. Optimize SEM/FIB beam conditions.
3. E-beam/FIB deposition: a strip of Pt for TEM sample surface protection.
4. Two steps of FIB rough cutting.
5. Cleaning cross section with weaker FIB beam.
6. FIB cutting one side and the bottom of TEM sample.
7. Attach the TEM sample top surface to Omniprobe tip.
8. FIB cutting the other side and lift out TEM sample.
9. Attach TEM sample to TEM grid.
10. Final thinning TEM sample to electron-beam transparent thickness with FIB.

As shown in Fig. 8.10, the TEM sample was cut from 4H-SiC chip sample with Cr/Au metallization layers. After attached to TEM grid, the sample need to be further thinning to electron-beam transparent thickness (less than 200 nm and less than 20 nm for high resolution TEM) with several steps of FIB cutting, using lower and lower voltage and current. As a result, a cross-sectional TEM sample of 4H-SiC chip with Cr/Au metallization layers was successfully prepared and can be used for further TEM imaging and evaluations.

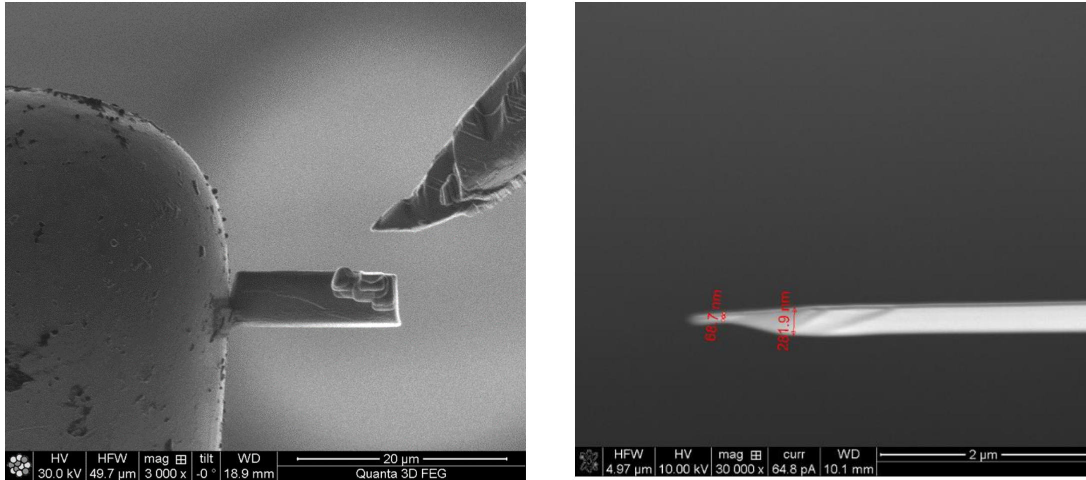

Fig 8.10 FIB cut/lift-off TEM sample as attached to the TEM grid and detached from Omniprobe (left) and the TEM sample electron electron-beam transparent thickness as finished the final steps of FIB thinning with low voltage (5 kV) and small current.

Furthermore, the cross-sectional TEM sample of 4H-SiC chip was evaluated under TEM, using FEI/Philips CM-20 conventional TEM. As shown in Fig. 8.11, the picture of Cr/Au layers on the 4H-SiC chip are captured with the bright field TEM imaging. From the picture, the author can clearly the E-beam Cr/Au layers have a well-controlled thickness (130 nm) and grains within several nano-meters.

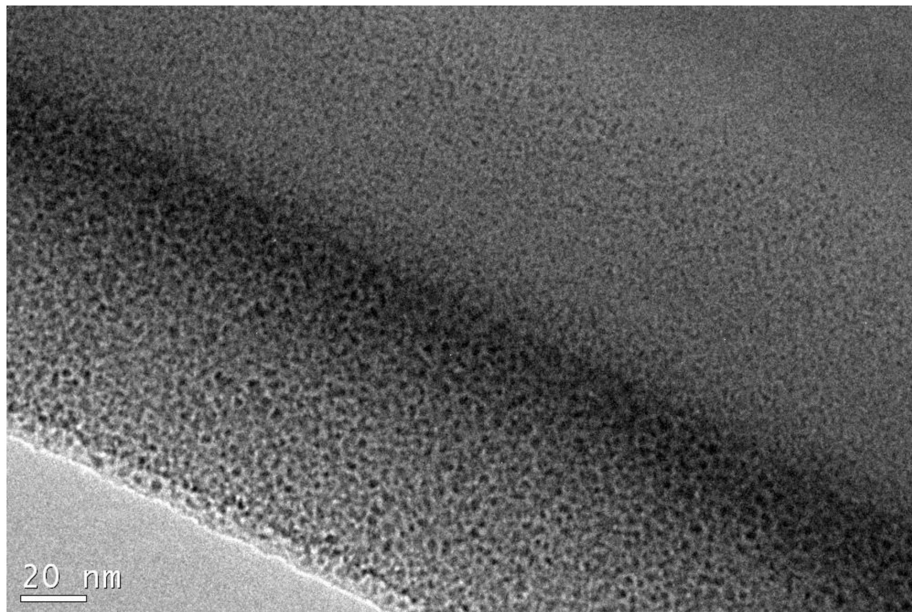

Fig. 8.11 The bright field TEM imaging of Cr/Au E-beam layers on the 4H-SiC chip.

FEI/Philips CM-20 conventional TEM is relatively old instrument, so that it is very hard to get a good picture of high resolution TEM (HRTEM). With the new equipped TEM in IMRI TEM center, JEOL 2800 TEM, the HRTEM can be captured from the prepared cross-sectional TEM sample of 4H-SiC chip with Cr/Au e-beam layers. As shown in Fig. 8.12, the fringes of the single crystal SiC lattice can be clearly observed from the HRTEM imaging, which ensure the good quality of the grown single crystal 4H-SiC wafer. Moreover, a Fast Fourier Transformation (FFT) can be done to show the electron diffraction patterns of our TEM sample under the viewing image. The diffusing plate of the electron diffraction patterns means that there is a certain degree of amorphous portion in the Cr/Au e-beam layers. The multiple rings corresponds to the nano-polycrystalline of the Cr/Au layers. The space group symmetry of 4H-SiC single crystal can be observed from the spots of the electron diffraction patterns. This is only very beginning of our TEM study. With the FIB TEM sample preparation and HRTEM imaging techniques available to our research group, the true nature of the bonding structure in atomic-level will be unveiled very soon. An advanced solid-state bonding technique and theory for the utility of the high-temperature power electronics can be possibly developed from this fancy experimental technique. Personally, I would to thanks to my colleague, Dr. Jiaqi Wu, in our research group in developing the TEM sample preparation with me and in providing the TEM images.

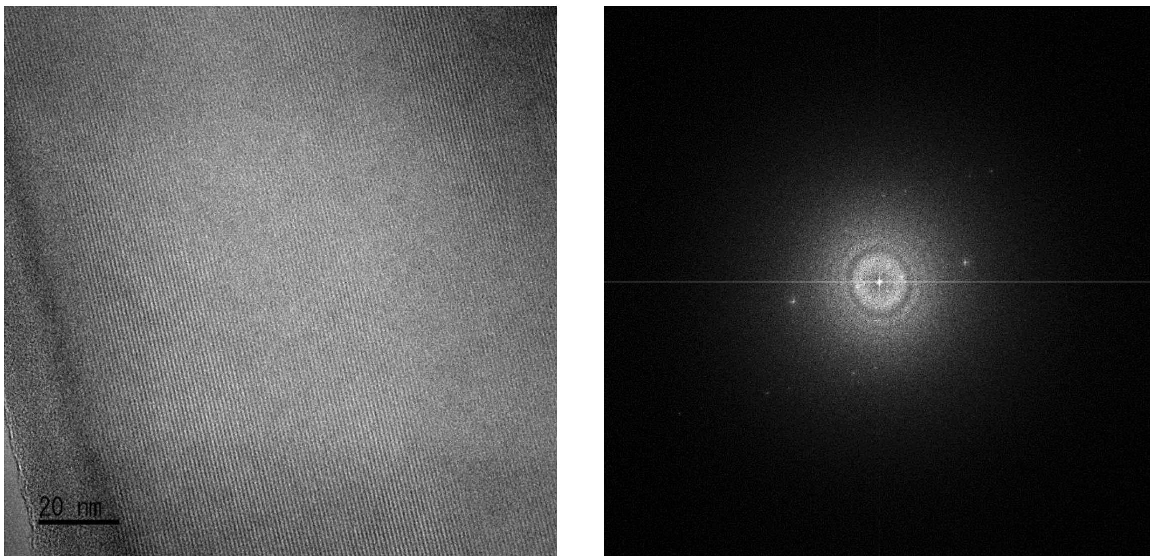

Fig. 8.12 HRTEM imaging of Cr/Au layers on the 4H-SiC single crystal (left) and FTT electron diffraction patterns under the view of HRTEM (right).

8.6 Summary

In this chapter, the author has demonstrated that the design and successful fabrication of bondable Cu substrates with silver-indium solid solution coatings without using any steps of annealing. In addition, the quality of coating layers of the bondable Cu substrates was examined by SEM/FIB and AFM. At last, the 4H-SiC single crystal chip with Cr/Au metallization layers has been made into TEM cross-sectional sample, using FIB cut/lift-off technique, and was further examined and evaluated by using conventional TEM and HRTEM. In terms of real applications, the industry should be able to have ability to transfer the bondable Cu substrates into mass-production products cost-effectively. The preliminary bonding results have implied that the bondable Cu substrate with silver-indium solid solution coating is a promising candidate for high-power electronic devices die-attachment applications. With distinct advantages of silver-indium solid solution and its high melting temperature (>700°C), it is expected to be a promising candidate of metallic interconnection material which is compatible with emerging WBG semiconductor technology. Therefore, it should have a very broad applications in the fields of high-power electronics and photonics under extreme working environment, such as, electric utility vehicle (EUV), electrical power grid, solar-electrical power generation and outer-space exploration.

Reference in Chapter 8

1. T. Kimoto and J. A. Cooper. Fundamentals of Silicon Carbide Technology: Growth, Characterization, Devices and Applications. John Wiley & Sons, 2014.
2. H. S. Chin, K. Y. Cheong, and A. B. Ismail, "A review on die attach materials for SiC-based high-temperature power devices," Metallurgical and Materials Transactions B, vol. 41, No.4, pp.824-832, 2010.
3. K. N. Tu, Solder Joint Technology. New York: Springer, 2007.
4. G. S. Matijasevic, C. C. Lee, and C. Y. Wang. "Au-Sn alloy phase diagram and properties related to its use as a bonding medium," Thin Solid Films, vol. 223, No.2, pp. 276-287, 1993.
5. R. R. Chromik, D. N. Wang, A. Shugar, L. Limata, M. R. Notis, and R. P. Vinci, "Mechanical properties of intermetallic compounds in the Au–Sn system," Journal of Materials Research, vol. 20, No.8, pp.2161-2172, 2005.
6. M. Maruyama, R. Matsubayashi, H. Iwakuro, S. Isoda, T. Komatsu, "Silver nanosintering: a lead-free alternative to soldering," Applied Physics A, vol. 93, No. 2, pp. 467-470, 2008.
7. S. J. Zhao, S. Q. Wang, D. Y. Cheng, and H. Q. Ye, "Three distinctive melting mechanisms in isolated nanoparticles," The Journal of Physical Chemistry B, vol. 105, No. 51, pp.12857-12860. 2001.
8. P. Peng, A. Hu, A. P. Gerlich, G. Zou, L. Liu, and Y. N. Zhou, "Joining of Silver Nanomaterials at Low Temperatures: Processes, Properties, and Applications," ACS Applied Materials & Interfaces, vol. 7, No. 23, pp. 12597–12618, 2015.
9. S. Y. Zhao, X. Li, Y. H. Mei and G. Q. Lu, "Study on high temperature bonding reliability of sintered nano-silver joint on bare copper plate," Microelectronics Reliability, vol. 55, No. 12, pp. 2524-2531, 2015.
10. S. A. Paknejad, G. Dumas, G. West, G. Lewis, and S. H. Mannan, "Microstructure evolution during 300° C storage of sintered Ag nanoparticles on Ag and Au substrates," Journal of Alloys and Compounds, vol. 617, pp.994-1001, 2014.
11. S. T. Chua, and K. S. Siow, "Microstructural studies and bonding strength of pressureless sintered nano-silver joints on silver, direct bond copper (DBC) and copper substrates aged at 300° C,"

Journal of Alloys and Compounds, vol. 687, pp. 486-498, 2016.

12. Yi-Chia Chen, William W. So, and Chin C. Lee, “A fluxless bonding technology using indium-silver multilayer composites”, IEEE Transactions on Components, Packaging and Manufactuing technology - Part A, vol. 20, No.1, pp. 46-51, 1997.
13. R. W. Chuang and C. C. Lee, “Silver-indium joints produced at low temperature for high temperature devices,” IEEE Transactions on Components and Packaging Technologies, vol. 25, No. 3, pp. 453-458, 2002.
14. Y. Y. Wu, W. P. Lin, and C. C. Lee, “A study of chemical reactions of silver and indium at 180° C. Journal of Materials Science: Materials in Electronics, vol. 23, No. 12, pp.2235-2244, 2012.
15. Y. Huo and C. C. Lee, “The growth and stress vs. strain characterization of the silver solid solution phase with indium,” Journal of Alloys and Compounds, vol. 661, pp. 372-379, 2016.
16. Y. Huo, S. W. Fu, Y. L. Chen, C. C. Lee, “A reaction study of sulfur vapor with silver and silver-indium solid solution as a tarnishing test method,” Journal of Materials Science: Materials in Electronics, vol. 27, No. 10, pp. 10382-10392, 2016.
17. Y. Y. Wu, C. C. Lee, “The stregenth of high temperature Ag-In joins produced between copper by fluxless low-temperature processes,” Journal of Electronic Packaging, vol. 136, pp. 0110061-6, 2014.
18. Y. L. Chen, Y. Huo, and C. C. Lee, “Design and Fabrication of Silver Solid Solution Layer on Silicon and Its Solid-State Bonding Applications,” in Electronic Components and Technology Conference (ECTC), 2016 IEEE 66th, pp. 420-425. Las Vegas, NV, May 2016.
19. M.R. Baren, in Binary Alloy Phase Diagrams, ed. by T.B. Massalski, H. Okamoto (ASM Intl, Materials Park), pp. 47–48, 1990.
20. C. C. Lee, D. T. Wang and W.S. Choi, “Design and construction of a compact vacuum furnace for scientific research. Review of Scientific Instruments,” vol. 77, No. 12, pp. 125104-1–125104-5, 2006.
21. C.C. Lee and L. Cheng, “The quantum theory of solid-state atomic bonding,” in Electronic Components and Technology Conference (ECTC), 2014 IEEE 64th, pp. 1335–1341, May 2014.

Chapter 9

Conclusions and Future Perspectives

In the content of this dissertation, various physical properties of silver-indium solid solution and other silver-based alloys are studied for the research and development of future electronic packaging technology for the SiC-based high-temperature power electronics applications. The author has discovered that silver-indium solid solution exhibits superior mechanical properties, a great anti-tarnishing property and reasonable good thermal, electrical and optical property. Therefore, the silver-indium solid solution should have potential wide applications in the electronics industry as high-temperature die-attachments material for SiC-based power devices, using rapid solid-state bonding techniques. Moreover, a comprehensive semi-quantum-mechanical theory that incorporated with HN d-band model has been developed, within the context of HSAB and its conceptual DFT formalization, in order to explain the underlying mechanism behind the mysterious anti-tarnishing property of Ag-In alloys. Solid solution softening phenomenon has been observed in Ag-based solid solutions (FCCs), which could possibly correlate with high ductility of Ag-In solid solutions. With the preliminary solid-state bonding results, the bondability of Ag-In solid solution to Cu substrate and semiconductor chip has been investigated and proven to be good enough for future industrial utility.

In terms of future study, some insights perspectives can be shared to the point of view of the author. First of all, one could try to apply Ag-In solid solution to SiC-based high-temperature power electronics applications to utilize its superior mechanical properties and anti-tarnishing property. Further Investigations can be conducted on the research topic of solid solution softening mechanism in FCCs. With the FIB/TEM sample preparation techniques available, one could study bonding structures/interfaces with advanced experimental techniques, such as, high-resolution TEM (HRTEM) and high-angle annular dark-field imaging (HAADF). One could also conduct more comprehensive studies on thermal, electrical and optical properties of Ag-In Alloys. Since all of the physical properties are close related to the valence and conduction band electrons, in principle, we could develop a multi-physical quantum-mechanical model as a co-design guidance to the metallic materials development in electronic packaging technology, best of all, from electrons to the system.

At last, I would like to express my gratitude towards all of the people who have helped me through my journey of PhD. education. Without those kindness and help, I could never finish this dissertation on my own. Thank you all!